Winter 12-15-2017

Investigation of Neonatal Pulmonary Structure and Function via Proton and Hyperpolarized Gas Magnetic Resonance Imaging

Nara Savoye Higano
Washington University in St. Louis

WASHINGTON UNIVERSITY IN ST. LOUIS

Graduate School of Arts and Sciences

Department of Physics

Dissertation Examination Committee:

Jason C. Woods, Chair

Mark S. Conradi, Co-Chair

Sophia E. Hayes

James G. Miller

Shankar Mukherji

Investigation of Neonatal Pulmonary Structure and Function via Proton and
Hyperpolarized Gas Magnetic Resonance Imaging

by

Nara Savoye Higano

A dissertation presented to

The Graduate School

of Washington University in

partial fulfillment of the

requirements for the degree

of Doctor of Philosophy

December 2017

St Louis, Missouri

Contents

List of Figures

List of Tables

List of Abbreviations

A-P   anterior-posterior

ADC   apparent diffusion coefficient

ANOVA   analysis of variance

au   arbitrary units

BPD   bronchopulmonary dysplasia

BW   bandwidth

CDH   congenital diaphragmatic hernia

CF   cystic fibrosis

CFD   computational fluid dynamics

CI   confidence intervals

CLD   chronic lung disease (of prematurity)

COPD   chronic obstructive pulmonary disease

CPAP   continuous positive airway pressure

CT   x-ray computed tomography

CXR   chest x-ray radograph

DOL   day of life

EA   esophageal atresia

FA   flip angle

FID   free induction decay

FOV   field of view

FT   Fourier transform

GA   gestational age

GRE   gradient-recalled echo

HP   hyperpolarized

iPFT   infant pulmonary function test

IRB   Institutional Review Board

MRI   magnetic resonance imaging

NHLBI   National Heart, Lung, and Blood Institute

NICHD   National Institute of Child Health and Human Development

NICU   neonatal intensive care unit

NMR   nuclear magnetic resonance

NRDS   neonatal respiratory distress syndrome

OP   optical pumping

PAH   pulmonary arterial hypertension

PETRA   pointwise encoding time reduction with radial acquisition

PFT   pulmonary function test

PIG   pulmonary interstitial glycogenosis

PMA   post-menstrual age

PPV   positive pressure ventilation

qCT   quantitative CT

qMRI   quantitative MRI

R-L   right-left

RF   radio frequency

ROI   region of interest

S-I   superior-inferior

SD   standard deviation

SE   spin exchange

SEOP   spin exchange optical pumping

SLR   Shinnar-Le Roux (RF pulse)

SNR   signal-to-noise ratio

T$_1$ spin-lattice relaxation time

T$_2$ spin-spin (transverse) relaxation time

T$_2$* effective transverse relaxation time

TE echo time

TEF tracheoesophageal fistula

TLV total lung volume

TR repetition time

UTE ultrashort echo time

ZTE zero echo time

List of Physical Constants

Avogadro's number	$N_A = 6.022 \cdot 10^{23}$
Bohr magneton	$\mu_B = 9.274 \cdot 10^{-24}$ J/T
Boltzmann constant	$k = 1.381 \cdot 10^{-23}$ J/K
Electron mass	$m_e = 9.109 \cdot 10^{-31}$ kg
Elementary charge	$e = 1.602 \cdot 10^{-19}$ C
Gas constant	$R = 8.205 \cdot 10^{-5}$ $(\text{m}^3 \cdot \text{atm}) / (\text{K} \cdot \text{mol})$
Gyromagnetic ratio of ^{1}H	$\gamma(^1\text{H}) = 2\pi \cdot 42.577$ MHz/T
Gyromagnetic ratio of ^{3}He	$\gamma(^3\text{He}) = 2\pi \cdot 32.434$ MHz/T
Gyromagnetic ratio of ^{129}Xe	$\gamma(^{129}\text{Xe}) = 2\pi \cdot 11.777$ MHz/T
Vacuum permeability	$\mu_0 = 4\pi \cdot 10^{-7}$ V $\cdot$ s/A $\cdot$ m
Nuclear magneton	$\mu_N = 5.051 \cdot 10^{-27}$ J/T
Planck's constant	$h = 6.626 \cdot 10^{-34}$ J $\cdot$ s
Proton mass	$m_p = 1.673 \cdot 10^{-27}$ kg
Speed of light	$c = 2.998 \cdot 10^8$ m/s

Acknowledgements

I would like to express my utmost gratitude to Professor Jason Woods, who regularly goes above and beyond the typical expectations of a research advisor. Joining Jason's lab from afar was a bit of a gamble, with little guarantee beforehand that it was a good fit, but the payoff has been immeasurable. Jason has truly embodied the role of a mentor for me, and I am ever thankful for his guidance, both explicitly and implicitly modeled, in my scientific and professional development.

I want to acknowledge the guidance and support of Mark Conradi, who provided me with a strong base in NMR physics and allowed me to get my experimentalist toes wet in his lab. Credit is due to Jim Miller and Sophia Hayes, who have provided helpful feedback since the beginning of my research, and to Shankar Mukherji, who has helped to make this dissertation stronger.

It has become increasingly clear to me throughout my graduate student tenure that networks and teams are a crucial component of the research process, so I sincerely thank each of my many collaborators for their contributions to our shared ideas and projects. Likewise, much of my work has built upon the cutting-edge MR engineering accomplishments of the Cincinnati Children's Imaging Research Center (IRC) and also has relied heavily on the dedication of the IRC patient coordinators and staff. I also want to thank the clinical teams from the Division of Pulmonary Medicine, the Department of Neonatology and Pulmonary Biology, and the Department of Radiology at Cincinnati Children's Department for their unwavering belief in the translational potential of this work, in addition to the NICU patients, organ donors, and families that participated in this research.

Starting a new chapter of life in an unknown town with unknown faces has the potential to make for difficult times; I had the opportunity to pack up and move not once but twice for my graduate studies. In both cases, the friendships I've found through the Physics Department at Washington University and the Center for Pulmonary Imaging Research at Cincinnati Children's Hospital were invaluable to me in making St. Louis and Cincinnati feel like home.

Thank you to all of my family members for your love and support. My parents have been unwaveringly proud of me through thick and thin, and have been often-uncredited contributors to many of my accomplishments. My brothers are the other peas in my pod, always helping me to stay grounded.

Finally, to Ali: the happiness and love we share has brought richness to my life. Thank you for being my teammate day in and day out.

<div style="text-align: right">

Nara Savoye Higano

Washington University in St. Louis

December 2017

</div>

Abstract

Investigation of Neonatal Pulmonary Structure and Function via Proton and Hyperpolarized Gas Magnetic Resonance Imaging

by

Nara Savoye Higano

Doctor of Philosophy in Physics

Washington University in St. Louis, 2017

Professor Jason C. Woods, Chair

Professor Mark S. Conradi, Co-Chair

Magnetic resonance imaging (MRI) is a modality that utilizes the phenomenon of nuclear magnetic resonance (NMR) to yield tomographic images of the body. Proton (^{1}H) MRI has historically been successful in soft tissues but has suffered in the lung due to a variety of technical challenges, such as the low proton-density, rapid T_2* relaxation time of the lung parenchymal tissue, and inherent physiological motion in the chest. Recent developments in radial ultrashort echo time (UTE) MRI have in part overcome these issues. In addition, there has been much progress in techniques for hyperpolarization of noble gases (^{3}He and ^{129}Xe) out of thermal equilibrium via spin exchange optical pumping, which can greatly enhance the gas NMR signal such that it is detectable within the airspaces of the lung on MRI.

The lung is a unique organ due to its complex structural and functional dynamics, and its early development through the neonatal (newborn) period is not yet well understood in normal or abnormal conditions. Pulmonary morbidities are relatively common in infants and are present in a majority of patients admitted to the neonatal intensive care unit, often stemming from preterm birth and/or congenital defects. Current clinical lung imaging in these

patients is typically limited to chest x-ray radiography, which does not provide tomographic information and so has lowered sensitivity. More rarely, x-ray computed tomography (CT) is used but exposes infants to ionizing radiation and typically requires sedation, both of which pose increased risks to pediatric patients. Thus the opportunity is ripe for application of novel pulmonary MRI techniques to the infant population. However, MR imaging of very small pulmonary structure and microstructure requires fundamental changes in the imaging theory of both ^{1}H UTE MRI and hyperpolarized gas diffusion MRI. Furthermore, such young patients are often non-compliant, yielding a need for new and innovative techniques for monitoring respiratory and bulk motion.

This dissertation describes methodology development and provides experimental results in both ^{1}H UTE MRI and hyperpolarized ^{3}He and ^{129}Xe gas diffusion MRI, with investigation into the structure and function of infant lungs at both the macrostructural and microstructural level. In particular, anisotropically restricted gas diffusion within infant alveolar microstructure is investigated as a measurement of airspace size and geometry. Additionally, the phenomenon of respiratory and bulk motion-tracking via modulation of the k-space center's magnitude and phase is explored and applied via UTE MRI in various neonatal pulmonary conditions to extract imaging-based metrics of diagnostic value. Further, the proton-density regime of pulmonary UTE MRI is validated in translational applications. These techniques are applied in infants with various pulmonary conditions, including patients diagnosed with bronchopulmonary dysplasia, congenital diaphragmatic hernia, esophageal atresia/tracheoesophageal fistula, tracheomalacia, and no suspected lung disease. In addition, explanted lung specimens from both infants with and without lung disease are examined.

Development and implementation of these techniques involves a strong understanding of the physics-based theory of NMR, hyperpolarization, and MR imaging, in addition to foundations in hardware, software, and image analysis techniques. This thesis first outlines the theory and background of NMR, MRI, and pulmonary physiology and development (Part I), then proceeds into the theory, equipment, and imaging experiments for hyperpolarized gas diffusion MRI in infant lung airspaces (Part II), and finally details the theory, data processing methods, and applications of pulmonary UTE MRI in infant patients (Part III). The potential for clinical translation of the neonatal pulmonary MRI methods presented in this dissertation is very high, with the foundations of these techniques firmly rooted in the laws of physics.

Part I

Introduction and Background

The lung is a unique organ, in part due to its complex structure and function dynamics, as well as the fact that its function depends crucially upon its structural design. In this respect, breathing is a process that relies not only on biology but decidedly on physics, and the study of respiration must necessarily consider physical and engineering perspectives.

The development of the lung structure, microstructure, and function in early life is not well understood in normal or abnormal conditions. Infant pulmonary morbidities are present in many infants in the neonatal intensive care unit (NICU), typically related to premature birth or congenital defects. However, the imaging options currently available in the clinic are limited to chest x-ray radiography, which provides low sensitivity, or more rarely x-ray computed tomography (CT), which yields informative structural images but exposes infants to ionizing radiation and increased risks. Thus there is high value in the development of neonatal pulmonary imaging modalities that are both safe and effective, with the prime candidate being magnetic resonance imaging (MRI). This dissertation examines the structure and function of the pulmonary system in neonatal and infant humans via novel ^{1}H ultrashort echo time (UTE) MRI and hyperpolarized gas diffusion MRI techniques.

MRI utilizes the phenomenon of nuclear magnetic resonance (NMR) to yield tomographic images of the body and has seen great clinical successes with soft tissues. However, MRI of the lung has suffered over the years from various technical challenges, such as the low proton-density, rapid T_2* relaxation time of the lung parenchyma, and physiological chest motion. Recent developments in radial ^{1}H UTE MRI have begun to address many of these issues. Additionally, there has been strong progress in methods for hyperpolarization of noble gases (such as ^{3}He and ^{129}Xe) out of thermal equilibrium via spin exchange optical pumping

(SEOP), which can greatly enhance the gas NMR signal such that it is detectable within the airspaces of the lung with MRI. These developments have opened up new opportunities in pulmonary MRI applications, yielding in-vivo information on the structure, microstructure, and function of the lung. In particular, gas diffusion MRI is capable of in-vivo measurements of alveolar airspace sizes and microstructural morphometry based on anisotropic diffusion models, with validation via comparison to ex-vivo histological morphometry.

The application of these techniques to the very small pulmonary structures and microstructures in neonates requires fundamental changes in the imaging physics of both ^{1}H UTE MRI and hyperpolarized gas diffusion MRI. Further, neonatal patients are often non-compliant, yielding a need for innovative techniques for monitoring and processing data corrupted by respiratory and bulk motion. This thesis describes methodology development and experiments in UTE and hyperpolarized gas MRI for investigation of the structure, microstructure, and function of neonatal and infant lungs. Development and implementation of these techniques involves a strong understanding of the physics theory of NMR, hyperpolarization, and MR imaging physics, as well as foundations in hardware, software, and imaging analysis techniques. In Part I, this dissertation outlines the background of NMR, MRI, and pulmonary physiology. In Part II, details are presented on noble gas hyperpolarization techniques and diffusion MRI experiments with ex-vivo infant lungs. Finally in Part III, imaging physics theory, imaging data analysis, and translational applications are discussed for radial UTE MRI in neonatal patients. Major contributions include optimization of research MRI sequences for both ^{1}H UTE and gas diffusion acquisitions, novel retrospective motion-tracking and respiratory-gating methodology using the modulated phase and magnitude of the MR k-space center point, and new approaches for quantitative analysis of MR images. The potential for clinical translation of the neonatal pulmonary MRI methods presented in this dissertation is very high, with the foundations of these techniques firmly rooted in the laws of physics.

Sections of this dissertation contain peer-reviewed and co-authored published work, for which the author was a major contributor. The published work is indicated in the relevant sections.

1 Nuclear Magnetic Resonance

Nuclear magnetic resonance (NMR) is a phenomenon that occurs when certain atoms with non-zero nuclear spin angular momentum (I) are exposed to a static magnetic field B_0. The nuclear spins of these atoms align parallel or anti-parallel to the field direction. Most of the commonly-examined nuclei in NMR have a nuclear spin of $I = \frac{1}{2}$ (such as ^{1}H, ^{3}He, and ^{129}Xe), yielding two energy levels via nuclear Zeeman splitting with an energy difference of $\Delta E = hf = \hbar\omega$ (Figure 1.1). The frequency associated with this energy splitting is known as the Larmor frequency (ω_0), calculated with the governing equation of NMR:

$$\omega_0 = \gamma B_0, \tag{1.1}$$

where γ is the gyromagnetic ratio, an inherent quantity for a specific nucleus. These nuclei have the potential for absorption and emission of photons with the appropriate energy ΔE. The intent of this section is to provide a broad overview of NMR fundamentals in quantum mechanical and net magnetization vector descriptions. The reader is referred to several resources for a more in-depth discussion of spin dynamics [1, 2, 3].
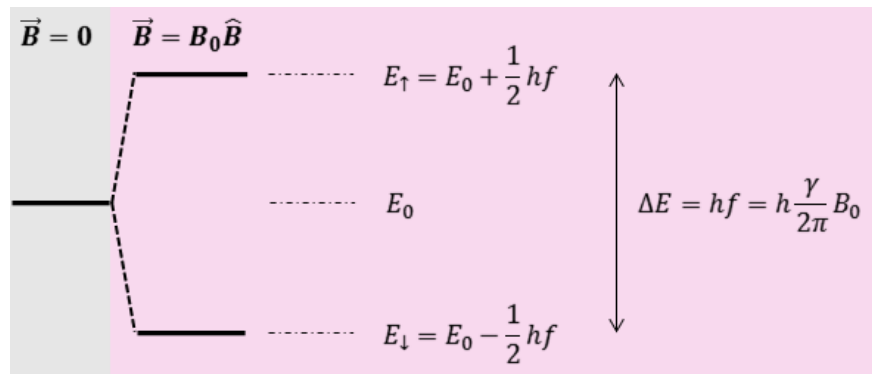
Figure 1.1: When placed in a magnetic field, a nuclear spin-$\frac{1}{2}$ system will yield two energy levels: one aligned with the field ($E_\downarrow$) and one aligned against the field ($E_\uparrow$), with an energy difference of ΔE.

4

1.1 Boltzmann Polarization

Nuclear spins in Boltzmann (thermal) equilibrium are the source of signal in nearly all NMR and MRI studies. Here we review the nuclear spin-$\frac{1}{2}$ case, as it is relevant to the ^{1}H, ^{3}He, and ^{129}Xe methods detailed later in this dissertation (Parts II and III). Recall from statistical mechanics that the probability p_i of being in the ith state of a system is

$$p_i = \frac{g_i e^{-\epsilon_i/kT}}{Q}, \tag{1.2}$$

where g_i is the degeneracy of the ith state (g $= 1$ for each state in the spin-$\frac{1}{2}$ case), ϵ_i is the energy of the ith state, k is the Boltzmann constant, T is the temperature, and $Q = \sum g_i e^{-\epsilon_i/kT}$ is the partition coefficient, essentially the sum of all probabilities. In the spin-$\frac{1}{2}$ case, the ratio of number of spins aligned with the field ($n_\downarrow$) to number of spins aligned against the field ($n_\uparrow$) can thus be calculated as

$$\frac{n_\downarrow}{n_\uparrow} = \frac{e^{-\epsilon_\downarrow/kT}}{e^{-\epsilon_\uparrow/kT}} = e^{-\Delta E/kT}. \tag{1.3}$$

In typical conditions, the energy level splitting $\Delta E = hf$ is much smaller than the thermal energy kT ($hf \ll kT$), and so the ratio of aligned to anti-aligned spins at thermal equilibrium can be approximated via Taylor expansion as

$$\frac{n_\downarrow}{n_\uparrow} \approx 1 - \frac{hf}{kT}. \tag{1.4}$$

Nearly all aligned and anti-aligned spins cancel in thermal equilibrium, yielding a ratio $\frac{n_\downarrow}{n_\uparrow}$ that is nearly equal to 1 (typically up to parts per million, ppm). Importantly, the ratio is not exactly 1; a small excess of spins exists in the lower energy state, such that the absolute polarization P is

$$P = \frac{n_\downarrow - n_\uparrow}{n_\downarrow + n_\uparrow}. \tag{1.5}$$

When $P = 1$, all spins are in the lower energy state; when $P = 0$, the energy states are populated equally. In systems at equilibrium, the absolute polarization can be written using Equation 1.2 and 1.5 and the small-angle approximation of $tanh(x) \approx x$:

$$P \approx \frac{hf}{2kT}. \tag{1.6}$$

With parameters from a typical ^{1}H MR system ($f \approx 60$ MHz and $T = 300$ K), the absolute polarization is $P \approx 5 \cdot 10^{-6}$. Summing over N spin-$\frac{1}{2}$ magnetic moments yields a total magnetization M_0 aligned with the field, known as the Curie Law:

$$M_0 \approx \frac{N\gamma^2\hbar^2 B_0}{4kT}. \tag{1.7}$$

1.2   Nuclear Spin, Magnetic Moment, and Relaxation

Since nuclei of NMR interest have non-zero spin angular momentum I, they correspondingly have a non-zero nuclear magnetic moment $\vec{\mu}$, Hamiltonian $\mathcal{H}$, and torque $\vec{\tau}$ in the presence of a magnetic field $\vec{B}$:

$$\vec{\mu} = \gamma \vec{I} \tag{1.8}$$

$$\mathcal{H} = \vec{\mu} \cdot \vec{B} \tag{1.9}$$

$$\tau = \vec{\mu} \times \vec{B}. \tag{1.10}$$

However, in NMR it is often more convenient to consider the macroscopic collection of spins rather than individual spins. In this perspective, spins with nuclear magnetic moment are in a spin ensemble and experience the same magnetic field. The net magnetic moment can be described as a single net magnetization vector $\vec{M}$ that is proportional to the spin population difference in the upper and lower energy states.

When an NMR system is at equilibrium, it is convenient to say that both the static field and the net magnetization lie along the z-axis, such that $M_z = M_0$ (all longitudinal) with no components of M_x or M_y (no transverse). A pulsed magnetic field (B_1) orthogonal to the B_0 field can be applied to the net group of spins with a radio-frequency (RF) coil. This causes them to nutate (rotate) about the direction of the applied B_1 field away from z-axis (longitudinal) alignment into the x-y (transverse) plane. The angle of nutation β (often referred to as the "flip angle") can be calculated with the following, where t_1 is the duration of the applied field pulse:

$$\beta = 2\pi\gamma B_1 t_1. \tag{1.11}$$

After a nutation of β, the transverse magnetization component is equal to $M_0 sin\beta$, and the longitudinal magnetization component is equal to $M_0 cos\beta$.

The nutated magnetization precesses about the longitudinal z-axis at the Larmor frequency, which can be detected with a receiver RF coil (typically a tuned LC circuit). The received signal is referred to as a free induction decay (FID), with the detected signal attenuated exponentially as a function of time due to two different types of relaxation, the rates of which depend on physical properties of the system under investigation. Since these relaxation rates vary between different bodily tissues, they are exploited in appropriately-weighted MRI scans for contrast imaging.

The first type of relaxation is called spin-lattice relaxation. The net spin magnetization

system relaxes in this way by transmitting energy into the surrounding system ("lattice"); for spin-$\frac{1}{2}$ nuclei, spin-lattice relaxation is typically due to weak dipole-dipole interactions. Such recovery of the longitudinal magnetization $M_z(t)$ is governed by an associated time constant T_1:

$$M_z(t) = M_0(1 - e^{-t/T_1}).\qquad(1.12)$$
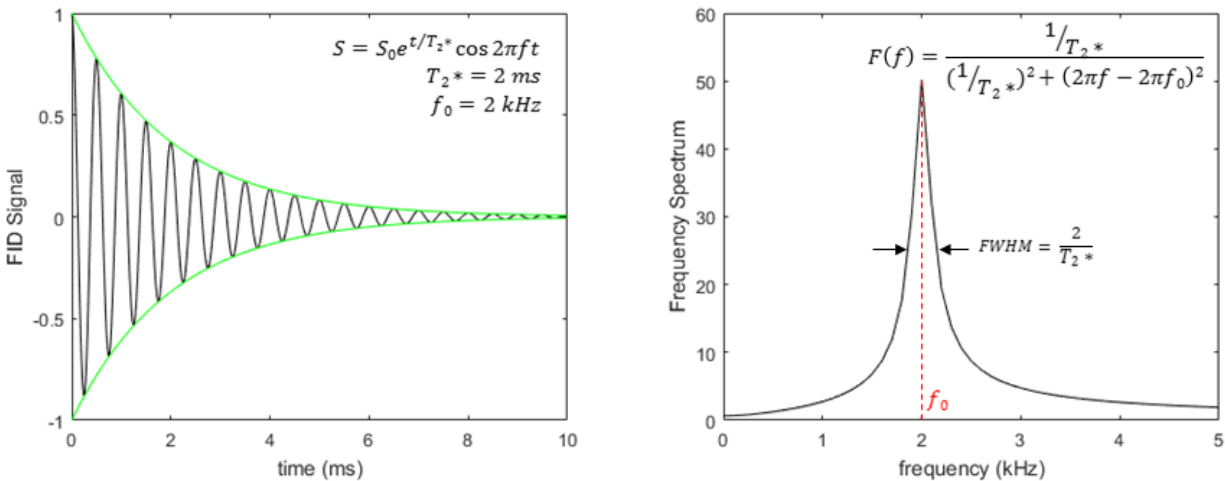
Figure 1.2: Left: A representative free induction decay (FID), here shown with exponential decay from spin-spin relaxation with a time constant of $T_2* = 2$ ms. Oscillations in the signal are due to an off-resonance frequency of $f_0 = 2$ kHz; if perfectly on resonance, the FID would appear as a pure exponential. Right: The Fourier transform of the time-regime FID data, illustrating this FID's frequency spectrum in the form of a Lorentzian. The line-width (represented by the full-width half-maximum, FWHM) spreads with decreasing T_2*, representative of spins within an ensemble dephasing more quickly with a broader spread of precession frequencies.

The second type of relaxation is called spin-spin relaxation, with an associated time constant called T_2. When the net magnetization vector is nutated into the x-y plane, it precesses around the z-axis at the Larmor frequency. However within the ensemble, spins may be experiencing slightly heterogeneous magnetic fields and so have slightly varying precessional frequencies. This yields dephasing of the spins within the ensemble (magnetization "decay"),

8

as well as broadening of a frequency spectrum peak. Thus the transverse magnetization components immediately after a nutation toward the x-axis are

$$M_x(t) = M_0 cos(\omega_0 t) e^{-t/T_2} \tag{1.13}$$

$$M_y(t) = M_0 sin(\omega_0 t) e^{-t/T_2}, \tag{1.14}$$

where M_0 is the transverse magnetization at $t = 0$, following the RF pulse. The contributing factors to transverse magnetization decay include inherent and homogeneous molecular interactions (related to the chemical environment of the nuclei, considered to be "pure" T_2) and macroscopic inhomogeneities in the B_0 field:

$$\frac{1}{T_2^*} = \frac{1}{T_2} + \frac{1}{T_{2,inhomog}}. \tag{1.15}$$

After a straightforward RF excitation (nutation), an observed FID will decay with a time constant of T_2*, which can be calculated using the full-width half-maximum of the FID's frequency spectrum peak (Figure 1.2).

The relationships represented in Equations 1.12, 1.13, and 1.14 are derived by solving a set of differential equations known well as the Bloch equations, which describe the 3D components of a system's magnetization as a function of time:

$$\frac{dM_x}{dt} = (\omega_0 - \omega)M_y - \frac{M_x}{T_2} \tag{1.16}$$

$$\frac{dM_y}{dt} = -(\omega_0 - \omega)M_x + 2\pi\gamma B_1 M_z - \frac{M_y}{T_2} \tag{1.17}$$

9

$$\frac{dM_z}{dt} = -2\pi\gamma B_1 M_y - \frac{(M_z - M_0)}{T_1}. \tag{1.18}$$

2 Magnetic Resonance Imaging

Magnetic resonance imaging (MRI) utilizes the phenomenon of NMR in order to spatially localize spins within a given sample or specimen using magnetic field gradients. Excitation and detection of spins in the presence of a static magnetic field with specifically-manipulated local inhomogeneities generates an ability to spatially map detected frequencies and thus create a real-space image of those spins. As discussed below, the conversion of spatial frequency data ("k-space") into spatial position data ("x-space") necessarily requires use of Fourier theory.

2.1 Fourier Transform

The continuous Fourier transform and its inverse are complex operations that convert time-domain functions $f(t)$ to and from sinusoidal frequency-domain functions $g(\omega)$:

$$\mathcal{F}\{f(t)\} = g(\omega) = \int_{-\infty}^{+\infty} f(t)e^{-i\omega x}dx, \tag{2.1}$$

$$\mathcal{F}^{-1}\{g(\omega)\} = f(t) = \int_{-\infty}^{+\infty} g(\omega)e^{i\omega x}d\omega. \tag{2.2}$$

When dealing with discretely sampled data sets, such as in typical MR applications, a discrete Fourier transform is necessary. A sampling rate of Δt over a period of T yields a spectral width of $2f_{max} = \frac{1}{\Delta t}$ and a frequency resolution of $\Delta f = \frac{1}{T}$. If the sampling rate is too slow ($\frac{1}{\Delta t} < 2f_{max}$), meaning the Nyquist criterion is not satisfied, then sampling errors can occur via "wrap-around" artifacts in the frequency spectrum.

2.2 k-Space

In imaging, detected MR signals are sampled into a 2D or 3D time-domain called "k-space" $(g(k_x, k_y, k_z))$, which can be decomposed via Fourier transform into the 2D or 3D encoded spatial-frequency domain, i.e. "image-space" $(f(x, y, z))$. Since the Fourier pair in imaging is $k - x$ rather than $t - f$, the continuous Fourier transform and its inverse (in 3D) can be written as

$$\mathcal{F}\{f(x, y, z)\} = g(k_x, k_y, k_z) = \int \int_{-\infty}^{+\infty} f(x, y, z) e^{-2\pi i(k_x x + k_y y + k_z z)} dx dy dz \qquad (2.3)$$

$$\mathcal{F}^{-1}\{g(k_x, k_y, k_z)\} = f(x, y, z) = \int_{-\infty}^{+\infty} g(k_x, k_y, k_z) e^{2\pi i(k_x x + k_y y + k_z z)} dk_x dk_y dk_z, \qquad (2.4)$$
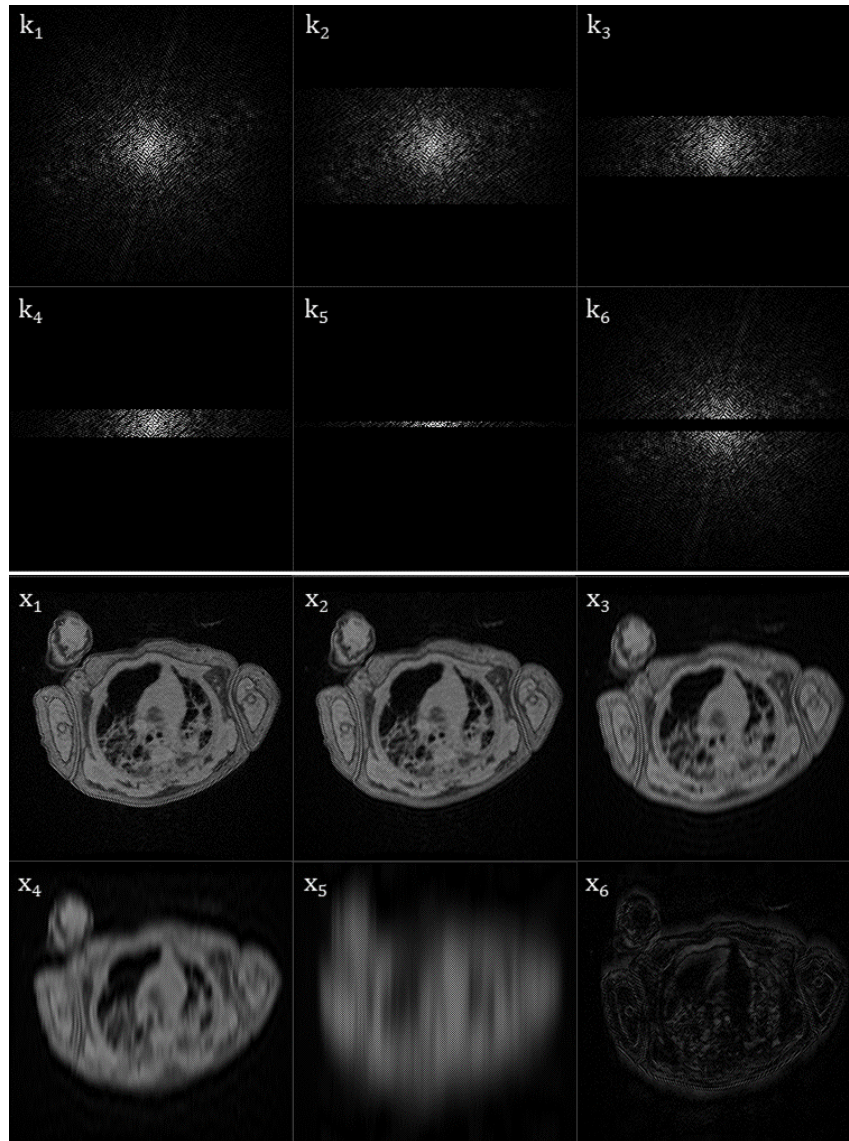
Figure 2.1: Gradient echo MRI data acquired in a neonatal lung disease patient. At top are identical k-space data sets, but with specific k_y lines + selectively removed (k_1 through k_6). The corresponding image reconstructions via Fourier transform are shown at bottom (x_1 through x_6), demonstrating that outer regions of k-space corresponds to spatial high-frequency image data ("edges"), while central k-space corresponds to spatial low-frequency image data.

Unsurprisingly, the coordinates near the center of k-space represent low-frequency data in image-space (i.e. slow spatial changes in the sample's spin density), while coordinates near the edges of k-space represent high-frequency data in image-space (i.e. rapidly changing spa-

tial edges of the sample's spin density). Figure 2.1 illustrates this relationship by increasingly removing outer k_y lines from 2D k-space, obtained during a neonatal pulmonary MRI; the corresponding image reconstructions show increasingly more blur in the y-direction, demonstrating that image edge definition is lost without the outer regions of k-space. On the flip side, when the central k_y lines are removed, only the image edges are preserved. Notably, an image is comprised of $n_x \cdot n_y$ pieces of data (real only), while k-space is comprised of $2 \cdot n_x \cdot n_y$ (real and imaginary). Thus k-space contains redundant information since the Fourier transform integrates over both positive and negative k-values; indeed, k-space is Hermitian, and the difference between negative and positive frequencies in image space is undefined.

2.3 Spatial Encoding

MRI is performed by spatially localizing spins via frequency and phase manipulation in magnetic field gradients. Following Equation 1.1, a spin in a magnetic field $B_0(t)$ for a time T will accrue a phase $\varphi(t)$ of

$$\varphi(t) = \int_0^T \omega_0(t)dt = \int_0^T \gamma B_0(t)dt. \tag{2.5}$$

If a magnetic field gradient of $G(t) = G_x x$ is applied in that time, the k-space coordinate reached and additional phase accumulated will be represented by

$$k(t) = \frac{\gamma}{2\pi} \int_0^T G(t)dt \tag{2.6}$$

$$\varphi_G(t) = \gamma \int_0^T G(t)dt = 2\pi k x. \tag{2.7}$$

In order to selectively excite a spin density $\rho(x, y, z)$ in a slice located at $z_0 \pm \Delta z$ in the static magnetic field (with slice plane conventionally chosen orthogonal to the field direction

13

$\hat{z}$), the frequency of those desired spins must be known ($\Delta\omega = \gamma B_z \Delta z$). Thus a specified magnetic field gradient B_z is applied to effect the desired localized frequency, and an RF pulse is applied with a specific bandwidth $\Delta\omega$ that excites only those spins in the desired frequency range. This is called "slice selection", and any detected signal will originate only from those spins located in the specified slice.

In conventional MRI, two other spatial encoding steps typically follow a slice selection: a phase encoding and a frequency encoding. If a linear gradient $B_z(y) = G_y y$ is applied in one direction of the selected slice for a time T_{phase}, then the k_y-coordinate reached is $k_y = \gamma G_y T_{ph}$. If then an additional linear gradient $B_z(x) = G_x x$ is applied, with simultaneous data acquisition ("read-out"), the acquired signal would be governed by

$$s(G_y, t) = \int\int \rho(x, y, z_0)e^{-i(\gamma y G_y T_{phase} + \gamma x G_x t)}dxdy \tag{2.8}$$

$$s(k_x, k_y) = \int\int \rho(x, y, z_0)e^{-2\pi i(k_x x + k_y y)}dxdy. \tag{2.9}$$

This basic sequence of an RF pulse and spatial-encoding gradient pulses comprises a conventional "gradient echo" MRI sequence; see Section 6.7 and 9.1 for further detail.

2.4 Application to Medical Imaging

Medical imaging applications of NMR began to flourish in the 1970s and onward, with rapid developments in using spatial encoding and the Fourier transform. MRI is attractive as an imaging modality, especially in pediatrics and for longitudinal imaging, since it is utilizes non-ionizing radio-frequency radiation. It can produce strong and diverse contrasts between types of tissues via various weightings of proton density, T_1, and T_2, as well as elucidate information on flow, metabolism, and spectroscopy. Historically, traditional ^{1}H MRI has not had strong success in imaging of lung parenchymal tissue, due to its intrinsically low

14

volumetric density, relatively rapid $T_2{}^*$ decay, and susceptibility to respiratory and cardiac motion in the chest. Details on these historical obstacles, recent developments with new pulmonary ^{1}H and hyperpolarized noble gas MRI techniques, and comparison to standard clinical options for pulmonary imaging will be discussed further throughout this dissertation.

3   Respiratory System

3.1   Lung Architecture and Physiology

The lung has two essential responsibilities: 1) providing sufficient gas exchange to deliver oxygen into the bloodstream and remove carbon dioxide from the blood stream, and 2) defending against any airborne pathogens and particulates [4]. This latter function is important; while an adult human's body surface area is ~1.8 m^2 [5], the surface area of an adult human's lung parenchymal tissue is approximately 50-100 m^2 [4], and so for an internal organ the lung has non-negligible exposure to external atmospheric agents. However, the first function of the lung – gas exchange – is of greater interest in this work. Efficient gas exchange demands that there be a large surface area that is positioned very closely to pulmonary vasculature, and this task must be accomplished within a limited thoracic volume. This is a problem solved by the lung's architectural design, which in adulthood contains many generations of branching airways to conduct air into millions of alveoli. The alveolar wall structures contain pulmonary capillaries to perfuse the lung tissue with blood for oxygenation. Like many organs, lung function is governed to some degree by biochemical processes; however, the lung is unique because its function depends heavily upon its structural design. In this respect, the study of respiration mechanics must necessarily consider physical and engineering perspectives.
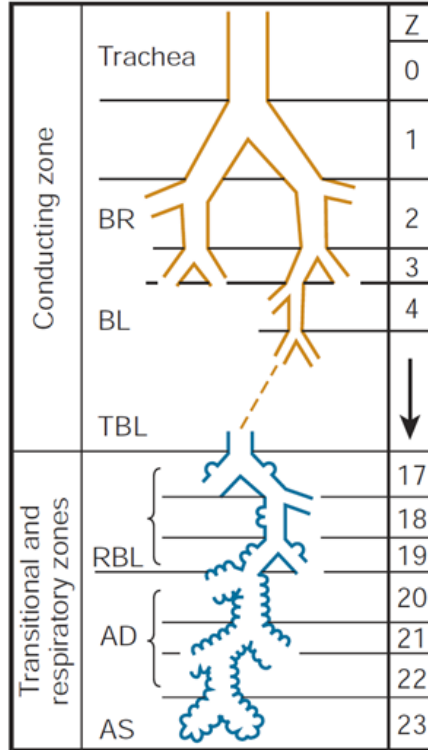
Figure 3.1: A diagram of the branching structure of the lung airways. The 1st through 16th generations comprise the conducting zone (sometimes referred to as the anatomical dead space because no gas exchange can occur here). Then a brief transitional zone occurs as alveoli begin to appear, with transitional and then respiratory zones comprising the 17th through 23rd generations, where gas exchange can take place. BR - bronchi, BL - bronchioles, TBL - terminal bronchioles, RBL - respiratory bronchioles, AD - alveolar ducts, AS - alveolar sacs. Reproduced with permission from [4].

The basic structure of the lung airways consists of ∼23 generations of branching tubes (see Figure 3.1) [4]. Starting with the *trachea*, the 1st generation branch is the *main stem bronchi*. This is followed by the 2nd generation – *lobar bronchi* (which feed three lobes in the right lung and two lobes in the left lung) – and the 3rd generation. Branching continues in a self-similar pattern (length and diameter of the new generation are reduced by a constant factor), yielding *bronchioles* down through approximately the 17th generation. The last generation of bronchioles is called the *terminal bronchioles* These first ∼17 generations make up the *conducting zone*, where the function is to deliver inhaled gas to the airspaces that can

perform gas exchange. The conducting airspaces contain no alveoli and cannot participate in gas exchange, and so they are considered the "anatomic dead space" ($\sim$130-180 mL) [4].

The airspace beyond an individual terminal bronchiole is considered a single *acinus*, a respiratory unit for gas exchange, with all acini together comprising the *respiratory zone*, where gas exchange takes place. Terminal bronchioles branch into *respiratory bronchioles* ($\sim$3 generations), which are lined with occasional alveoli, and then branch into *alveolar ducts* ($\sim$3 generations) and *alveolar sacs* (the final generation), which are entirely lined with alveoli. The diameter of acinar airspaces are approximately uniform throughout the respiratory zone [4]. The cumulative cross-sectional area of the airways increases very little throughout the conducting zone, with gas primarily moving in convective flow. However, the total cross-sectional area rapidly increases with each branch of the respiratory zone (Figure 3.2), such that the primary type of gas transport transitions from convection to diffusion [4]. There are several hundred million alveoli in an adult human lung, with the surface area of alveolar airspace accounting for $\succ$99% of the surface area of the lung, which clearly supports the concept of gas exchange as a key lung function [4].
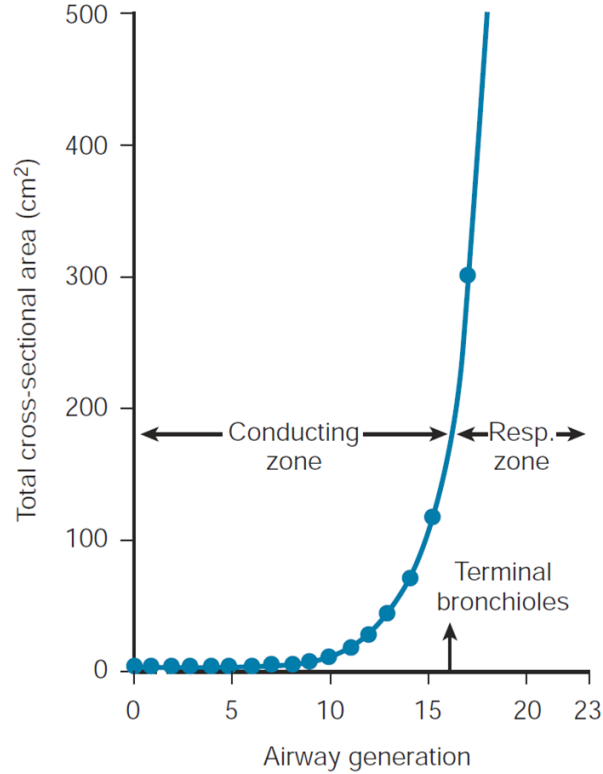
Figure 3.2: The relatively small changes in total lung cross-sectional area through the conducting zone airways, with rapid increase in area with each generation of the respiratory zone. Reproduced with permission from [4].

In convective air flow, the frictional and viscous forces on a gas will cause energy loss and pressure drop, which are dependent on the airway resistance, gas density and viscosity, and laminar versus turbulent flow. Laminar flow, where the gas particle velocity profile in the airway is parabolic (Figure 3.3A), follows Poiseuille's law:

$$\frac{dV}{dt} = \frac{\pi P r^4}{8 \eta l} = \frac{P}{R},$$
(3.1)

where $\frac{dV}{dt}$ is the volume flow rate, P is the difference in pressure between airway ends, r is the airway radius, η is the gas viscosity, l is the airway length, and R is the airway resistance. Clearly the airway radius is the most significant contributor to flow rate $(\frac{dV}{dt} \propto r^4)$ and airway resistance $(R \propto r^{-4})$. In turbulent flow, the gas moves in an unpredictable pattern (Figure

19

3.3B), with increased pressure drop through an airway ($P \propto \left(\frac{dV}{dt}\right)^2$) and increased resistance compared with in laminar flow [4].
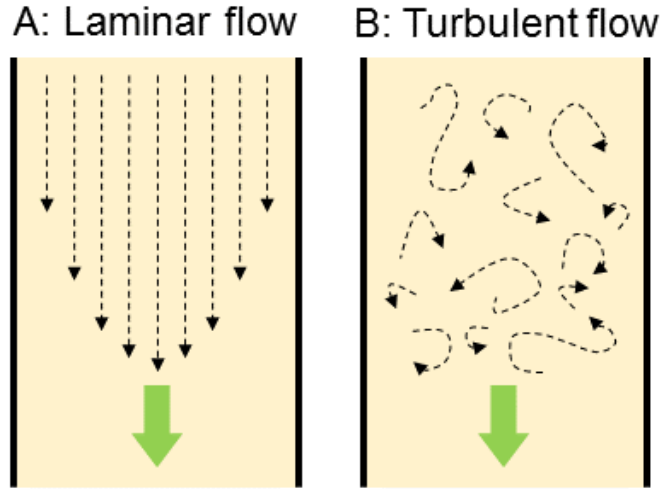
Figure 3.3: Representation of the flow profiles of laminar (A) and turbulent (B) flow through an airway, with downward bulk flow in the direction of the green arrow.

In this dissertation, "diffusion" will typically refer to the Brownian motion of gas within airspaces that participate in gas exchange (see Section 6.1.1). However, it is important to distinguish this motion from the Brownian diffusion of gas across the blood-gas barrier (i.e., oxygen moving from the airspace into the blood, or carbon dioxide moving from the blood into the airspace). The rate of diffusion across this barrier (or "membrane") between the blood and airspace regions is governed by Fick's law for diffusion:

$$J = \frac{D \cdot A \cdot \Delta P}{x}. \tag{3.2}$$

where J is the rate of diffusion, D is the diffusion constant for a given gas in a given membrane, A is the surface area of the membrane, ΔP is the difference in partial gas pressures between the two sides of the membrane, and x is the thickness of the membrane. The structure of a lung is ideal for efficient membrane diffusion; the distance from an airspace

to the bloodstream is very thin (typically~0.3 μm in an adult human), while the surface area of the respiratory zone is typically between 50-100 m^2 [4]. In emphysema, the loss of surface area – via destruction of alveolar wall tissue – leads to severe gas exchange impairment. Likewise, patients with fibrotic lung diseases suffer due to thickened alveolar walls and the resulting decrease in oxygenation.

A diaphragm is comprised of two muscles connected by a tendon. During inspiration, the diaphragm contracts away from the thoracic cavity, which pushes the rib-cage outward and yields a negative intrapleural (intrathoracic) pressure. This negative pressure allows for gas transport into the lungs. The intrapleural pressure returns to zero (atmospheric) in order to facilitate exhalation, which occurs passively due to the lung's inherent elasticity. This elastic recoil on collapse is mostly due to surface tension at the air-liquid interface within the many alveolar airspaces [4]. Following Laplace's law ($P = \frac{2T}{r}$), if one assumes that an alveolus with physiological dimensions ($r \approx$0.1 mm) had the surface tension of water (T_{H_2O} $\approx$72 $\frac{mN}{m}$), it would yield an alveolar airspace pressure ($P_{alveolus,H_2O}$) of ~1400 $\frac{N}{m^2}$; in this scenario, alveoli would be unable to open at physiologic pressures (~300-500 $\frac{N}{m^2}$) [4]. However, lung surfactant ("pulmonary surface-active material", a lipoprotein complex) performs a critical function within the alveoli and small airspaces by reducing the surface tension at the air-liquid interface from that of water ($T_{surfactant} \approx$25 $\frac{mN}{m}$) to prevent alveolar collapse ($P_{alveolus,surfactant}$ of ~50 $\frac{N}{m^2}$) [4, 6, 7]. In fact, alveolar surfactant has dynamic properties and reduces its surface tension when compressed during exhalation, when shrinking alveoli develop larger pressures and so would otherwise collapse. Thus, lung surfactant increases alveolar stability throughout respiration.

3.2 Early Pulmonary Development

While *in utero*, a fetus is supported with an adequate gas exchange through the placenta. However, the lungs must be prepared to breathe independently immediately after birth. This developmental process *in utero* has historically been divided into five stages [4, 7, 8] (see Figures 3.4 and 3.5).
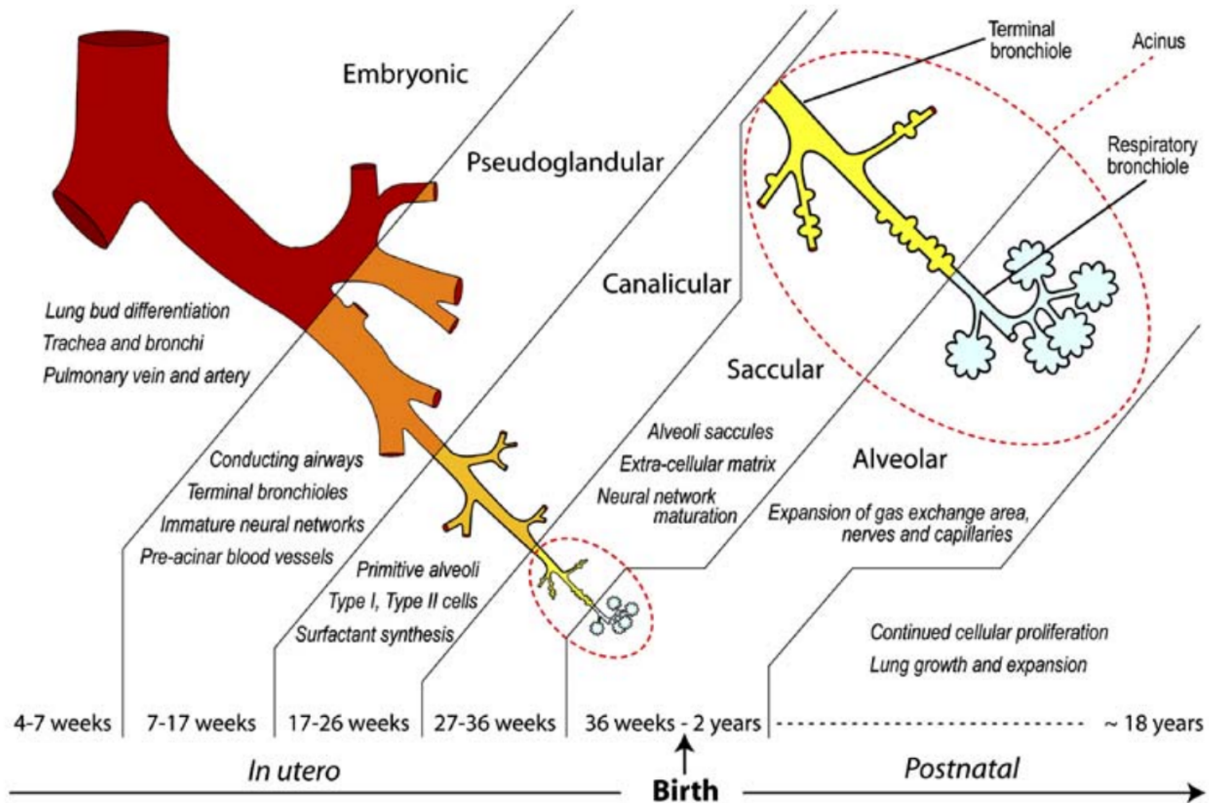
Figure 3.4: A diagram of the stages of lung development, from a simple lung bud in the embryonic stage to a fully functional, alveolated lung in the alveolar stage. Reproduced with permission from [8].

1st stage: Embryonic This stage lasts approximately from 3 weeks to 7 weeks of gestation. During the 4th week of gestation, the laryngotracheal tube develops, and the trachea and larynx split from the esophagus. Concurrently, the lung bud forms from the laryngotracheal tube, which later will develop into the respiratory tract organs. This lung bud elongates and

bifurcates into the right and left bronchial buds, and eventually branches into three buds in the right lung and two buds in the left lung to form the basis of the primary lung lobes.

Esophageal atresia and tracheoesophageal fistula (see Section 3.3.3), common congenital malformations of the trachea and esophagus, are associated with this stage of development.

2nd stage: Pseudoglandular   This stage lasts approximately from 5 weeks to 17 weeks of gestation. During this stage, branching of the lung epithelium continues and establishes the final pattern of the pulmonary tree ($\sim$23 generations of bronchiole airways). The terminal bronchiole airways branch to form the basis of acinar airspaces (alveolar airways distal to the bronchioles). Cellular proliferation is rapid in this stage, with the pulmonary vasculature branching in parallel with the airways.

Large airway developmental abnormalities, such as absence or weakened cartilage associated with tracheal collapse during respiration (see Section 3.3.4 on tracheomalacia) are related to this stage of development. In addition, the pleuroperitoneal membrane, i.e. the division between the chest and abdominal cavities, typically will close at this stage. Incomplete or failed closure leads to the herniation of abdominal organs into the space typically filled with lung tissue (see Section 3.3.2 on congenital diaphragmatic hernia), leading to incomplete development of the lung and abnormally low number of acinar airspaces.

3rd stage: Canalicular   This stage lasts approximately from 16 weeks to 26 weeks of gestation. Pulmonary tree patterning is completed near the beginning of this stage. The buds of the acinar airspaces begin to expand and branch into respiratory bronchioles, alveolar ducts, and alveoli. Cell differentiation in the airspace walls leads to development of the blood-gas barrier, and small amounts of surfactant are present.

The end of this stage is considered critical to the survival of very premature infants, since gas exchange and blood oxygenation is only possible with some degree of acinar airspace

surface area and surfactant production.

4th stage: Saccular   This stage lasts approximately from 24 weeks to 38 weeks of gestation. The development of the acinar airspaces continues with further branching and increasing airspace size. The pulmonary capillary vasculature is brought closer to the surface of the airspace walls, increasing efficiency of gas exchange by reducing the diffusion distance between gas and blood.

Generally, transition into this stage increases chances of viability, as long as a preterm infant has access to intensive care respiratory support. Mortality rates for infants born at 23 weeks gestational age is approximately 70-85%, but survival rates improve with each week. For example, approximately 60% of infants born at 25 weeks gestation will survive, though most will endure significant pulmonary morbidities associated with preterm birth, such as bronchopulmonary dysplasia (see Section 3.3.1) or neonatal respiratory distress syndrome (NRDS – related to surfactant deficiency).

5th stage: Alveolar   This stage lasts approximately from 36 weeks of gestation through the several years of life. Alveoli are formed in terminal airspaces, and septa (epithelial walls that separate neighboring alveoli) grow and become thin, with septation contributing to an increase in alveoli number from tens of million at term birth to several hundred million in an adult.

Alveolarization through childhood and early adulthood is not well understood, but there is hope for significant lung function recovery and compensatory lung growth in patients that suffer from early-life respiratory morbidities.
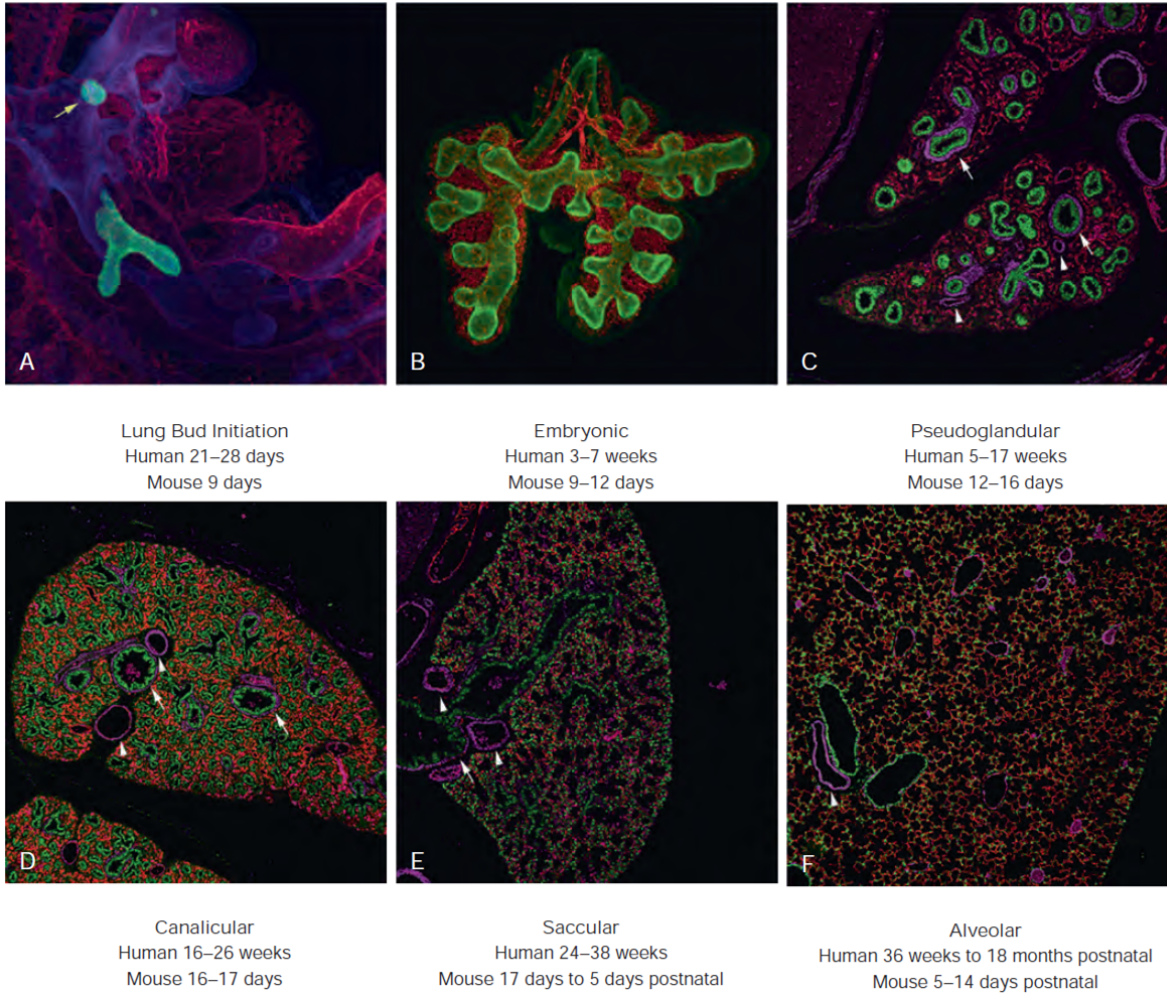
Figure 3.5: Histological morphometry of mouse lungs across the stages of lung development. A) Lung buds develop at the beginning of lung development. B) In the embryonic stage, branching of the lung epithelium continues, with vasculature developing in parallel. C) In the pseudoglandular stage, the lung is primarily epithelial airspaces with thick wall tissue. D) In the canalicular stage, development of the acinar airspaces begins. E) In the saccular stage, the size of acinar airspaces increases. F) In the alveolar stage, septa are formed, lengthen, and thin to increase the surface area of the lung epithelium. Panels C-F are shown at the same magnification. Epithelial cells on the surface of airspaces are shown in green, vascular cells are shown in red, and smooth muscle cells are shown in magenta. White arrows indicate smooth muscle cells surrounding airspaces, and white arrowheads indicate vessels. Reproduced with permission from [4].

3.3 Neonatal Pulmonary Morbidities

While pulmonary morbidities are present in over 60% of our Neonatal Intensive Care Unit (NICU) patients at Cincinnati Children's Hospital Medical Center (CCHMC), these morbidities and their time-course are poorly defined and understood. There are few strong prognostic indicators of later outcomes, particularly for BPD infants, with inadequate clinical ability to reliably predict which infants will require long-term ventilation, which will be discharged with oxygen requirement, and which will be discharged with no further respiratory support.

3.3.1 Bronchopulmonary Dysplasia

Bronchopulmonary dysplasia (BPD) is a serious and challenging neonatal pulmonary condition often associated with premature birth, but the underlying parenchymal disease and time course are poorly characterized [9, 10, 11, 12]. Infants born in the first and second stages of lung development (embryonic and pseudoglandular, respectively; see Section 3.2) do not have sufficiently developed airspaces to survive outside the uterus, while infants who survive birth in the late third or early fourth stages (canalicular or saccular) often have significant pulmonary abnormalities related to interrupted development of alveolar saccules, conducting airways, and interstitium [13]. In addition, the surfactant production and cardiopulmonary vascular development of these surviving premature infants are often dysregulated and impaired [4, 13].

While the prenatal lung development stage at which birth occurs plays a large role in post-natal pulmonary morphology and development, disease progression can depend on certain postnatal exposures, such as quality of neonatal resuscitation and duration of exposure to oxygen and positive pressure ventilation (PPV) and/or mechanical ventilation [13], which are significantly related to inflammation and can affect both short-term and long-term res-

26

piratory outcomes [14, 15].

Although infants affected by BPD account for a small percentage of live births (10,000-15,000 new cases reported each year) [9, 16, 17], they represent a large percentage of neonatal healthcare costs [18]. As clinical respiratory care and survival rates of extremely premature infants continue to improve (i.e. improved surfactant replacement therapy), we will likely see an increased prevalence of patients suffering BPD-related sequelae related to having fewer alveoli, larger and more simplified airspaces, and abnormal pulmonary vasculature [19]. These premature infants' impaired ability to properly ventilate and oxygenate may worsen as bodily growth increases the demand on pulmonary function. As clinical care and survival rates of extremely premature infants continue to improve, the medical community will likely see an even greater need for understanding neonatal lung development, especially since this condition can persist through adulthood.
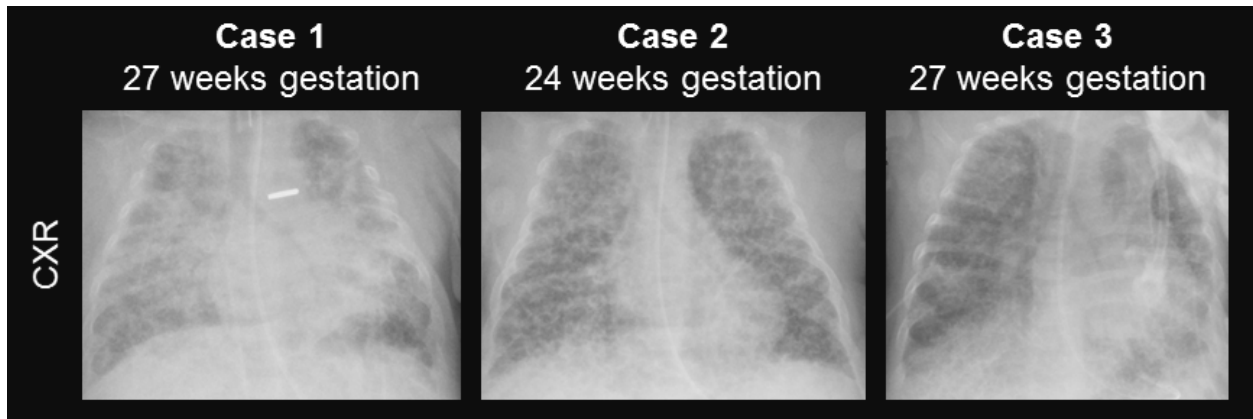
Figure 3.6: The current standard clinical imaging of neonatal bronchopulmonary dysplasia includes chest x-ray radiograph (CXR), which is a non-tomographic modality and so provides limited regional and structural information. Shown here are CXR images for three severe BPD cases, demonstrating high-intensity fibrosis/inflammation and pockets of low-density (presumably alveolar simplification).

The current National Institute of Child Health and Human Development/National Heart, Lung, and Blood Institute (NICHD/NHLBI) consensus definition of BPD is based only on use of oxygen for at least 28 days (not necessarily consecutive) and a clinically-assessed need

for supplemental respiratory support at 36 weeks post-menstrual age (PMA) [17]. However, debate continues on the utility of this and other definitions of BPD, with concerns that diagnosis at a single time-point of 36 weeks PMA does not adequately predict a neonatal patient's risk for lung disease in later childhood [20, 21]. Indeed, there are currently few prognostic indicators of later outcomes, with inadequate clinical ability to reliably predict the levels and durations of respiratory support.
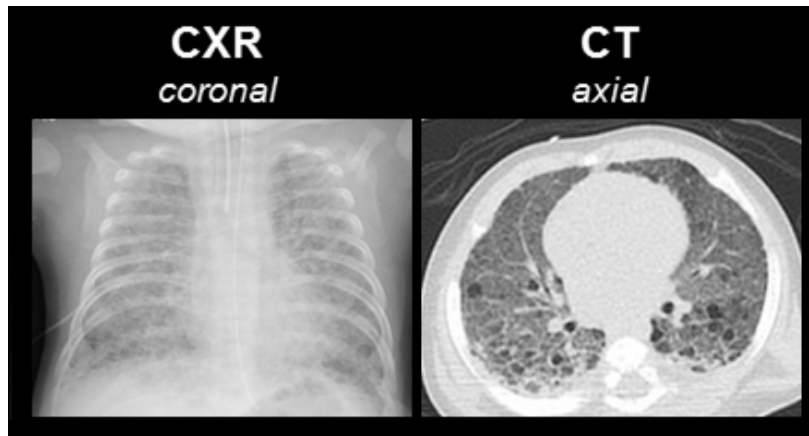
Figure 3.7: While x-ray CT is tomographic, a clear advantage over chest x-ray radiograph (CXR), CT scans exposes neonatal patients to a non-trivial amount of ionizing radiation. Further, CT often requires sedation and/or anesthesia and intubation for those patients not already intubated, which poses additional medical risks to young pediatric patients. Shown here are CXR and CT images for a severe BPD patient born at 26 weeks gestation.

The current standard of care for BPD infants includes chest x-ray radiograph (CXR – Figure 3.6) and can be used for initial inspection of pulmonary disease, serial assessment, and management guidance. While CXR is widely used, abnormalities can be subtle, and sensitivity and specificity can be limited. Meanwhile, x-ray computed tomography (CT) scans, which utilizes varying beam attenuation through different tissues, may be used in more severe cases to further discern underlying pathology (Figure 3.7). However, there are concerns regarding the ionizing radiation exposure associated with CT (Table 3.1), particularly for the non-trivial cumulative X-ray exposures from longitudinal monitoring in pediatric and

neonatal populations [22, 23, 24]. Further, neonatal CTs often require sedation, exposing patients to additional medical risks [25, 26]. As such, CT may not be a preferred method for serial diagnostic imaging of neonatal BPD, and there is a clinical need for safer, informative imaging modalities to assess patients with BPD.

Radiation Source	Effective Radiation Dose (mSv)
U.S. annual per-capita background dose 2006	2.4
Smoking for 1 year	2.8
Coast-to-coast U.S. flight (∼3000 miles)	0.03
Living near coal-fired power plant	0.0003
Living within 50 miles of nuclear power plant	0.00009
Standard chest CT	5-8
"Low-dose" chest CT	2
Chest MRI	0 (exact)

Table 3.1: Typical effective radiation dose sizes (approximate) associated with various chest imaging and background/environmental sources [4].

3.3.2   Congenital Diaphragmatic Hernia

Congenital diaphragmatic hernia (CDH) is a fetal developmental condition affecting approximately 1 in 3000 pregnancies. In patients with CDH, the abdominal viscera (stomach, intestine, liver and biliary system, pancreas, spleen, kidneys, ureters, and suprarenal glands) herniates into the thoracic cavity and impedes lung growth in the second and third trimesters, causing potentially life-threatening pulmonary hypoplasia (malformations characterized by incomplete development of lung tissue) in the newborn infant [27]. Figure 3.8 shows MR images acquired in a neonatal patient with CDH, with the ipsilateral lung on the same side as the herniation and the contralateral lung on the side opposite to the herniation. A handful of recent studies have examined fetal lung growth during the prenatal period; for example,

one group found that survival correlated with change in total lung volume (TLV) in the third trimester [28].

Once the fetus is born, this condition is considered a surgical urgency, and operative repair of the pleuroperitoneal (diaphragmatic) surface typically takes place within the first few days or weeks of life. Various repair methods exist, with the most common technique involving primary closure of the native diaphragm. However, in some cases there is not enough available diaphragmatic muscle tissue for primary closure, and so a non-primary material must be used as a "patch". It is not yet well characterized whether diaphragmatic and respiratory function vary between the various repair methods and materials, and if so in what ways. With understanding of post-repair lung growth so limited, it remains difficult to predict postnatal clinical outcomes, with the factors that affect lung growth in CDH patients remaining uncertain. Structural and functional assessment via MRI has the potential to provide novel measurements of post-operative neonatal lung development in CDH patients.
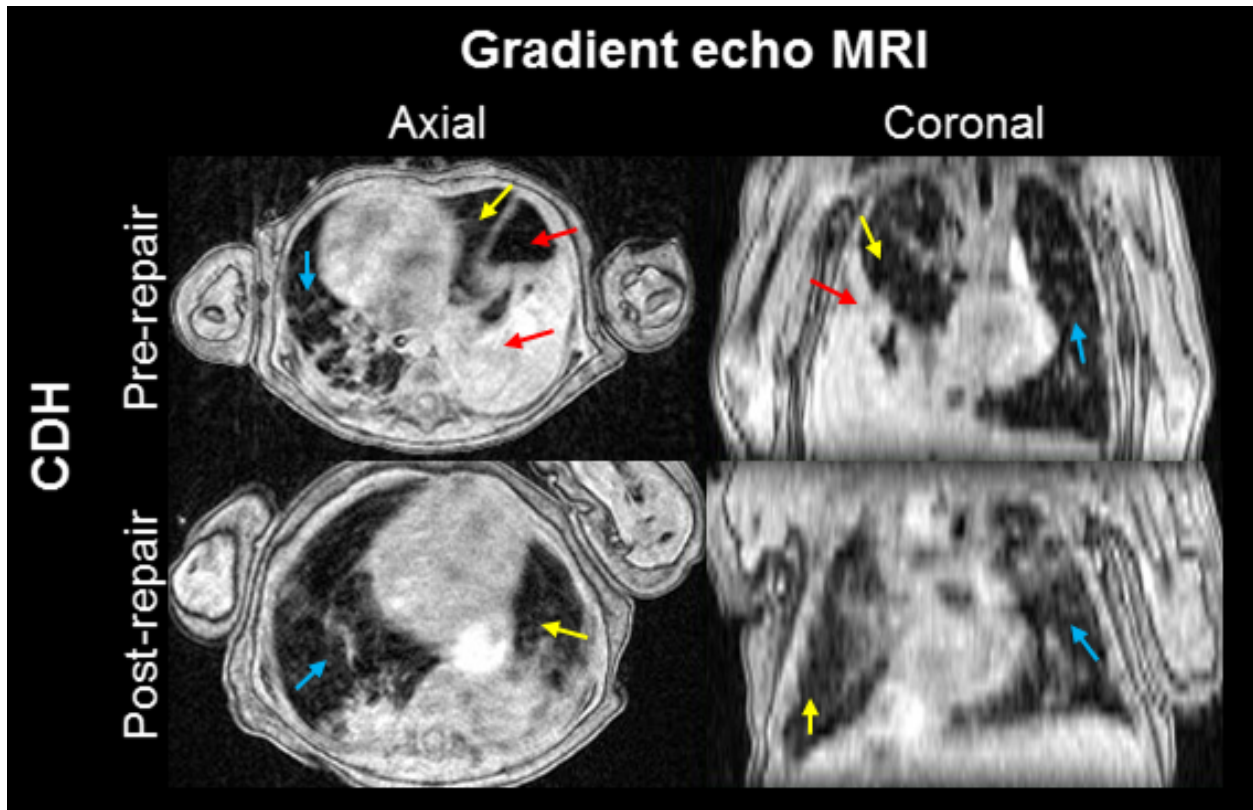
Figure 3.8: Conventional (gradient echo) MR images of congenital diaphragmatic hernia (CDH) in a neonatal patient, with pre-surgical repair anatomy (top row, demonstrating visceral herniation into the thoracic cavity) and post-surgical repair anatomy (bottom row, demonstrating repair of the diaphragmatic surface). The ispilateral lung (on the same side as the herniation) is indicated by yellow arrows, the contralateral lung (on the opposite side from the herniation) is indicated by blue arrows, and the herniated organs on the ispilateral side are indicated by red arrows. Axial images are shown in the left column, and coronal image are shown in the right column. Resolution suffers in the superior-inferior direction because the gradient echo was acquired axially with a slice thickness (3 mm) larger than the in-plane resolution (0.78 x 0.78 mm^2).

3.3.3 Esophageal Atresia / Tracheoesophageal Fistula

Esophageal atresia (EA) is a relatively uncommon congenital malformation that affects approximately 1 in 2500 to 4000 live births [29]. EA is typically observed in conjunction with a tracheoesophageal fistula (TEF), typically between the trachea and distal esophageal pouch (Type C); other classification subtypes include Type A (EA without TEF), Type B (EA with

proximal TEF), Type D (EA with proximal and distal TEF), and Type E (TEF without EA) (Figure 3.9) [30, 31]. Often infants with EA/TEF have trouble breathing or feeding on their own. After birth, these infants typically present with respiratory distress and have excessive salivation, vomiting, coughing, and choking; these sometimes results in aspiration, reflux, pneumonitis, and gaseous distention of the stomach [7]. Ventilation can be negatively affected due to reduced tidal volumes, and gastric distention can reduce lung compliance via an elevated diaphragm [32]. EA/TEF is considered a surgical urgency, involving ligation of the fistula and anastomosis of the esophagus, and operation for repair is required.
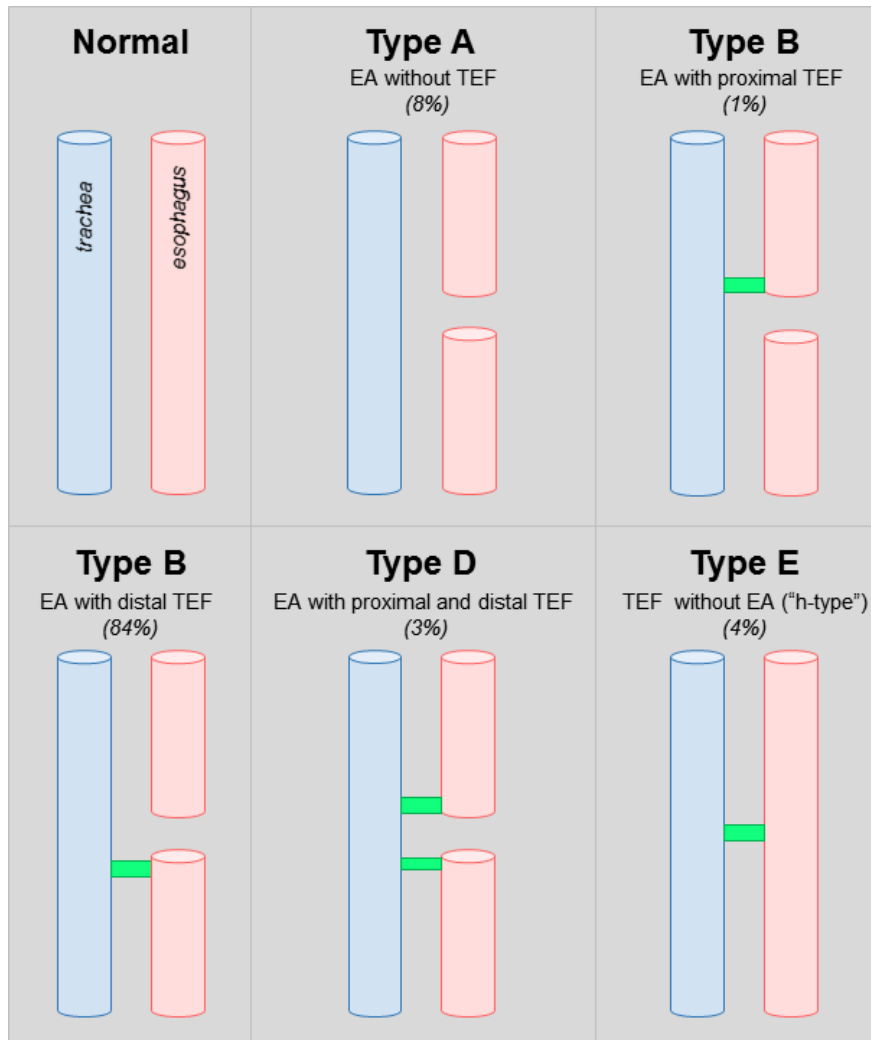
Figure 3.9: Types of esophageal atresia/tracheoesophageal fistula (EA/TEF) and each variation's relative frequency: EA without TEF (Type A), EA with proximal TEF (Type B), EA with distal TEF (Type C, the most common variation), EA with proximal and distal TEF (Type D), and TEF without EA (Type E).

Currently, there are no acceptable tools for evaluating EA/TEF anatomy prior to repair. In most patients, the EA/TEF diagnosis is confirmed only with a plain chest x-ray showing a coiled feeding tube within the upper esophageal pouch. Importantly, this approach to "confirmation" cannot determine the anatomic subtype of EA/TEF, the number or location of TEFs, the size of the gap between proximal and distal esophagus, or the presence of tracheomalacia. A few studies have evaluated computerized tomography (CT) scanning in

33

pre-surgical evaluation of EA/TEF and found that CT could frequently identify the origin of the fistula and the size of the EA gap (Figure 3.10) [33, 34]. Although these studies suggested a benefit from preoperative CT scans improving surgical planning in 40% of cases, they also demonstrated a significant and unacceptably high exposure to ionizing radiation. Thus, there is a need for safe, non-invasive, non-ionizing imaging methods for visualizing and assessing pre-surgical EA/TEF anatomy, which would add value in surgical planning; this need may be met with high-resolution structural MRI. Such imaging may help identify infants at risk for complications and offer clinical teams an opportunity to reduce these risks. Additionally, post-operative imaging may provide an opportunity to evaluate surgical efficacy and developing function within the repaired anatomy.
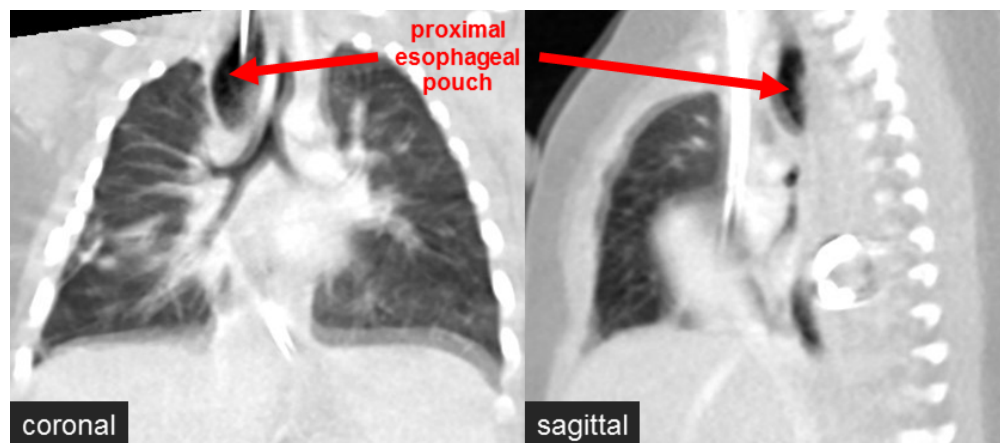
Figure 3.10: Neonatal chest CT of esophageal atresia/tracheoesophageal fistula (EA/TEF). The current clinical standard for pre-surgical-repair diagnosis is chest x-ray radiograph, though in this particular case, CT was clinically required. In this case, the CT findings were indicative of a proximal esophageal pouch, despite non-negligible respiratory motion artifacts. Typical x-ray radiographs demonstrate coiling of a feeding tube and provide no information on the rest of the possible EA/TEF malformation.

3.3.4 Tracheomalacia

Tracheomalacia (TM) is the most common pediatric abnormality of the trachea, affecting ~10-50% of neonates with BPD [35, 36, 37, 38, 39, 40], and is sometimes observed in patients

with CDH or EA/TEF morbidities. TM is characterized by a diffuse or focal weakness of the tracheal airway walls, due to deficiencies in smooth muscle or underdeveloped/absent cartilaginous tracheal rings. This airway wall weakness results in dynamic collapse of the tracheal lumen during expiration, when positive intrathoracic pressure is induced by diaphragmatic motion (Figure 3.11) [41]. Narrowing of the intrathoracic trachea, whether global or local, increases airway resistance and decreases airflow. Clinical symptoms of TM include dyspnea (labored breathing), wheezing (high-pitched lung sounds, typically during exhalation), or stridor (high-pitched, "rough" sound, typically more prominent during inhalation), and can lead to recurrent infections [42].
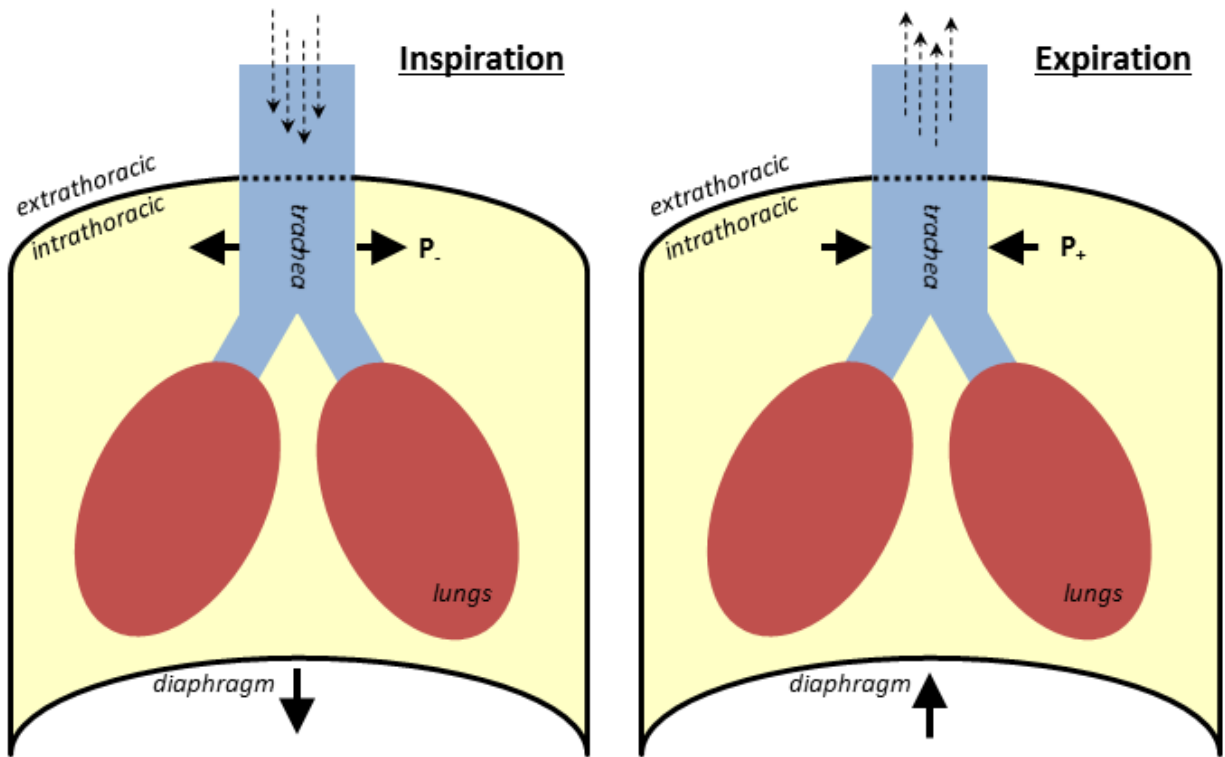
Figure 3.11: Schematic of the intrathoracic pressure during respiration. At inspiration the intrathoracic pressure is negative due to the descending diaphragmatic motion, allowing the intrathoracic tracheal lumen to remain fully expanded. However, the intrathoracic pressure is positive at expiration, and when combined with underdeveloped or weak airway walls will result in dynamic tracheal collapse, or tracheomalacia (TM).

Premature patients, especially those with BPD, are particularly susceptible to TM because of underdeveloped tracheal structures and damage induced by prolonged positive pressure ventilation [43, 44]. These infants with BPD and concomitant TM tend to have longer and more complex NICU hospitalizations, with increased medical and surgical co-morbidities and increased medical support at discharge [39]. TM can often be life-threatening, with "dying spells" (i.e. sudden events of central airway obstruction) often demand resuscitation with ventilation.

The current clinical standard for diagnosing TM is a semi-quantitative measure of dynamic collapse during a bronchoscopy with endotracheal intubation (Figure 3.12), which requires sedation and increased risk to the patient. The requirement of a sedated, invasive procedure for obtaining diagnosis presents a significant challenge in the study of TM, since the use of an endotracheal tube and sedation often masks the dynamic mechanisms presented by TM that a clinician is attempting to observe [45]. As such, there remains a need for a safe method to quantitatively evaluate neonatal airway collapse.
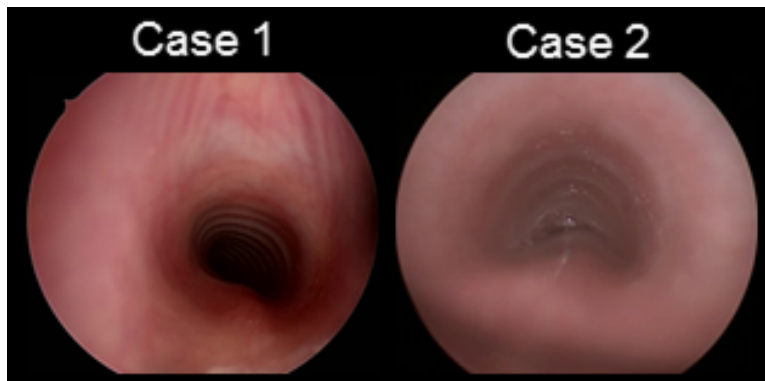
Figure 3.12: Clinical bronchoscopies of neonatal patients with EA/TEF, shown at expiration. Note that the intrathoracic trachea remains open during inspiration but collapses dynamically during expiration. The patient at left (Case 1) has only mild collapse of the posterior tracheal wall (shown here at the bottom of the lumen), while the patient at right (Case 2) has near-complete collapse at expiration.

Part II

Hyperpolarized Gas MRI

Historically, most MRI has utilized NMR specific to ^{1}H in Boltzmann (thermal) equilibrium; while the equilibrium polarization of ^{1}H is very small (approximately parts per million), its high proton density in human and animal tissue more than compensates to yield a detectable NMR signal (see Section 1.1). However, conventional MRI focused on a nucleus much less abundant within the body than ^{1}H has typically been less successful, due to an insufficient number of spins generating an undetectable NMR signal. This has been the case for gases within the lung airspaces at physiologic pressures (1 atm), which have a nuclear spin density lower than that of ^{1}H in soft tissues and liquids by approximately three orders of magnitude.

Beginning several decades ago, techniques for hyperpolarizing nuclear spin populations in gases have been developed [46, 47, 48, 49], with spin exchange optical pumping (SEOP) methods increasing the polarization of spin-$\frac{1}{2}$ noble gases by approximately five orders of magnitude (approximately parts per ten), overcoming the low gas spin density and yielding a very detectable NMR signal. The process of SEOP aligns spins via an angular momentum transfer from circularly polarized light. The hyperpolarized gas can be inhaled by subjects or patients and imaged via MR to illuminate the gas spins in the lung airspaces, rather than the ^{1}H spins in the lung tissue.

Research studies that utilize hyperpolarized gas pulmonary MRI are now abundant. However, clinical application of these methods has been limited by several challenges: the scarcity of ^{3}He; demand of high expertise and complex equipment for performing SEOP of noble gases; difficulties in implementing multi-nuclear capabilities on commercially available MRI scanners; and lack of Food and Drug Administration (FDA) approval for the gas substance. Despite these challenges, researchers have now focused on a number of dis-

ease applications for both adults and pediatrics, such as asthma, COPD, and cystic fibrosis [50, 51, 52, 53, 103, 54, 55], and the potential is high for hyperpolarized gas MRI techniques to non-invasively elucidate the obstructive and restrictive components of lung disease. Currently there has been limited application in very young pediatrics and infants, due to the low compliance and high vulnerability of this patient population. The healthy and diseased ex-vivo infant lung work detailed in this thesis represents the first gas diffusion MRI data to be acquired in lungs of such a young age.

4 Spin Exchange Optical Pumping

A primary method for generating hyperpolarized gases is spin exchange optical pumping (SEOP), which involves optical pumping of the electron spins of an alkali-metal vapor from circularly polarized light, which is then transferred via spin exchange to nuclear spins of a noble gas. While possible for all noble-gases, the SEOP method is most effective for spin-$\frac{1}{2}$ nuclei because the relaxation time T_1 is longer for such nuclei. Further, the only stable spin-$\frac{1}{2}$ noble gases are ^{3}He and ^{129}Xe, so this work is specific to these nuclei.

4.1 Depopulation Optical Pumping of Rubidium

The most common choice of alkali-metal for optical pumping is rubidium (Rb), due to the historical availability of lasers at the Rb D$_1$ transition. An optical pumping cell containing the Rb metal vapor and the noble gas of choice are placed in a magnetic holding field (typically $\sim$30 G) in order to create a spin axis along direction of the laser light and the angular momentum. The Rb electron energy levels and optical pumping transitions are shown in Figure 4.1. The lowest two electronic energy levels are shown (ground state 5s$_{1/2}$and first excited state 5p$_{1/2}$), with an optical transition from resonant photons at 794.7 nm. Here, the following notation is used: $n = 5$ is the principal quantum number; s and p indicate orbital

angular momentum $l = 0$ and 1, respectively; and $\frac{1}{2}$ refers to the total angular momentum

(sum of spin and orbital angular momentum) as $j = \frac{1}{2}$. When in the presence of a weak

magnetic field (usually ~30 G), the first two states are split into spin-up ($m_j = +\frac{1}{2}$) and

spin-down ($m_j = -\frac{1}{2}$) states. Left-handed and circularly polarized light (σ^+) has one unit

of angular momentum (selected to be aligned parallel to the field), and is only able to excite

an electronic transition between the spin-down state of $5s_{1/2}$ and the spin-up state of $5p_{1/2}$,

as shown by the blue transition line; this is due to the magnetic selection rule $\Delta m_j = +1$,

which relates to the conservation of the angular momentum component parallel to the field

axis [56].
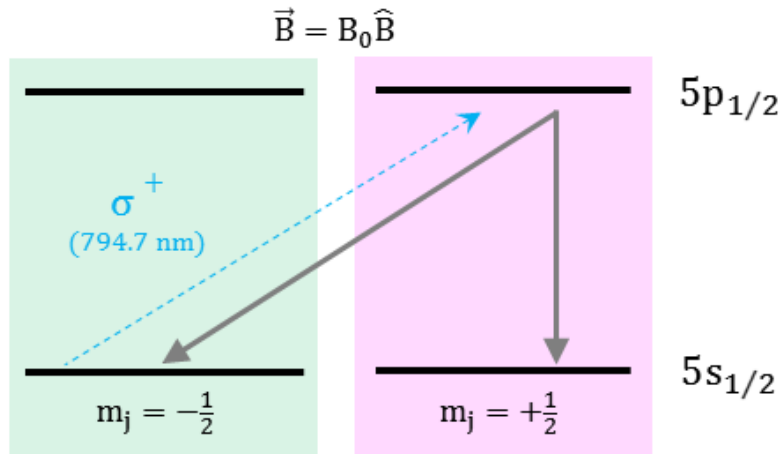
Figure 4.1: The rubidium electron energy levels and optical pumping transitions. The lowest two energy levels ($5s_{1/2}$ and $5p_{1/2}$) are shown, with an optical transition of 794.7 nm (D_1 absorption line of Rb). Due to the magnetic selection rule $\Delta m_j = +1$, the left-handed, circularly polarized light (σ^+) is only able to excite an electronic transition between the spin-down state ($m_j = -\frac{1}{2}$; green) of $5s_{1/2}$ and the spin-up state ($m_j = +\frac{1}{2}$; purple) of $5p_{1/2}$, as shown by the blue transition line. These excited electrons will transition to the ground state evenly between the two m_j states, but with constant optical pumping, the spin-up ground state will contain almost the whole population, while the spin-down ground state will become depopulated.

These excited electrons in the spin-up state will transition back to the ground level with

equal probability between the two m_j states, but with continuously supplied photons, the

spin-up ground state will eventually contain almost the whole population, while the spin-down ground state will eventually become depopulated. It is possible for electrons in the spin-up ground-state to relax to the spin-down ground-state, and so the rate of photons added to the system is dependent on the rate of ground-state relaxation; within one relaxation time, there must be at least two photons added per Rb atom to overcome an overall zero gain in the depopulation scheme [56]. During de-excitation, photon emission is possible, with such photons typically having a different polarization and direction than those from the laser source; if in a pure mixture of Rb and noble gas, these photons would be reabsorbed in the thick Rb vapor cloud and re-emitted again, in a cycle of radiation trapping which can depolarize the system. Such catastrophic effects can be avoided by adding in small concentrations of N_2 buffer gas ($\sim$1%) that generate collisional de-excitation by taking the excitation energy as rotational or vibrational energy [56].

4.2   Spin Exchange with Noble Gases

In this context, spin exchange is a process in which the polarization of the Rb electrons is transferred to the nuclei of the noble gas of interest (here, ^{3}He or ^{129}Xe), e.g.: $e_\uparrow^- + {^3}He_\downarrow \Longrightarrow e_\downarrow^- + {^3}He_\uparrow$ [57, 58, 59]. During collisions between the Rb and noble gas atoms (Figure 4.2), the wavefunctions of the Rb electrons and the noble gas nuclei overlap to generate a quantum mechanical Fermi contact interaction represented by the following Hamiltonian:

$$\boldsymbol{\mathcal{H}} = \alpha(r)\boldsymbol{I} \cdot \boldsymbol{S} = \frac{\alpha(r)}{2}\left[S_+ I_- + S_- I_+\right] + \alpha(r)S_z I_z. \tag{4.1}$$

e⁻Rb
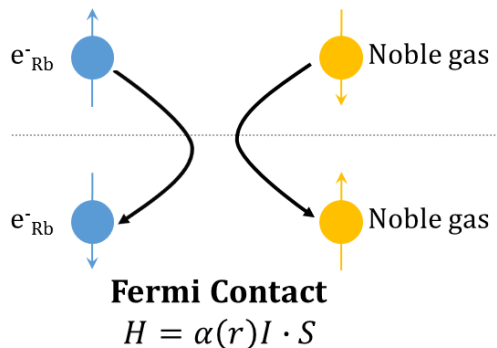
Fermi Contact
$$H = \alpha(r)I \cdot S$$

Figure 4.2: The wavefunctions of Rb electrons and noble gas nuclei overlap during collisions, generating a Fermi contact interaction $\boldsymbol{H} = \alpha(r)\boldsymbol{I} \cdot \boldsymbol{S}$, where $\boldsymbol{I}$ is the noble gas nuclear spin operator, $\boldsymbol{S}$ is the Rb electronic spin operator, and $\alpha(r)$ is representative of the overlap.

where $\boldsymbol{I}$ is the noble gas nuclear spin operator, $\boldsymbol{S}$ is the Rb electronic spin operator, and $\alpha(r)$ is representative of the overlap (a strong exponential dependence on separation distance, such that the interaction is negligible at relatively large distances; $\alpha(r) \propto e^{-\beta r}$). This Hamiltonian includes a magnetic-dipole interaction as the dominant interaction of spin exchange between the Rb electrons and noble gas nuclei. This interaction has terms $I^{+}S^{-}$ and $I^{-}S^{+}$ for the exchange of spin (angular momentum) between the Rb electron (S) and the noble gas nucleus (I). A description of Fermi contact interaction via binary collisions is sufficient to explain spin exchange between Rb electrons and ^{3}He nuclei. However, since ^{129}Xe nuclei are a much heavier noble gas, spin exchange between Rb electrons and ^{129}Xe nuclei predominantly takes place via interactions in van der Waals molecules (Figure 4.3). These weakly bound van der Waals molecules form at a rate of $(T_{Rb})^{-1}$ per Rb atom and $(T_{Xe})^{-1}$ per ^{129}Xe atom and move freely for a lifetime of duration τ, before being broken up by a collision with other atoms or molecules at a rate of τ^{-1}. [57] The spin exchange cross section for ^{3}He is $\sigma_{SE} = 2.1 \cdot 10^{-8} \mathring{A}^{2}$, while for ^{129}Xe it is $\sigma_{SE} = 1.6 \cdot 10^{-4} \mathring{A}^{2}$ [60, 61], and the van der Waals molecule interaction is relevant for ^{129}Xe but not for ^{3}He due to a several orders of magnitude difference between ^{129}Xe and ^{3}He in the strength of the spin-rotation interaction from the noble gas nucleus [58]. As the spin exchange cross section and the

interaction time for ^{3}He ($\tau \propto 10^{-12}$) are both small, spin exchange via the binary collisions for ^{3}He is relatively slow (typically on order of a day for steady state to be reached); however, the destruction of the spin polarization is correspondingly slow, with T_1 relaxation back to Boltzmann equilibrium typically lasting between 10-50 hours. On the other hand, interaction times for ^{129}Xe are relatively longer ($\tau \propto 10^{-9}$), with polarizing times on order of 1 hour, but with T_1 relaxation also on order of 1 hour.
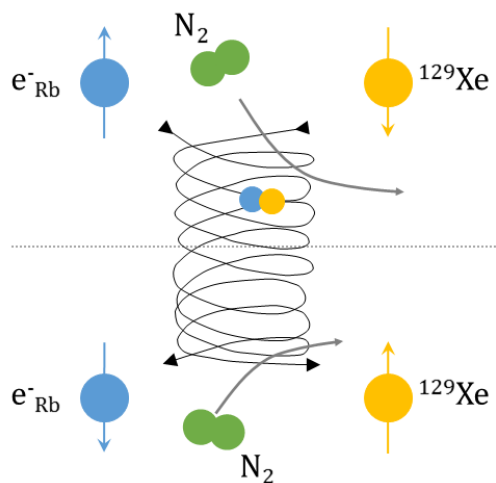
Figure 4.3: Three-body collisions occur between Rb atoms, ^{129}Xe atoms, and N$_2$ atoms and generate van der Waals molecules, yielding spin exchange between the Rb electrons and ^{129}Xe nuclei.

The process of spin exchange takes place with a certain rate, γ_{SE}, and is linearly dependent on the Rb vapor density and the collision rate. Because of the strong dependence on separation, $\alpha(r)$, the rate of spin exchange interactions is small. For example, experimentally-measured values for γ_{SE} of ^{3}He have been found to be $\sim$0.125 hours^{-1}, yielding $\sim$95% ^{3}He polarization in $\sim$ 24 hours [56]. Intrinsic nuclear-spin T_1 relaxation processes act to destroy the build-up of noble gas polarization. Most of the relaxation stems from collisions of the noble gas with the walls of the polarizing cell. The build-up rate of noble gas polarization (P) during SEOP can be described by:

$$\frac{dP}{dt} = \gamma_{SE}(P_{Rb} - P) - T_1^{-1}P, \tag{4.2}$$

where P_{Rb} is the electron polarization of Rb. The first term, $\gamma_{SE}(P_{Rb} - P)$, represents the build-up noble gas polarization via interactions with polarized Rb, while the second term, $T_1^{-1}P$, represents the destruction of noble gas polarization via T_1 relaxation processes. Thus the noble gas polarization can be modeled by

$$P = \frac{P_{Rb}\gamma_{SE}}{\gamma_{SE} - T_1^{-1}} \cdot (1 - e^{-t(\gamma_{SE} - T_1^{-1})}), \tag{4.3}$$

if one assumes that there is no polarization at time t $= 0$. With a larger γ_{SE} , the achievable maximum polarization level is higher, with steady state more quickly reached; with a shorter T_1, the time to reach steady state is shorter, but the maximum achievable polarization is lower (Figure 4.4). For short polarization times, such that the exponential argument is very small, this polarization build-up is linear and independent of T_1:

$$P = P_{Rb}\gamma_{SE}t. \tag{4.4}$$

At large times, the polarization build-up limit follows

$$P = \frac{P_{Rb}\gamma_{SE}}{\gamma_{SE} - T_1^{-1}}. \tag{4.5}$$

When $\gamma_{SE} \gg T_1^{-1}$, P approaches the P_{Rb}.

Destruction of spin polarization (T_1) can yield from several sources:

$$\frac{1}{T_1} = \frac{1}{T_{1,intrinsic}} + \frac{1}{T_{1,oxygen}} + \frac{1}{T_{1,surfaces}} + \frac{1}{T_{1,B_0 gradients}}. \tag{4.6}$$
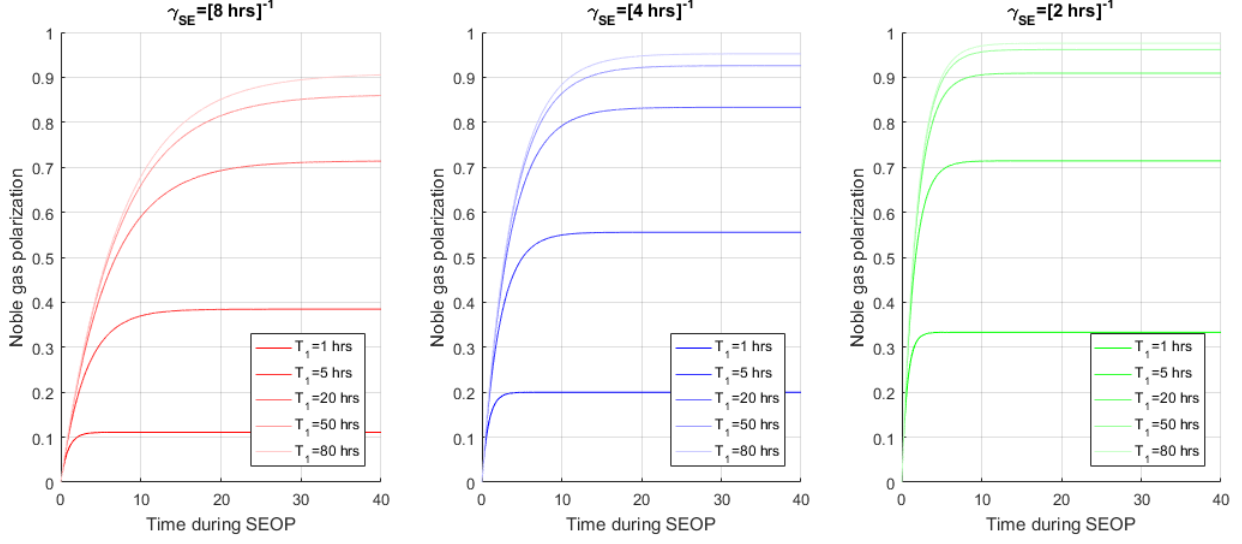
Figure 4.4: The build-up of noble gas polarization as a function of time during spin exchange optical pumping (SEOP), following Equation 4.3, for varying relaxation times ($T_1 = 1$, 5, 20, 50, and 80 hours, in decreasing color intensities) and spin exchange rates ($\gamma_{SE} = [8$, 4, and 2 hours$]^{-1}$, at left, center, and right). This data assumes a 100% Rb electron polarization. With a larger γ_{SE} , the achievable maximum polarization level is higher, and steady state is more quickly reached. Note that at short times (dependent on T_1 and γ_{SE}), the polarization build-up is linear, following Equation 4.4.

A gas's intrinsic relaxation is due to interactions with atoms of the same gas and depend on the gas's concentration; these relaxation rates have been well established for ^{129}Xe ($\frac{1}{T_{1,intrinsic}} \sim \frac{1}{52}$ amagat/hr) and ^{3}He ($\frac{1}{T_{1,intrinsic}} \sim \frac{1}{800}$ amagat/hr) [62], which provide a lower limit on the relaxation rates (i.e. upper limit on the T_1 relaxation times) for our noble gases of interest. $\frac{1}{T_{1,oxygen}}$ is relaxation due to interactions with highly paramagnetic oxygen molecules (O_2); this relaxation in-situ is mostly obviated with careful purging and leak testing of experimental gas handling equipment. $\frac{1}{T_{1,surfaces}}$ is relaxation due to interactions with the surface of the polarizing cell ("wall relaxation"), and is the dominant source of spin-lattice relaxation for noble gas polarization. This surface relaxation is theoretically proportional to the nucleus RMS velocity and the cell surface area, and inversely proportional to the volume, although the mechanism is still not well understood [56]. $\frac{1}{T_{1,B_0 gradients}}$ generates from

45

the diffusion of the polarized spins through local gradients of the applied holding field B_0, which is typically negligible in typical experimental conditions.

5   Multi-nuclear Experimental Equipment

Here, we present select details on the hardware used in the production and imaging of hyperpolarized gases. The author has been involved more heavily with the design and construction of a home-built ^{129}Xe polarizer, but has not performed ^{129}Xe MRI with gas from this device. Additionally, the author was less involved with the construction of a home-built ^{3}He polarizer, but has performed SEOP troubleshooting on this polarizer, and has performed ^{3}He MRI using gas from this device. Thus more detailed discussion is provided here for home-built ^{129}Xe polarizer components, as well as for ^{3}He SEOP troubleshooting and an RF coil and scanner optimized for ^{1}H/^{3}He multi-nuclear MRI. For similar reasons, less detail is provided on the design and construction of the home-built ^{3}He polarizer equipment and for ^{1}H/^{129}Xe multi-nuclear imaging.

The key components and basic schematic of a noble gas polarizer device are detailed in Figure 5.1, and include: a laser with high output ($> \sim$50W) centered narrowly on the D_1 transition line of Rb ($\sim$794.7 nm); optics to convert linearly polarized light from the laser to circularly polarized; coils for a homogeneous magnetic holding field ($B_0 \sim$10-100 G); an optical pumping cell (typically held at 10 atm for SEOP) with outlet for dispensing gas; an optical pumping oven to heat Rb in the polarizing cell to vapor temperatures; and an NMR spectrometer and RF coil to monitor the NMR signal from the hyperpolarized noble gas.

5.1 ^{129}Xe Polarizer Hardware

The author was involved in the design and construction of multiple components of a home-built polarizer for ^{129}Xe, which is a scaled-up version of an open-source design. The polarizer
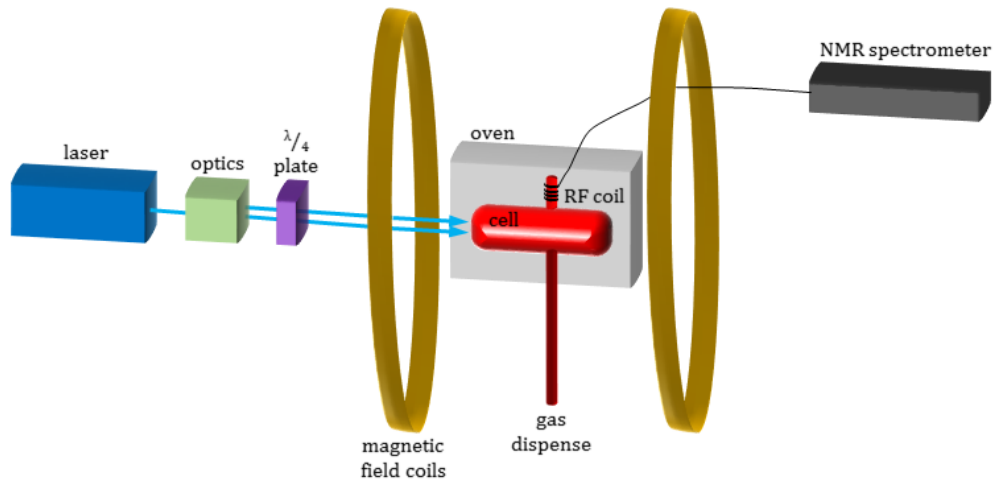
Figure 5.1: Basic schematic of the key components of a hyperpolarizer device.

has approximate dimensions of 1.6 m × 0.8 m × 1.5 m (length × width × height). Figure 5.2 shows the layout of various components within the polarizer and highlights equipment for which the author made significant contributions with asterisks. These particular components are detailed below more thoroughly.
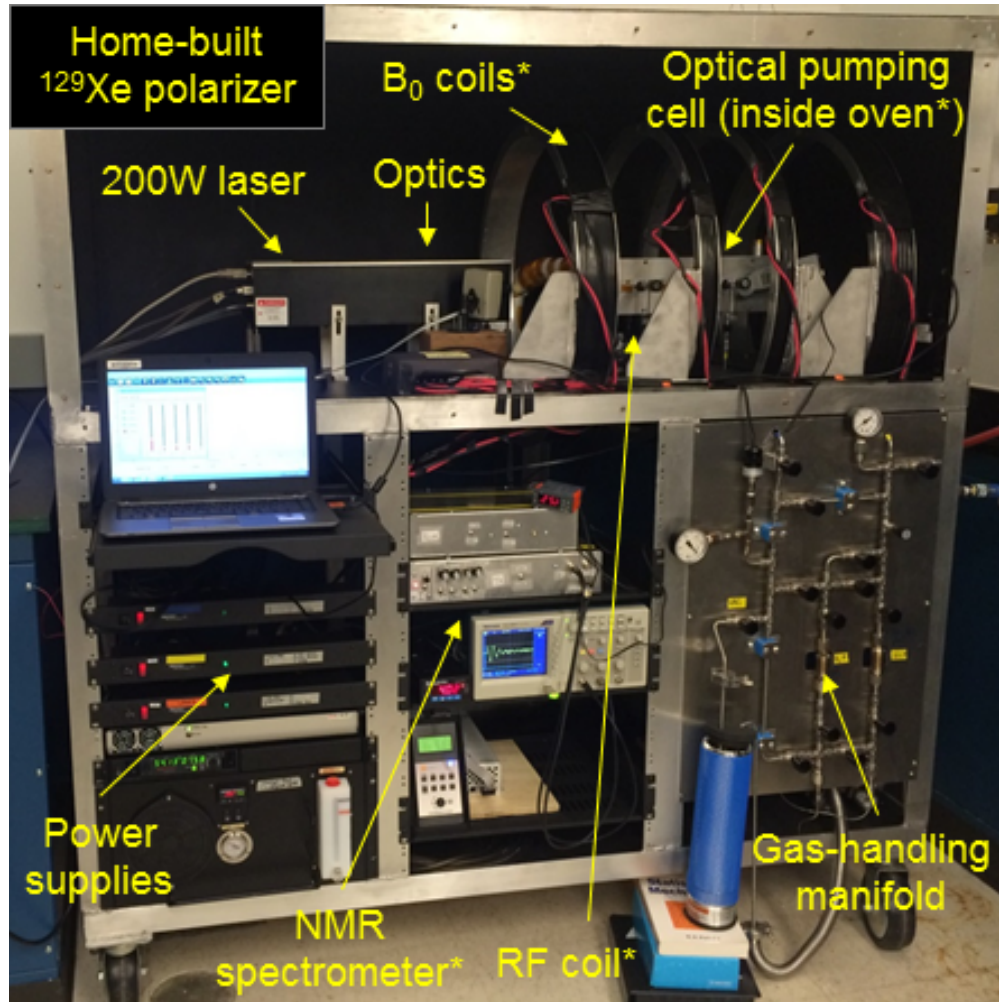
Figure 5.2: A home-built ^{129}Xe hyperpolarizer device located in the Center for Pulmonary Imaging Research in Cincinnati Children's Hospital. This polarizer is capable of producing $\sim$25% absolute polarization in ^{129}Xe gas. Asterisks indicate components of equipment for which the author made significant contributions. This polarizer is a scaled-up version of a previously published open-source polarizer design [63].

Home-built Homogeneous B$_0$ Holding Field A key component for SEOP is a static and homogeneous B$_0$ holding field, consistent with the Larmor frequency over the volume of the optical pumping cell. The polarizer has four electromagnetic coils (Figure 5.3-top), providing a field of $\sim$53 G and a ^{129}Xe Larmor frequency of $\sim$62.5 kHz. Each coil frame is made of aluminum and has a diameter of 60 cm. The four coils are spacing in Barker

configuration [64], to yield improved field homogeneity across the optical pumping cell beyond that provided by a 2-coil Helmholtz pair. Following Barker's work considering coaxial circular coils arranged symmetrically about a central coil or pair of coils [64], the field component parallel to the axis is

$$B_{\parallel} = 2\pi \left[C_1 + C_3 r^2 P_2(cos\theta) + C_3 r^4 P_4(cos\theta) + C_7 r^6 P_6(cos\theta) + ... \right], \qquad (5.1)$$

while the field component perpendicular to the axis is:

$$B_{\perp} = -2\pi sin\theta \left[(C_3'3) r^2 P_2'(cos\theta) + (C_5'5) r^4 P_4'(cos\theta) + ... \right], \qquad (5.2)$$

where r and θ represent the polar coordinates at a specified location, the coefficients C_n are functions of the coil currents, radii, and positions, and $P_n(cos\theta)$ are the Legendre functions. Because of the system symmetry, all even coefficients C_n are zero. However, to yield a particularly homogeneous field, it is desirable to force early odd coefficients to go to zero as well, such that any remaining coefficients dependent on location are of high powers of r and account for small contributions to the field. One method of achieving this is to have identical coil radii with adjusted coil separations and current values [64]. A Helmholtz coil pair is the simplest example of this arrangement. Barker investigated a four-coil system of this arrangement and found that in the following arrangement, the coefficients C_3, C_5, and C_7 disappear [64]:

$$\frac{D_{inner}}{r} = 0.243186, \qquad \frac{D_{outer}}{r} = 0.940731, \qquad \frac{I_{inner}}{I_{outer}} = 0.442391, \qquad (5.3)$$

where D_{inner} is the distance of either inner coil from the center of the system, D_{outer} is the distance of either outer coil from the center of the system, r is the radius of any coil, I_{inner}

is the current of the inner coils in series, and I_{outer} is the current of the outer coils in series.

Thus for the home-built ^{129}Xe polarizer, a four-coil system was chosen with identical radii for each ($R = 30cm$), with a D_{inner} value of 7.3 cm, and a D_{outer} value of 28.2 cm. The outer and inner coils have 208 and 92 wire turns, respectively, in keeping with Equation 5.3 to yield a current ratio of 0.4423. Following the Biot-Savart law, the magnetic field from a current element $d\vec{B}$ is

$$d\vec{B} = \frac{\mu_0}{4\pi} \frac{I d\vec{l} \times \hat{r}}{r^2}, \tag{5.4}$$

where μ_0 is the vacuum permeability, I is the current, $d\vec{l}$ is the length element carrying current, and $\hat{r}$ is the vector specifying the direction of the current element to the field point at r. The on-axis field B_z for N loops of current overlaying each other is given by

$$B_z = \frac{\mu_0 N I}{2} \frac{R^2}{(z^2 + R^2)^{3/2}}, \tag{5.5}$$

where R is the loop radius and z is the distance from the center of the loop to the on-axis field point. Thus the theoretical magnetic field at the center of our four-coil system is $B_{center} = 6.905 \cdot I \frac{gauss}{A}$; with 7.69 A of current, $B_{center} = 53.07$ gauss. The field was experimentally measured with a gaussmeter along and across the coil axis (Figure 5.3-bottom), with results demonstrating a homogeneous field profile of ~ 53 gauss across the optical pumping cell volume ($\pm$ 0.2% variation).

The wire turns on the coil were wound at tension in an orderly manner by hand with magnet wire (12-gauge copper wire, insulated with polyurethane) while the coil frame was mounted on a slowly rotating lathe; this work was performed with much appreciated assistance from the Machine Shop in the Department of Physics at Washington University in St. Louis. The aluminum frames were wrapped with electrical tape prior to wire wrapping, to avoid possibility of a scratch in the wire shorting to ground. For similar reasons, protective

shrink wrap was fit around the wire at entry points onto each frame. The wire resistance for the magnet wire was $\rho = 1.589\Omega$ / 1000 ft at 20°C, making the resistance of one turn $R \approx 0.00998\ \Omega$. Thus with the outer coil of 208 turns having a wire length of ~ 1300 ft and the coil of 92 turns having a wire length of ~ 580 ft, the outer coil's resistance is $R \approx 2.1\ \Omega$, and the inner coil's resistance is $R \approx 0.9\ \Omega$.
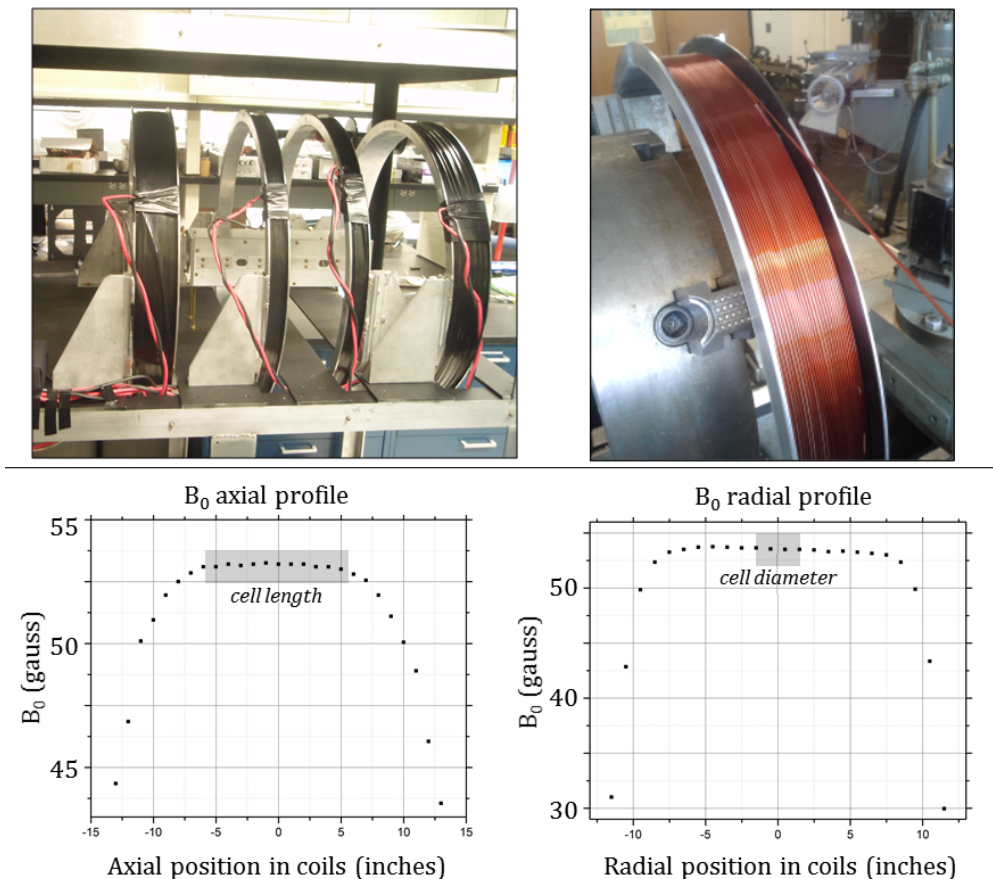
Figure 5.3: Top left: Coils for a B_0 holding field ($\sim$53 gauss) for SEOP in a Barker spacing configuration. Top right: A close-up of the magnet wire winding. Bottom left/right: The homogeneous field profile across the coil axis/diameter at central radial/axial positions, where the cell is positioned.

Home-built Spin Exchange Optical Pumping Oven   An optical pumping oven was designed by the author and constructed in conjunction with the Machine Shop in the Department of Physics at Washington University in St. Louis, with adaptations from previous

models [63], shown in Figure 5.4. The purpose of an optical pumping oven is to immerse the optical pumping cell in temperatures sufficient for vaporization of Rb alkali metal. This oven accommodates 3" optics, necessary for the 2.5" diameter of the polarizer's laser. At the front end of the oven (first oven surface to encounter laser light) is a 3"-diameter anti-reflection optical window, and in the rear is a 3"-diameter retro-reflection mirror, to force photons that were not absorbed at first pass to pass back through the cell upon reflection. A rectangular viewing window is included on one side to allow for monitoring of infrared photons.

Figure 5.4: Photos of an optical pumping oven designed by the author, and a photo of two glass optical pumping cells, designed by colleagues of the author.

With an inlet near the top front and an outlet near the rear side, this oven also allows for external forced-air flow to both heat to desired cell temperatures during SEOP and to cool after polarizing to quickly condense the Rb vapor before dispensing of the hyperpolarized noble gas for imaging. The temperature is regulated with a thermocouple and temperature controller, and the heating/cooling air is supplied by a liquid N_2 dewar and passes through a heat-pipe to set the desired air temperature.

Holes in one side panel (Figure 5.4-bottom left) are necessary to allow for the optical pumping cell's arms (for gas flow). Interchangeable Teflon "cradles" (with top and bottom) secure the optical pumping cells during use and allow for flexibility to change between various sizes of optical pumping cells (schematic drawing shown in Figure 5.5). Set in a groove in the cradles are large silicone rubber o-rings to avoid heating of the cradles from the optical pumping cell. This oven is mounted at the center of the B_0 field using threaded brass legs, and thus all materials are MR-compatible and high-temperature compatible (aluminum oven, Teflon cradles, brass screws, and Delrin washers).
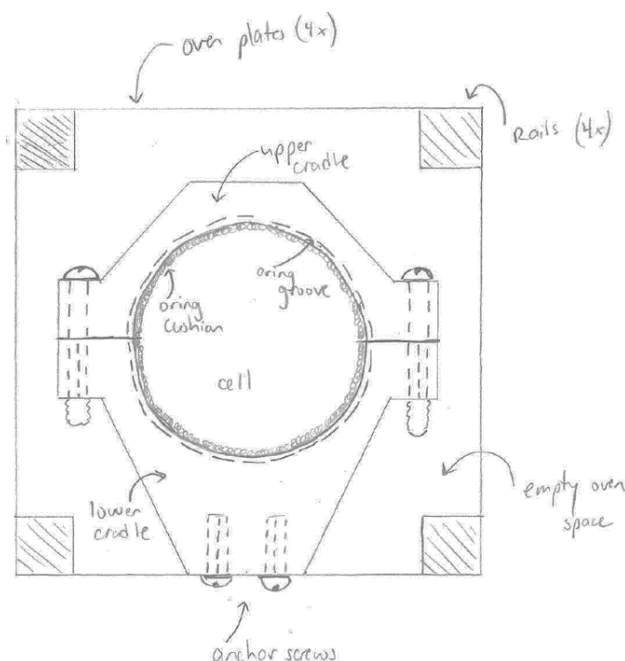
Figure 5.5: A face-on schematic of a holding cradle (top and bottom) for keeping the optical pumping cell secure.

NMR Detection via Home-built RF Surface Coil   Progress of the [129]Xe polarization build-up can be monitored via an NMR probe and spectrometer (spectrometer details below). Here, we measure polarization via a simple surface coil that rests on the outer surface of the optical pumping cell's bottom. This coil is wrapped with 22-gauge wire on a Teflon

frame consists of a small solenoid of 1" diameter and 0.2" length, with 186 turns, yielding an inductance of $L \approx 1300 \ \mu H$, which when paired with a variable capacitor set to $C \sim 5$ nF yields the proper resonant frequency to detect ^{129}Xe spins at $\sim$53 gauss ($\sim$62.5 kHz, following $\omega = (LC)^{-1/2}$). In order to not destroy built-up hyperpolarization of the spins, small flip angles are used. The field from this "bobbin" (Figure 5.6) penetrates strongly approximately one radius away from the coil's plane (where $B_{coil} \propto \frac{1}{r}$ on the coil axis), so in a scenario where the NMR signal resulting from small flip angles was not detectable above the noise, the coil radius could be expanded to penetrate and excite spins deeper into the cell. Teflon washers of the same diameter were constructed, to boost the height of the coil when mounted, depending on which size of optical pumping cell was desired for a given experiment.
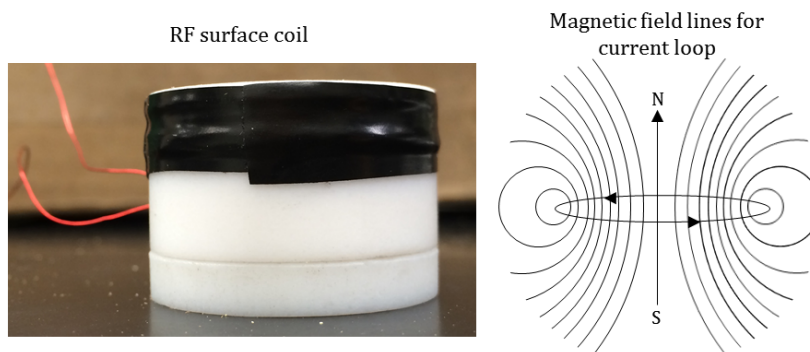
Figure 5.6: ^{129}Xe polarization in-situ can be monitored during SEOP via an RF surface coil and home-built NMR spectrometer (spectrometer details below). Shown here is a home-built 1"-diameter, 0.2"-length, 186-turn surface coil, along with the theoretical magnetic field lines.

NMR Detection via Home-built Spectrometer An NMR spectrometer design was adapted from previous publication by Saam et al. [65] and constructed by the author (Figure 5.7). This spectrometer is inexpensive, self-contained, and compatible with the Larmor frequency of ^{129}Xe nuclei in the holding field ($\sim$53 G; see below), $\sim$62.5 kHz, and it allows for straightforward and convenient NMR monitoring of the polarization. The circuitry is built upon perforated board with manual wire-wrap techniques, with primarily analog components

and limited digital timing.
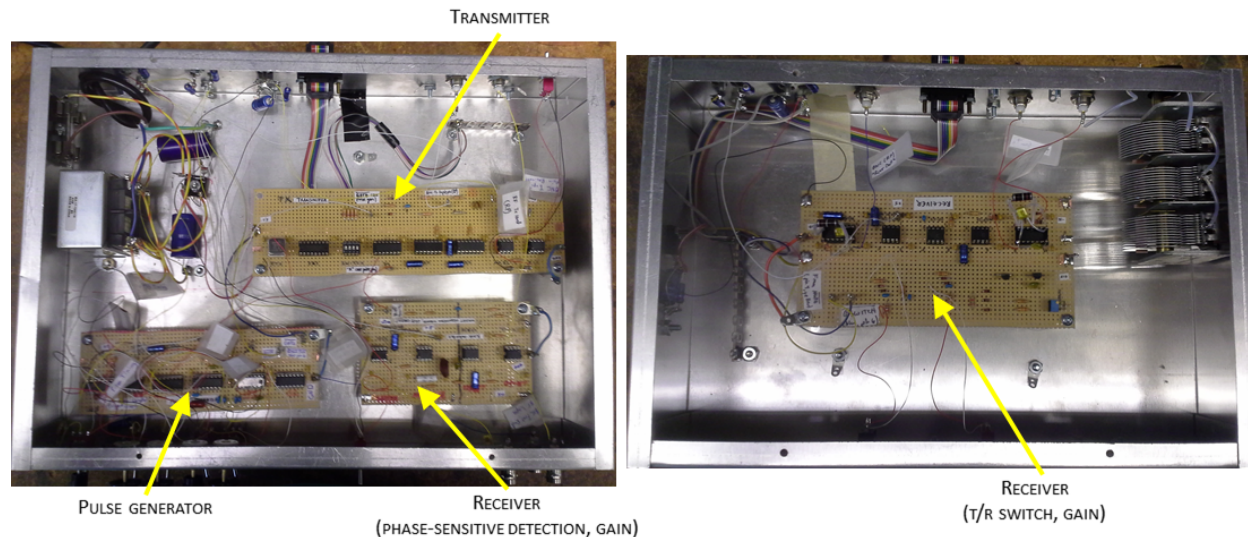
Figure 5.7: A home-built ^{129}Xe NMR spectrometer constructed by the author, with design adapted from [65]. This spectrometer is intended to monitor hyperpolarized gas signal in-situ.

The spectrometer is comprised of four general sections: a pulse generator, a transmitter, a receiver, and a power supply. The pulse generator allows for either a single shot pulse as desired (push-button) or an adjustable, free-running acquisition repetition for periodic pulses. The receiver is gated off with a mute during LC ring-down of the NMR probe. The transmitter includes a 1 MHz crystal oscillator for frequency generation, as well as a preset counter that selects the desired frequency via an "divide-by-2n" circuit (where n = 8 to give a frequency of 62.5 kHz), along with an amplification stage yielding transmitter outputs on order of 1-10 V. The receiver contains a T/R switch to send and receive signal from the NMR probe, and performs phase-sensitive detection and another stage of gain and low-pass filtering of the received signal. The receiver is constructed in two different electrical boxes, such that the main receiver doesn't pick up stray signal from the transmitter and pulse generator. The received NMR signal can be viewed on an oscilloscope.

Successes in Detecting and Imaging Hyperpolarized ^{129}Xe Gas from the Home-built Polarizer   Excitingly, this polarizer had early success in detecting hyperpolarized ^{129}Xe in-situ; Figure 5.8-left shows a free induction decay (FID) (from gas polarized on a commercial polarizer, not the home-build device, due to missing SEOP components at the time), acquired by colleagues of the author. Further, this home-built polarizer has generated hyperpolarized ^{129}Xe and been used in high-quality imaging of subject lungs in-vivo; Figure 5.8-right shows an axial ventilation image of the hyperpolarized gas within the lungs of a healthy 6-year-old subject, also acquired by colleagues of the author.
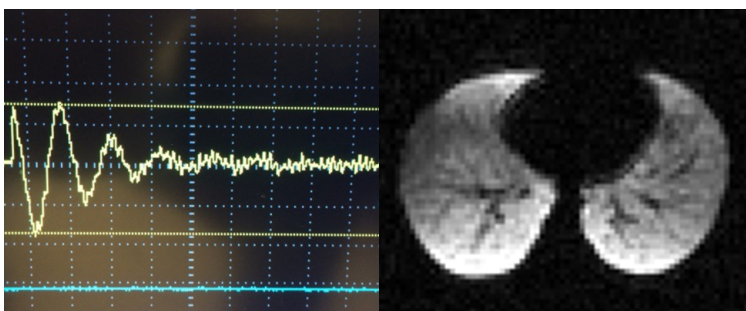
Figure 5.8: Left: A free induction decay (FID) from ^{129}Xe gas hyperpolarized in our home-built device. This FID was detected from 0.5L of 1:1 ^{129}Xe:N_2 gas in-situ, demonstrating success in both hyperpolarization and in detection of the hyperpolarized signal. Right: An axial hyperpolarized ^{129}Xe MR ventilation image of a healthy pediatric volunteer (6 years old) using gas from the home-built polarizer.

5.2 ^{3}He Polarizer Hardware

A home-built ^{3}He polarizer was originally designed and constructed by colleagues at Washington University in St. Louis [56], and is currently in operation in the Center for Pulmonary Imaging Research at Cincinnati Children's Hospital (Figure 5.9). This polarizer is capable of producing $\sim$50% absolute polarization in ^{3}He gas. The author did not participate in the design and construction of this polarizer; however, she has participated in the operation and troubleshooting of the SEOP process on this polarizer, with the latter discussed in more detail here.
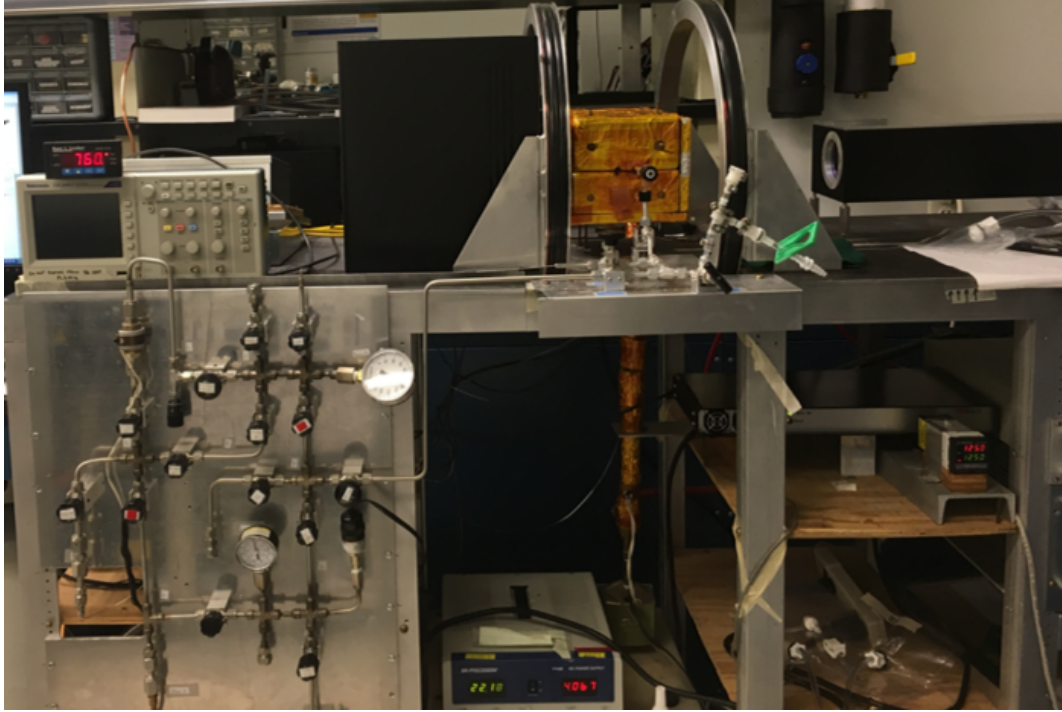
Figure 5.9: A home-built ^{3}He hyperpolarizer device located in the Center for Pulmonary Imaging Research in Cincinnati Children's Hospital. This polarizer is capable of producing $\sim 50\%$ absolute polarization in ^{3}He gas. This polarizer was previously designed and constructed by lab members of the Center [56].

In normal operation, NMR monitoring of this ^{3}He polarizer yields a typical build-up ("spin-up") curve, as shown in Figure 5.10. This experimental data can be fit to Equation 4.3, and separately the short-time and long-time data can be fit to Equations 4.4 and 4.5, respectively, to provides two different methods of extracting the parameters P_{Rb}, T_1, and γ_{SE}. With the entire curve fit to Equation 4.3 in MATLAB, the following SEOP parameters were generated: $P_{Rb} = 40\%$, $T_1 = 43$ hours, and $\gamma_{SE} = (3.7 \text{ hr})^{-1}$. When fitting short-time linear data to Equation 4.4 and long-time constant data to Equation 4.5, the following parameters are generated: $P_{Rb} = 42\%$, $T_1 = 45$ hours, and $\gamma_{SE} = (4.8 \text{ hr})^{-1}$, indicating that results from the two methods agreed well with each other.
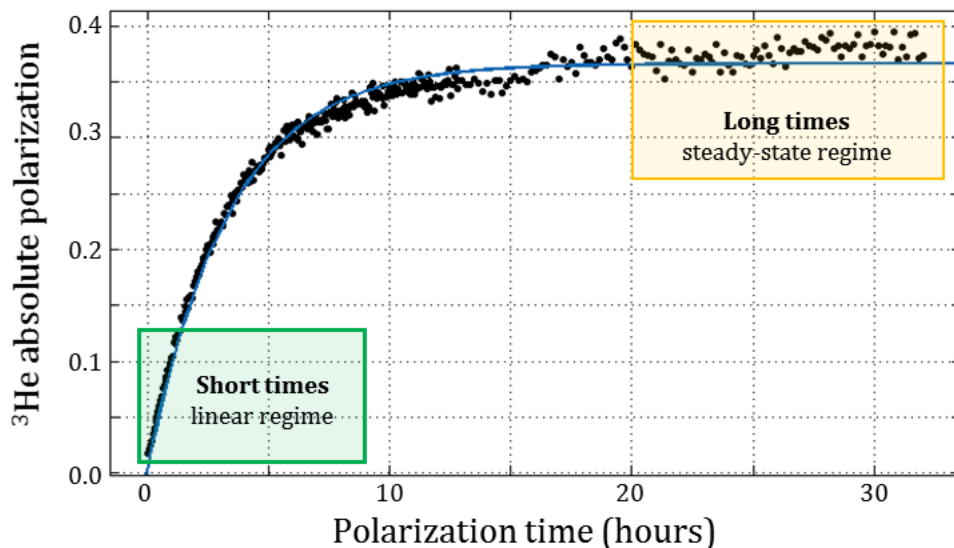
Figure 5.10: Experimental polarization build-up data collected from our lab's ^{3}He hyperpolarizer devices. The optical pumping cell temperature was 120°C. This experimental data can be fit to Equation 4.3, and separately the short-time and long-time data can be fit to Equations 4.4 and 4.5, respectively, to provides two different methods of extracting the parameters P_{Rb}, T_1, and γ_{SE}.

However, sometimes suboptimal hyperpolarized gas signal is detected, as was experienced by the author during her research. This is sometimes a results of issues with the SEOP process (decreased laser output at the desired wavelength, decreased T_1 of the optical pumping cell due to oxygen contamination, inappropriate gas concentrations). Other times it results from NMR detection issues (NMR malfunction via faulty coil or spectrometer, drift of the B_0 field with subsequent reduced flip angle).
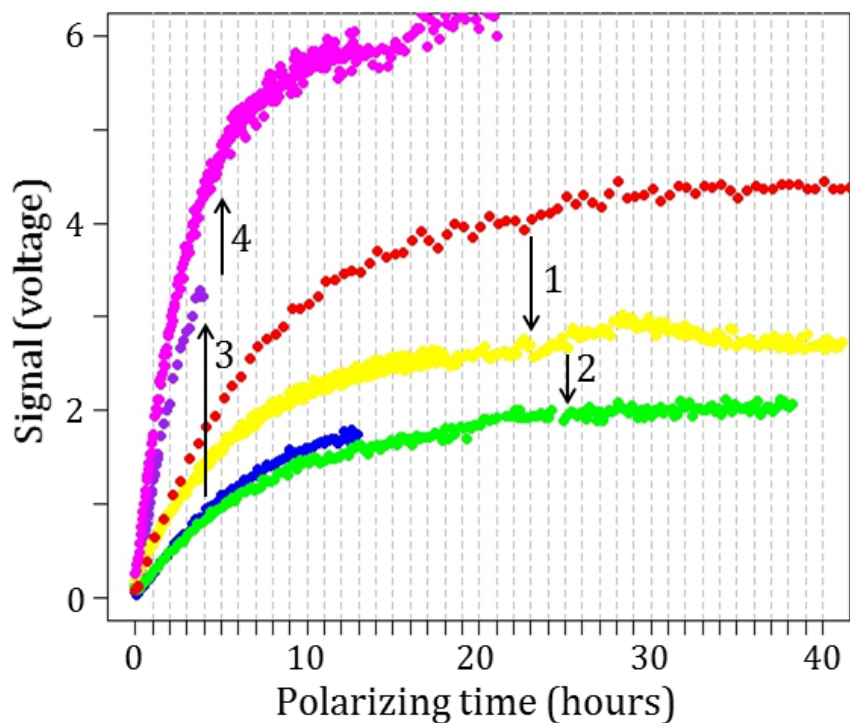
Figure 5.11: Polarization build-up curves for troubleshooting poor hyper-polarized signal from a home-built ^{3}He polarizer, in order of acquisition (red→yellow→green/blue→purple→magenta), as measured by voltages that scales with polarization. The red data demonstrates a lower polarization than expected, which only decreased as the fraction of N_2 buffer gas in the cell was accidentally decreased (Steps 1 and 2). The polarization increased as the concentration of buffer gas was subsequently increased (Steps 3 and 4). See text for further explanation.

Shown in Figure 5.11 is a "timeline" of polarization build-up curves, with specific actions taken between each of the displayed data sets. Initially (red data), it was noted that the ^{3}He polarization (as measured by voltage via an NMR probe and spectrometer that scales with polarization) was reaching steady-state at a voltage lower than expected (typically $\sim$6 V; here $\sim$4 V). Upon two rounds of dispensing the gas to 1 atm and refilling the cell to 10atm from the bottle of ultra-pure ^{3}He, the steady-state polarization dropped even further (yellow, then green/blue data), to $\sim$2.5 V, then $\sim$1.5 V, respectively; this trend indicated that it was likely not a B_0 off-resonance issue, as that would have remained consistent with

cell re-fillings. The output of the laser was found to be consistent with past performance via measurement by optical spectrometer, so laser emission was not an issue. The cell was then inspected for the "tell-tale" signs of oxygen contamination (golden-yellow coloring of the inner cell walls and solid Rb, indicative of oxidation); such signs were absent, so it was likely not an oxygen contamination issue. Further, the T_1 of the gas inside this optical pumping cell was found to be consistent with measurements from the immediate past ($\sim$50 hours), thus further indicating no oxidation issues.

The next potential culprit examined was the gas mixture. Our cells are typically loaded from a bottle with a gas mixture of 99.25% ^{3}He and 0.75% N_2. However upon further investigation, it was discovered that the new bottle recently hooked up to the polarizer consisted of higher purity ^{3}He than anticipated (99.9%), yielding virtually no N_2 buffer gas (0.5 ppm). This qualitatively agreed with our observations, since each dispense/refill step resulted in less buffer gas during SEOP, with polarization decreasing each time. The bottle was then replaced for one with the typical ^{3}He/N_2 mixture, and was re-polarized briefly with stronger results (purple data), although polarizing ended before steady-state was reached. Two additional dispense/refill steps were performed with gas from the appropriate tank, resulting in a polarization build-up curve reaching the expected steady-state voltage of $\sim$6 V. Thus the problem was solved.

This exercise in troubleshooting provided a strong demonstration for the necessity of a buffer gas in the optical pumping process; without N_2 gas to carry away energy from de-excited electrons as rotational and vibrational energy, photons of the wrong polarity are re-emitted and re-absorbed by Rb vapor, thus ensuring low polarization through radiation trapping.

5.3   Neonatal-Sized Multi-Nuclear 1.5T MRI Scanner

A small 1.5T MRI system was adapted by Cincinnati Children's Hospital's MR engineering team from a system originally designed for orthopedic applications (originally MSK Extreme 1.5 T by ONI Medical systems, Wilmington, MA; ONI was purchased by GE, so currently the scanner is marketed as the OPTIMA MR430s by GE Healthcare, Waukesha, WI) [66, 67]. The scanner was modified to accommodate neonatal-sized whole-body subjects rather than adult-sized limbs, with the magnet orientation moved from oblique-diagonal to horizontal, the magnet height increased, and the patient chair replaced with a neonatal-sized patient bed (in this case, a "half-pipe") (Figure 5.12). This system was the first in the world to address the challenges of neonatal MRI by scaling the system to the size of the neonatal subject [68].
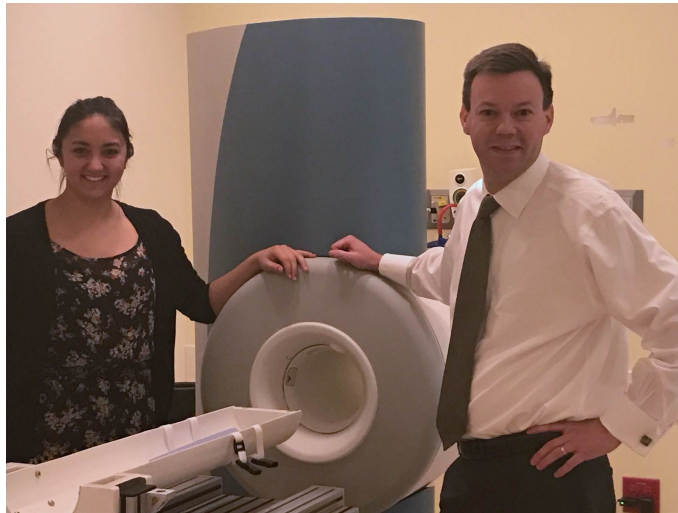
Figure 5.12: Neonatal-sized 1.5T MR system. The scanner shown here (pictured with two enthusiastic researchers, for scale) is located within the Cincinnati Children's Hospital NICU and regularly images NICU patients with respiratory morbidities, while a twin scanner is located in the institution's preclinical research area and is used for explant lung imaging experiments.

The orthopedic gradient system has a maximum gradient strength of 70 mT/m and maximum slew rate of 300 T/m/s; however, the system is operated with GE v16 software,

which limits the system to 33 mT/m and 120 T/m/s, without override instructions. This scanner is located on site in the preclinical research area; a twin scanner (operating with GE HDx v23 software) is sited within the institution's neonatal ICU (NICU) (see Sections 7 and 11 for further detail). The neonatal-sized scanner has a 21.8-cm bore diameter (without RF coil), which is typically reduced to approximately 18 cm with insertion of a body coil, and it operates with an average acoustic noise $\sim$13 dB lower than that of a conventional MRI system ($\sim$74 dB and $\sim$87 dB, respectively) [69]. While this scanner was originally a proton-only system, it was adapted by the Cincinnati Children's MR engineering team for multi-nuclear ^{3}He imaging [68].

5.4 Switched-Frequency ^{1}H/^{3}He Neonatal-Sized Birdcage Body Coil

While gas imaging can provide unique insights into lung ventilation and alveolar airspace microstructure, there is a persistent need for complementary ^{1}H imaging in order to obtain anatomic reference images and structural proton images. Since the signal from HP gases is depleted to some degree by every RF pulse, localization on proton structures is preferred. Imaging two nuclei typically would require two separate imaging coils or a dual-tuned RF coil. The latter is preferred so that there is are similar B_1 profiles for each nucleus, and it obviates the need for a suite of coil structures. In the context of neonatal scanning on our unique small-bore system, space limitations constrain us to the use of a single coil structure, and in general it is preferred that localizing and structural images be acquired without removing the subject or altering their position, such that the subject's position will match in both proton and gas images.

With this in mind, a neonatal-sized, 16-rung, high-pass, switched-frequency ^{1}H/^{3}He birdcage body coil was designed and constructed by with the Cincinnati Children's MR engineering team for use in coordinated studies of both ^{1}H and HP ^{3}He gas imaging (Figure

62

Figure 5.13: A switched-frequency ^{1}H/^{3}He neonatal-sized birdcage body coil to image lung specimens at both 63.38 MHz (for ^{1}H at 1.5T) and 48.65 MHz (for ^{3}He at 1.5T).

5.13) [68]. A dual-tuned coil was avoided in this case so that coil performance at one or both frequencies was not reduced by the addition of inductive and capacitive elements to improve isolation between two tuned circuits. Rather, this switched-frequency coil utilizes a mechanical "switch" to twist a shell on the coil body, which places additional capacitors into the circuitry and reduces the resonant frequency from 63.38 MHz (for ^{1}H at 1.5T) to 38.65 MHz (for ^{3}He at 1.5T) (Figure 5.14). This design offers the advantage of rapid switching times (10-20 seconds total) between ^{1}H and ^{3}He modes without disturbing the patient or specimen. See [68] for further details of coil design and validation.
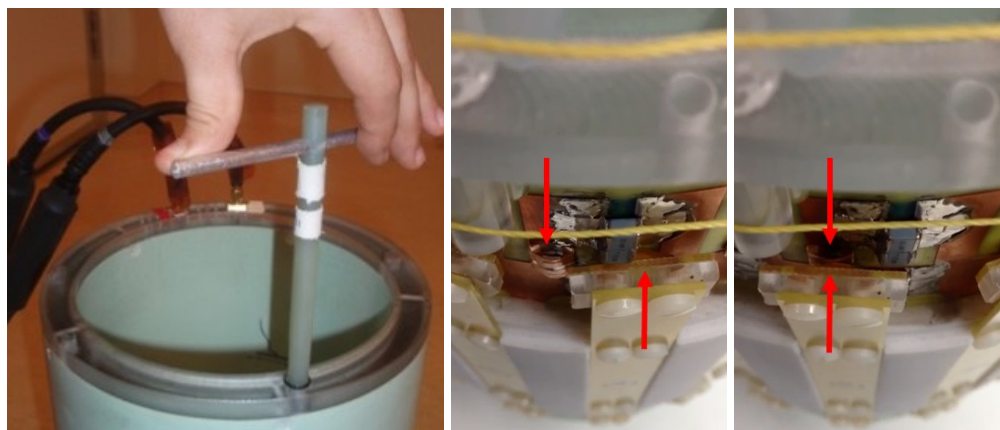
Figure 5.14: Left: Mechanical "switch" to twist between nucleus modes. Middle: A close-up of the coil in ^{1}H mode (additional capacitors not connected to the circuit, as indicated by red arrows). Right: A close-up of the coil in ^{3}He mode (additional capacitors now connected to the circuit, as indicated by red arrows), bringing the resonant frequency from 63.38 MHz (for ^{1}H at 1.5T) to 48.65 MHz (for ^{3}He at 1.5T).

6 ^{3}He Diffusion MRI

As discussed in Part I, neonatal patients in the NICU have many pulmonary morbidities, often associated with abnormally large airspaces (likely related to alveolar simplification and/or emphysema). Currently, little is understood about the multiple underlying pathologies. Standard clinical pulmonary imaging of neonatal patients includes chest x-ray radiograph and chest x-ray CT, with ^{1}H UTE MRI research techniques approaching the tomographic resolution of CT (dimensions on order of 10^{-4} m) and offering strong potential for clinical implementation (as discussed further in Part III), with no ionizing radiation exposure [22, 23, 24, 26]. However, these clinical and research imaging modalities only probe the macroscopic structure of the lung. Infant alveolar airspace development has not been extensively studied, largely because of the reliance on rare post-mortem samples and the lack of non-invasive in-vivo techniques to examine microstructural alveolar airspace development in the neonatal lung. Correspondingly, the short-term and long-term outcomes are not well predicted in infants with microstructural abnormalities, and it remains clinically difficult to tailor patient care accordingly. Hyperpolarized (HP) gas diffusion MRI may have a role to play in providing meaningful in-vivo measurements of alveolar airspaces in both normal and abnormal infant pulmonary development.

The diffusion of HP gas (in this context, referring to Brownian motion of gas) has been utilized for several years as an MRI contrast parameter [70]. Indeed, ^{3}He and ^{129}Xe HP gas diffusion MRI has developed as an established research technique and has been shown to be directly sensitive to a broad range of alveolar airspaces regimes – in adults [71], pediatrics [72], canines [73], and mice [74, 75] – but has not yet been applied in the regime of young infants and neonates. There has been some recent ^{3}He diffusion work in preschool-aged children [76, 77] and ^{3}He ventilation work in older infants [78]. However, it may be of interest to investigate lung structure at even earlier stages of development; in the long-term, HP gas

MRI techniques could be more widely implemented to provide localized, quantitative MRI biomarkers (alveolar size and microstructure) of infant pulmonary structural and functional evaluation, adding to our general knowledge of the underlying pathologies associated with infant pulmonary diseases. Further, there is potential for benefit to NICU patients as a means of outcomes prediction and follow-up assessment.

6.1 Diffusion MRI Theory

6.1.1 Apparent Diffusion Coefficient and Mono-exponential Decay Model

Without any restricting barriers, a particle will diffuse freely in its medium in Brownian motion with a free diffusion coefficient D_0. During a diffusion time of Δ, a gas particle and will move an m-dimensional mean linear (RMS) displacement l_0 of

$$l_0 = \sqrt{m2D_0\Delta}. \tag{6.1}$$
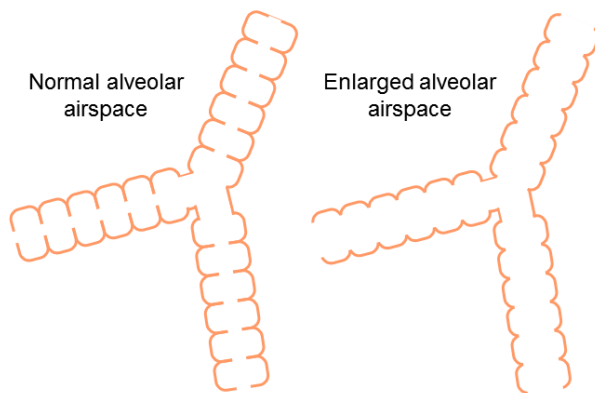
Figure 6.1: Representative diagrams of the anisotropic structure of human alveolar airspaces. The compartments represent individual alveoli in sleeves along each duct. The structure at right qualitatively contrasts with the normal structure at left to represent the abnormal enlargement of airspaces in some disease (for example, COPD in emphysematous smokers' lungs, or alveolar simplification in premature BPD infants' lungs).

Typical diffusion times achievable are on the order of a few milliseconds, such that ^{3}He

gas dilute in air at physiologic pressure and temperature ($D_0 \approx 0.88$ cm^2/s) will diffuse approximately 0.5-1 mm, if unrestricted by barriers. However, in the human lung, diffusing gas particles are restricted by alveolar airspace structures (Figure 6.1). Healthy adult alveoli has dimensions on the order of approximately 0.2 mm, meaning that for very short diffusion times ($\Delta \ll 1$ ms), ^{3}He gas diffusion in-vivo will appear to experience free diffusion, and the airspace will be undersampled. If the mean linear displacement is much longer than alveolar airspace dimensions, then ADC values will be independent of diffusion time, since there is a lack of relative length scale; here, the airspace will be oversampled. However, at more typical experimental diffusion times ^{3}He gas diffusion in-vivo will be restricted by lung microstructure, with an apparent diffusion coefficient (ADC) that is reduced from the free diffusion value ($D \approx 0.20$ cm^2/s in the healthy adult human lung); here, the airspace is sufficiently sampled. With selection of a diffusion time in the "sweet spot" between yielding an ADC equal to free diffusion and an ADC that is no longer dependent on diffusion time, measurements of ADC have so far been a straightforward but informative metric for measuring lung microstructural airspaces. A convenient and straightforward method for extracting ADC values from gas diffusion MRI in lungs is to model the diffusion-weighted signal in mono-exponential decay as a function of *b-value*:

$$S = S_0 e^{-b \cdot ADC}. \tag{6.2}$$

The *b-value* parameter is essentially the amount of diffusion attenuation imparted onto the spin and is implemented with a Stejskal-Tanner pulsed field gradient experiment (i.e. bipolar diffusion-sensitizing lobes; Figure 6.2) to perform a straightforward MR measurement of diffusion [79]. Spins will experience a net phase shift proportional to their displacement during a specified diffusion time, which yields diffusion-weighted MR signal attenuation; a static spin will experience zero cumulative phase shift, while a highly-diffusing spin will
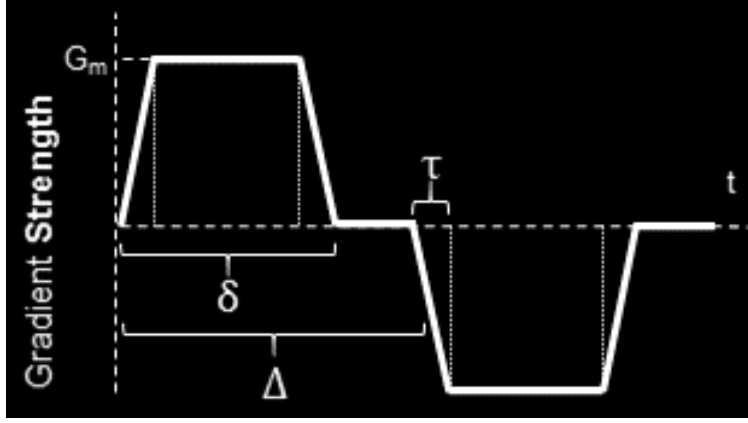
Figure 6.2: Bipolar diffusion-weighting gradient lobes. The symmetric lobes are used to encode diffusion in the MR signal with net phase shifts; little-diffusion spins would accumulate relatively little net phase shift (and little MR signal attenuation), while highly-diffusion spins would accumulate a relatively large net phase shift (and large MR signal attenuation). The timing variables (Δ, diffusion time; δ, pulse width; and τ, ramp time) and maximum gradient strength (G_m) contribute in the calculation of the b-value (see Equation 6.4).

experience a very large phase shift. For generic diffusion lobes lasting a total of T, the b-value can be calculated as [81]

$$b = \gamma^2 \int_0^T \left[\int_0^{t'} G(t'')dt'' \right] dt'. \tag{6.3}$$

For the bipolar pulse shapes in Figure 6.2 ($T = \Delta + \delta$), the resulting b-value is [82]

$$b = (\gamma G_m)^2 \left[\delta^2 \left(\Delta - \frac{\delta}{3} \right) + \tau \left(\delta^2 - 2\Delta\delta + \Delta\tau - \frac{7}{6}\delta\tau + \frac{8}{15}\tau^2 \right) \right]. \tag{6.4}$$

This expression can be simplified if one assumes perfect hardware response such that there is negligible rise time ($\tau = 0$):

$$b = (\gamma G_m)^2 \left[\delta^2 \Delta - \frac{\delta^3}{3} \right]. \tag{6.5}$$

This expression can be further simplified if one assumes that each lobe's duration (δ) is much smaller than the separation between bipolar lobes (diffusion time Δ) (i.e. $\delta \ll \Delta$), such that

the lobes are essentially impulses:

$$b = (\gamma G_m \delta)^2 \, \Delta. \tag{6.6}$$

See Section 6.3.2 for further description of implementation of diffusion-weighted gradient lobes and experimental b-values.

Typical ADC analysis assumes mono-exponential MR diffusion weighting and ignores the anisotropy of the lung microstructure (and correspondingly the anisotropic gas diffusion through those microstructural airspaces). However, the diffusion-weighted MR signal is affected by this anisotropy and decays in an *approximately* mono-exponential fashion. Even so, mono-exponentially-determined ADC values have been well validated to still correspond to alveolar airspace size more generally, regardless of precise microstructure [71, 83, 84].

6.1.2 Diffusion in Anisotropic Lung Airspaces

However, there has been some previous work aimed at using gas diffusion MRI to extract the anisotropic microstructural parameters of the alveolar airspaces [71, 73, 74, 75, 82]. Following the work of the anatomist Weibel, alveolar airspaces can be modeled as long cylinders decorated with alveolar sleeves, with duct radius R and alveolar depth h (Figure 6.3) [85]. Non-exponential diffusion attenuation of the MR signal in the anisotropic lung microstructure can be used to determine parameters of diffusion longitudinally (D_L) and transversely (D_T) across the cylindrically-structured alveolar airspaces. Previously developed mathematical models relate anisotropic diffusivity results to microstructural geometric parameters of cylindrical alveolar airspaces (R and h).

The mathematical models of anisotropic gas diffusion depend on a diffusion time that allows for a particle to diffusion out of a single alveolus and across and along a single cylindrical duct, with the diffusion restricted by alveolar and duct walls. If diffusion-encoding

69
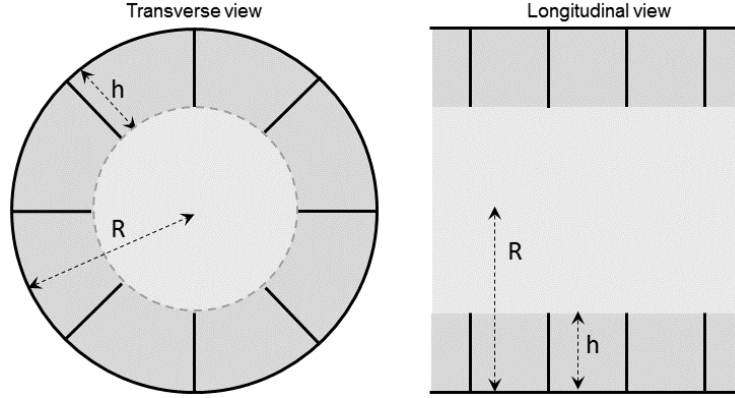
Figure 6.3: The Weibel model of alveolar airspaces, which describes long cylindrical ducts (duct radius R) covered in alveolar sleeves (alveolar depth h).

gradients are applied along either the longitudinal or transverse axis of a specific duct, then the measured ADC would equal either D_L or D_T, respectively. For a duct oriented at an arbitrary angle α from the diffusion gradient (Figure 6.4), the ADC is [82]

$$ADC = D_L \cos^2 \alpha + D_T \sin^2 \alpha. \tag{6.7}$$
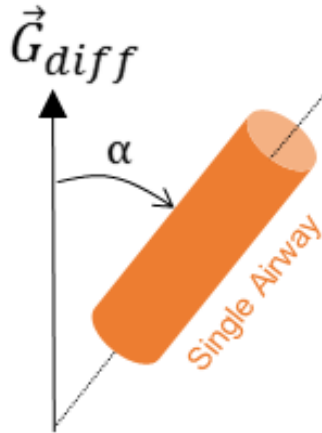
Figure 6.4: A single cylindrical alveolar duct oriented at an arbitrary angle α with respect to the diffusion-encoding gradient $\vec{G}_{diff}$.

However, with an image resolution on the order of 1 mm, gas diffusion MRI cannot resolve a single alveolar duct; rather, each voxel contains hundreds of ducts with no preferential

orientation distribution. While the signal from a single duct decays exponentially with its ADC value, the signal decay from one voxel is non-exponential. One can reasonably assume that the orientation of all duct elements within a single voxel has uniform angular distribution (normalized), where α is the polar angle on the sphere (range 0-π) and φ is the azimuthal angle (range 0-2π):

$$g(\alpha) = \frac{1}{4\pi} \int_0^\pi \sin\alpha \left[\int_0^{2\pi} d\varphi \right] d\alpha = \int_0^\pi \frac{\sin\alpha}{2} d\alpha. \tag{6.8}$$

Assuming uniform duct angular distribution (Equation 6.8), that the ADC of a single duct follows Equation 6.7, and that each duct has identical structure and so identical diffusion coefficients D_L and D_T, then the voxel signal becomes [82]

$$S = S_0 \int_0^\pi \frac{\sin\alpha}{2} e^{-b(D_L \cos^2\alpha + D_T \sin^2\alpha)} d\alpha. \tag{6.9}$$

A strategic move is to define a new variable z such that

$$z^2 = b(D_L - D_T) \cos^2\alpha \tag{6.10}$$

$$dz = -\sqrt{b(D_L - D_T)} \sin\alpha d\alpha). \tag{6.11}$$

Using Equations 6.10 and 6.11, trigonometric identities, and even integral properties, Equation 6.9 then becomes

$$S = S_0 \frac{2e^{-bD_T}}{\sqrt{b(D_L - D_T)}} \int_0^{\sqrt{b(D_L - D_T)}} e^{-z^2} dz. \tag{6.12}$$

This integral can be recognized as the error function, where $y = \sqrt{b(D_L - D_T)}$:

71

$$\Phi[y] = \frac{2}{\sqrt{\pi}} \int_0^y e^{-x^2} dx. \tag{6.13}$$

Thus Equation 6.12 can be rewritten as [82]

$$S = S_0 e^{-bD_T} \sqrt{\frac{\pi}{b(D_L - D_T)}} \Phi[\sqrt{b(D_L - D_T)}], \tag{6.14}$$

where the detected gas diffusion MR signal from each voxel is now a function of the experimentally-implemented *b-value* and the anisotropic diffusivities D_L and D_T. By taking the alveolar duct anisotropy into account, the diffusion-weighted signal decay is no longer modeled as a pure exponential [82].

Building from this description of anisotropic diffusion, previous work has established relationships between the anisotropic diffusion coefficients (D_L and D_T) and the microstructural geometric parameters (R and h). These dependences were generated using Monte Carlo simulations of particles experiencing a diffusion-sensitizing gradient while performing random walks within the cylindrical duct structure, with individual particles accumulating phase while diffusing, which then can be averaged across all particles to yield the MR signal [86]. Since the microstructural dimensions and diffusion times vary between different species, ages, and conditions, these simulations have been fine-tuned to yield population-specific phenomenological results, including for healthy adult humans [86], healthy adult canines [73], and healthy adult mice [74, 75]. Population-specific parameters for anistropic diffusion models are shown in Table 6.1.

6.2   Explant Infant Lung Specimens

Prior to in-vivo imaging with the vulnerable population of live infants in the NICU, however, imaging techniques and experimental design for quantitative regional ventilation and diffusion must be refined and validated with *ex-vivo* lung samples. Explanted infant human lung

Population-specific model	Lung volume (mL)	Expected duct radius R (μm) (based on MR and histological results)	Implemented diffusion time Δ (ms)	l_0 (μm), 1D and 2D	$\frac{R}{l_0}$, 1D and 2D
Healthy adult human	5000	300	1.6	620 and 876	0.48 and 0.34
Healthy adult canine	1000	230	1.8	657 and 930	0.35 and 0.25
Healthy adult mouse	1	100	0.44	325 and 460	0.30 and 0.21
Healthy infant human	***~100***	***?***	*-*	*-*	*-*

Table 6.1: Population-specific parameters for anistropic diffusion models, assuming a 1:1 gas mixture of ^{3}He:N_2 ($D_0 \approx 1.2$ cm^2/s). Previous work has described models for the diffusion regime of healthy adult humans [86], healthy adult canines [73], and healthy adult mice [74, 75]. A model specific to infant humans (in health or disease) has not yet been described.

samples are rare and precious, with healthy specimens typically obtained from autopsy after non-respiratory-related infant death, and diseased specimens typically obtained post-autopsy or after extremely rare pediatric lung transplantation.

Seven healthy ex-vivo infant human lung specimens (left-upper-lobes only) were obtained post-autopsy with informed parental consent via the United Network for Organ Sharing, in collaboration with the University of Rochester Medical Center and the NHLBI-funded LungMAP consortium. The donor subjects had died from non-respiratory related conditions (typically head trauma), with ages ranging from 1 day old to ~16 months old (on average, 6 $\pm$ 6 months old) (Figure 6.5, left). Additionally, one left lung (age 11 months old) was obtained after a lung transplantation at Cincinnati Children's Hospital. This donor subject

had filamin-A deficiency, which is associated with diffuse and emphysematous lung disease (Figure 6.5, right) [87].

Upon receiving each lung, the lung was examined for any significant leaks from damage to the pleural surface. Any such defects were identified and repaired via small nitrile glove patches adhered to the lung surface with VetBond tissue glue. The main airway of the specimen (lobar bronchus for healthy left upper lobes; main bronchus for the diseased left lung) was plumbed with typical plumbing barbed in order to ventilate for imaging.
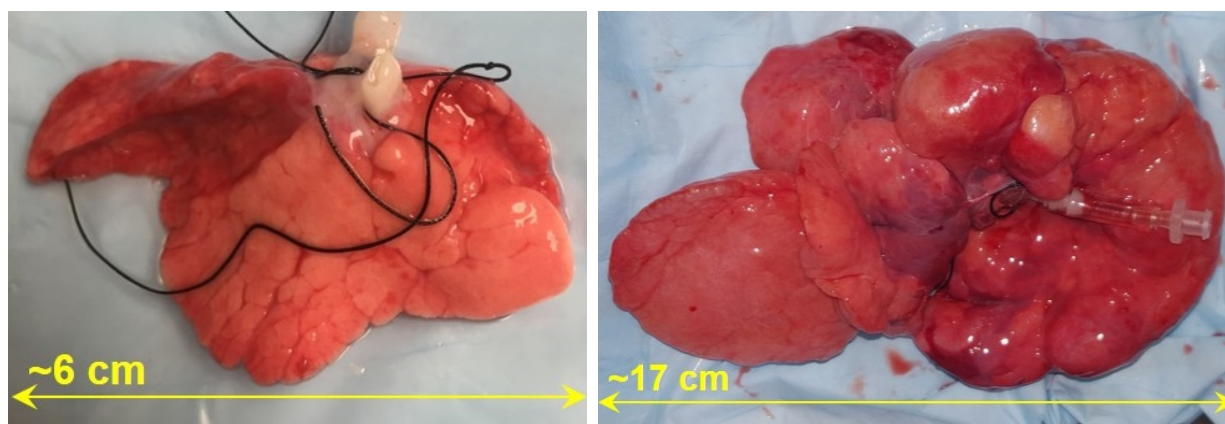
Figure 6.5: Left: a healthy human 1-day-old left upper lobe, obtained after autopsy. Right: a diseased human 11-month-old left lung (Filamin A deficiency), obtained after pediatric lung transplantation.

6.3 Hyperpolarized ^{3}He Imaging Protocol and Strategies

When working with hyperpolarized gas MRI, one must take on a hyperpolarized mindset during experimentation. In conventional MRI with nuclear spins at Boltzmann equilibrium, T_1 represents a recovery time for MR signal. However in the hyperpolarized regime, T_1 represents the irreversible loss of hyperpolarized signal ($\sim 10^{-1}$ absolute polarizations) down to the equilibrium polarization (an order of 10^5 reduction, since at thermal equilibrium the polarization of ^{3}He is approximately $4 \cdot 10^{-6}$). Thus, unnecessary use of the nonrenewable polarization should be avoided; for example, typical MRI sequences will execute an abundance

of RF pulses to yield an image, but RF pulses must be minimized in HP MRI, since the signal always decays and never recovers. In addition, long delays between polarizing/dispensing and imaging of the gas should be avoided in order to minimize polarization losses back to equilibrium.

6.3.1   Flip Angle Calibration

Use of small flip angles (φ) (typically on the order of 1°) is required for imaging with hyperpolarized gases, such that sufficient magnetization persists through the end of a single scan when repeatedly sampling the same spins. However, there can be differences between a flip angle prescribed on a scanner interface and a flip angle delivered to the spins. In conventional ^{1}H MRI, implemented flip angles are typically larger than those used in gas MRI; since MR signal is proportional to $\sin \varphi$, a miscalibration by a few degrees can have a much larger difference with a flip angle of 5° than of 50°. Thus, precise flip angle calibration is desired in hyperpolarized MRI to avoid reducing the magnetization at each RF pulse by an amount greater than anticipated. The hyperpolarized signal will be reduced at each RF pulse by a factor of $\cos \varphi$, so the relative amount of original signal remaining (A) after n excitations of flip angle φ would be (Figure 6.6, left)

$$A = \cos^n \varphi. \tag{6.15}$$

The relative amount detected after n excitations is (Figure 6.6, right)

$$A = \cos^{n-1} \varphi \sin \varphi. \tag{6.16}$$

Rather than a straightforward parameter entry on the user-friendly MRI scanner interface, the particular multinuclear package on the preclinical neonatal scanner requires both hardware and software calibrations at multiple levels in order to control the desired gain
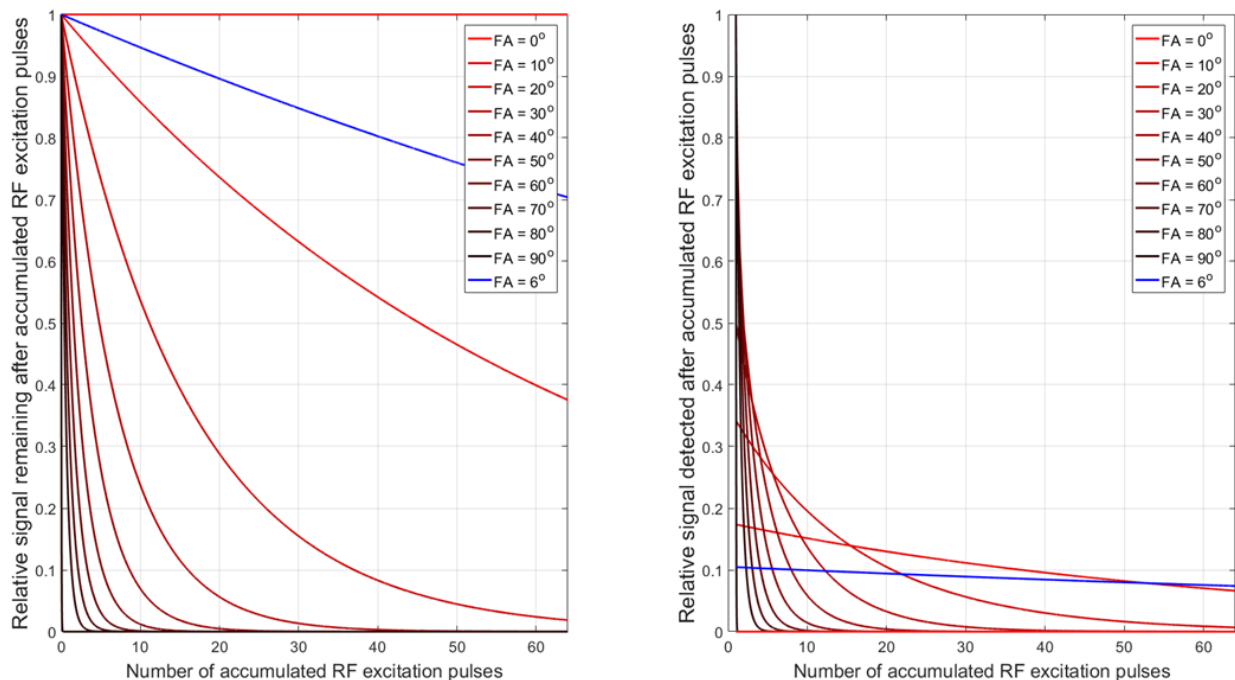
Figure 6.6: The amount of hyperpolarized ^{3}He signal remaining (left) and detected (right) after an accumulation of RF excitation pulses, relative to the original, untouched signal. Shown are results for flip angles from 0° (red) through 90° (black), with the experimentally-implemented flip angle value of 6° in blue. Typical diffusion imaging experiments presented in this work use either 32 or 64 RF excitation pulses, such that at the final acquisition the relative signal remaining is 0.84 and 0.70, respectively, and the relative signal detected is 0.09 and 0.07, respectively.

or attenuation sent to the RF coil. This includes a multinuclear amplifier, as well as two steps of attenuation instruction at the software level. The software instructions were set at constant values for all experimentation, so only amplifier settings were varied. A gradient echo sequence (as described below, with imaging gradients disabled such that FIDs were acquired during read-out following only an RF pulse) was acquired multiple times with a hyperpolarized ^{3}He gas phantom, starting with relatively high attenuation settings to err on the side of too little RF excitation, rather than too much RF excitation and kill the polarization of the sample. With incremental decreases in attenuation (i.e. increases in flip angle), an amplifier setting was found that yielded a flip angle of approximately 6°, by

fitting the maximum amplitude of the Fourier transform of each acquired FID to Equation 6.15 (performed in MATLAB). For a 64-excitation scan with a flip angle of 6°, the signal at the end will be reduced by approximately 30%.

6.3.2 ^{3}He Diffusion MR Image Acquisition and Analysis

Diffusion-weighted MR data were acquired using a conventional gradient echo sequence with bipolar diffusion-encoding gradient lobes inserted prior to read-out (Figure 6.7), which utilizes the Stejskal-Tanner pulsed field gradient experiment (see Section 6.1.1 and Figure 6.2) to perform a straightforward MR measurement of diffusion [79].

Typical imaging parameters were as follows: flip angle (FA) = 6°; repetition time (TR) = $\sim$5.6 ms; echo time (TE) = $\sim$3.8 ms; Δ = 0.91 ms; δ = 0.91 ms; τ = 0.17 ms; matrix = 64 x 40 (frequency x phase); field of view (FOV) = $\sim$13 x 8 cm (frequency x phase); in-plane pixel resolution = $\sim$2 x $\sim$2 mm; slice thickness = 10 mm; and b-value = [0, 0.95, 1.9, 2.85, 3.8, 4.75, 5.7, 6.65, 7.6] s/cm^2 (nine values total). Representative diffusion-weighted images and MR signal weighted with the nine b-values are shown in Figure 6.8. Each scan was acquired during a $\sim$15-s sustained inflation at 25 cmH$_2$O of pressure, with typical inflation volumes of $\sim$10-150 mL, depending on gross size of the specimen. With the selected diffusion lobe timing parameters and gas composition, the characteristic 1D mean linear displacement is 470 μm.

Phase encoding lines in k-space were acquired in a centric ordering (Figure 6.9), with the motivation of filling the center of k-space with "fresh" HP gas signal (minimal signal reduction from RF pulses from previously acquisitions), and allowing the edges of k-space to be populated with HP signal already exposed to the majority of the RF pulses in one scan. Furthermore, k-space data were acquired in an interleaved manner, such that the same line in k-space was acquired for all b-values before progressing to the next k-space line. This acquisition strategy minimizes sensitivity to motion in diffusion-weighting analysis.
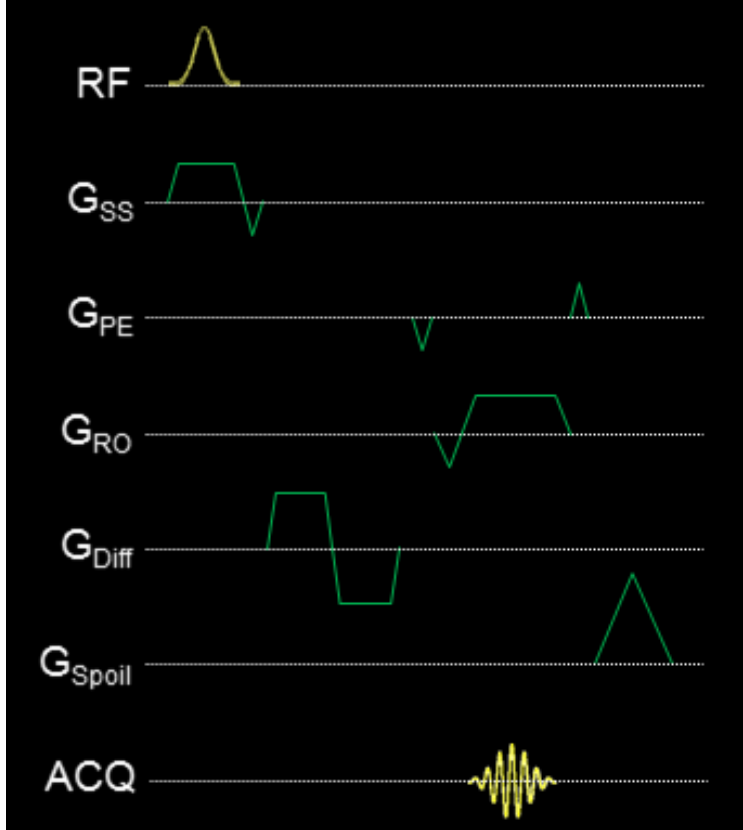
Figure 6.7: The pulse sequence diagram of a typical gradient echo with diffusion weighting lobes. An RF pulse is simultaneously applied during a slice selection gradient (G_{ss}), which selectively excites spins across a specific bandwidth. Bipolar lobes (G_{Diff}) are applied to impart a diffusion weighting to the acquired signal. The phase encode gradient (G_{PE}) specifies a k_{PE} coordinate in k-space, and k-space is traversed in the k_{RO} direction during the read-out gradient (G_{RO}) while data is acquired (ACQ). Finally, all remaining transverse magnetization is dephased with a large spoiler gradient (G_{Spoil}). In the presented experiments, each b-value (increments of G_{Diff} parameters) are all acquired for one k_{PE} line before moving on to the next G_{PE} parameters.

The switched-frequency ^{1}H/^{3}He coil and multinuclear neonatal-sized 1.5T scanner described in Sections 5.4 and 5.3 were used in this study. The gradient settings in these experiments (G_{max} = 50 mT/m, slew rate = 300 mT/m/ms) exceeded the software limitations imposed by the GE software (G_{max} = 33 mT/m, slew rate = 120 mT/m/ms), but out of an abundance of caution the maximum gradient was set below the ONI hardware limitations (G_{max} = 70 mT/m, slew rate = 300 mT/m/ms). These settings yielded a minimized

78
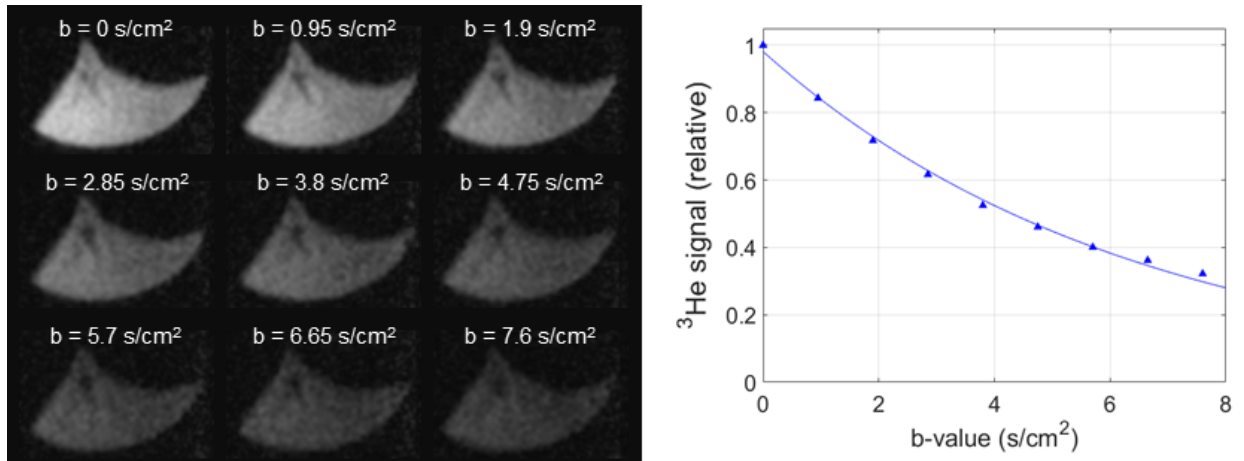
Figure 6.8: Representative diffusion-weighted ³He images from an explant infant left upper lung lobe (left panel). Nine b-values were used: 0, 0.95, 1.9, 2.85, 3.8, 4.75, 5.7, 6.65, and 7.6 s/cm². Representative normalized signal decay from regions-of-interest as a function of b-value are shown at right, with a mono-exponential fit demonstrating a near-exponential decay (with subtle non-exponential behavior, due to the anisotropically restricted diffusion in the lung microstructural airspaces).

diffusion time Δ of 0.91 ms.

Hyperpolarized gas was prepared with the home-built ³He polarizer detailed in Section 5.2 [56, 65], with absolute ³He spin polarizations of $\sim$50% as measured by a commercial polarimeter (Polarean, Durham, North Carolina). The concentration of gas used in these experiments was $\sim$1:1 of ³He:N$_2$, yielding a diffusion coefficient of $\sim$1.2 cm²/s.

As an initial straightforward approach, the diffusion-weighted hyperpolarized ³He gas MR data will be fit to a mono-exponential decay to yield ADC maps in order to elucidate whether ADC can detect subtle increases in ADC with development and whether ADC can detect differences between healthy and diseased cases. In further analysis, this work seeks to investigate whether microstructural parameters of the infant alveolar airspaces can be detected using previously developed anisotropic diffusion models. The diffusion regime implemented in the present experiments with infant alveolar airspaces (expected $\frac{R}{l_0^{1D}} = 0.21$-0.32 and $\frac{R}{l_0^{2D}} = 0.15$-0.23) is not described well in any of the previous anisotropic models.
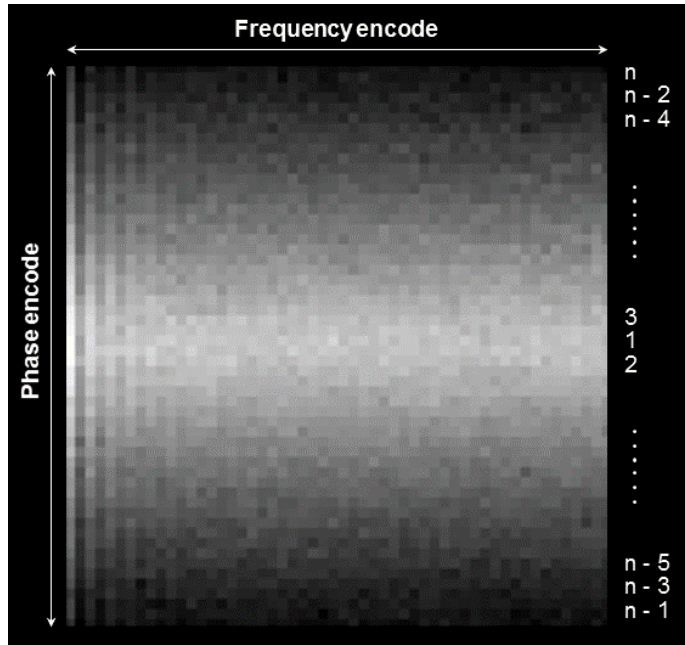
Figure 6.9: Demonstration of the Cartesian centric ordering of 64 acquisitions from hyperpolarized ^{3}He k-space data using a gradient echo. Since the gas is hyperpolarized, RF at each acquisition reduces the overall magnitude of the nuclear spin signal. The flip angle used here was approximately 20°, to clearly demonstrate the decay of hyperpolarized signal with each excitation. All imaging gradients were off for this acquisition, such that data along the x-direction represents a free induction decay after RF excitation, rather than read-out frequency encoding, and data distributed in the y-direction represent the centric k-space ordering of all acquisitions, rather than the implemented phase encoding.

Even though it is an invalid application of the mouse model, this work attempts to fit the infant diffusion MR data to the mouse model ($\frac{R}{l_0^{1D}} = 0.30$ and $\frac{R}{l_0^{2D}} = 0.21$; see Table 6.1), since that model was generated with the closest diffusion regime to that of present experiments.

6.4   Validation by Histological Morphometry

Historically, the primary method for studying the microstructure of the lungs (i.e. alveoli, alveolar walls, capillaries, etc.) was histological microscopy, with a parameter called mean linear intercept (L_m) being the typical histological metric of emphysematous airspaces (essentially a measure of line segment length per intersection). While this is still currently the

standard technique for lung morphometry, it poses several measurement problems. First, any histological sample of a large organ will necessarily be a tiny fraction of the organ's overall size, so this is a sampling issue. Second, any 2D measurement on a microscopy slide will only account for some projection of a 3D alveolar surface, with little confidence in the angle at which an alveolar geometry has been sampled. Third, histological techniques tend to have problems with preservation of structure and/or size, meaning that there can be non-isotropic shrinkage of the lung tissue when processed and placed on a microscopy slide for viewing. These issues together shed some doubt onto the validity of histological lung morphometry. However, since this is indeed the current standard for such measurements, we utilized morphometric results from histology for validation of our diffusion MRI morphometry results.

After imaging, lungs were inflation-fixed with formalin at 25 cmH_2O of pressure (the same inflation pressure as during diffusion MRI). A slice of lung tissue corresponding to that of an imaging slice was cut and processed to yield a microscopy slide of lung section. The lung sections were examined via microscopic digital photos to measure lung morphometry parameters R_{hist} (30 averages per sample) and $L_{m,hist}$ (20 averages per sample) (Figure 6.10). Measurements were corrected for shrinkage via comparison of sample size measurements before and after slide processing.

6.5   Results and Discussion in Explanted Infant Human Lungs

In Figure 6.11 are [3]He diffusion analysis results and qualitative comparisons to histology for four representative lung specimens: a 1-day-old healthy human infant, a 6-month-old healthy human infant, a 16-month-old healthy human infant, and an 11-month-old diseased human infant (Filamin-A deficiency). In the histological images, there are clear differences in development and alveolarization level between each of the healthy cases, both in tissue
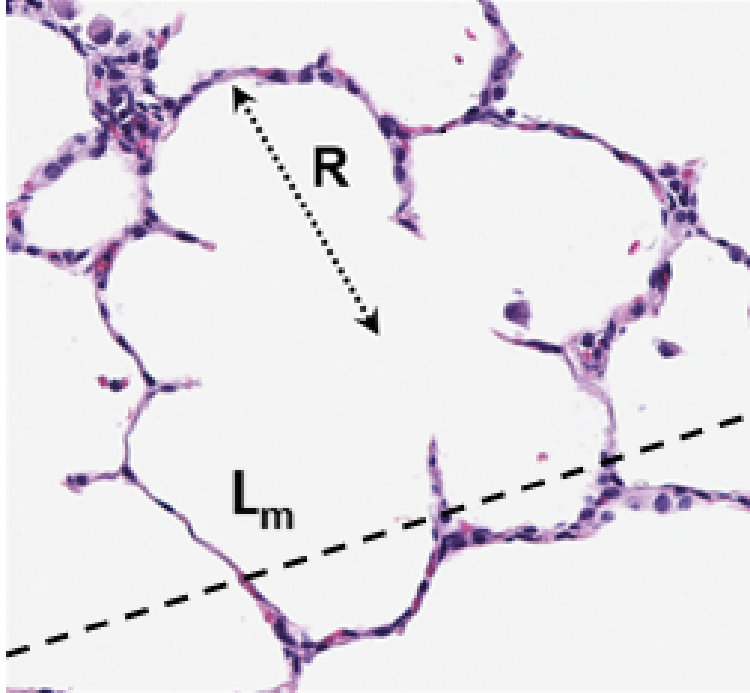
Figure 6.10: Histology and measurements of an alveolus from a healthy infant lung sample. The projection shown here is likely near transverse across the alveolar duct; note that the alveolar sleeves can be approximated by the transverse cylindrical model shown in Figure 6.3 (left panel).

wall thickness (which thins with development), and within airspace size itself. In comparing healthy histological lung tissue to the diseased case, there again are stark differences in the airspace size and amount of alveolarization between healthy and pathological alveolar airspaces. We see subtle changes in homogeneous ADC values with healthy lung development $(0.11 \pm 0.04 \ \text{cm}^2/\text{s}$ for the 1-day-old, $0.13 \pm 0.03 \ \text{cm}^2/\text{s}$ for the 6-month-old, and 0.17 ± 0.02 cm^2/s for the 16-month-old), again stark contrast to the elevated and heterogeneous ADC value of the diseased case $(0.23 \pm 0.07 \ \text{cm}^2/\text{s})$.

However, geometric airspace parameters from the anisotropic mouse model were not reflective of histological measurements, with the posterior probability distributions not converging to physiological values (model R results were homogeneous around 100 μm), particularly for the diseased specimen (Figure 6.12); the error between R_{hist} and R_{model} values

	b₀ images	Histology slides	Monoexponential ADC	R_model
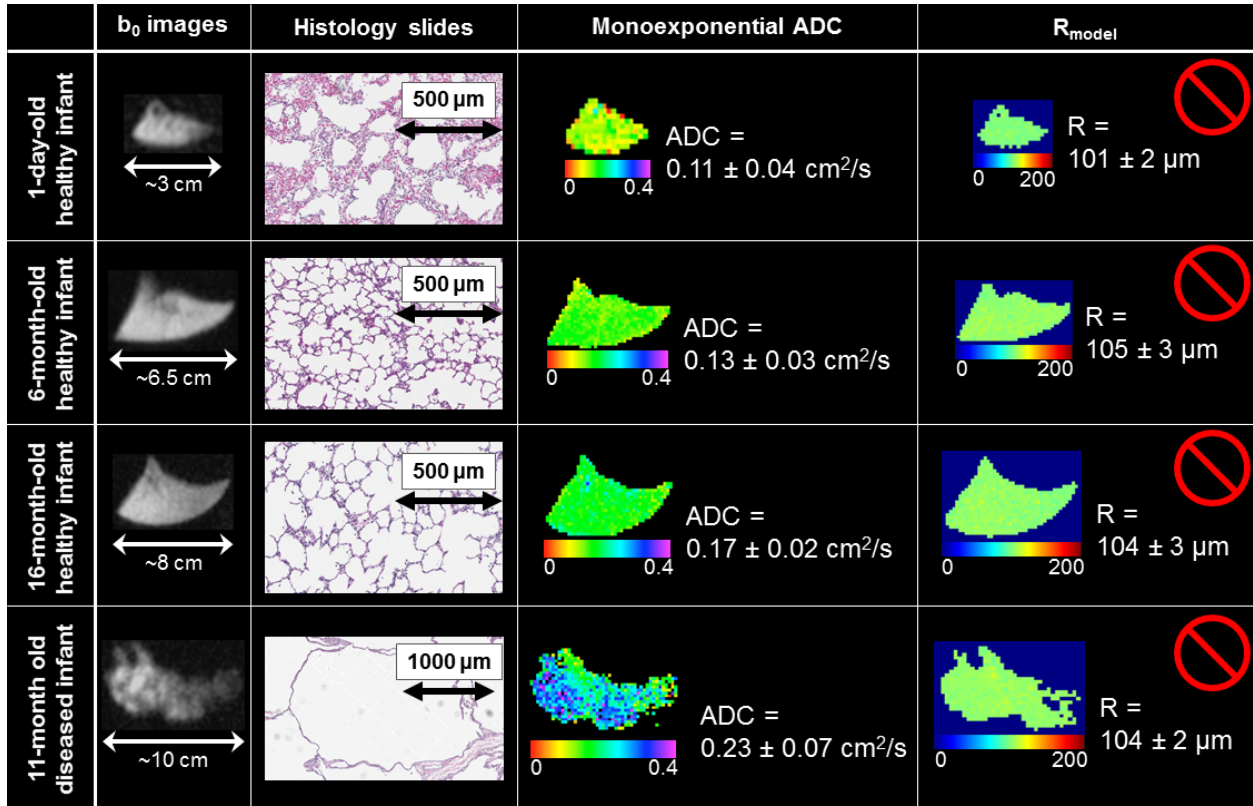
Figure 6.11: Results from four representative lung specimens: a 1-day-old healthy human infant, a 6-month-old healthy human infant, a 16-month-old healthy human infant, and an 11-month-old diseased human infant (Filamin-A deficiency). Shown are results from [3]He diffusion analysis from the mono-exponential model (ADC) and the anisotropic mouse model (duct radius R), along with a representative image from lung tissue histology. ADC results are representative of findings via histology, while R values from the mouse model are not physiologically valid.

measured in the healthy infant lung explants was 31.8% ± 15.2% (range 3.6%-46.7%). Lower sensitivity to changes in airspace size may be expected in the infant lung, since the ratio of expected duct radius to diffusion length is below the physical diffusion regime for which the mouse model was intended (Table 6.1). With a lower ratio of radius compared to diffusion length than intended, the experiment suffers from motional averaging and thus less sensitivity to length scale. Further, the Weibel alveolar airspace model (cylindrical ducts with alveolar sleeves) may not be adequate to describe infant microstructural geometry, since there is a varying amount of developing smooth and alveolated spaces cross-sectionally at a

single age, and even within an individual infant.
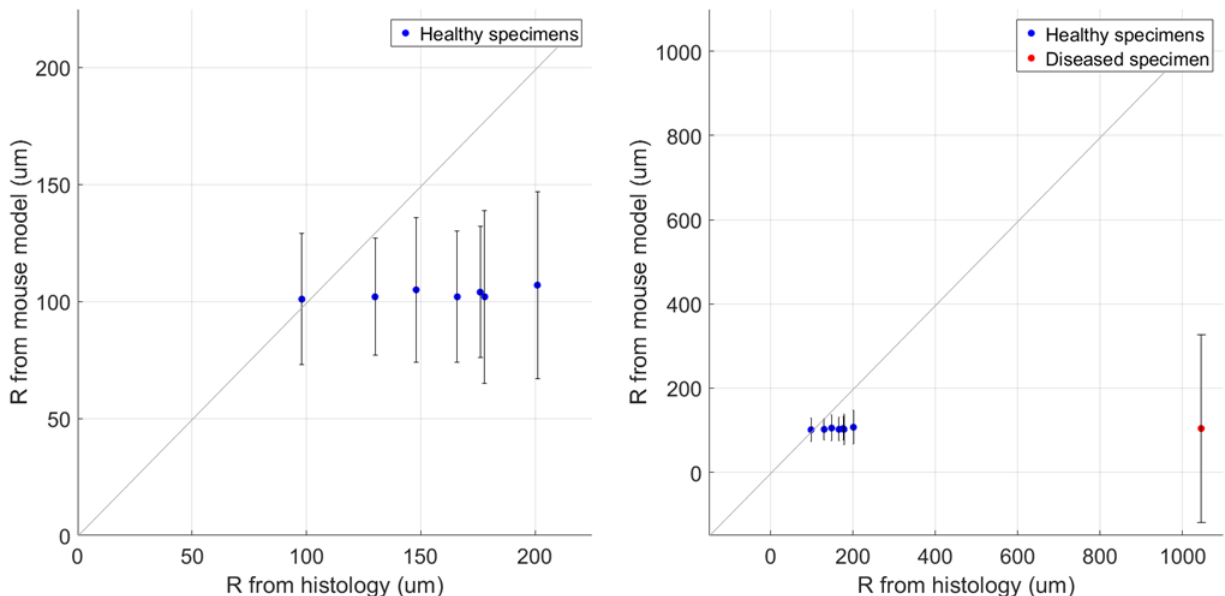
Figure 6.12: A comparison of duct radius (R) from the anisotropic mouse model to the R values measured via histology. Ideally, data would lie along y=x. Even if some systematic factor were yielding a non-unity scaling relationship between the model and histology results, the sensitivity of the mouse model results would be insufficient to distinguish between various airspace sizes, and the lack of physical accuracy of the morphometric parameters yielded by the mouse model reduces usefulness in application of this model to this data set.

While the ADC metric does not probe the specific geometry of airspaces, the results comparing mono-exponential ADC to histological parameters were more encouraging. For all specimens in the healthy group, histological measurements (group mean ± SD) of duct radius (R_{hist} = 158 ± 35 µm) and mean linear intercept ($L_{m,hist}$ = 131 ± 29 μm) correlated significantly to MR measurements of mono-exponential ADC (0.14 ± 0.03 cm^2/s) (for R_{hist} versus ADC, Pearson P = 0.037 and r = 0.78; for $L_{m,hist}$ versus ADC, Pearson P = 0.042 and r = 0.69) (Figure 6.13). There was a distinct elevation and heterogeneity in ADC (0.23 ± 0.07 cm^2/s), R_{hist} (1052 ± 225 μm), and $L_{m,hist}$ (761 ± 273 μm) for the diseased lung case (mean ± SD within specimen) when compared to healthy cases, with a clear non-linearity in the larger airspaces that is consistent with reduced restriction to gas diffusion in the diseased

lung.

While the anisotropic mouse model is invalid in the infant diffusion regime, ADC measurements reflect changes in alveolar-airspace size. This method shows promise for longitudinal in-vivo acinar-airway monitoring in neonatal patients.

To our knowledge, this ex-vivo work represents the first hyperpolarized gas diffusion MRI in infant lungs. These results demonstrate that ADC measurements from ^{3}He diffusion MRI are sensitive to relative changes in alveolar-airspace sizes in infants 0-16 months old, by direct comparison to histology. The disagreement between histologically-based and mouse-model-based geometric parameters in healthy infant lungs suggests the currently existing ^{3}He lung anisotropic morphometry models are not valid for the diffusion regime of infant acinar-airways; any extension of this model to infant lungs must take into account not only the different diffusion regime, but also the individual variability in stage of alveolar development. Even so, the encouraging ADC-histology comparisons support the potential of HP gas MRI to detect normal and abnormal changes in acinar-airspace size in-vivo. Moreover, hyperpolarized gas MRI has an established safety record in pediatrics [72, 88] and adults [89, 90] as a non-invasive and non-ionizing modality that shows translational promise in neonatal patients for monitoring normal and abnormal lung development longitudinally.
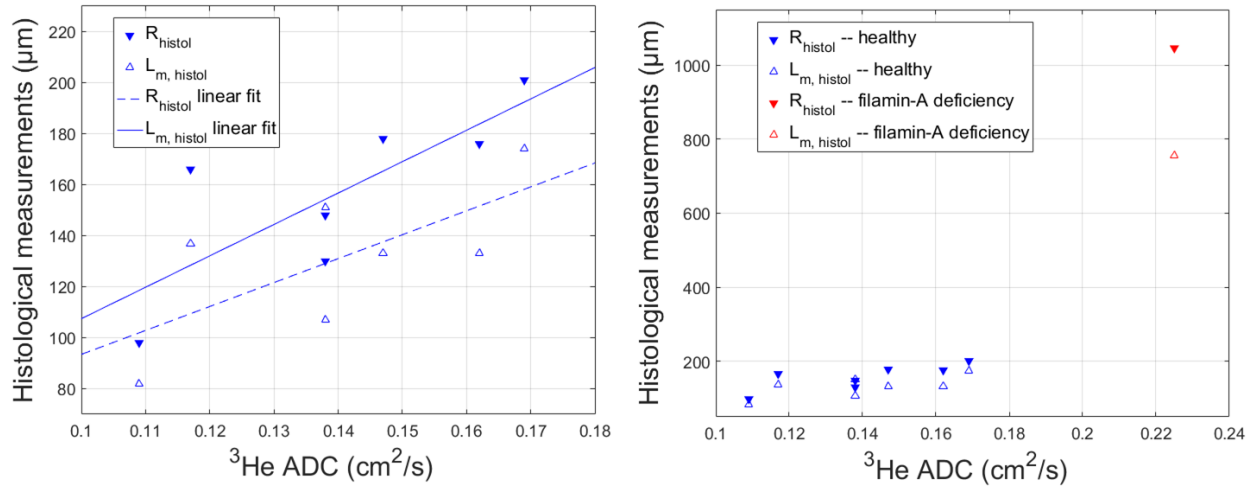
Figure 6.13: Comparison of histological parameters (R_{hist} and $L_{m,hist}$) with ^{3}He ADC values. For healthy cases, R_{hist} correlated significantly with ADC (P = 0.037 and r = 0.78), and $L_{m,hist}$ correlated significantly with ADC (P = 0.042 and r = 0.69).

7 Moving Toward In-Vivo Neonatal ^{129}Xe MRI

Historically ^{3}He has been preferred over ^{129}Xe in hyperpolarized gas MRI studies for a variety of scientific reasons (Table 7.1). Importantly, the gyromagnetic ratio of ^{3}He is approximately 275% that of ^{129}Xe and with modern polarizer technology (such as high-power diode laser arrays) one can achieve approximately twice the maximum polarization with ^{3}He as with ^{129}Xe. However, from a practical standpoint ^{129}Xe may be preferable; the natural abundance of ^{3}He is very low, so the price per volume is relatively high in comparison to ^{129}Xe.

Property	Units	^{3}He	^{129}Xe
Gyromagnetic ratio (γ)	MHz/T	32.43	11.78
Self-diffusivity (D_0)	cm^2/s	2.05	0.061
Dilute diffusivity (D)	cm^2/s	0.88	0.14
Longitudinal relaxation in cell (T_1)	hours	∼25-50	∼0.3
Longitudinal relaxation in-vivo (T_1)	seconds	∼30	∼30
Ostwald coefficient of gas solubility [paraesthetic effects]	–	0.0085 [none]	0.17 [mild]
Spin-up time	hours	∼20	∼0.5
Maximum polarization	–	∼50%	∼25%
Natural abundance	–	0.0001%	26%
Financial cost	$/L	800	200

Table 7.1: A comparison of the physical and practical properties of ^{3}He and ^{129}Xe gas.

Both ^{3}He and ^{129}Xe are similarly capable of providing information on ventilated airspaces. However, a move toward ^{129}Xe gas in diffusion MRI applications, particularly in infant lungs, may be a strategic choice beyond just financial burden. At dilute concentrations (as would be used with in-vivo imaging), the diffusivity is 0.88 cm^2/s for ^{3}He and is 0.14 cm^2/s for ^{129}Xe. Thus the 1D characteristic free diffusion length for the diffusion time used in the present work (Δ=0.91 ms) is 400 μm for ^{3}He and 160 μm for ^{129}Xe, and so imaging in the proper diffusion regime with appropriate length scale sensitivity becomes very achievable. For example, with a dilute-limit diffusivity of 0.14 cm^2/s and a diffusion time of 3 ms, the diffusion length becomes 290 μm, much more appropriate for the anticipated infant alveolar radii of

approximately 100-150 μm. Additionally, [129]Xe is slightly soluble into the bloodstream and has a large chemical shift between lung airspaces and blood spaces (>200 parts per million) [88], which provides the potential for gas exchange dynamics [91, 92, 93, 94], which could be used to measure infant alveolar interstitial wall thicknesses in health and disease.

7.1 Hyperpolarized Gas Safety Data

The preference for[3]He MRI over [129]Xe MRI has been prevalent particularly in pediatrics studies [89, 95, 96, 97, 98], where [3]He has an established safety record in imaging various pediatric diseases (e.g. asthma and cystic fibrosis) [77, 99, 100, 101, 102, 103, 104] and in quantification of alveolar development throughout healthy childhood and adolescence [72, 105]. More recently, there has even been a proof-of-concept study that acquired [3]He ventilation images in infants as young as 2 months old [78]. However, the hyperpolarized imaging community has had renewed interest in [129]Xe applications in recent years, due to the increasing scarcity and costs of [3]He [106], along with significant advancements in [129]Xe polarization technology [63, 107, 108, 109, 110].

With this renewed interest in [129]Xe came a need for validations of xenon safety and tolerability within various patient groups; both [3]He and [129]Xe are noble gases, but [3]He is virtually insoluble from the lung airspaces into the bloodstream (Ostwald coefficient of solubility = 0.0085), so safety concerns are minimal; in contrast, [129]Xe has a slight tissue solubility (Ostwald coefficient of solubility = 0.17) [111] and so poses potential slight paraesthetic effects. At typical xenon concentrations (function residual capacity $+ \sim \frac{1}{6}$ of total lung capacity) and breath-holds used in imaging studies (< 16 s), these mild effects could include euphoria, dizziness, and peripheral numbness/tingling [112], whereas at sustained, higher concentrations effects include anesthesia [113]. Previous work in adults has established a strong record of safety when using [129]Xe as an MR agent [90, 114], and more recent work in pediatrics

(down to the age of 6 years old) [88] has again demonstrated the safety, tolerability, and feasibility of this technique, with some reports of transient, mild paraesthetic effects but no clinically significant effects on subject heart rate, SpO_2 level, or blood pressure.

Cohort	Size of cohort	SpO_2: Mean Baseline Mean Nadir Mean 2-min post	Heart rate: Mean Baseline [Individual change from baseline at 2-min post] (beats per min)
No support	3	99.3% 94.0% 99.7%	152 [-4, +7, -12]
Nasal cannula (≤ 2 L/min)	3	98.3% 86.3% 98.0%	141 [+17, +9, -3]
Nasal cannula (≥ 2 L/min)	3	92.7% 99.0% 97.3%	147 [+4, +7, -25]

Table 7.2: Anoxic N_2 3-second breath-hold safety data for neonatal subjects in the NICU. Cohort 1 subjects are on no respiratory support (room air), and Cohort 2 subjects are on mild nasal cannula. Note that the SpO_2 of one subject in Cohort 2 dropped to 73% for less than 5 seconds and self-resolved without requiring additional respiratory support, indicating an only transient effect. Note that large variations in heart rate are normal for the NICU patient population.

While this tolerability is expected in pediatrics younger than 6 years old, there has yet to be any safety demonstration in neonatal subjects. Indeed, our group hopes to be the first to demonstrate this and to image neonates with any HP gas MRI technique, and in particular HP [129]Xe MRI. However in this vulnerable population, safety testing must be performed very incrementally. To this end, we have started to acquire safety data for a bedside anoxic breath-hold in NICU subjects on increasing levels of respiratory support (3 subjects per cohort; Cohort 1, room air/no support; Cohort 2, mild nasal cannula; Cohort 3, high-flow nasal cannula or other higher level of respiratory support). A breathing mask is attached to a pressure transducer and a bag filled with 100% ultra-high purity N_2 (99.9999%). The subjects are removed from their clinical respiratory support, and the breath-hold is

immediately induced via application of the mask and squeezing of the N_2 bag, for a total breath-hold duration of 3 seconds (the expected approximate duration of a gas diffusion MRI scan for a neonatal-sized subject. Immediately following the 3-second breath-hold, the subject is returned to clinical support. Heart rate and SpO_2 are monitored for 2 minutes following the breath-hold. At the time of writing, this 3-second anoxic breath-hold has been performed for three subjects in Cohort 1 and three subjects in Cohort 2; recruitment for Cohort 3 is pending. Table 7.2 details the results for each subject; in short, this short anoxic breath-hold after an N_2 inhalation seems to have no clinically significant effects on patient status. After this small N_2 breath-hold study is performed, we plan to perform similar 3-second breath-hold tests with an imaging dose of xenon before moving to xenon breath-holds in the magnet bore during imaging.

7.2   Multi-Nuclear MRI Scanner in the NICU

With adequate safety data for hypoxic breath-holds in NICU patients and a protocol approved by the Institutional Review Board (IRB) for in-vivo hyperpolarized ^{129}Xe infant MRI, acquisition of ^{129}Xe diffusion data in-vivo can proceed. Furthermore, the NICU MRI scanner (see Section 5.3) must be capable of performing multi-nuclear ^{129}Xe diffusion imaging. This requires both software and hardware updates: a diffusion sequence capable of both ^{129}Xe ventilation and diffusion imaging with appropriate parameters, and a ^{1}H/^{129}Xe switch-tuned body coil of similar design to our ^{3}He switch-tuned body coil used in preclinical experiments (see Section 5.4).

Most of the code for a ^{129}Xe diffusion sequence will be taken from the ^{3}He diffusion sequence code implemented in experiments described earlier (Section 6.3). However, since the diffusivity of ^{129}Xe is lower than that of ^{3}He, a longer diffusion time and thus higher b-values are required. A healthy or diseased neonatal alveolar duct radius can be expected to

be approximately 100 - 150 μm. As mentioned earlier, the ^{129}Xe gas diffusion length becomes 290 μm with a dilute-limit diffusivity of 0.14 cm^2/s and a diffusion time of 3 ms, much more appropriate for the anticipated infant alveolar radii of approximately 100-150 μm. Through increasing Δ, the b-values will correspondingly increase, with appropriate^{129}Xe diffusion b-values ranging between 0 and approximately 25-35 s/cm^2 [88].

In conjunction with the Cincinnati Children's MR engineering team, the design of the neonatal-sized, 16-rung, high-pass, switched-frequency ^{1}H/^{3}He birdcage body coil (Section 5.4) will be updated to image at the ^{1}H/^{129}Xe resonance frequencies. Coil construction and testing is currently in progress and being performed by the engineering team.

8 HP Gas MRI Journal and Conference Papers

The following journal and conference papers have resulted from the material presented in Part II: Hyperpolarized Gas MRI.

- Published papers:

  1. Ronald Pratt, Randy Giaquinto, Christopher Ireland, Barret Daniels, Wolfgang Loew, Nara Higano, Xuefeng Cao, Robert Thomen, Jason Woods, Charles Dumoulin. A novel switched frequency ^{3}He/^{1}H high-pass birdcage coil for imaging at 1.5 tesla. *Concepts Magn Reson B* 2015, 45(4):174-182.

- Papers in preparation:

  1. Nara Higano, Robert Thomen, James Quirk, Heidie Huyck, Andrew Hahn, Sean Fain, Gloria Pryhuber, Jason Woods. Hyperpolarized ^{3}He gas MRI in infant lungs: investigating alveolar-airspace size with restricted gas diffusion. *Magn Reson Med* [in preparation].

  2. Robert Thomen, Laura Walkup, David Roach, Nara Higano, Zackary Cleveland, John Paul Clancy, Robert Fleck, Alan Brody, Jason Woods. Relating regional pathologic structure-function in cystic fibrosis lung disease. *Am Journal Resp Crit Care Med* [in preparation].

- Conference papers presented by Nara Higano:

  1. **Oral**: Hyperpolarized ^{3}He restricted diffusion MRI in ex-vivo infant lungs: alveolar-airspace size. *Polarization in Noble Gases Conference*, Park City, UT 2017.

  2. **Oral**: Hyperpolarized ^{3}He gas MRI in infant lungs: investigating airspace size. *American Thoracic Society*, Washington, DC 2017.

3. **Oral**: Hyperpolarized ^{3}He gas MRI in infant lungs: investigating alveolar-airspace size with restricted gas diffusion. *International Society for Magnetic Resonance in Medicine*, Honolulu, HI 2017.

Part III

^{1}H Ultrashort Echo Time MRI

MRI has promise as a technique for longitudinal assessment of pulmonary diseases and respiratory function. However, structural ^{1}H lung MRI is challenging and at present plays a limited role in clinical diagnosis of pulmonary pathologies. One of the major challenges arises from the low proton density of the lung parenchyma, which is approximately $\sim20\%$ of the density of muscle and other soft tissues in adults and $\sim50\%$ in neonates [115]. In addition, magnetic susceptibility gradients at the many air-tissue interfaces within the lung parenchyma yield an increased B_0 heterogeneity (ΔB_0) result in a short T_2* value of approximately $\sim$0.5-3 ms at typical clinical field strengths (recall $T_2* = \left[\frac{1}{T_2} + \gamma\Delta B_0\right]^{-1}$) [115, 116, 117, 118, 119]; this is compared with typical T_2* values in muscle tissue of ~30 ms [120] (see Figure 8.1 for a comparison between muscle and lung tissue for relative signal magnitudes and decay associated with T_2*). This then requires rapid data sampling after spin excitation and maximizing k-space coverage while minimizing acquisition time. The long pulmonary T_1 ($\sim$1 second) [121, 122] requires small FA or long imaging times, and image quality is further degraded by respiratory and cardiac motion. As a result of these obstacles, advancements in pulmonary MRI have historically been slow.

X-ray computed tomography (CT) is the traditional gold standard for tomographic lung imaging in the clinical setting. However, there is increasing concern that CT exposes patients to sufficiently high doses of ionizing radiation to increase cancer risk, particularly for longitudinal studies and in pediatric populations [22, 23, 24]. The mean lung dose per chest CT for patients under 5 years old is ~10 mGy, with one radiation-induced solid cancer projected to result from every ~360 and every ~1200 chest CT scans for girls and boys, respectively [22]. However, with the technical challenges associated with MRI of the lung, CT has remained
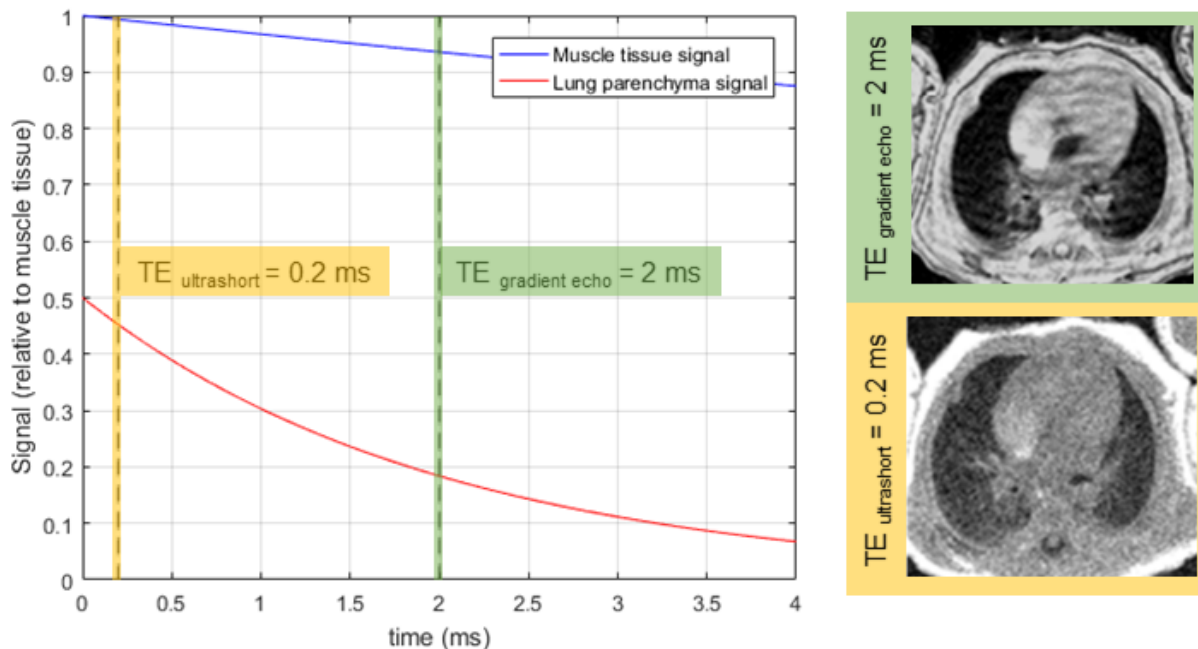
Figure 8.1: Left: The relative MR signal decay of lung tissue (red, $T_2* \approx 2$ ms at 1.5T) and muscle tissue (blue, $T_2* \approx 30$ ms at 1.5T). MR signal from muscle tissue has decayed to $\sim$94% of its original signal by typical Cartesian gradient echo acquisition times (green, TE $\sim$2 ms) and $\sim$99% at typical ultrashort TE values (yellow, TE $\sim$0.2 ms). However, lung tissue decays to $\sim$37% of its original signal at gradient echo TE values, and $\sim$90% at ultrashort TE values. Thus, extremely short echo times characteristic of radial MRI acquisitions are crucial for imaging lung parenchymal tissues with short T_2* values. Right: gradient echo axial MR image (green) and UTE MR axial image (yellow) from a neonatal patient with no known lung disease.

the pulmonary tomographic imaging modality of choice.

Even with the disadvantages associated with Cartesian imaging (TE values equal to or longer than the lung parenchymal T_2*; sensitivity to motion), several studies have demonstrated that useful information can still be obtained with these acquisitions. Schopper et al. assessed lung volume growth between prenatal and postnatal CDH infants, and also evaluated differences in lung growth between ispilateral and contralateral lungs after surgical diaphragmatic repair [123]. Using comparisons of quantitative parenchymal intensity thresholding, Walkup et al. demonstrated ability to differentiate between infants with BPD

and infants with no lung disease [124]. Further, Stahl et al. showed comparative sensitivity between lung clearance index (LCI, a clinical measure of lung function) and global morphology and perfusion MRI scores in the detection of antibiotic therapy response in cystic fibrosis patients [125]. Despite demonstration of the utility of Cartesian images, these sequences are still susceptible to subject motion and short T_2* values in the non-fibrotic lung tissues.

More recently, effective structural pulmonary MRI has benefited from widespread development of ultrashort echo time (UTE) techniques that use a variety of radial k-space sampling schemes, i.e. raw data is acquired starting at the center of k-space, where $\overrightarrow{k_{3D}} = (0,0,0)$, and then projects outwards [126, 127, 128, 129, 130]. These techniques not only provide increased SNR in the lung parenchymal tissue by decreasing TE to well below the lung T_2* value, but also are more robust against physiologic (respiratory and cardiac) and bulk motion as compared to Cartesian acquisition schemes [131] (see Section 9.1). Interestingly, the earliest MR sequences were 'radial' in nature, in that they were FID-based and inspired by the projection acquisitions of x-ray CT.

There has also been recent work on 3D zero echo time (ZTE) MRI techniques in other short-T_2* tissue, such as bone, in which spatial encoding gradients are turned on prior to an RF pulse, such that the beginning of acquisition truly is at TE = 0 (ignoring a few microseconds of dead time for transmit/receive switching and digital filtering). However, there are a few challenges with ZTE methods, one of which being that the center of k-space is not acquired, since phase is accumulated during the RF pulse and not rewound before data acquisition/read-out; this is typically addressed with radial oversampling and extrapolation. Additionally, the RF pulse duration must be short enough to yield a broad enough pulse bandwidth (i.e. a large enough excited volume in the gradient to span the object of interest) but still have a large enough amplitude to yield a convenient flip angle [132]. However, clinical scanners typically have switching time limited to tens of microseconds, and often protons are excited in materials and equipment near the object/organ of interest that result in aliasing

artifacts [132]. In addition, ZTE is often praised for its virtually silent acquisition, achieved by keeping gradients on all the time with only slight adjustments for the next excitation and acquisition. This is equivalent to saying that the radial projections acquired in k-space are stepped through slowly and systematically. However, as will be explored further in Sections 10 and 11, randomization of the radial projection directions is crucial to the ability to retrospectively track respiratory-modulation in the k-space data, as well as discard data acquired during bulk motion events.

The recent renaissance of radial UTE MRI sequences allow for further refinement of structural evaluation of lung disease using ^{1}H MRI [121, 129, 133, 134, 135], and have allowed MRI to emerge as a viable structural pulmonary imaging modality, particularly in children and infants, who are possibly the most difficult patient populations to image. As has been demonstrated by several groups, UTE MRI performs comparably to CT in evaluating cystic fibrosis disease [126, 136, 137, 138]. The results of these studies support the integration of UTE MRI into routine clinical exams for more comprehensive evaluation of early CF lung disease. Further, recent radiological scoring in neonatal BPD patients using early life MRI (UTE and short-TE gradient echo) has demonstrated that structural MRI in early life may shed light on disease trajectory and may help to identify prematurely-born infants at higher risk for respiratory morbidities [139]. Pulmonary UTE MRI has the potential to play a role in determining prognosis, evaluating efficacy of individualized therapies, and informing clinical management of neonatal and pediatric patients, and importantly can be implemented serially without requiring ionizing radiation, sedation, or anesthesia.

9 UTE MRI Theory and Background

9.1 Cartesian MRI Acquisitions

Convention MRI acquisitions currently used in clinical settings typically acquire k-space in a Cartesian scheme (a 2D Cartesian gradient echo is shown in Figure 9.1). Since the k-space data is already sampled on a Cartesian grid, real-space images are easily reconstructed via a fast Fourier Transform. While sequences like a fast gradient echo have been optimized to shorten the TE value to approximately 2 ms, this acquisition time is still approximately equivalent to the lung parenchymal T_2* and so does not effectively capture signal from such parenchymal tissue. Further, due to the Cartesian k-space acquisition, gradient echo images are still susceptible to image artifacts from physiological motion (cardiac, respiratory, or bulk), which can partially or totally corrupt the diagnostic image quality. Periodic motion, such as that associated with respiration, contributes to inter-view effects (between different phase encoding lines in the k$_y$ direction, as in Figure 9.1) and yields discrete ghosting artifacts in the phase-encode direction, with image separation of the ghosts (Δy_g) calculated by

$$\Delta y_g = \frac{FOV_{PE} \cdot TR}{T_m},$$ (9.1)

where FOV_{PE} is the field of view along the phase-encode direction, TR is the repetition time per view, and T_m is the period of the physiologic motion. Random motion contributes to intra-view effects (during a single phase-encode acquisition) and yields diffuse blurring in the phase-encode direction.

9.2 Radial MRI Acquisitions

The schematic pulse sequence diagram of a neonatal UTE acquisition structure is shown in Figure 9.2-left. This pulse sequence includes an RF pulse, a z-direction slab-select gradient
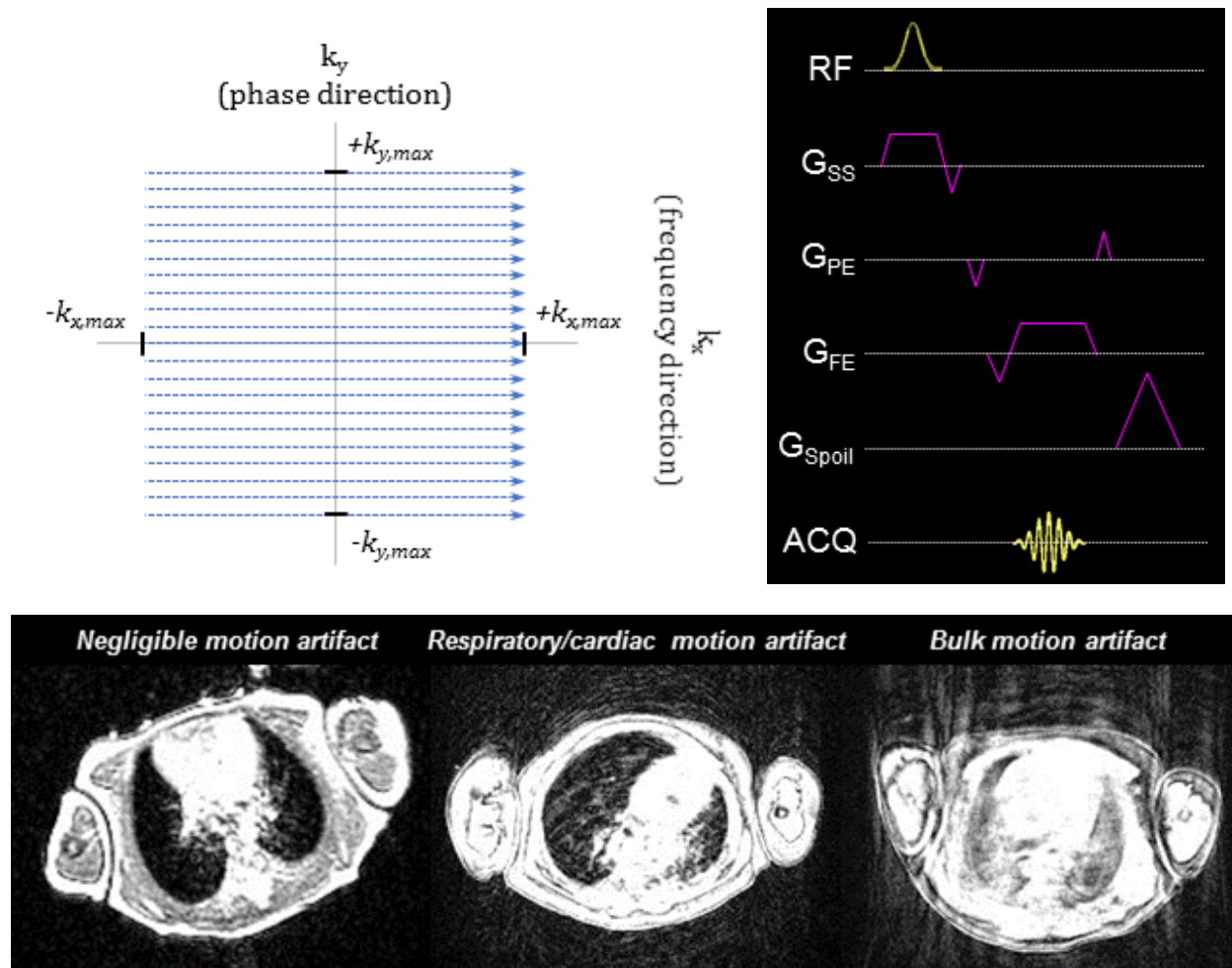
Figure 9.1: Left: The Cartesian k-space acquisition scheme for a typical 2D gradient echo, with frequency encoding lines (k_x) acquired during readout at various phase encoding coordinates (k_y). Right: The pulse sequence diagram of a typical 2D gradient echo. An RF pulse is simultaneously applied during a slice selection gradient (G_{ss}), which selectively excites spins across a specific bandwidth. The phase encoding gradient (G_{PE}) specifies a coordinate in k_y, and k-space is traversed in the k_{FE} direction during the frequency encoding (sometimes called read-out) gradient (G_{RO}) while data is acquired (ACQ). Finally, all remaining transverse magnetization is dephased with a large spoiler gradient (G_{Spoil}). Bottom: Representative neonatal gradient echo images, with varying degrees of motion artifact (from none, to some mild respiratory/cardiac, to extreme bulk motion that degrades image quality to little diagnostic utility.

pulse, a rewinder gradient pulse, a read-out gradient pulse, a fly-back gradient pulse, and a spoiler gradient pulse. Radial schemes have no need for phase encoding gradients and thus

reduces the TE compared with traditional Cartesian (i.e. gradient echo) sequences. The RF pulse implemented in typical radial UTE sequences is a Shinnar-Le Roux (SLR) pulse, which imparts minimal phase to the spins during excitation, yielding substantially higher signal at the end of an excitation pulse when compared to a hard or sinc pulse [128] as well as a shorter duration for the RF rewinder pulse and so a shorter TE value. The phase of each RF pulse is incremented by 117° for RF spoiling in order to avoid residual transverse magnetization build-up. The simultaneous slab-select gradient excites a slab volume over the desired region and is followed by a slice rewinding pulse to refocus the dephasing of the spins that occurred while the slab-select pulse was active. Note that the slab thickness and image field of view (FOV) are set separately in the sequence; it is ideal to select a FOV large enough to cover the slab-select volume to avoid aliasing artifacts.

The data acquisition window is simultaneous with the read-out gradient, placing the beginning of the FID (i.e. TE) at the center of k-space, with each FID acquisition tracing a radial projection in k-space (Figure 9.2-right). The shape (and components of G_x, G_y, and G_z, i.e. the polar and azimuthal angles) of the read-out pulse dictates the density (and trajectory) of the radial projection sampled in k-space; varying shapes could produce a center-out, spiral, conical, or other radial trajectory in k-space. This spherical coverage of 3D k-space yields a spherical FOV and isotropic image resolution. The repeated sampling of the k-space center mitigates motion artifacts and allows for tracking of bulk and respiratory motion, as described further in Section 10. Radial projections are acquired with pseudo-random view ordering using a bit-reversal algorithm [128]. This time-randomized coverage of k-space is important both for mitigation of structured artifacts from physiological periodic motion and for respiratory-binned image reconstruction and analysis (see Section 10).

Because of the short T_2* in lung parenchyma ($\sim$2ms, on order of the read-out time), it is advantageous to sample the periphery of k-space more quickly after excitation (i.e. to "fly out" as quickly as possible from the k-space center). During a typical trapezoidal gradient
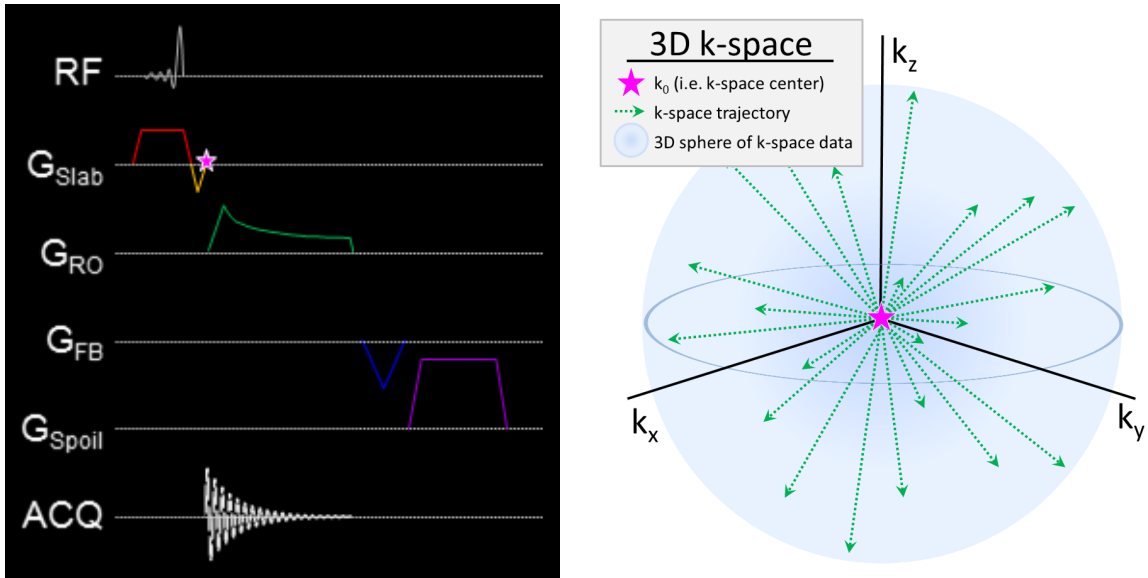
Figure 9.2: Left: The pulse sequence diagram for the neonatal UTE MRI sequence: an SLR RF pulse, a z-direction slab-select gradient (red), a rewinder pulse (yellow, behind magenta star), a variable-density read-out gradient (green), a fly-back gradient (blue), a spoiler gradient (purple), and a data acquisition window simultaneous with the read-out gradient that detects the FID signal. The pink star represents TE (the beginning of the radial projection), typically occurring at the k-space center, and coinciding with the beginning of acquisition (read-out). Right: A schematic of 3D radial UTE k-space acquisitions, with the center of k-space (i.e. TE) shown at the pink star and radial projections shown in green (both matching the sequence diagram). The k-space sphere shown in blue will be filled with radial projections acquired in randomized trajectory directions throughout the entire UTE scan.

pulse (see Figure 9.3 - black data) k-space data is sampled evenly along the radial direction of a single trajectory (once the amplitude plateau is reached). However, this pulse shape requires sampling density compensation, since the angular sampling at the edges of k-space is sparser, which leads to noise amplification. Thus variable density read-out pulses are desirable in neonatal radial acquisitions (see Figure 9.3 - ; red, lower G_{max} and slew rate capabilities; blue, higher capabilities). While the center of k-space is sampled less densely along a single view, the center is sampled sufficiently when all views are combined altogether. The variable-density shape allows for a constant sampling density beyond a specific k-space radius dependent on the slew rate capability, yielding higher SNR and better edge sharpness

in image space [128].
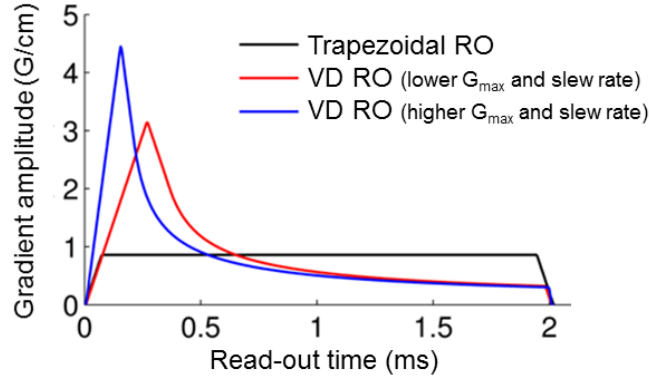
Figure 9.3:   Three possible read-out pulse shapes for a neonatal UTE MRI scan. The black pulse represents a trapezoidal gradient pulse. The red and blue lines represent variable density read-out gradients at two different gradient strength capabilities (G_{max} and slew rate; red, lower capabilities; blue, higher capabilities).

The spoiler gradient is implemented on the z-axis (in the direction of slab-select) and acts to "kill" (i.e. dephase) any residual transverse magnetization before the next acquisition. The size of the spoiler changes on each acquisition, such that the area under the readout and spoiler combined stays constant (i.e. residual magnetization is brought to the same large k_z coordinate at the end of every TR). Prior to the z-direction spoiler, a fly-back gradient is implemented on the x-axis and y-axis to return the to-be- spoiled magnetization to the z-axis (i.e. the area under the readout and rewinder combined equals zero). If spoiling were implemented directly out from each projection's trajectory (i.e. variable direction spoiling) in order to increase the spoiler efficiency time, the spoiler performance becomes sensitive to view ordering and thus requires a less randomized, more slowly progressing scheme for projection acquisition to maintain steady state and avoid refocused magnetization. However, the randomized view ordering is crucial for respiratory binning of k-space for respiratory-gated imaging applications (see Section 10).

9.3 Neonatal-Specific Sequence Adjustments

Pulmonary MRI faces unique challenges when applied to a neonatal subject population. In particular, the small size of neonatal lungs ($\sim$100 mL, about 2% of the volume of the adult lung) requires higher spatial resolutions to resolve the correspondingly smaller anatomical structures. Several modifications were made to a UTE MRI pulse sequence originally developed for adults [128] in order to optimize the sequence for neonatal imaging [140].

Variable Density Read-Out Trajectories

In order to achieve higher image resolution, the radial maximum in k-space (k_{max}) needs to be higher for a neonatal scan than for an adult scan. Typical read-out gradient duration for an adult UTE sequence is 1 ms. Through lengthening the read-out gradient to 2 ms, $k_{x',max}$ is increased by a factor of 2, effectively decreasing $\Delta x'$ (voxel size) by a factor of 2 and increasing image resolution by a factor of 2:

$$\Delta x' = \frac{1}{k_{x',max}}. \tag{9.2}$$

Decreased Slab Width

The torso size of a neonate is unsurprisingly smaller than that of an adult. Therefore, the selectively-excited S-I (z-direction) slab width should be smaller for a neonate than for an adult, so that the neonatal-scaled FOV covers the slab-select volume to mitigate aliasing. Here, a 12-14 cm slab thickness was selected to match the scale of a neonatal body. However, this increased the required time for excitation and for refocusing the through-slab phase, and thus increased the minimum TE from 80 ms (for adult UTE) to 200 ms (for neonatal UTE). Assuming a $\sim$2-ms T_2* relaxation rate in parenchymal lung tissue [115, 116, 117, 118, 119], this increase in TE results in a $\sim$6% relative SNR reduction.

Gradient Calibrations The actual read-out trajectory in k-space typically deviates from the prescribed ideal trajectory specified in the gradient timing and amplitude instructions, due to imperfect hardware performance and induced eddy currents from gradient pulses (Figure 9.4). For instance, during gradient ramping or switching, an amplifier could be driven into a non-linear range. Mis-registration of k-space data with the expected sampling pattern results in reduced image quality and increased image artifacts upon reconstruction. Trajectory errors can be measured in a separate calibration scan acquisition on either the subject itself or an MR phantom; following the methods of Duyn et al., the actual k-space trajectories are measured on various subsets of spins within various xy-plane, yz-plane, and xz-plane slices displaced to specified positions from the magnet isocenter [141]. In a first measurement for a single slice, the active gradients include the slab-select gradient and the read-out gradient specific to that slice's offset from isocenter (all read-out gradients from other directions are turned off). In a second measurement, the same acquisition is repeated, but with only the slab-select gradient active. The difference in accrued phase between the two MR signals ($\Delta\varphi$) is

$$\Delta\varphi_{x'}(t) = \int_0^t \gamma \cdot G_{x'}(t) \cdot x_0 \cdot dt = x_0 \cdot k_{x'}(t), \tag{9.3}$$

where γ is the gyromagnetic ratio of the nucleus ($\sim$42.6 MHz/T for ^{1}H), x' is the specified read-out direction, $G_{x'}(t)$ is the read-out gradient amplitude for the specified direction, and x_0 is the distance of the specified slice to the magnet isocenter. From the measured $\Delta\varphi$, the k-space trajectory $k_{x'}(t)$ can be calculated in a straightforward manner.
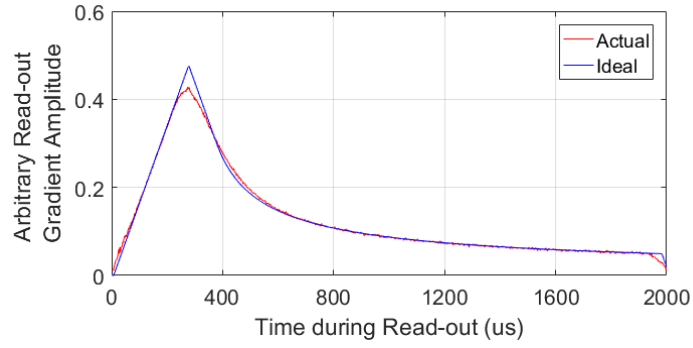
Figure 9.4: The ideal and actual read-out gradient pulse shapes from a neonatal UTE scan, which often deviate from each other, typically due to imperfect hardware performance and response. The actual pulse shape (i.e. trajectory) is measured using methods from Duyn et al. [141] (here, using an external phantom). At the amplitude peak shown here, one can observe the imperfect ability of the gradient to change slew rate directions from maximum positive to maximum negative.

10 Motion-Modulation of the Initial Point on the UTE Free Induction Decay

10.1 Potential Sources of the Modulation Phenomenon

A phenomenon has been observed in the radial imaging community [142, 143, 144, 145, 146, 147], which utilizes the time-course of the phase or magnitude of the k-space center (i.e. the first point on each radial FID) to track physiologic motion in imaging subjects. As shown in Figure 10.1-A for a neonatal UTE MRI scan, the time-course clearly indicates periods of quiescent breathing and of bulk motion events. Figure 10.1-B shows a 5-second interval from the same neonatal scan, demonstrating the clear modulation of this waveform with respiratory motion, and Figure 10.1-C shows the quiescent breathing rates from the neonatal subject. This section will detail some potential theories into the origins of this motion-modulation phenomenon; see Section 11 for further application descriptions. Preliminary investigations into the potential origins of this phenomenon are described here, with future exploration on this topic including quantification of contribution to the changes in magnitude and phase, both in respiratory and bulk motion changes.

Changes in Local Magnetic Field   One potential source of the respiratory-modulation phenomenon (and more generally the motion-modulation phenomenon) is a change in B_{local} experienced by a subset of spins in the excitation volume, which would change local spins' precessional Larmor frequencies, $\omega_{local}(t)$. Thus the amount of phase φ_{local} accrued over time t by local spins would depend on that local magnetic field value B_{local}:

$$\omega_{local}(t) = \frac{d}{dt}\varphi_{local}(t) = \gamma B_{local}(t) \tag{10.1}$$
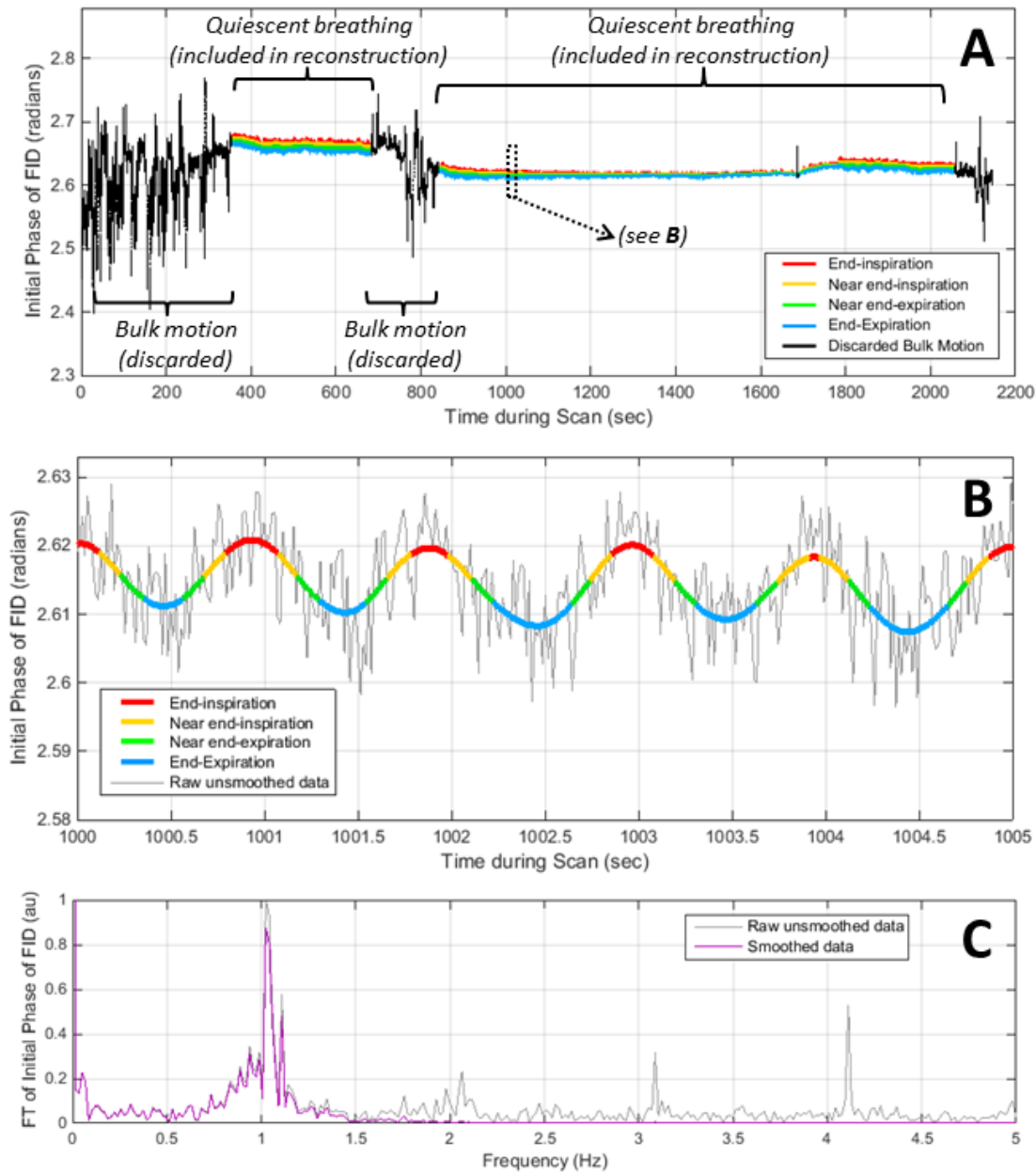
Figure 10.1: A) The motion-tracking phase time-course for a ∼36-min neonatal UTE scan demonstrates periods of quiescent breathing (colored, 25%-gated data; red, end-expiration; yellow, near end-expiration; green, near end-inspiration; light blue, end-inspiration) and periods of discarded bulk motion (black). See Section 11 for more details on the respiratory binning process. B) The raw (grey) and smoothed phase time-courses (colored) of quiescent breathing match well, as shown during a representative 5-s interval. C) The frequency spectrum (raw data, grey; smoothed data, purple) of a ∼100-s interval of quiescent breathing, highlighted by a large respiratory peak (∼1.1 Hz, ∼66 bpm). Reprinted with permission from [135].

$$\varphi_{local}(t) = \int_0^{TE} \gamma B_{local}(t) dt. \tag{10.2}$$

One explanation for changes in B_{local} with motion is that the B_0 field of the magnet is relatively inhomogeneous (on order of parts per million). So any motion, whether bulk or respiratory, will shift the local Larmor frequency for any spins displaced during that motion (i.e. from lungs, heart, liver, muscle, etc., depending on the motion). This frequency shift should be observable on the Fourier transforms of FIDs acquired at end-inspiration and end-expiration, for example, but theoretically should shift smoothly during any changes in body position. This analysis has not yet been performed but will be the subject of future exploration.

Another possible explanation for changes in B_{local} with motion is that bulk magnetic susceptibility changes with motion. Specific to respiratory motion, the O_2 content in the lungs will increase with inhalation. O_2 is paramagnetic and will weakly align with and strengthen the B_0 field of the magnet, thus increasing induced field inhomogeneities that ^{1}H parenchymal tissue will experience. Also specific to respiratory motion, the bulk density of lung tissue will decrease as lungs exhale; this will not affect the magnetic susceptibility χ of one alveolar wall, but "deflating" lung tissue will likely yield a more homogeneous B_{local} due to the changing proximity of other alveolar walls ($\chi_{parenchyma} \approx 10^{-5}$, close to water). However, the motion modulation of the k-center waveform is still observed even with a stationary phantom placed at several positions in the magnet, and so likely the primary source is not related specifically to changes specific to the lung content, but rather to bulk displacement of the body's spins more generally, as discussed above.

Changes in Coil Tuning Another potential source of the respiratory-modulation phenomenon is a variation in phase due to changes in RF coil tuning (i.e. coil loading) due to respiratory motion. If this were the sole or primary contributor to the phase variation
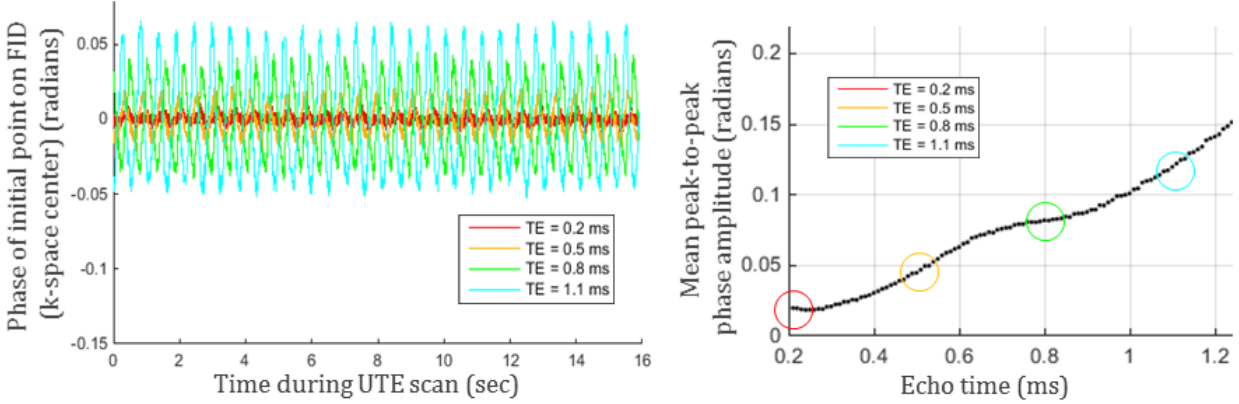
Figure 10.2: These respiratory-modulation data from UTE scans run on a ventilated mouse indicate that peak-to-peak phase accrues with increasing TE values, indicating that a one-time phase contribution imparted by slight coil tuning shifts is not a primary source for the respiratory-modulation phenomenon.

phenomenon, then one might expect a constant phase contribution for each excitation at a specific body position (i.e. specific coil tuning), such as at end-expiration, no matter the delay between excitation and acquisition (i.e. the echo time, TE). Thus a constant peak-to-peak phase amplitude would be expected for the constant body displacement during respiration.

To address this question, an experiment was devised with help from the author's colleagues to see how the duration of TE affects the respiratory-modulated waveform. A healthy adult mouse was imaged with a UTE MRI sequence using a 7T Bruker small-bore animal scanner and a birdcage body coil while on a ventilator with a constant respiratory rate of ∼0.5 Hz. Several UTE scans were acquired for ∼16 seconds each, yielding highly undersampled k-space acquisitions, but with enough duration to examine the respiratory waveform. Each scan implemented a different TE value between 0.2 - 2.0 ms.

Respiratory waveforms for representative TE values are shown in Figure 10.2-left, indicating a non-zero phase accrual for the minimum TE of 0.2 ms, with increased phase accruals as TE increases (i.e. as the interval between excitation and acquisition increases). Figure 10.2-right shows the peak-to-peak respiratory phase amplitude as a function of TE, with a

clear trend the peak-to-peak phase between end-inspiration and end-expiration grows when the spin system is allowed to evolve for longer times. This indicates that the predominant source for this phenomenon is not a one-time phase contribution, imparted by slight shifts in coil tuning during respiration. Rather, the difference in accrual of phase between end-expiration and end-inspiration indicates that this phenomenon may be at least in part due to a shift in frequency (between end-expiration and end-inspiration) via a shift in B_{local} that the spins experience, as discussed above.

Changes due to the Fourier Shift Theorem An additional potential source of the respiratory-modulation phenomenon is a variation in phase is due to the Fourier shift theorem. Recall the Fourier transform definition from Equation 2.3; the Fourier shift theorem states that for a translation x_0 in image space, there will be a phase shift of $e^{-i2\pi kx_0}$ imparted onto the transformed data in k-space:

$$F\{f(x - x_0)\} = e^{-i2\pi kx_0}g(k). \tag{10.3}$$

Notably, this phase shift of $e^{-i2\pi kx_0}$ due to image-space translation will be imparted onto *every* point in k-space, except where $k = 0$ (i.e. at the k-space center, k_0). One hypothesis is that the x-space translation of spins in the body during respiration imparts a periodically varying phase shift onto all k-space data besides k_0. Notably, this hypothesis requires that each FID actually starts off the center of k-space, which is a feasible scenario, given the possibility that timing instructions for rewinder gradient pulses and acquisition are not always perfectly synced. See Figure 10.3 for a demonstration of a respiratory waveform generated when each UTE FID starts away from the k-space center (right), and a waveform consisting of noise when each UTE FID starts at the k-space center (left). This thinking could be applied beyond just respiratory motion to non-periodic motion, such as bulk motion,

First point on FID is at k₀

First point on FID is off-k₀
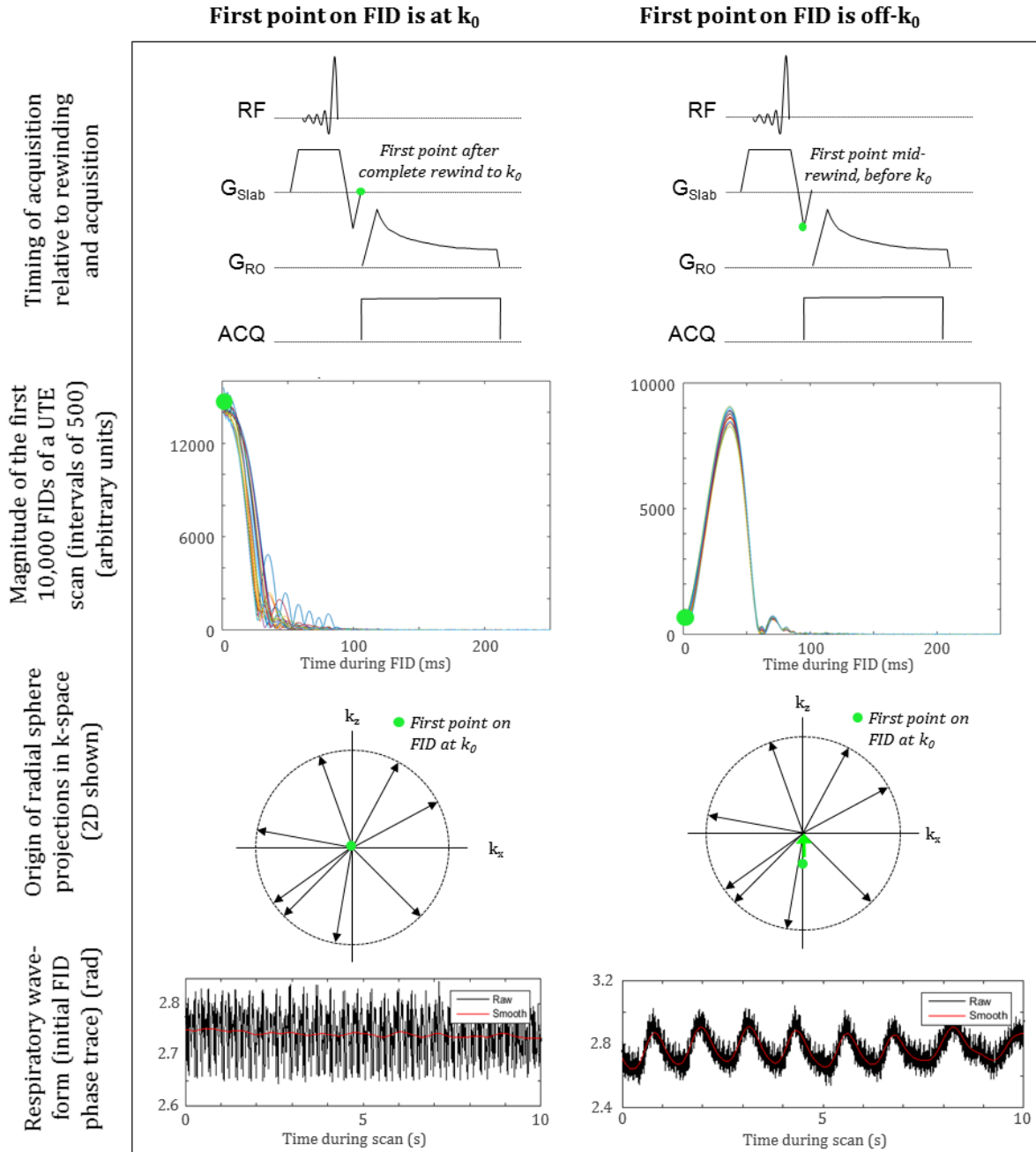
Figure 10.3: Respiratory modulation of the first point of each FID from a free-breathing neonatal 3D radial UTE scan. Left: data acquisition begins after complete slab-select rewinding to k_0 (following phase accrual during excitation/slab-selection). Right: data acquisition begins before complete rewinding. Top row: relevant UTE pulse instruction timing. Second row: representative magnitude FIDs. Third row: k-space position of the first point on each FID. Fourth row: phase time-courses of the FIDs' initial point (10-s interval), demonstrating that only in the case at right does the waveform oscillate with respiration ($\sim$1 Hz respiratory rate).

that would impart non-periodically varying phase shifts to spins. As discussed in Section 10.2, the initial phase of each FID can most definitely be used to track non-respiratory (i.e. bulk) motion as well.

In order to see if this effect, respiratory phase waveforms (i.e. phase time-course during a scan) can be examined from various time-points along the rephasing FID, with acquisition intentionally begun during the slab-select rewinder gradient pulse. If oscillations due to Fourier shift theorem were a primary contributor to the respiratory waveforms, then respiratory-modulations in the phase time-course would disappear as the FID is more fully rewound (i.e., as the data is rephased increasingly closer to k_0). An additional experiment to further investigate the contributions due to Fourier shift includes turning off all imaging (i.e. spatial encoding) gradients and simply executing an RF pulse, data acquisition, and a spoiler gradient (to destroy remaining transverse magnetization and obviate unexpected refocused signal); in this case, the first point of each FID should definitely be at the center of k-space, so if a respiratory waveform is still observed in this case, then there must be an additional substantial contribution from another source.

10.2   Validation of Motion-Tracking with a Volunteer Subject

Work throughout Section 10.2 has been previously published in a peer-reviewed journal [135], from which content is selectively included here as per copyright regulation.

To validate the methodology of this motion-discarding technique, a healthy adult volunteer subject (29-year-old female) was recruited with Institutional Review Board (IRB) approval and written consent. The volunteer subject was imaged on a conventional adult-sized GE Signa HDx 1.5T MRI system using a standard 8-channel cardiac coil, with a maximum gradient amplitude of 33 mT/m and a maximum slew rate of 120 mT/m/s (matching the NICU scanner capabilities). The subject was imaged using a neonatal-adapted 3D radial

UTE sequence and a conventional Cartesian fast-recalled gradient echo (GRE) sequence as a comparison reference (sequences previously described in Section 9). Acquisition parameters for UTE images were: $TE = 120$ μs; $TR = 3.9$ ms; $FA = 5°$; $FOV = 40$ cm; number of radial projections = $\sim$200,000; 3D isotropic resolution = 0.78 mm; and scan time = $\sim$13 min. Acquisition parameters for GRE images were: $TE = 1.5$ ms; $TR = 4.2$ ms; $FA = 4°$; $FOV = 40$ cm; matrix = 512 x 512; in-plane resolution = 0.78 x 0.78 mm; slice thickness = 3.5 mm; number of partitions = 80; number of averages = 4; and scan time = $\sim$7 min. During a first set of UTE and GRE scans ("Scan 1"), the volunteer subject was instructed to mimic patient compliance by maintaining quiescent breathing and avoiding bulk motion. During a second set of scans ("Scan 2"), the subject was instructed to perform a specified sequence of quiescence and bulk motion ($\sim$100 seconds of quiescence at Position 1, $\sim$100 seconds of quiescence at Position 2, and bulk motion for the remainder of the scan) to mimic representative neonatal motion (i.e. bulk shift of chest and moving limbs).

Images acquired during Scan 1 (quiescence) and Scan 2 (intentional bulk motion events) are shown in Figure 10.4. The motion-tracking phase waveform (i.e. the time-course of the first point on each UTE FID) clearly matches the specified patterns of quiescence and bulk motion events (plots on right in Figure 10.4). When all of the data collected during the motion-corrupt UTE scan were used for reconstruction (Figure 10.4B plot – black data), only undesirable blurring was introduced into the UTE images, whereas the corresponding GRE images were severely degraded (Figure 10.4B – images). When UTE images were reconstructed excluding data acquired during the period of sustained bulk motion (Figure 10.4C plot – grey data) but including quiescent data from Positions 1 and 2 (Figure 10.4C plot – black data), images demonstrate lower parenchymal SNR but appreciably less blurring, as well as a 'doubling' effect for specific anatomical features that shifted between the two positions (Figure 10.4C images, green arrows; anterior lung wall and anterior chest tissue). Finally, UTE images were reconstructed with a reduced subset of raw data acquired from

113

only Position 1 (Figure 10.4D plot – black data); these images demonstrate further decreased parenchymal SNR but a clear increase in structural detail as compared to UTE images reconstructed with motion-corrupt data.

From this experiment, we conclude two main ideas. First, a radial acquisition sequence is indeed more robust to motion than a Cartesian sequence (see Section 9.1). Second, it is possible to discard desired intervals of radially-acquired data and still reconstruct diagnostic-quality images. This technique is only possible because the radial k-space projections are acquired in a pseudo-random ordering, so that any typically-selected reconstruction interval will still cover k-space uniformly. If the 3D k-space were acquired but in an ordered radial-out manner (for example, the end of each projection tracing out spiral on a spherical surface from the +z-axis to the -z-axis), then any selected interval would preferentially acquire all data within one section of 3D k-space and would not acquire any data in other sections.
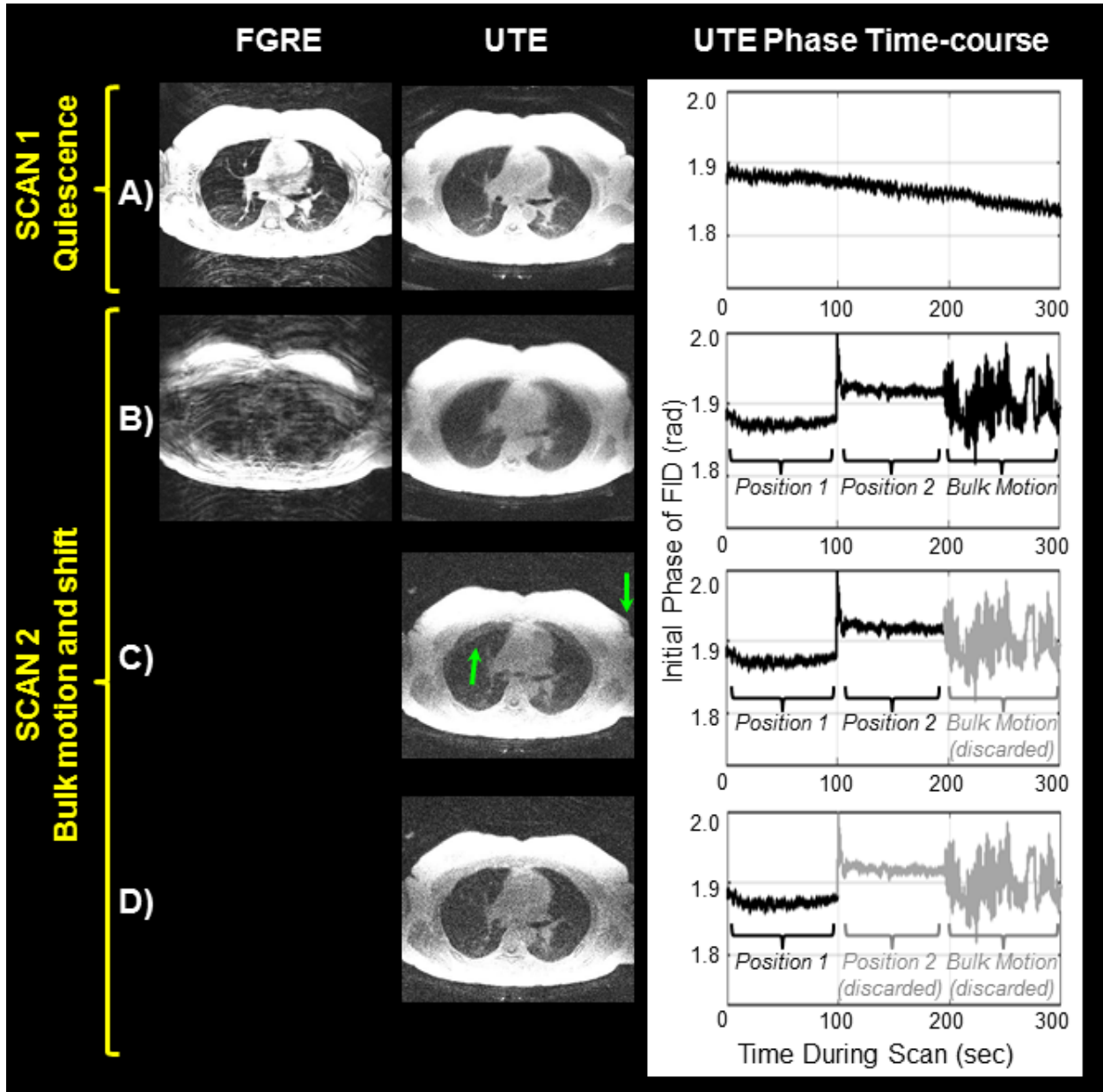
Figure 10.4: Fast GRE (left) and UTE (middle) images in one adult volunteer subject (without respiratory gating). Corresponding plots of the phase time-course of each UTE FID's initial point are shown (right); the time-courses for Scan 1 (A) and Scan 2 (B-D) clearly reflects the sequence of positioning and motion performed by the subject. UTE images are reconstructed only from the corresponding black data, while grey data are discarded prior to reconstruction. Note in C that the anterior lung wall and chest tissue are 'doubled', demonstrating a shift between two positions (green arrows), and in D parenchymal signal has been further exchanged for improved spatial resolution of anatomy. Reprinted with permission from [135].

11 Applications of UTE MRI in Neonates

Our group has generated the first results using UTE MRI in neonatal subjects. This research has resulted in several peer-reviewed publications [135, 172, 182], from which content is selectively included throughout Section 11 as per copyright regulation.

11.1 Need for Motion-Tracking and Respiratory Gating in Neonatal Imaging

In general, MRI is susceptible to artifacts from both gross bulk and physiologic (i.e. respiratory and cardiac) motion, with pulmonary MRI in particular suffering from respiratory motion artifacts. When scanning with conventional sequences that last only a few seconds, most adults and some cooperative children are able to remain still and also perform a sustained breath-hold, which mostly mitigates both bulk and respiratory motion artifacts. On the contrary, neonates are unable to perform breath-holds and will not predictably remain motionless for a scan of any duration. Neonatal cardiac imaging has seen some success using "the feed-and-swaddle" method without sedation or anesthesia [148]. However, these scans typically last only a few minutes, whereas the duration of typical UTE scans exceeds 10 min, during which unpredictable intervals of bulk motion can also occur. The technique of retrospective motion-tracking and respiratory gating, as described in Section 10, obviates the currently common practice of administering sedation and/or anesthesia during neonatal imaging. While the benefits of this motion-tracking are clear for infant imaging, benefit is also envisioned for any non-compliant pediatric or adult patient population, since application of this technique for a typical ∼10-15 min scan of quiet breathing will reduce the rate and severity of motion artifacts in any population.

Historically there has been little success with neonatal external respiratory detection equipment (i.e. respiratory bellows) or with cardiac-like respiratory navigator windows, due

116

to the neonate's rapid respiratory rate ($\sim$1 Hz) and small displacement of the diaphragm and chest wall during free-breathing (approximately a few mm) [149]. For these rapid and small respiratory excursions, image-navigator and respiratory bellows methods generally lack time-efficiency and/or sensitivity [150]. Several gating techniques have recently been developed to minimize respiratory and/or cardiac motion during MR imaging, with varying drawbacks. Some studies have attempted to use the inherent tracking property of the k-space center via 2D or 3D radial acquisition schemes [145, 146, 151, 152, 153, 154]. Others have sampled the k-space center separately from the data required for imaging via navigator echoes [155], which increases overall scan time, or use Cartesian acquisition schemes [156], which are susceptible to bulk-motion artifacts. Prospective gating allows for reconstruction of cine images [157, 158], but acquires data only at a specific phase of the respiratory cycle and prevents a true steady state from being established.

Separate from the reduction of motion artifacts, effective respiratory gating for lung imaging has the potential to provide several important quantitative functional measurements. While adult pulmonary function tests (PFTs) routinely identify volumes at various stages of inflation, infant PFTs (iPFTs) are technically challenging, pose significant risks, and require sedation or anesthesia. Thus, iPFTs are typically only performed at large research institutions and are rarely if ever performed within the NICU. Lung segmentation from end-phase (i.e. end-expiration and end-inspiration) respiratory-gated images can provide functional measurements of tidal volumes in neonates and adults and has the potential to assess regional ventilation [159].

Described in the following sections are several clinical applications of the retrospective motion-tracking and respiratory gating technique using 3D radial pulmonary UTE MRI in neonates, as described in Section 10. This work represents the first application of the k-space center to track and discard motion-corrupt MR data and the first FID-based respiratory-gating of neonatal pulmonary MR images to be reported. These results demonstrate strong

117

potential for retrospective respiratory-gating and removal of bulk motion in any population, but particularly in neonatal and young pediatric patients, for whom there is a great need for reliable, non-ionizing lung imaging and pulmonary disease quantification at multiple lung volumes.

As detailed in Sections 5.3 and 7, Cincinnati Children's Hospital has unique access to neonates with respiratory morbidities due to a unique neonatal-sized 1.5T scanner sited within the institution's NICU [66, 67]. All in-vivo neonatal data presented in this thesis was acquired on this MRI system.

11.2   Retrospective Respiratory Gating

The retrospective respiratory gating UTE MRI technique detailed in this section (along with the retrospective motion-discarding method detailed in Section 10) are applied in neonatal patient populations in the following several sections. Imaging details are given where appropriate in the following sections; however, this particular section will assume that UTE MR imaging data have already been collected and will provide post-imaging data processing details.

For all adult and neonatal UTE scans, a respiratory waveform was generated from the time-course of either the phase or magnitude of the initial point of each projection's FID, which is modulated by respiratory motion [144]. These respiratory waveforms (i.e. motion-tracking waveforms) clearly demonstrate periods of quiescent breathing and of bulk motion events (as seen in Figure 10.4 for an adult subject and in Figure 10.1A for a neonatal subject; see Section 11.2.1 for neonatal imaging details). The choice between using phase or magnitude was based on which waveform had higher peak-to-peak respiratory signal to noise ratio during quiescence. For the 6 adult and 16 neonatal subjects detailed in Section 11.2.1 , the average peak-to-peak respiratory SNR ratio during quiescence was 3.6 ± 1.6 and

2.9 ± 1.8 for phase and magnitude waveforms, respectively.

The chosen raw waveform was processed in MATLAB (Mathworks, Natick, MA) via smoothing using an 800-ms Savitzky-Golay sliding-window average filter (2nd degree polynomial), which is a very commonly-used digital smoothing filter in signal processing [160]. Filter width was chosen to be slightly shorter than the typical neonatal respiratory period (∼1 s) to suppress higher frequency components unrelated to respiration (e.g. cardiac, ∼0.4 s period) while avoiding the need for higher-order models of respiratory modulations within the window. Periods of intermittent bulk motion were identified in MATLAB using estimated breath-wise respiratory periods determined from automatically-identified local minima and maxima, which are heavily corrupted by bulk motion. Projections acquired in regions with estimated respiratory periods greater than 4 times the interquartile range above the median were excluded from image reconstruction.

All remaining projections acquired during quiescent periods were binned to specified acceptance windows (i.e. a percentage of time spent near end-expiration and end-inspiration) by applying a custom 16-s adaptive sliding-window algorithm to the smoothed respiratory waveform in MATLAB. At each window position, data points within the window are binned into quantiles according to amplitude values, resulting in each point receiving multiple bin assignments within the sliding window interval. Each data point's final bin assignment is calculated from the mean of all bin assignments for that point. By examining a local 16-s interval of the modulated respiratory waveform, the algorithm accounts for any variation in respiratory rate during data binning. Typically, 25% and 50% acceptance windows were explored, yielding 4 and 2 bins associated with different respiratory phases, respectively. Fifty-percent acceptance windows were chosen initially for preliminary demonstration of image gating via this technique, and 25% acceptance windows were later used to increase the amount of gating while still maintaining sufficient image quality and SNR. Ideally, the size of the acceptance windows could be reduced further; however, the k-space subset representing each bin much

119
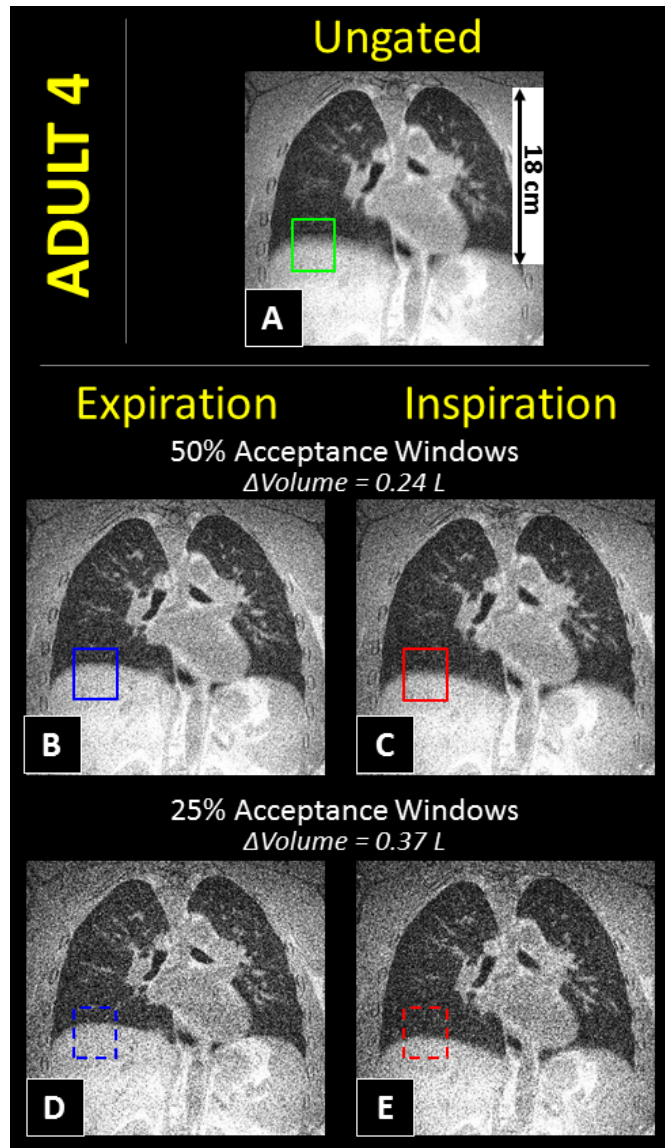
Figure 11.1: 3D radial UTE pulmonary MR images (coronal plane reformats) of an adult subject (Adult 4), with 3D isotropic resolution of ∼0.8 x 0.8 x 0.8 mm. Ungated images (A) use all k-space projections (here, ∼200k projections). Images gated with 50% acceptance windows (B, end-expiration; C, end-inspiration; ∼100k projections each) separately depict inspiratory and expiratory phases of the respiratory cycle. Similarly, images gated with 25% acceptance windows (D, end-expiration; E, end-inspiration; ∼50k projections each) depict end-phases of respiration with more narrow windows and less apparent respiratory-blurring artifact, particularly around the heart and vasculature and at the lung-diaphragm transition. Reprinted with permission from [135].

have sufficient oversampled data to fulfill the Nyquist criterion. Retrospectively-gated images were reconstructed for each bin, with end-expiration and end-inspiration images being of particular interest for calculation of lung tidal volume.

The bin assignments for data acquired during normal tidal breathing are shown for 25% acceptance windows in Figure 10.1B. Example reconstructions demonstrate the utility of the self-gating technique (Subjects Adult 4 in Figure 11.1 and Control 6 in Figure 11.2) with improvement most apparent at the lung-diaphragm boundary. Ungated images (Figures 11.1A and 11.2A) were reconstructed with all acquired projections and thus have higher k-space oversampling and higher parenchymal SNR (for example, ungated SNR = $\sim$21.5 for a mid-slice right lung ROI in Figure 11.2A). However, since these images are reconstructed from data acquired during free-breathing, they are blurred by respiratory motion, particularly at the lung-diaphragm boundary. Images retrospectively gated with 50% acceptance windows (Figures 11.1 and 11.2, middle rows) demonstrate an improvement in spatial resolution of anatomical features, at the cost of a small decrease in parenchymal SNR (SNR = $\sim$14.5 in Figure 11.2B, a factor of $\sim\sqrt{2}$ relative to the ungated SNR). Likewise, images retrospectively gated with 25% acceptance windows (Figures 11.1 and 11.2, bottom rows) exhibit an additional reduction in parenchymal SNR (SNR = $\sim$10.1 for Figure 11.2D, a factor of $\sim\sqrt{4}$ relative to the ungated SNR) but depict a narrower window of respiration with less respiratory blurring.

More finely-resolved structure is evident for several anatomical features in the gated images of Figures 11.1 (Subject Adult 4) and 11.2 (Subject Control 6), particularly for the 25% binning scheme: the major pulmonary vessels, the diaphragm, and (for Subject Control 6) the inferior vena cava (Figure 11.2 – magenta arrows). Signal intensity profiles extracted from UTE images along the superior-inferior (S-I) direction (Figure 11.3) show the quantitative transition from lung to diaphragm tissue for ungated, 50%-gated, and 25%-gated images, with a larger transition slope indicating decreased image blurring for smaller
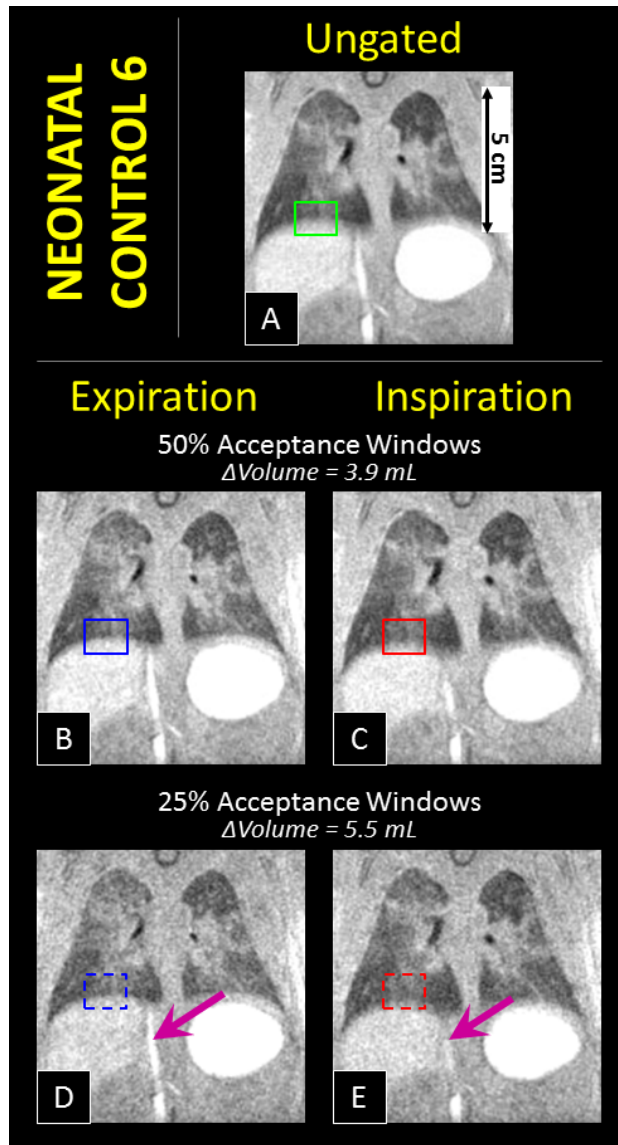
Figure 11.2: 3D radial UTE pulmonary MR images (coronal plane reformats) of a neonatal patient (Subject Control 6), with 3D isotropic resolution of $\sim$0.7 x 0.7 x 0.7 mm. As with the adult images in Figure 11.1, ungated images (A) use all quiescent k-space projections (here, $\sim$190k projections). Images gated with 50% acceptance windows (B, end-expiration; C, end-inspiration; $\sim$95k projections each) separately depict inspiratory and expiratory phases of the respiratory cycle. Similarly, images gated with 25% acceptance windows (D, end-expiration; E, end-inspiration; $\sim$48k projections each) depict end-phases of respiration but with more narrow windows and less apparent respiratory-blurring artifact. Note that the inferior vena cava (magenta arrows) is more finely-resolved with a 25% acceptance window (D, E). Reprinted with permission from [135].

acceptance windows. Ungated, 50%-gated, and 25%-gated slope values for Adult 4 are 0.032 mm-1, 0.041 mm-1, and 0.058 mm-1, respectively; slope values for Control 6 are 0.072 mm-1, 0.079 mm-1, and 0.094 mm-1, respectively.

11.2.1 Tidal Lung Volumes

Five additional healthy adult subjects were recruited and imaged (during quiescence only) in the same manner as the first validation subject detailed in Section 10.2, for a total of six validation subjects (Table 11.1). GRE and UTE MRI (see Section 9) was performed on a neonatal scanner sited within the NICU (see Section 5.3) in 16 neonatal patients recruited from the NICU with IRB approval and written parental consent. This neonatal population consisted of 6 control patients (defined as NICU patients with putatively normal pulmonary function), 5 BPD patients, and 5 CDH patients (Table 11.2). These diseased populations were chosen because they represent the most common pulmonary morbidities seen in this NICU, with clear potential to benefit from further definition of disease via MRI. Neonates were fed, swaddled, and equipped with standard ear protection before placement on the MRI bed. Patients were imaged during quiet-breathing (i.e. room air) with the exception of three mechanically-ventilated patients. No intravenous contrast agent or sedation was administered as part of this protocol. The patients' heart rates and SpO_2 levels were monitored by clinical staff throughout each exam.

Typical neonatal UTE parameters were: $TE = 200$ μs; $TR = 4.4$–5.2 ms; $FA = 5$ or $10°$; $FOV = 18$ cm; number of radial projections $= \sim108{,}000$–$200{,}000$ (during early scan parameter optimization, a few patient scans acquired $\sim36{,}000$-$76{,}000$ projections); 3D isotropic resolution $= 0.70$-0.86 mm; and scan time $= \sim9$-16 min. The number of acquired projections was sometimes reduced due to scan time limitations; scans with a slightly reduced number of projections demonstrated slightly lower SNR in parenchymal tissue. Typical neonatal GRE parameters were: $TE = 1.9$ ms; $TR = 7.7$ ms; $FA = 4°$; $FOV = 18$-20 cm;

123
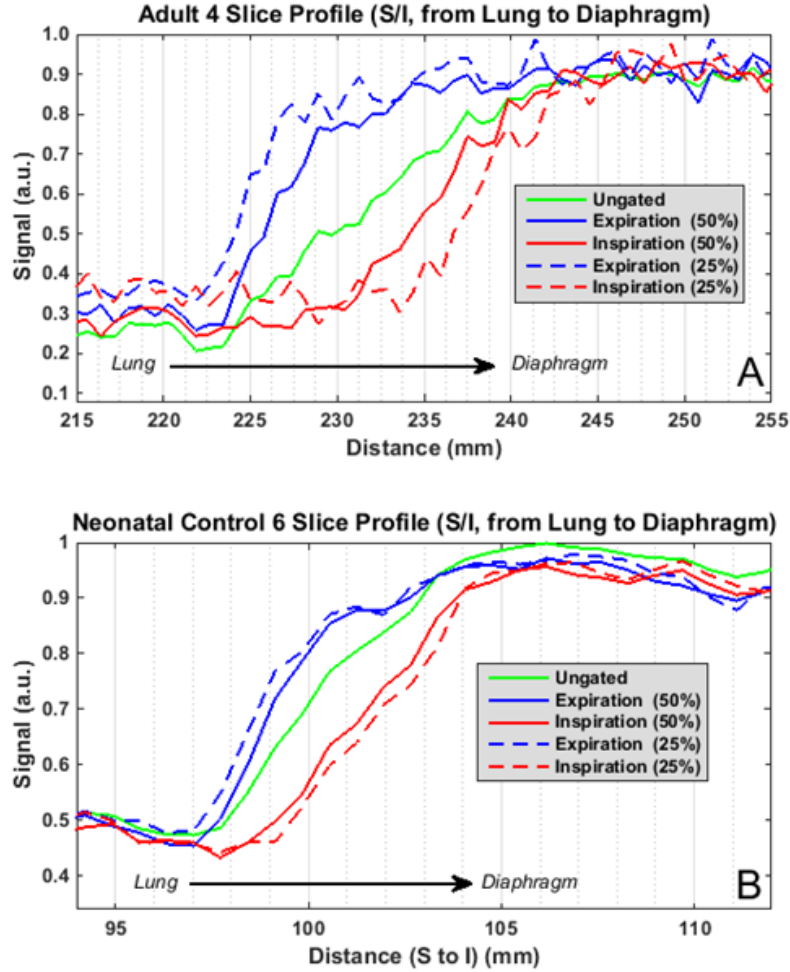
Figure 11.3: Signal intensity profiles extracted from adult (A) and neonatal (B) UTE images along the lung-diaphragm transition. The relevant adult and neonatal S-I regions are shown with corresponding colored boxes in Figures 11.1 and 11.2, respectively (ungated: solid green; 50% and 25% end-expiration: solid and dashed blue, respectively; 50% and 25% end-inspiration: solid and dashed red, respectively). The profiles shown here are averaged from the signal of 50 and 20 pixels in the right-left direction for the adult and neonatal subjects, respectively. The ungated profiles clearly demonstrate a blurred transition (i.e. smaller slope) across ∼20 mm and ∼7 mm for the adult and neonatal subjects, respectively. In contrast, the reduction in respiratory-blurring artifact is evident in the gated profiles, with sharpness at the lung-diaphragm boundary particularly improved (i.e. larger slope at the transition) when using the 25%-gating scheme. Ungated, 50%-gated, and 25%-gated slope values for the adult subject are 0.032 mm^{-1}, 0.041 mm^{-1}, and 0.058 mm^{-1}, respectively; slope values for the neonatal subject are 0.072 mm^{-1}, 0.079 mm^{-1}, and 0.094 mm^{-1}, respectively. Reprinted with permission from [135].

Subject	Sex	Age at MRI (yr)	Mass at MRI (kg)
Adult 1	M	23	68
Adult 2	F	29	77
Adult 3	M	32	95
Adult 4	M	28	82
Adult 5	F	23	74
Adult 6	M	27	70

Table 11.1: Demographic information for subjects that were imaged to validate the retrospective respiratory gating technique via MR-based tidal volume and respiratory rate calculations.

matrix = 256; in-plane resolution = 0.70 x (0.70 - 0.78) x 0.78 mm; slice thickness = 3 mm; number of partitions = 25-32; number of averages = 5; and scan time = ~5 min. Neonatal GRE parameters were varied slightly as needed for full chest coverage of each patient.

Subject	Sex	Post-menstrual age at MRI (wk)	Mass at MRI (kg)	Respiratory Support at MRI	Ventilator rate (breaths per min)
Control 1	M	36	2.7	None	N/A
Control 2	F	40	3.2	None	N/A
Control 3	F	38	2.5	None	N/A
Control 4	F	41	2.6	None	N/A
Control 5	F	38	2.5	None	N/A
Control 6	M	33	2.2	None	N/A
BPD 1	M	38	3.0	None	N/A
BPD 2	F	37	2.3	None	N/A
BPD 3	M	40	3.7	None	N/A
BPD 4	M	39	3.5	Ventilator	40
BPD 5	M	43	3.1	None	N/A
CDH 1	M	39	3.0	Ventilator	25
CDH 2	M	43	3.0	Ventilator	46
CDH 3	M	43	3.7	None	N/A
CDH 4	M	41	2.9	None	N/A
CDH 5	M	42	3.7	None	N/A

Table 11.2: Demographic information for subjects that were imaged and analyzed with the retrospective respiratory gating technique via MR-based tidal volume and respiratory rate calculations.

For all 16 neonatal subjects and all six adult validation subjects, whole-lung segmentations were generated semi-automatically from end-expiration and end-inspiration images (25%-gated and 50%-gated) using Amira (FEI Visualization Sciences Group). Images from both acceptance window sizes were analyzed for adults and neonates to demonstrate the increase in measured tidal volumes when using narrower gating windows. Major vessels were consistently excluded from segmented parenchymal regions based on visual identification. MRI-determined tidal volumes were calculated from the difference between end-expiration and end-inspiration volumes.

Two standard adult PFTs were performed to measure respiratory rates for all adult validation subjects using a KoKo portable spirometer (nSpire, Longmont, CO). In both tests, adult subjects were free-breathing and supine, to match their position during imaging. The first test was performed immediately following imaging, with the subjects recumbent on the MR bed (after removal from the magnet room). It was originally thought that this immediate measurement would most closely replicate the breathing conditions during imaging. However, this method potentially affected tidal breathing by rapidly moving subjects from the MR scanner to a crowded control room. Thus, a second test was performed several weeks after imaging to more closely replicate the restful breathing conditions during imaging, with the subjects recumbent on a patient bed and resting quietly for $\sim$5 min prior to measurement. Three spirometry measurements of adult subjects' tidal volume were acquired and averaged per test for comparison to MRI-based tidal volume measurements. Clinical measures of neonatal tidal volumes were unavailable, since iPFTs were not performed as part of a research study nor as part of the NICU patients' clinical care. For neonatal comparison, physiologically-predicted tidal volumes were calculated from literature-based scaling values based on mass (4-6 mL/kg [161]).

Adult tidal volumes from the first and second spirometric measurements compared well with MRI-based tidal volumes from 25%-gated images (P = 0.071 and 0.040, respectively).

126

Bland-Altman biases were 0.14 L and 0.09 L for the first and second spirometric tests, respectively (mean spirometric results shown in Figure 11.4 A). MRI-measured tidal volumes, with comparisons to spirometry (adults) and physiological predictions (neonates) are detailed in Tables 11.3 and 11.4, respectively. Neonatal MRI-measured tidal volumes were in general smaller than physiologically-predicted tidal volumes [161]; these MRI-based tidal volumes were on average 8.6 ± 3.2 mL and 4.6 ± 1.7 mL for 25% and 50% acceptance windows, respectively. For all neonates' 25%-gated and 50%-gated tidal volumes, Bland-Altman biases were 6.2 ± 3.5 mL and 10.3 ± 2.4 mL (difference range 0.4-10.1 mL and 6.9-15.2 mL), respectively. Specifically, MRI-measured tidal volumes were within the physiologically-predicted range for four neonatal patients (Subjects Control 1, BPD 2, BPD 5, and CDH 1) and below the physiologically-predicted range for the remaining twelve neonatal patients.

Subject	Tidal Volume (L)		
	Spirometry-based[a]: Mean from two tests (first test / second test)	MRI-measured (50% bins):	MRI-measured (25% bins):
Adult 1	0.50 (0.46 ± 0.02 / 0.53 ± 0.06)	0.23	0.40
Adult 2	0.82 (0.89 ± 0.04 / 0.75 ± 0.09)	0.23	0.38
Adult 3	1.01 (1.07 ± 0.12 / 0.95 ± 0.18)	0.78	1.17
Adult 4	0.54 (0.60 ± 0.11 / 0.47 ± 0.05)	0.24	0.37
Adult 5	0.38 (0.39 ± 0.09 / 0.36 ± 0.04)	0.23	0.340
Adult 6	0.45 (0.44 ± 0.08 / 0.46 ± 0.06)	0.20	0.34
[a]Two spirometry tests were performed, with three measurements per test.			

Table 11.3: Functional measurements of tidal volumes for adult validation subjects.

MRI-measured tidal volumes likely underestimate the true tidal volumes due to the non-zero size of the acceptance windows of end-phase respiration. This is evidenced by the fact

Subject	Tidal Volume (mL)		
	Physiologically-predicted range[a]:	MRI-measured (50% bins):	MRI-measured (25% bins):
Control 1	10.8-16.2	6.3	12.5
Control 2	12.8-19.2	4.4	8.3
Control 3	10.0-15.0	1.4	5.1
Control 4	10.6-15.8	6.1	8.6
Control 5	10.0-15.0	5.1	5.4
Control 6	8.8-13.2	3.9	5.5
BPD 1	12.0-18.0	3.9	5.1
BPD 2	9.2-13.8	2.6	9.5
BPD 3	14.8-22.2	5.5	9.8
BPD 4	14.0-21.0	2.3	8.9
BPD 5	12.4-18.7	5.2	14.7
CDH 1	12.8-19.2	6.3	14.6
CDH 2	12.0-18.0	3.1	7.9
CDH 3	14.8-22.2	6.8	8.7
CDH 4	11.6-17.4	3.3	4.4
CDH 5	14.6-22.0	7.3	9.3
[a]Predicted tidal volumes are calculated with a 4-6 mL/kg scaling factor [161].			

Table 11.4: Functional measurements of tidal volumes for neonatal retrospective respiratory gating subjects.

that both the adult (Figure 11.3A) and neonatal MRI-measured tidal volumes were slightly smaller than the spirometrically-measured and reference values (and we expect slightly lower values in babies with CDH). Even with gating, images demonstrate slightly blurred anatomical structures, particularly at the diaphragm for this analysis. In this case, blurring at the lung-diaphragm boundary makes accurate segmentation of the lung challenging. This effect is more noticeable in the 50%-gated images than in the 25%-gated images (Figures 11.1 and 11.2), and correspondingly the tidal volumes from 50%-gated images are lower (and less accurate) than those from 25%-gated images. Ideally, further narrowing of the acceptance windows would yield more structurally-resolved images of end-phase respiration, thus improving segmentation accuracy and generating more accurate MRI-based tidal volume measurements. However, smaller window sizes provide fewer projections for the re-

construction of each retrospectively-gated image, resulting in degraded image quality via either decreased SNR or pixel resolution. There was one outlier data point for adult tidal volumes: the spirometrically-measured tidal volume of subject Adult 2 was larger than the MRI-measured volume. This may be reflective of environmental differences affecting tidal volumes during scanning and post-scan testing (applicable to all subjects). Our spirometric equipment was not MRI-compatible and could not be used during the scan itself. Differences between MRI-measured and physiologically-predicted neonatal tidal volumes may be due to a number of factors, including disease state, sleep, or anxiousness during the scan. Indeed, infants born premature and/or with pulmonary disease may have tidal volumes that vary widely from this predicted physiological scaling. Although neonatal pulmonary MRI is not currently common, it is an emerging modality, and UTE MRI is becoming accessible on all MR platforms. Since tidal volume cannot easily be measured in neonates by any other means, these MRI-determined tidal volumes may represent the safest and most accurate measurements available, particularly in diseased and at-risk patients.

11.2.2   Respiratory Rates

The Fourier transform of the UTE respiratory waveform during quiescent breathing provides a spectrum of physiologic frequency components, with the respiratory rate being of particular interest. Subjects' respiratory rates during quiescence were estimated via calculation of the approximate center-of-mass of the main low-frequency peak in order to appropriately weight the subjects' slightly varying respiratory rate during scanning. An example frequency spectrum, calculated from the respiratory phase waveform during a 100-s period of quiescent breathing, depicts the respiratory frequency peak during this interval of time (spectra from raw and smoothed waveforms of Subject Control 2 shown in Figure 10.1C).

During the same PFTs detailed in Section 11.2.2, One measurement of respiratory rate was acquired (estimated from number of breaths observed over approximately 60 s; Subject
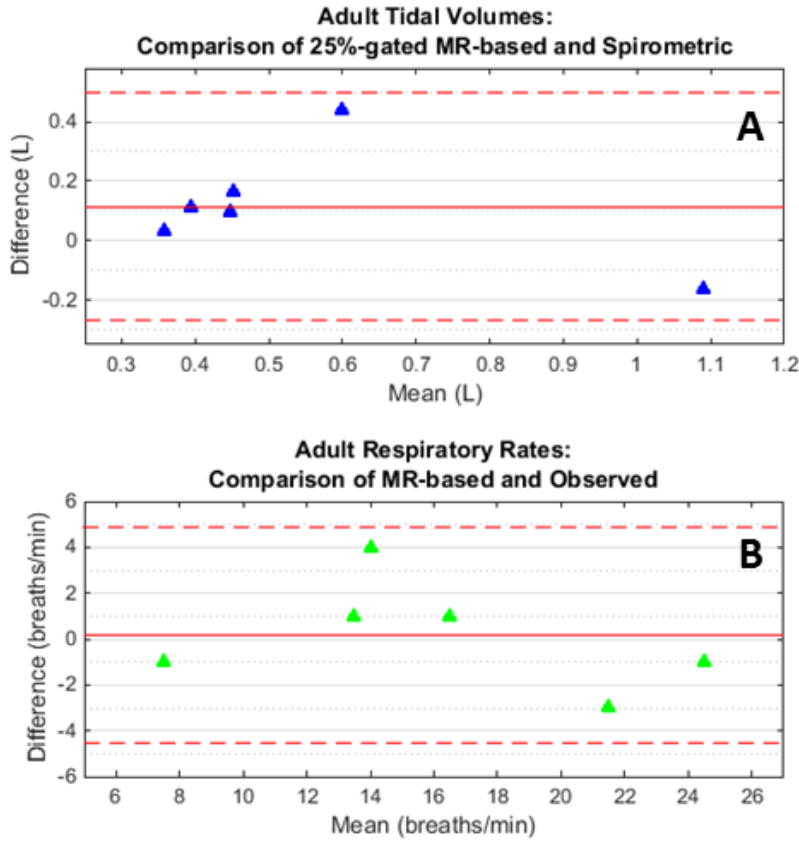
Figure 11.4: Bland-Altman plots for validation of pulmonary function measurements from adult UTE MRI. Shown are comparisons of tidal volumes acquired by 25%-gated image segmentation to tidal volumes acquired by spirometry (A, bias = 0.11 L), and comparisons of MRI-based respiratory rates to observed respiratory rates (B, bias = 0.2 breaths/min). Reprinted with permission from [135].

Adult 3 was observed for 120 s due to this subject's low respiratory rate). Respiratory rates of all neonatal patients were recorded by clinical staff four times at bedside (2 measurements at 0-3 hr pre-MRI, 2 measurements at 0-4 hr post-MRI; ∼60 s of measurement). Ventilator settings for respiratory rates were recorded for the three ventilated neonates (Table 11.2).

MRI-calculated and bedside-observed respiratory rates compared well (detailed in Table 11.5), with P = 0.006 and 0.184 and Bland-Altman biases = 0.2 breaths/min (bpm) and -0.5 bpm for adults (Figure 11.4B) and neonates, respectively. The mean MRI-calculated respiratory rate was 16.3 ± 5.7 breaths per minute (bpm) (mean $\pm$ standard deviation

Subject	Respiratory Rate (bpm)	
	Mean Observed at bedside[a] :	Calculated from MR-waveform:
Adult 1	13	14
Adult 2	12	16
Adult 3	8	7
Adult 4	16	17
Adult 5	25	24
Adult 6	23	20
[a]One bedside observation was recorded.		

Table 11.5: Functional measurements of respiratory rates for adult validation subjects.

Subject	Respiratory Rate (bpm)	
	Observed at bedside[a]: Mean ± SD (range)	Calculated from MR-waveform:
Control 1	50 ± 5 (44-55)	44
Control 2	40 ± 10 (25-46)	33
Control 3	55 ± 4 (49-59)	65
Control 4	49 ± 11 (39-63)	46
Control 5	42 ± 2 (40-44)	62
Control 6	48 ± 7 (40-57)	62
BPD 1	55 ± 12 (40-69)	53
BPD 2	42 ± 15 (33-64)	53
BPD 3	56 ± 8 (45-62)	51
BPD 4	50 ± 11 (40-62)	46
BPD 5	45 ± 10 (36-59)	36
CDH 1	59 ± 8 (52-70)	33
CDH 2	45 ± 1 (43-45)	45
CDH 3	66 ± 4 (61-70)	65
CDH 4	61 ± 15 (42-74)	59
CDH 5	45 ± 3 (41-48)	47
[a]Four bedside observations were recorded.		

Table 11.6: Functional measurements of respiratory rates for neonatal retrospective respiratory gating subjects.

(SD)) and 50.0 ± 10.8 bpm, compared with the observed respiratory rate of 16.2 ± 6.6 bpm and 50.5 ± 7.5 bpm, for adults and neonates, respectively. While some neonatal patients' bedside-observed respiratory rates (4 measurements taken a few hours apart) were very

consistent (9 of 16 patients with SD/Mean $\leq$ 15%), others' rates were widely variable (7 of 16 patients with 15% < SD/Mean $\leq$ 36%). Furthermore, the ventilator rate setting for the three ventilated neonates (Subjects BPD 4, CDH 1, and CDH 2) compare well with their MRI-calculated respiratory rates (within 15%, 32%, and 2%, respectively). Notably, bedside-observed respiratory rates can be significantly different from ventilator settings due to spontaneous breathing (true in two mechanically-ventilated neonates, Subjects BPD 4 and CDH 1).

Notably, MRI-measured and bedside-observed respiratory rates correlated well for adults (P = 0.006) but not for neonates (P = 0.184), with narrow adult and wide neonatal Bland-Altman 95% limits of agreement ($\pm$5 bpm and $\pm$21 bpm, respectively). It is important to emphasize that MRI-measured respiratory rates are calculated from a weighted average of a neonate's quiescent breathing rate during several minutes of scanning, while the observed rates are the average of four 1-min 'snapshot' clinical measurements at different time-points. Thus the MRI-measured value may be a more accurate and representative measure of a subject's respiratory rate during the scan. Notably, two mechanically-ventilated neonates had bedside measurements (obtained while mechanically-ventilated) that do not match well with ventilator settings (Subjects BPD 4 and CDH 1), but we note that the supported ventilation allows spontaneous breathing, making consistent respiratory-rate measurements challenging.

11.2.3   Diaphragmatic Motion in CDH

Infants born with a congenital diaphragmatic hernia (CDH) defect typically undergo surgical repair of the incomplete diaphragm on the herniated side in the first few weeks of life, with various methods for closure/completion of the diaphragmatic surface (see Section 3.3.2 for further background). One application of the respiratory-gated UTE MR imaging technique involves visualization and assessment of the diaphragmatic motion. As a pre-

liminary demonstration of this technique, a patient with CDH was imaged post-repair of a non-primary ("patch") closure. It was noted after image reconstruction that this infant was undergoing asynchronous respiratory motion (Figure 11.5): while the contralateral lung (not originally herniated) was expanded at end-inspiration when compared to end-expiration positioning, the heart and ispilateral lung (originally herniated) appear to move slightly up and over toward the contralateral lung, as if that lung were not inflating at all, but rather was being pulled toward the mediastinal line by the properly expanding lung.
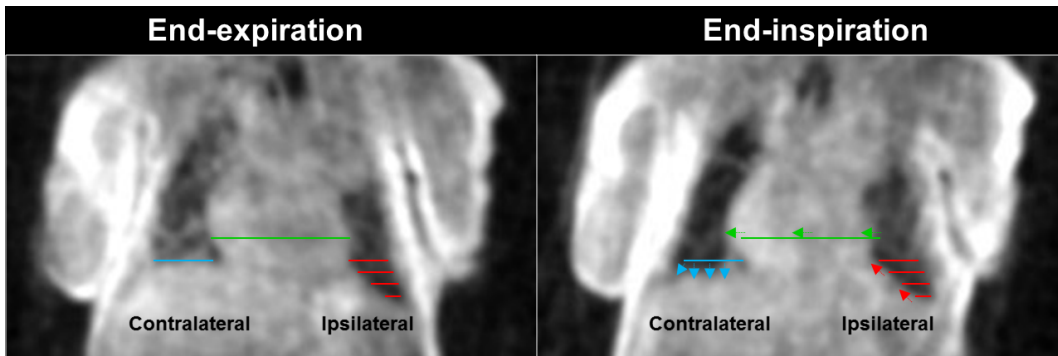
Figure 11.5: Smoothed UTE MR images of a post-repair CDH infant, gated to end-expiration (left) and end-inspiration (right). The solid lines are placed at the same pixels on each image, demonstrating that as the contralateral lung expands downward after inhalation (blue arrows), the heart is pulled toward the contralateral lung (green arrows), and the ipsilateral lung is pulled slightly up and toward the contralateral lung (red arrows). This may indicate that the ipsilateral lung is not inflating well, with a pressure difference between the two lungs, yielding a displacement in the cardiac tissue across the mediastinal line.

It is possible in this case that the asynchronous, abnormal respiratory motion is related to the non-primary material used in repair, perhaps suggesting that such non-primary repair methods are sub-optimal. However, the functional differences in repair methods are not yet well understood, with further investigation merited. Future work with larger numbers of CDH patients with primary repair and non-primary repair may yield a stronger comparison of such outcomes, with quantitative metrics desirable in assessing diaphragmatic motion.

11.2.4   Tracheomalacia in BPD

As discussed in Section 3.3.4, tracheomalacia (TM) is a common abnormality in BPD patients and is characterized by large airway collapse due to underdeveloped cartilaginous tracheal rings and/or deficient airway smooth muscle. With the current clinical standard for diagnosing TM (bronchoscopy – see Figure 3.12) requiring sedation and increased risk to the patient, there remains a need for a safe method to quantitatively evaluate airway collapse.

Just as the retrospective respiratory gating method via UTE MRI is able to visualize the lungs during various stages of respiration, this imaging technique can also be applied to tracheal airway anatomy at risk for dynamic collapse. We hypothesize that retrospectively respiratory-gated UTE MR images of the tracheal airway in neonates with BPD and suspected TM can evaluate extent of dynamic airway collapse, with good agreement of this quantitative MRI to bronchoscopy. As a preliminary investigation of this technique, we've performed the following methodology in one patient with severe BPD and concomitant TM who underwent both clinical bronchoscopy and research UTE MRI. This male subject was born at 23 weeks GA (birth weight = 0.59 kg) and was imaged on the neonatal MRI scanner (see Section 5.3) at 41 weeks PMA (MRI weight = 3.52 kg).

MRI-based Evaluation of Dynamic Tracheal Collapse   The methodology of this application closely follows that of the previously described retrospective gating scheme (Section 11.2), with one change in the binning algorithm. For reasons more fully explained in the following section on computational fluid dynamics (CFD) (Section 11.2), it is important to distinguish between data acquired during inhalation versus exhalation. In previous applications of this gating technique (tidal volumes, comparison of end-phase regional values, etc.), the respiratory phases of interest were primarily end-expiration and end-inspiration, so the direction of air flow during was essentially irrelevant for bins in between the end-frames.

Here, data acquired during inhalation are binned separately from those data acquired
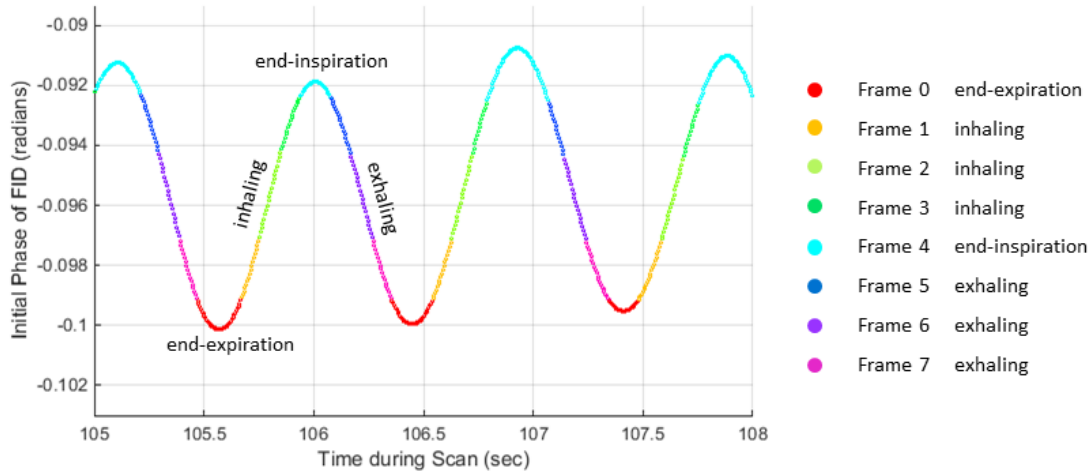
Figure 11.6: A motion-tracking respiratory waveform (via the initial phase of each FID) binned with a bi-directional scheme, such that data acquired during inhalation (frames 1, 2, and 3) are distinguished from data acquired during exhalation (frames 5, 6, and 7). Reconstruction of data binned in this fashion yields anatomy not only and end-inspiration and end-expiration, but also from inhalation and exhalation phases (see Figure 11.7).

during exhalation; Figure 11.6 shows an example motion-tracking waveform (via the phase of the initial point on each FID) from a 3-sec interval, with data binned into eight different frames in a bi-directional binning scheme: one at end-expiration, three during inhalation, one at end-inspiration, and three during exhalation. Representative UTE MR images of the BPD patient's airway reconstructed from each of these data bins are shown in Figure 11.7, with the tracheal lumen fully open at end-inspiration and partially collapsed at end-expiration, indicative of concomitant TM.

Once the respiratory-gated images are reconstructed (Figure 11.7 and 11.8B, tracheal surface renderings can be generated via semi-automatic flood-fill image segmentation (i.e. labeling of image voxels representing the tracheal lumen), performed in ITK-SNAP [162]. Figure 11.8C demonstrates tracheal surface renderings from the same BPD/TM patient shown in Figure 11.7, with the posterior tracheal collapse at end-expiration evident in the selected oblique perspective.

Geometric assessment of the trachea at the end-phases of respiration can be performed
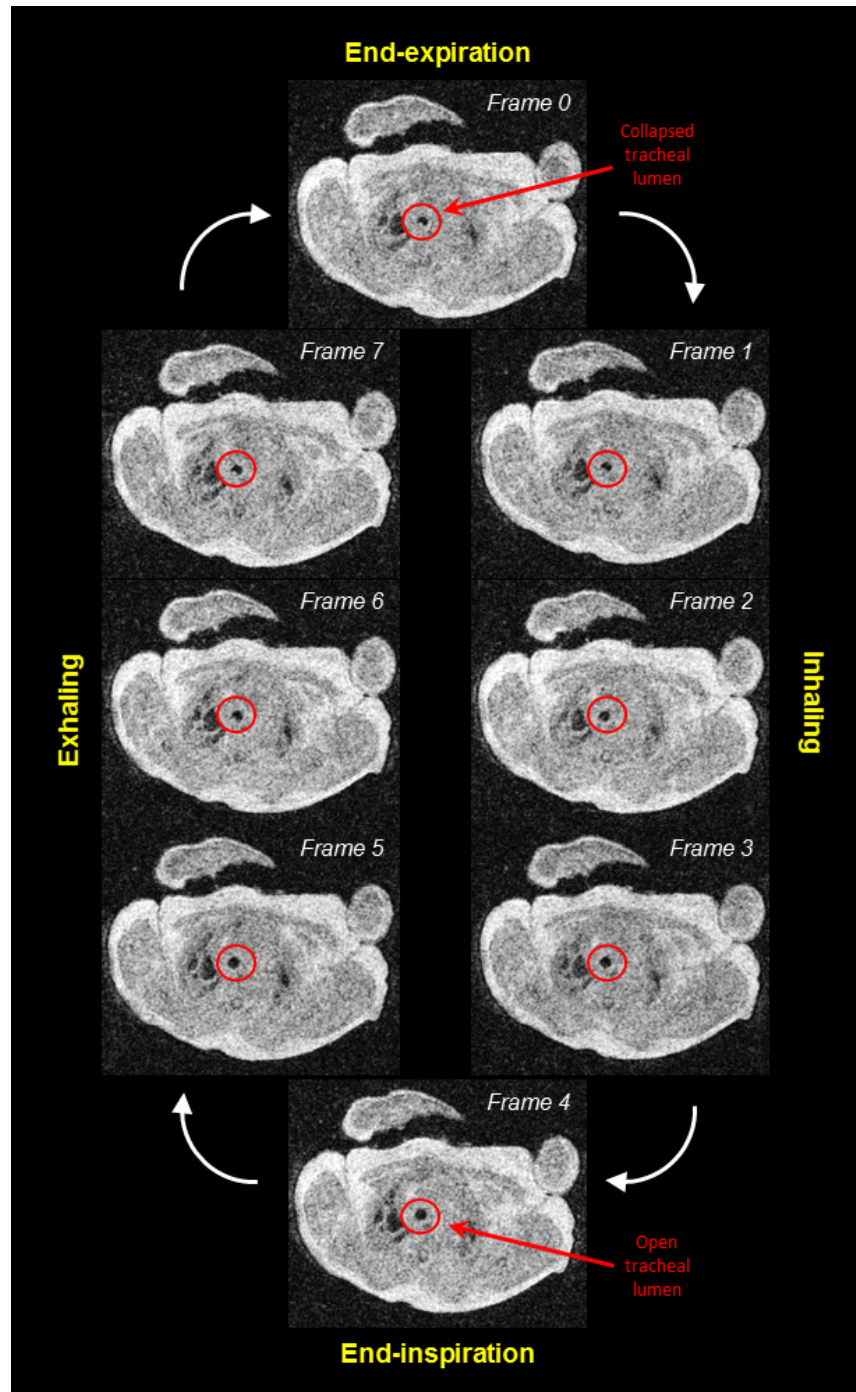
Figure 11.7: Axial UTE MR images binned with a bi-directional retrospective respiratory gating scheme. This neonate had tracheomalacia, so in the end-expiration phase (Frame 0) the tracheal lumen is partially collapsed, while the lumen at the end-inspiration phase (Frame 4) is open.

once surface renderings have been generated for end-expiration and end-inspiration. In order to quantitatively assess the airway anatomy, a centerline can be defined along the length of the trachea, following a method originally developed for the quantification of in-vivo, non-ideal, and variable 3D morphology in vascular networks [163]. The generation of a centerline obviates the need to assume that each image slice is aligned with the actual anatomical structure and thus allows for correction of anatomical deviations from a purely superior-inferior trachea (highly likely in-vivo, and particularly in diseased patients). Once a centerline is defined, a series of disks (spaced 1 mm apart) can be generated that are both normal to the centerline and bounded by the tracheal surface rendering. The cross-sectional area (CSA), or other desired geometric parameter (perimeter, roundness, etc.), of each disk can then be calculated and plotted against position in trachea for any frame in the respiratory cycle. The differences in CSA at end-expiration and end-inspiration at various positions provide a measure of regional dynamic collapse; Figure 11.8D shows the end-expiration and end-inspiration CSA curves for the BPD/TM patient (with the independent variable displayed on the y-axis in order to align with the vertical tracheal anatomy shown by the surface renderings in C), demonstrating localized tracheal collapse centered around ∼20 mm down the trachea. In the future, this regional measurement of collapse can be compared with more qualitative bronchoscopic readings from clinicians (Figure 11.8A).
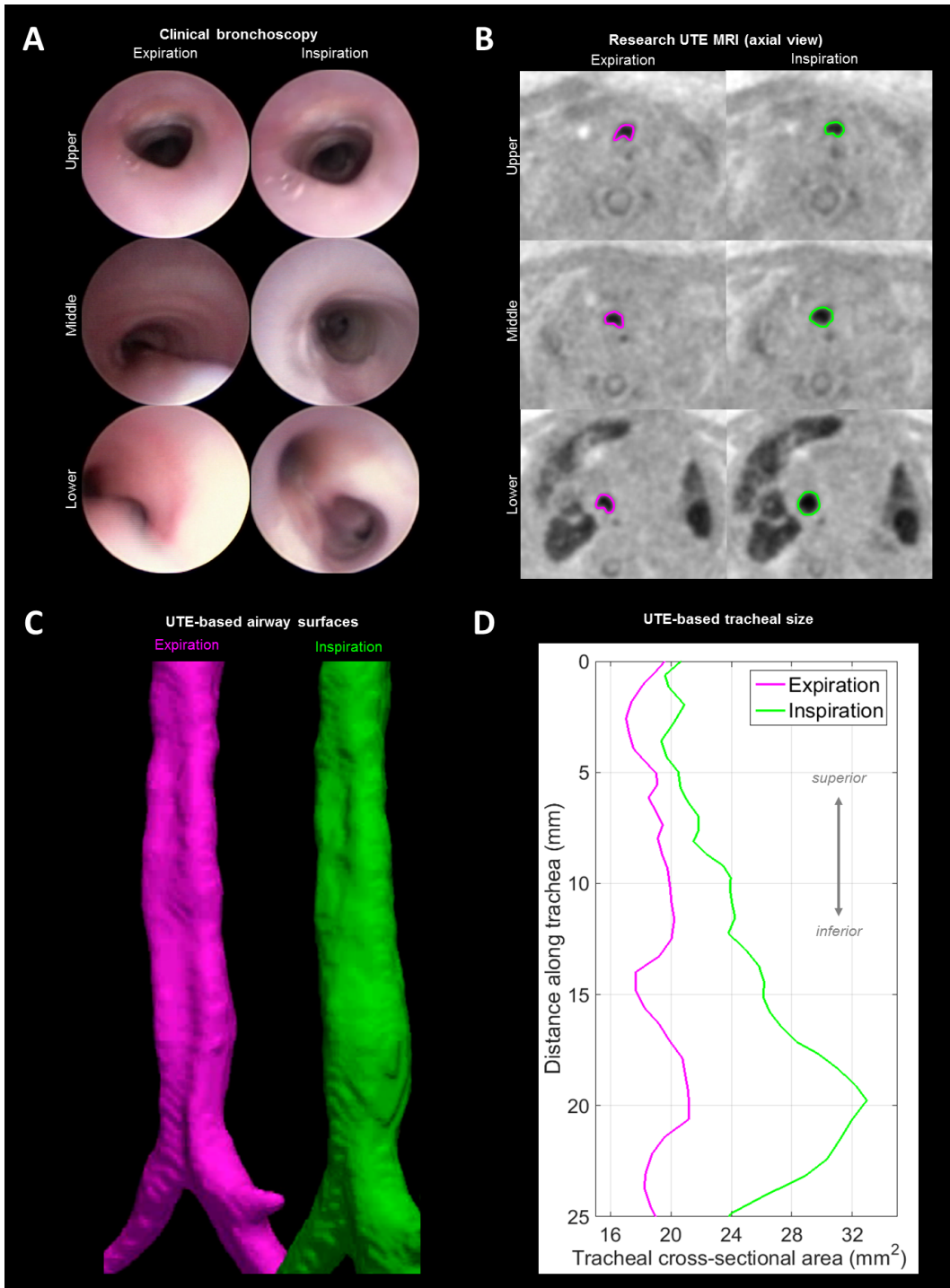
Figure 11.8: Bronchoscopic images (A) of the upper, middle, and lower trachea at expiration and inspiration from a patient with severe BPD and TM, compared with UTE MR images (B) at expiration (pink) and inspiration (green) (tracheas outlined). Corresponding UTE-based airway surfaces (C) and tracheal cross-sectional areas (CSA) (D) throughout the trachea are shown.

Potential for Computational Fluid Dynamics from Gated UTE MRI Computational fluid dynamics (CFD) has been used to determine respiratory effort in both static and dynamic airway pathologies, such as goiter [164, 165, 166], transplanted tracheas [167], and obstructive sleep apnea [168]. In the future, there may be potential to implement CFD-based measurements in diseased neonatal airways with dynamic airway collapse using the respiratory-gated UTE MRI methods described in Section 11.2.4. For dynamic pathologies like TM, a CFD simulation must take into account the motion of the airway anatomy between each respiratory frame [168]. This could be accomplished through non-rigid image registration [169], a process by which images from each respiratory frame are mapped onto the preceding frame. This image registration yields a 4D motion field that then informs how the first frame's airway segmentation will move throughout the rest of the respiratory frames. Using registered images, lung volume segmentation methods detailed in Section 11.2.1, and respiratory rate measurements detailed in Section 11.2.2, breathing flow rates could be calculated and would serve as boundary conditions for CFD simulations, which in previous applications then calculate pressure and velocity fields of the tracheal airflow. From these metrics, the energy necessary to drive flow against the airway resistance can be calculated [164, 165, 166, 167, 168, 170, 171]. In the future, the novel combination of dynamic UTE MRI, image registration, and CFD simulations could provide a measure of the amount of respiratory effort by neonatal patients with dynamic airway collapse.

11.2.5 Motion-robust Structural Imaging of EA/TEF Anatomy

Esophageal atresia (EA) is a relatively uncommon congenital anomaly in neonates, often observed in conjunction with tracheoesophageal fistula (TEF), but there is a lack of safe clinical imaging tools to visualize anatomy prior to surgical repair (see Section 3.3.3). With its inherent robustness to motion, lack of ionizing radiation, lack of sedation requirement, and high, CT-like image resolution, UTE MRI stands as a safe method for pre-operative

evaluation of EA/TEF anatomy, adding value in surgical planning.

While not investigated here, implementation of UTE MRI and the previously described retrospective respiratory method for large airways (Section 11.2.4) may also evaluate tracheal function and efficacy of repair after surgery. Here we show three representative cases in which the motion-robust structural imaging provided by UTE MRI was utilized in three EA/TEF patients.

Subject 1 On his first day of life, a male neonate (born at 38 weeks GA, i.e. term) presented with an inability to pass a nasal gastric tube, and family history showed a sibling diagnosed with EA/TEF. A chest radiograph on day-of-life (DOL) 0 demonstrated a coiling of the feeding tube in the upper esophagus, suggesting of EA, with possible TEF. The chest radiograph also suggested a long proximal esophagus and a short esophageal gap length (Figure 11.9A).

This patient underwent UTE MRI on DOL 1 on a neonatal scanner (Section 5.3) sited in the NICU, yielding structural images with 3D isotropic resolution of 0.7 mm (Figure 11.9B). Tracheoesophageal anatomy was semi-automatically segmented from UTE MR images using a flood-fill algorithm (ITK-SNAP 3.6.0, 3D structure segmentation, University of Pennsylvania and University of Utah [162]), and 3D surface renderings of tracheoesophageal anatomy were visualized with volume-rendered MR images (ParaView 5.4.0, data analysis and visualization) (Figure 11.9C). MRI results indicated the patient had a Type C EA/TEF with an esophageal gap length of approximately 1 cm, consistent with the chest radiograph. MRI also indicated a long, narrow fistula connecting the distal trachea to a caudally displaced distal esophagus, potentially increasing the effective esophageal gap length and increasing the surgical difficulty in connecting the distal and proximal esophagus. MRI also demonstrated a flattening of the trachea where it crosses the innominate artery, suggestive of a degree of tracheomalacia.

Due to the expected repair difficulty presented by the long, narrow fistula observed on MRI imaging, the surgical plan was changed from thoracoscopic to open approach, and the EA/TEF was repaired on DOL 2 by ligation of the TEF and primary anastomosis under mild tension. Bronchoscopy at the time of repair confirmed a TEF originating immediately proximal to the carina.
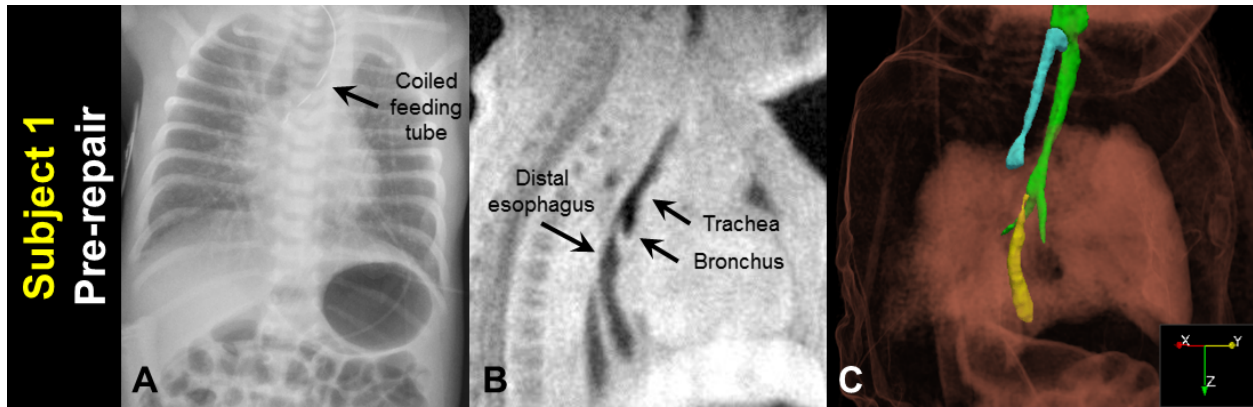
Figure 11.9: Subject 1 before surgical repair: A) a clinical chest radiograph, demonstrating a coiled feeding tube; B) a sagittal MRI slice (3D isotropic resolution of 0.7 mm); and C) oblique view of a MRI-based 3D surface rendering of EA/TEF anatomy (airways in green, proximal esophagus in cyan, distal esophagus in yellow), shown within a volume rendering of the body MR image. Reprinted with permission from [172].

Subject 2   On her first day of life, a female neonate (born at 38 weeks GA) presented with respiratory distress and an inability to pass a nasal gastric catheter. A chest radiograph demonstrated the catheter in the upper esophagus suggesting EA/TEF (Figure 11.10A). This patient underwent UTE MRI on DOL 1 with parameters and image processing identical to Case 1 (Figure 11.10B and 11.10C). MRI results indicated the patient had a Type C EA/TEF with an esophageal gap length of approximately 2 cm. Furthermore, MRI results indicated that the trachea curved posteriorly below the large proximal esophageal pouch, and a significant narrowing of this curved tracheal section (approximately 1 mm^2 cross-sectional area) was indicative of severe static tracheomalacia.

Open repair on DOL 2 demonstrated an esophageal gap of approximately 2.5 cm. The

TEF was ligated but primary esophageal anastomosis was not possible due to tension and the long esophageal gap. EA was repaired on DOL 47. The post-surgical clinical course was complicated by two operations to repair tracheal defects.
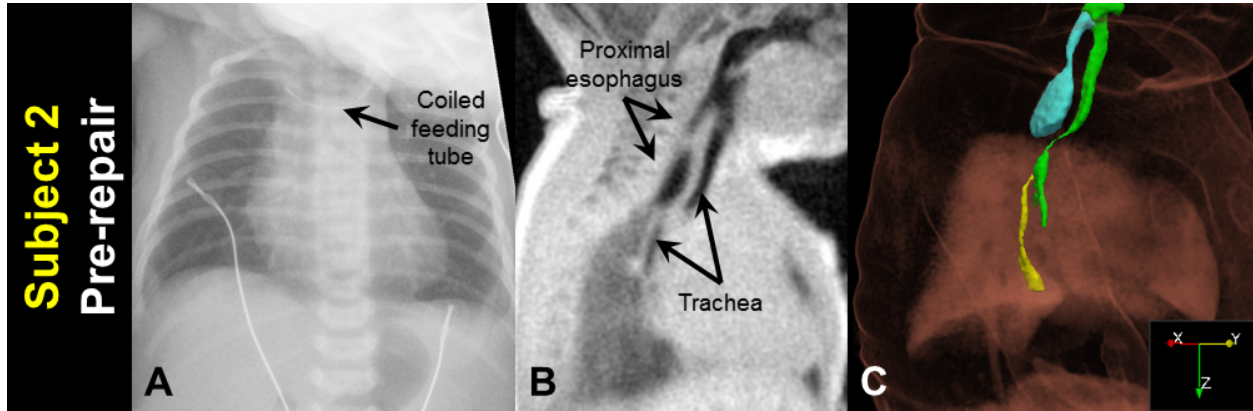
Figure 11.10: Subject 2 before surgical repair: A) a clinical chest radiograph, demonstrating a coiled feeding tube; B) a sagittal MRI slice (3D isotropic resolution of 0.7 mm); and C) oblique view of a MRI-based 3D surface rendering of EA/TEF anatomy (airways in green, proximal esophagus in cyan, distal esophagus in yellow), shown within a volume rendering of the body MR image. Reprinted with permission from [172].

Subject 3 On her fifth day of life, a female neonate (born at 37 weeks GA) presented with poor feeding and significant weight loss since birth. A chest radiograph on DOL 5 demonstrated a coiling of the feeding tube in the upper esophagus, suggesting EA/TEF (Figure 11.11A). This patient underwent UTE MRI on DOL 6 with parameters and image processing identical to Case 1 (Figure 11.11B and 11.11C). MRI results indicated the patient had a Type C EA/TEF with a short esophageal gap length of approximately 1 cm.

Open repair of the EA/TEF was performed on DOL 9. MRI at 12 days after repair (DOL 21) (Figure 11.11E and 11.11F) demonstrated an intact esophageal repair with a non-dilated proximal esophagus, and revealed a compression of the upper intrathoracic trachea by the innominate vein anteriorly and the proximal esophagus posteriorly, compatible with a degree of tracheomalacia.
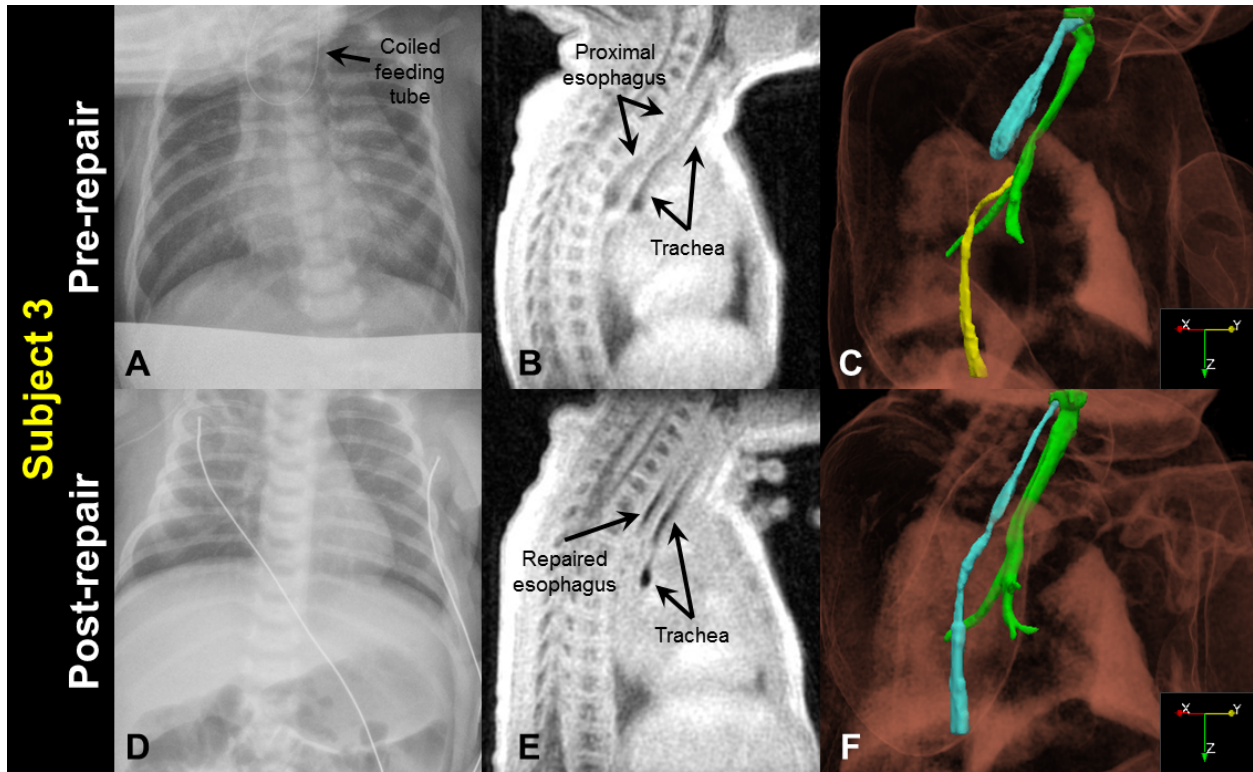
Figure 11.11: Subject 3 before and after surgical repair: A&D) a clinical chest radiograph, demonstrating a coiled feeding tube prior to repair; B&E) a sagittal MRI slice (3D isotropic resolution of 0.7 mm); and C&F) oblique view of a MRI-based 3D surface rendering of EA/TEF anatomy (airways in green, pre-repair proximal esophagus in cyan, pre-repair distal esophagus in yellow, and post-repair esophagus in cyan), shown within a volume rendering of the body MR image. Note the post-repair collapse of the trachea, indicating some degree of tracheomalacia. Reprinted with permission from [172].

Discussion To our knowledge, this is the first visualization and assessment of pre- and post-repair EA/TEF anatomy via MRI. This non-invasive, non-ionizing imaging technique does not require sedation/anesthesia and provides valuable structural information for both pre-operative planning and post-operative evaluation of surgical efficacy and subsequent evolution of the tracheoesophageal anatomy.

In Case 1, chest radiograph suggested a short esophageal gap length, but MRI indicated the effective gap length would be longer due to the caudally displaced distal esophagus and long, narrow fistula. Primary repair was completed in this patient, but the esophageal anas-

tomosis was under mild tension. In Case 2, MRI demonstrated a long esophageal gap and also significant tracheomalacia. Subsequent bronchoscopy and direct surgical visualization confirmed these findings, and the patient experienced multiple esophageal and tracheal complications. In Case 3, MRI clearly demonstrated a short esophageal gap and as a result, the clinical team and parents prepared for a primary esophageal repair. Post-repair imaging in Case 3 suggested an intact repair and, importantly, revealed a mild to moderate degree of tracheomalacia that will require long-term monitoring.

This technique is novel in its use of UTE MRI to assess EA/TEF structures. MRI is ideal for this application due to its tomographic imaging results, without requiring ionizing radiation. Further, UTE MRI is robust to motion due to its radial k-space acquisition scheme (9), and retrospective UTE MRI image reconstruction allows for discarding of image data acquired during periods of patient non-compliance (10), which obviates the need for sedation/anesthesia in a free-breathing neonate. The primary limitation of this MRI application is similar to that of x-ray CT — that the esophagus with a closed lumen can be challenging to segment from surrounding tissue.

This approach has three potential benefits. First, the pre-operative structural information provided by 3D MRI renderings allow for surgical planning with detail not provided by chest radiograph, and not possible via CT without significant ionizing radiation and sedation/anesthesia. Second, this approach allows for improved parental counseling with more thorough information on the infant's condition and potential surgical recovery. Finally, the ability to image patients both before and after repair provides the potential to evaluate surgical efficacy and to identify infants at risk for other complications, such as tracheomalacia and esophageal stricture.

In conclusion, structural MRI can be safely and effectively used to visualize and evaluate the pre- and post-surgical anatomy of neonatal EA/TEF. Ultimately, larger studies are needed to determine the validity and benefit of structural MRI in the evaluation of EA/TEF,

but this initial investigation suggests that this approach has strong potential.

11.2.6 Summary of Retrospective Motion-Tracking Techniques

The combination of 3D radial trajectories and the retrospective tracking of bulk and respiratory motion used here shows robustness to unpredictable and intermittent intervals of bulk motion. The flexibility to retrospectively select valid data in exchange for SNR highlights a strong advantage of radial UTE, particularly if a patient is non-cooperative or if the scan must be stopped early due to patient condition or discomfort. Due to the UTE sequence's motion-tracking capability, it is not necessary for the patient to remain motionless throughout the entire scan in order to obtain diagnostic quality images. The safety risks associated with sedation or general anesthesia in children are uncertain [25]. Moreover, atelectasis appears within 5 min of anesthesia induction [173]. Thus the UTE method provides a significant advantage over the need for sedation or general anesthesia during CT and conventional MRI in order to maintain the requisite quiescence in neonates and young children [26].

As mentioned, previous work describes the use of the k-space center acquired using various radial trajectories as a respiratory-gating signal. Tibiletti et al. processed the self-gating waveform via application of a Butterworth bandpass filter with the passband set to a window of 0.1 Hz around the frequency of the respiratory waveform's local maxima [146]. This filtering method assumes that subjects maintain a constant breathing rate (± 0.05 Hz, ± 3 bpm) over the course of several minutes, notably without any pauses in breathing (i.e. lower frequency components) or changes in the depth of respiration (which will broaden peaks). This is unrealistic for neonates and young children, who as individuals have widely varying respiratory rates (Table 11.6) and breathing patterns. In particular, neonatal lung imaging is restricted by fast respiration (~ 1 Hz) and small diaphragm displacement (on the order of 1 mm; Figure 11.3 shows full diaphragm displacement of $\sim$3-4 mm). Thus any proposed neonatal respiratory gating scheme must be efficient and accurate. Pencil navigators typically

145

utilize 5-mm acceptance windows ($\sim$10% of the anterior-posterior neonatal lung dimension), while low-resolution image navigators do not provide adequate temporal resolution for rapid respiratory rates.

The processing method used in the present work is effective, particularly in subjects whose respiratory rates may vary within a single scan. Unlike some previous self-gating work [156, 174], the gating scheme employed in this work requires no additional data beyond that needed to produce ungated images and maintains a high temporal resolution equal to the scan TR ($\sim$5 ms) before and after filtering. Furthermore, a true steady state is maintained, and data acquisition efficiency is not compromised, since it does not require the insertion of occasional navigator echoes or self-gating lines during acquisition. The algorithms for motion-discarding, respiratory-binning, and image reconstruction have a total run-time of $\leq$5 min, making it feasible for future use in a clinical workflow.

The present work demonstrates an effective and novel technique for retrospective tracking of bulk and respiratory-related motion using radially-acquired 3D UTE MRI, providing diagnostic-quality lung images at different stages of respiration, with validation in an adult cohort. This method is particularly useful for structural pulmonary MRI in non-cooperative patient populations, such as neonates or young children, since it does not require ionizing radiation, sedation, or anesthesia and can accommodate the high respiratory rates and small yet non-negligible amounts of chest wall and diaphragmatic motion presented by the neonate. The practical utility of this method is also demonstrated through its role in quantifying tidal volume, respiratory rates, diaphragmatic motion, dynamic airway collapse, and motion-robust high-resolution structural imaging of abnormal anatomy. Although additional work is needed, the potential for this motion-robust respiratory gating technique is high in the translational assessment of pulmonary disease and development early in life.

11.3 Lung Parenchymal Structures

As previously mentioned, MRI has potential as a technique for longitudinal assessment of pulmonary disorders but currently plays a limited role in clinical diagnosis. Thoracic X-ray CT scans are the current standard for structural lung imaging and have the ability to quantify volumetric mass density of parenchymal tissue with sub-millimeter in-plane image resolution. Whole-lung and regional measures are used in quantitative CT (qCT) of lung density in adults, which has been well validated in numerous studies to spatially map lung density and function [175, 176, 177], as well as identify pathological structures like emphysema [178] or ground glass opacities [179]. However, there are concerns regarding the ionizing radiation exposure associated with CT, particularly for longitudinal monitoring in pediatric and neonatal populations [22, 23, 24]. Further, pediatric CTs often require sedation or anesthesia, which exposes patients to additional medical risks [25]. Thus CT is a suboptimal option for longitudinal diagnostic imaging in the neonatal population, where the time course of pulmonary morbidities is poorly defined and understood; alternative neonatal imaging tools are desirable.

Since MRI is a non-ionizing modality, it is particularly appropriate for assessment of pediatric pulmonary pathologies, especially in light of our developments using raw data from radial UTE MRI acquisitions to yield images in free-breathing neonates without sedation or anesthesia [135, 140]. Quantitative MRI (qMRI) has seen some initial successes using conventional Cartesian sequences to measure regional ventilation in adults [180] and young cystic fibrosis (CF) patients [181] using relative image intensity differences, and to distinguish parenchymal intensities between neonates with and without pulmonary disease, such as bronchopulmonary dysplasia (BPD), using intensity thresholding [124]. Additionally, UTE MRI performs comparably with CT in pediatric CF patients to in radiological scoring of early CF disease; recent studies have demonstrated higher agreement between radial UTE MRI

and CT than with conventional T_1- or T_2*-weighted sequences [136], as well as agreement between different MRI scoring systems for CF [137]. Roach et al. recently demonstrated the comparable disease detection of CT and UTE MRI in ~1-4-year-old CF patients [138]. Using previously validated CF scoring systems for CT and UTE MRI, it was shown that the correlation between the average overall scores between the two modalities was significant in this young population (P < 0.001) [138]. The results of these studies support the integration of UTE MRI into routine clinical exams for more comprehensive evaluation of early CF lung disease.

With our recently developed neonatal UTE MRI techniques [128], we can achieve 3D whole-chest coverage, increased signal-to-noise (SNR) in tissue regions with very short T_2*, reduced sensitivity to motion, and the ability to generate respiratory-gated images at different levels of inflation from a single free-breathing scan, even in non-sedated neonates [135, 140]. Further, with our neonatal UTE MRI post-processing techniques, we can reconstruct images excluding data acquired during periods of bulk motion, which obviates the need for a sedated or anesthetized neonate, regardless of UTE scan duration [135].

11.3.1   Proton Density Regime via UTE MRI

Work throughout Section 11.3.1 has been previously published in a peer-reviewed journal [182], from which content is selectively included here as per copyright regulation.

At current clinical field strengths, the typical echo time (TE) of a UTE sequence (~0.2 ms) is well below parenchymal T_2*. The low flip angles (FA) used in the present UTE sequence (typically 5°), combined with the short TE, provide images with strong proton-density weighting. While MRI-measured intensity alone does not provide an absolute measure of volumetric mass density, the intensity can be calibrated by a reference tissue of known density. For example, muscle tissue, which has a density approximately equal to that of water on proton density-weighted images [183], can be used as a reference tissue within the field

of view of a typical thoracic volume image. Thus, parenchymal UTE MRI intensity in the lungs normalized to muscle can be expected to yield values comparable to true density [115]. Early quantifications via UTE MRI in healthy subjects yielded lung density values from measurements of "water content" [129], and in COPD subjects showed similar emphysema indices to CT [184].

In the following work, we demonstrate that UTE MRI can quantify volumetric mass density of neonatal lung parenchyma similar to that achievable with CT, with pathological variations in parenchymal proton density analogous to electron densities as measured by CT. Because infant CTs are used sparingly, and may involve sedation or anesthesia, parenchymal disease evaluation via UTE MRI has the potential for translational impact.

Study Subjects: Neonatal research MRI exams were performed with Institutional Review Board (IRB) approval and informed parental consent. Clinically-ordered chest CT exams were retrospectively obtained for research with IRB approval and waived consent. A prospective MRI cohort of pulmonary control subjects consisted of five neonatal patients recruited from the NICU and primarily diagnosed with seizures or gastrointestinal issues, but with no suspected lung disease. Further clinical information for the cohort is given in Table 11.7, including sex, age, respiratory support, administration of sedation, and administration of contrast at MRI. All subjects' heart rates and SpO_2 levels were monitored by NICU staff throughout each exam.

Clinically-ordered CT images were obtained and reviewed retrospectively in nine separate, similarly-aged control subjects. This retrospective control cohort was comprised of infants who had clinically-ordered CT scans, primarily to rule out lung involvement after rare childhood cancers; lung morbidities were subsequently ruled out, which supports their role as control subjects for this study. Further clinical information for this cohort is given in Table 11.7. A separate, prospective, diseased neonatal cohort was comprised of five NICU

149

Cohort	Cohort Size	Sex	Age at MRI (wk): Chronological / PMA	Respiratory Support	Sedation	Contrast
MRI controls	5	4F/1M	4±2 / 39±2	Free-breathing (n=5)	No (except clinically-indicated for n=1)	N/A
CT controls	9	8F/1M	11±9 / 49±9	Free-breathing (n=6); Unknown (n=3)	Yes (n=1); No (n=5); Unknown (n=3)	No (n=9)

Table 11.7: Clinical details at imaging for pulmonary-control neonatal subjects that were imaged with prospective research UTE MRI and retrospective clinical CT, in order to compare normalized lung image intensities to CT volumetric densities, to validate the UTE MRI proton density regime.

patients (Subjects A-E) with various pulmonary morbidities that received both a research MRI exam and a clinical CT exam (mean PMA at MRI = 41 ± 2 wk, mean PMA at CT = 43 ± 4 wk). Clinical information for each of the subjects at MRI and CT is given in Table 11.8.

MR Imaging Details: All MR imaging was performed on a unique, small-footprint, neonatal 1.5T MRI system with a quadrature body coil (see Section 5.3 for details) using a neonatal 3D radial UTE acquisition sequence with RF spoiling [128, 140] (see Section 9 for details). Typical MRI acquisition parameters were: TE = 200 μs; TR = 4.4–5.2 ms; FA = 5° or 10°; FOV = 18 cm; 3D isotropic resolution = 0.70-0.86 mm (in-plane isotropic pixel resolution identical to slice thickness); scan time = ∼10-16 min; and number of radial projections = ∼120,000–200,000. In some cases, the number of acquired projections was reduced due to exam time limitations. Flip angle values were chosen to yield very little difference in T_1-weightings of lung and muscle tissue (see Section 11.3.1 for further discussion). Using our previously described technique (Section 10) [135], images were reconstructed with retrospective respiratory gating to end-expiration with 50% acceptance windows, after discarding data acquired during bulk motion intervals, with a total run-time of ≤5 min. MRI exams included other non-UTE scans and lasted a total of ∼60-90 min. However, if shortened to include only a localizer and a UTE scan, the total exam time would be ∼15-20 min.

CT Imaging Details: Protocols for CT imaging varied as clinically indicated, without consideration of potential research design or standardization of acquisition methodology, and thus were necessarily subject to inconsistencies in acquisition parameters and inflation levels. CT imaging was performed on two different scanners: either a Toshiba Aquilion ONE (Toshiba America Medical Systems, Tustin, CA; 3 of 9 control subjects and 5 of 5 diseased subjects); or a GE Healthcare LightSpeed 16 (6 of 9 control subjects). In-plane axial isotropic

Subject (Sex)	Respiratory Diagnosis	Time between scans (days)	Chronological Age (wk) (MRI / CT)	PMA (wk) (MRI / CT)	Resp. Support (MRI / CT)	Sedation (MRI / CT)	Contrast (MRI / CT)
A (M)	severe BPD	77 (MRI first)	13 / 24	39 / 50	Ventilated (tidal) / Ventilated (expiratory breath-hold)	Yes (clinically-indicated) / Yes (procedurally-ordered)	NA / No
B (F)	PIG	7 (MRI first)	6 / 7	40 / 41	None / None	No / No	NA / No
C (M)	Poland syndrome, with under-developed left chest wall and rightward mediastinal shift	5 (CT first)	3 / 2	44 / 43	None / None	No / No	NA / Yes
D (M)	CLD, suspected PIG	1 (CT first)	9 / 9	43 / 43	None/ Ventilated (expiratory breath-hold)	No /Yes (procedurally-ordered)	NA / Yes
E (M)	EA/TEF, with right-sided pneumonia	0 (MRI first)	2 / 2	40 / 40	None/ None	No / No	NA / Yes

Table 11.8: Clinical details at imaging for pulmonary-diseased neonatal subjects that were imaged with prospective research UTE MRI and retrospective clinical CT, in order to compare normalized lung image intensities to CT volumetric densities.

resolution was 0.26-0.39 mm, with a slice thickness of 2.00-3.78 mm. Side-by-side CT and

UTE MR image comparisons for the five diseased subjects are shown in Figure 11.12.
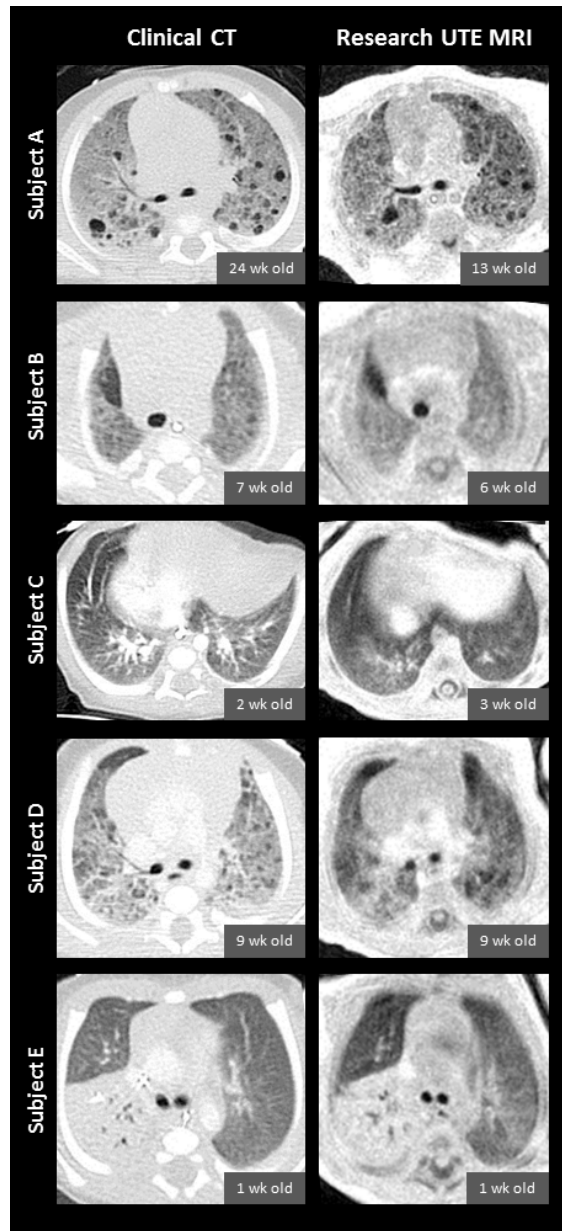
Figure 11.12: Slice-matched images comparing clinical CT scans (left column) and research UTE MRI scans (right column) in five diseased subjects (from top to bottom: Subjects A through E). CT and MRI exams were typically performed at different time-points for each individual subject; chronological ages at each subject's CT and MRI exams are provided. CT images have an in-plane isotropic pixel resolution of 0.29-0.39 mm with a slice thickness of 2.0-3.8 mm, and UTE images have an in-plane isotropic pixel resolution of 0.70 mm with a reconstructed slice thickness of 2.8 mm (reconstructed at 4x thicker than the nominal UTE z-resolution of 0.70 mm in order to optimize slice-matching). Note that contrast was administered for the clinical CTs of Subjects C, D, and E, and that the spinal-column appearance is influenced by components with different T_1 and T_2*, similar to lung. Reprinted with permission from [182].

Whole-lung Analysis: Whole-lung segmentations were generated semi-automatically from UTE MRI and CT images of control subjects using Amira (FEI Visualization Sciences Group). Region-growing segmentation was used, with manual guidance and editing to avoid intensity-based bias. Major vessels and atelectasis were excluded from segmented parenchymal regions. UTE-measured lung image intensities were calculated in arbitrary units (au) normalized to chest wall muscle intensity (averaged over multiple ROIs throughout the 3D FOV), meant to be analogous to macroscopic mass density. CT-measured lung densities were calculated via the following conversion:

$$\rho = \frac{I + 1000}{1000},\tag{11.1}$$

where ρ is the volumetric density in g/cm^3 and I is the CT pixel image intensity in Hounsfield units (HU). Water acts as a reference, with 0 HU equivalent to 1 g/cm^3. T_1 and T_2* corrections were applied to whole-lung UTE intensities, using relaxation time values measured for adults at 1.5T: $T_{1,lung} = 1.2$ s [185], $T_{1,muscle} = 1.1$ s [186], $T_2*_{lung} = 2$ ms [119], and $T_2*_{muscle} = 30$ ms [120]. Whole-lung mean densities from the CT cohort were compared to whole-lung mean image intensities from the UTE cohort (with and without T_1 and T_2* corrections).

Mean UTE-measured whole-lung parenchymal image intensity in the MRI control cohort was 0.51 ± 0.04 au when uncorrected for T_1 and T_2* (0.56 ± 0.05 au when corrected). Mean CT-measured whole-lung parenchymal density in the CT control cohort was 0.44 ± 0.09 g/cm^3 (Figure 11.13, left). Both the uncorrected and corrected UTE technique measured a slightly higher intensity value than the CT-measured density (P = 0.062 and 0.062, respectively). The 95%-CI of the difference of the means were [-0.159, 0.029] and [-0.210, -0.020] for uncorrected and corrected UTE values, respectively.

Anterior-Posterior Gradient Analysis: For each individual control subject, a mean anterior-posterior (A-P) lung gradient of normalized image intensity (UTE; uncorrected for
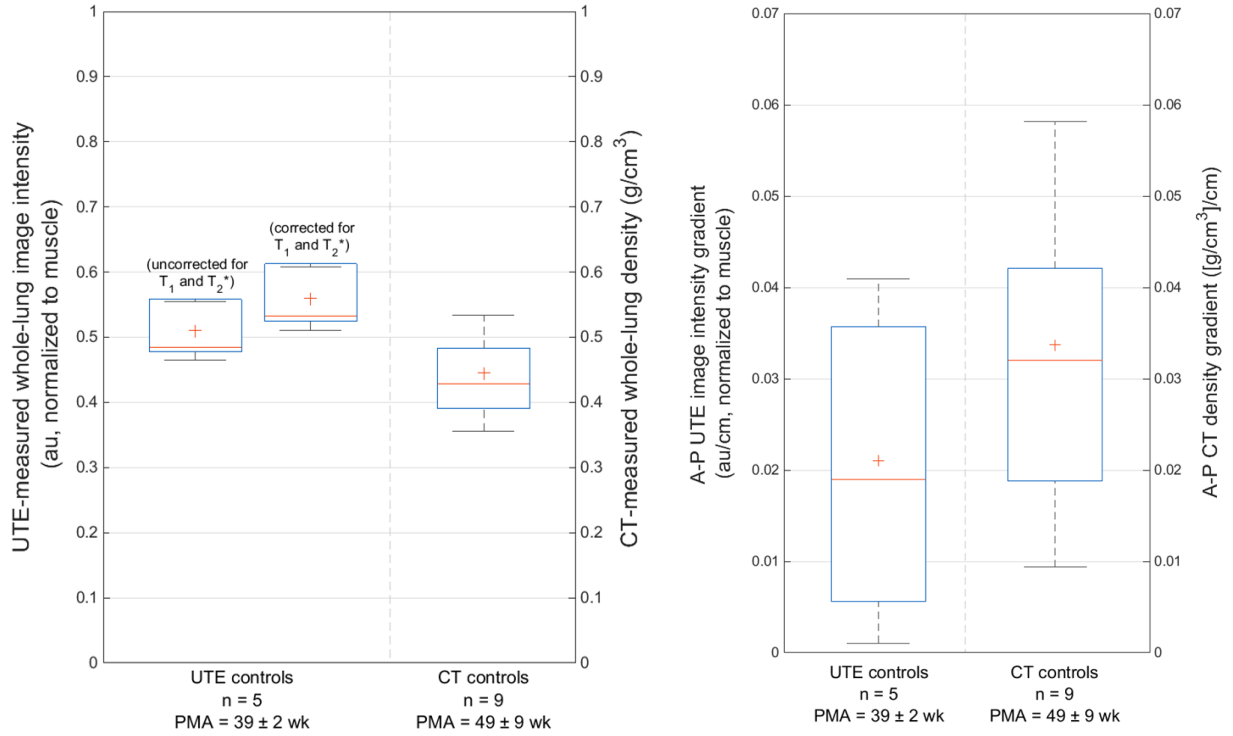
Figure 11.13: Left: A comparison of mean normalized UTE-measured image intensity (0.51 ± 0.04 au when uncorrected for T_1 and T_2*, left; 0.56 ± 0.05 au when corrected, middle) and mean CT-measured density (0.44 ± 0.09 g/cm^3, right) from whole-lung parenchyma in control neonatal subjects. Both uncorrected and corrected UTE-measured intensities measure a slightly higher value than CT-measured density (P = 0.062 and 0.062, respectively). Note that the CT control cohort was on average 10 weeks older than the MRI control cohort; post-menstrual ages (PMA) of both cohorts are provided (mean ± standard deviation). Right: A comparison of mean anterior-posterior (A-P) gradients in neonatal subjects with normalized UTE image intensity (0.021 ± 0.020 au/cm, left) and CT density (0.034 ± 0.024 [g/cm^3]/cm, right) (P = 0.351). Reprinted with permission from [182].

T_1 and T_2*, detailed in Discussion) or density (CT; g/cm^3) was calculated from the slopes of six A-P lines measured on one slice near the carina (three lines spaced from the lateral lung toward the mediastinum on both left and right lungs). For both the UTE and CT cohorts, a mean A-P gradient value was calculated from each subject's individual mean gradient value. Major vessels and atelectasis were excluded from measurements.

The mean A-P gradient for UTE-measured image intensity was 0.021 ± 0.020 au/cm and for CT-measured density was 0.034 ± 0.024 [g/cm^3]/cm (Figure 11.13, right) (P = 0.351).

The 95%-CI of the difference of the means was [-0.002, 0.004].

ROI Density Analysis: Approximately 33 (range 28-37) ROIs were selected throughout the lungs from each of the five diseased subjects' axial CT images, with no anatomical location preference, but spanning low- to high-density regions of both pathological and normal tissue. Each CT ROI had relatively homogeneous density, with a mean ROI standard deviation of 0.10 g/cm^3. ROIs from diseased patients' CT images (slice thickness = 2.0-3.8 mm) were position- and slice-matched to ROIs in axial UTE images with a slice thickness of 2.8 mm (reconstructed at 4x thicker than the nominal UTE z-resolution of 0.70 mm for improved slice-matching). Each UTE ROI had also had relatively homogeneous intensity, with a mean ROI standard deviation of 0.08 au. UTE ROI intensities (uncorrected for T_1 and T_2*) were normalized to chest wall muscle and compared to CT ROI densities (g/cm^3).

Representative slice-matched ROIs of various densities are shown in Figure 11.14. Significant Spearman correlations were observed from linear regression analysis between UTE-measured image intensity and CT-measured density for parenchymal ROIs in each of the five diseased subjects ($P < 0.007$ for all subjects) (Figure 11.15). Further linear fit details (R^2, slope, and ranges of UTE-measured intensity and CT-measured density) are given in Table 11.9.

ROI Classification Analysis: ROIs on UTE MRI and CT images from all five diseased subjects were evaluated by a radiologist (22 years of experience). Evaluation included classification of radiological findings within the ROI (six classifications: air trapping, air trapping/cysts, normal tissue, mixed cysts with ground glass opacities, ground glass opacities, and airspace opacities), as well as a degree of confidence in radiological assessment (score of 1-5: 1-none, 2-low, 3-moderate, 4-good, 5-high). All images were anonymized and evaluated in random order; UTE MRI and CT images for a single patient were read separately. For

Subject	Slope	P-value	R^2	Range of UTE-measured normalized image intensity (au, uncorrected)	Range of CT-measured density (g/cm³)
A	1.26	< 0.001	0.81	0.19-0.73	0.21-0.88
B	0.88	< 0.001	0.79	0.29-0.88	0.25-0.82
C	0.54	0.007	0.23	0.40-0.67	0.45-0.80
D	1.09	< 0.001	0.82	0.22-0.84	0.26-0.94
E	0.91	< 0.001	0.73	0.27-1.06	0.35-1.15

Table 11.9: Linear fit and Spearman correlation details for comparisons of UTE-measured image intensity (au) and CT-measured density (g/cm³) in regions of interest from diseased subjects (see also Figure 11.15).

each of the six radiological classifications, mean UTE ROI image intensities (uncorrected for T_1 and T_2*) and mean CT ROI densities were compared.

Representative ROIs from each radiological classification are shown in Figure 11.14. 99% and 100% of ROI classifications on UTE and CT images, respectively, were scored with a confidence level of 3 ("moderate") or greater (score from 1-5). A kappa test demonstrated moderate agreement between UTE-based classifications and CT-based classifications ($\varkappa =$ 0.57). Mean UTE ROI image intensities and mean CT ROI densities for each of the six classifications are shown in Table 11.10 and Figure 11.16, and relative differences of the means and 95%-CI of the difference of the means are shown in Table 11.10. We note that the differences between UTE intensities and CT densities were relatively small in each of these radiological classifications (range of 4%-25%). Further, the 95%-CI of the difference of the means contained zero in regions of air trapping, air trapping/cysts, and mixed cysts with ground glass opacities (see Table 11.10).

Statistical Tests: Whole-lung mean image intensities from the UTE control cohort and mean densities from the CT control cohort were compared by a Mann-Whitney U test and 95%-confidence intervals (CI) of the difference of means. Similar statistical evaluations were
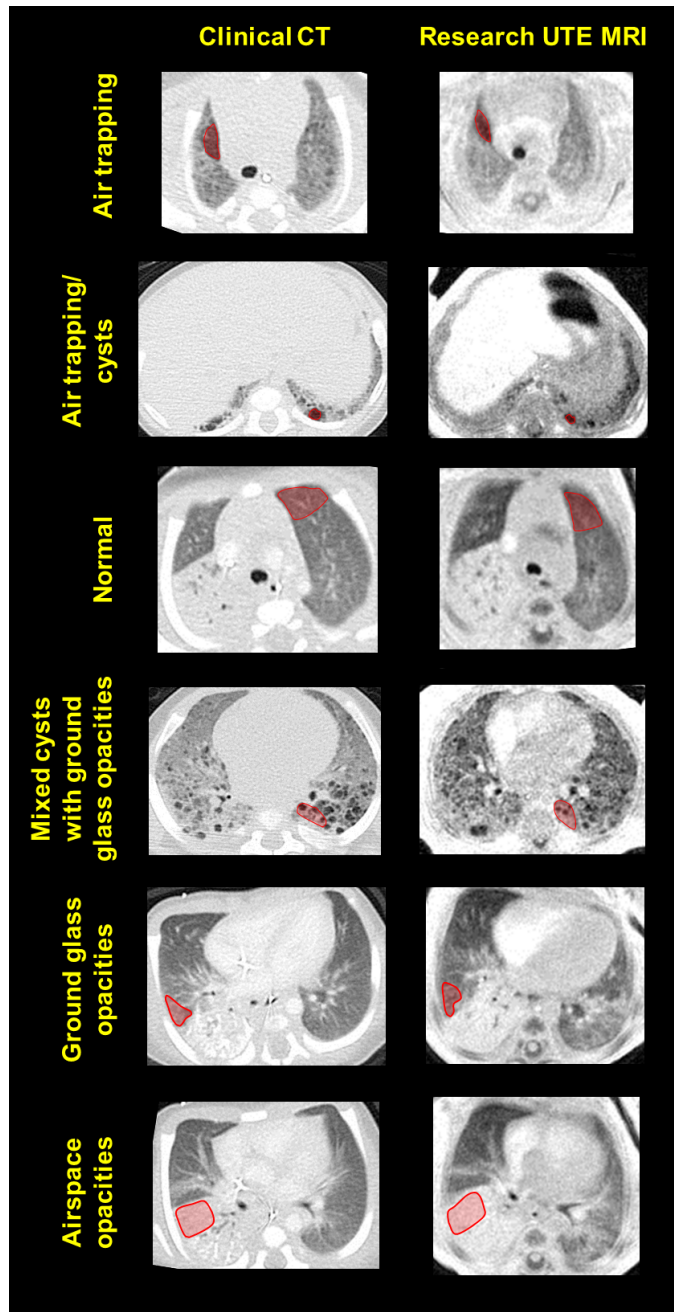
Figure 11.14: Representative regions of interest (ROIs – red overlay) of six radiological classifications with varying densities on slice-matched CT images (left column) and UTE MR images (right column) from neonates with pulmonary morbidities. From top to bottom: air trapping, air trapping/cysts, normal tissue, mixed cysts with ground glass opacities, ground glass opacities, and airspace opacities. Reprinted with permission from [182].
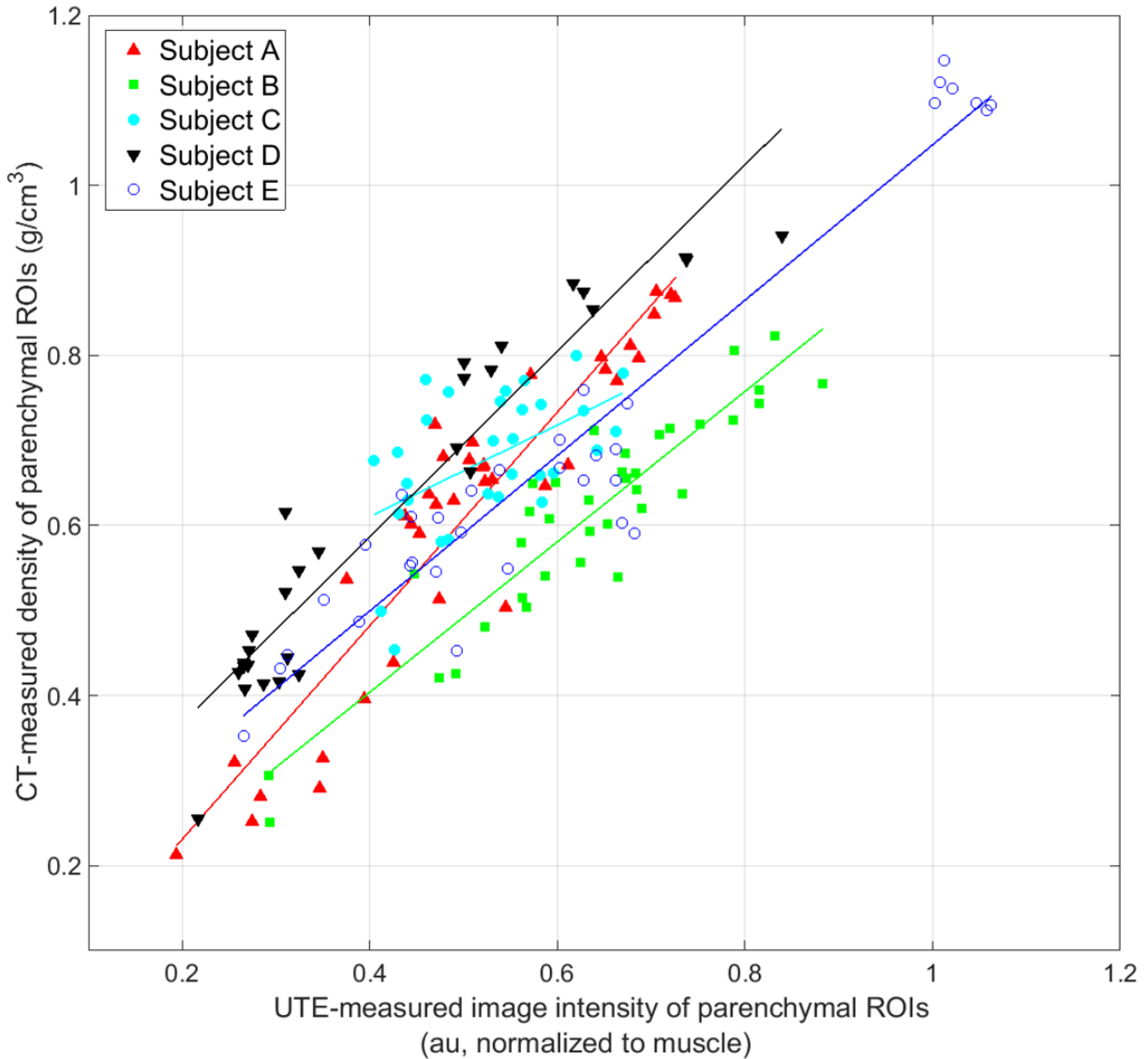
Figure 11.15: Comparisons of UTE-measured normalized image intensity (au; uncorrected for T_1 and T_2*) and CT-measured density (g/cm^3) in ∼33 regions of interest (ROIs) in diseased subjects with various pulmonary issues (red triangles for Subject A; green squares for Subject B; cyan circles for Subject C; black inverted triangles for Subject D; and blue hollow circles for Subject E). All Spearman correlations from linear regression analysis are significant (P < 0.001 for Subjects A, B, D, and E; P = 0.007 for Subject C), with slightly varying linear fits. Reprinted with permission from [182].

used for A-P gradient values from the UTE and CT control cohorts. In each diseased

subject, ROI UTE-measured intensities and CT-measured densities were compared using

Radiological classification	Mean UTE ROI image intensity (au; normalized to muscle, uncorrected for T_1 and T_2*)	Mean CT ROI density (g/cm^3)	Relative difference of means	Difference of means [95%-CI]
Air trapping	0.31 ± 0.06	0.39 ± 0.10	23%	0.079 [-0.010, 0.168]
Air trapping/cysts	0.33 ± 0.08	0.34 ± 0.10	4%	0.012 [-0.083, 0.108]
Normal	0.50 ± 0.12	0.59 ± 0.11	17%	0.092 [0.055, 0.129]
Mixed cysts with ground glass opacities	0.53 ± 0.09	0.68 ± 0.14	25%	0.153 [-0.037, 0.343]
Ground glass opacities	0.62 ± 0.11	0.72 ± 0.09	15%	0.098 [0.059, 0.137]
Airspace opacities	0.90 ± 0.21	1.11 ± 0.02	21%	0.208 [0.056, 0.359]

Table 11.10: Mean UTE ROI image intensities and CT ROI densities for six radiological classifications, with relative differences of the means and 95%-confidence intervals (CI) of the difference of the means (see also Figure 11.16).

Spearman correlations. The level for statistical significance was set at P < 0.05. A kappa test was used to assess inter-method reliability between UTE-based and CT-based radiological classifications for all ROIs from all patients. For each classification, relative differences of the means and 95%-CI of the difference of the means were calculated.

Discussion: Our results demonstrate the feasibility of using pulmonary UTE MRI to quantify lung parenchymal density in non-sedated, free-breathing neonates, and importantly indicate that on a linear scale from zero density (i.e. air, $\sim$0 g/cm^3) to solid tissue density (i.e. muscle, $\sim$1 g/cm^3), densities measured from CT and normalized UTE MRI yield ap-
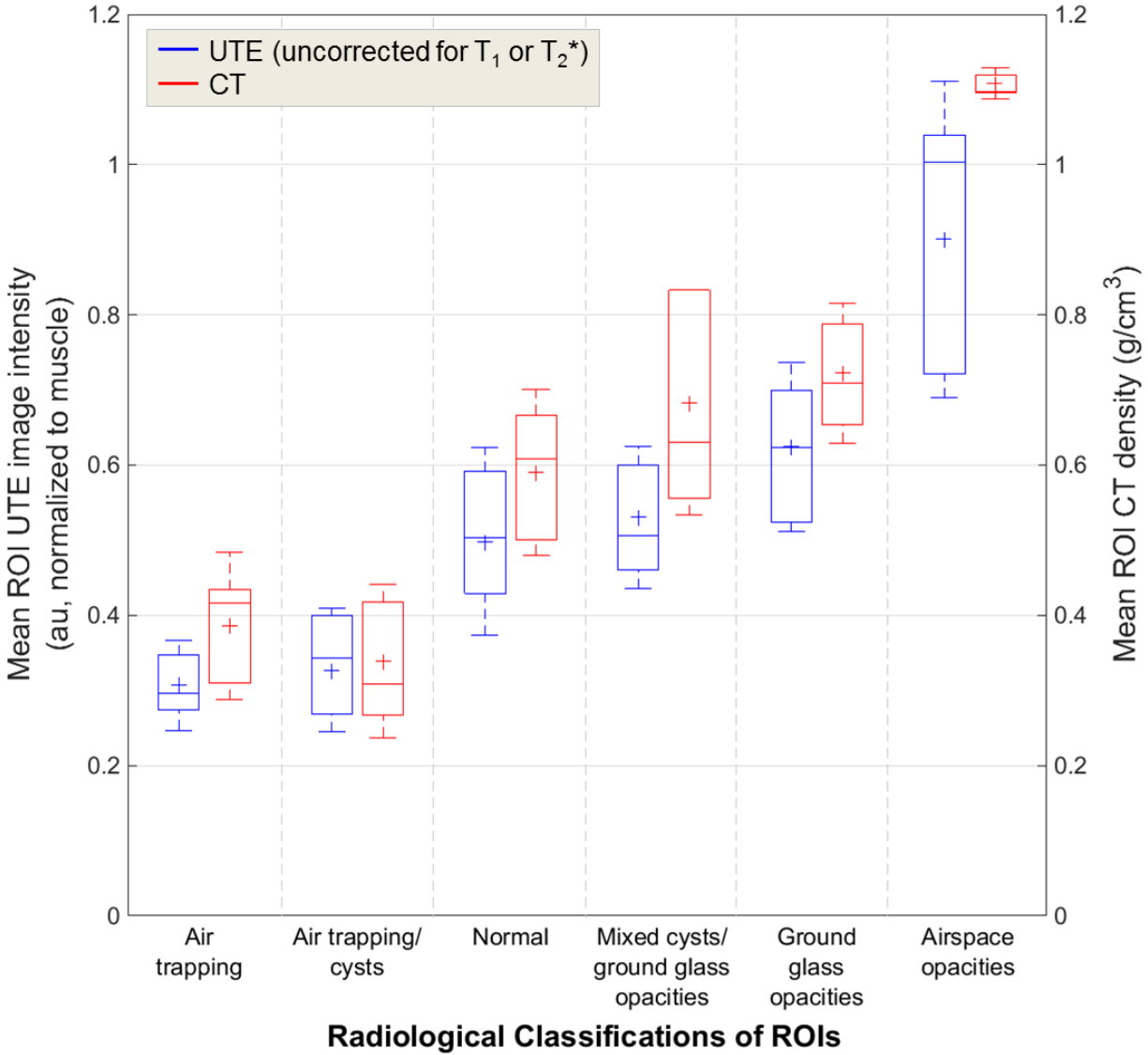
Figure 11.16: Comparisons of mean UTE ROI image intensities (au; uncorrected for T^1 or T^{2*}) and mean CT ROI densities (g/cm^3) for each of the six radiological classifications. Relative differences between mean UTE intensity and mean CT density were small (range of 4%-25%). Reprinted with permission from [182].

proximately the same value. To our knowledge, this work represents the first results that show a relationship between CT-measured lung density and UTE-measured normalized lung image intensity in pediatric subjects. Further, this work demonstrates that specific radiological pathologies present with similar CT-measured densities and UTE-measured intensities,

indicating that similar diagnostic information can be obtained from both imaging modalities. More importantly, the relative densities of these radiological pathologies within a given UTE MRI slice are consistent to that seen on CT and thus create recognizable pathologies for radiologists and clinicians similar to CT.

Correlations between the two density measures were particularly strong in diseased patients with a wide range of density variation within the lungs. These data suggest that UTE MRI and CT can provide similar measures of density in patients with a range of pediatric lung pathologies. We note that Subject C had a more narrow range of tissue densities than the other subjects, due to the less heterogeneous nature of this subject's pulmonary pathologies (Poland syndrome), and so has a higher (though still significant) P-value and a slope that deviates further from unity than the other subjects' slopes.

Future work may evaluate the potential for UTE MR images with CT-like lung parenchymal densities to diagnosis and assess neonatal lung disease. Compared to traditional MRI sequences with comparatively long TE values (such as a gradient echo), UTE MRI provides increased intensity in tissues with short T_2*. This UTE-specific capability offers the potential for improved visualization of regions of lucency in diseased neonatal lungs, compared to conventional Cartesian MRI, through increased contrast between short-T_2* tissue and true low-density tissue. Using pointwise encoding time reduction with radial acquisition (PETRA) UTE MRI, a previous study of CF disease scoring and assessment of lung morphological changes in pediatric and adult patients (9-48 years old) found agreement between CT and MRI methods [136]. By combining the present work's UTE MRI methods with a reader-based scoring system, such as the Ochiai score used for BPD [124, 187], there is potential to grade the severity of individual pathological features, such as hyperexpansion, emphysema, or fibrous/interstitial abnormalities, which could play an important role in the evaluation of therapeutic interventions and individual patient management (see Section 11.3.2). Furthermore, recently developed techniques for retrospective respiratory gating

of free-breathing neonates using UTE MRI [135] can generate images at different points of the respiratory cycle, providing the potential for trapped-gas assessment. This also allows for the possibility of quantifying regional ventilation in neonates, similar to work performed in asthmatic and emphysematous adults using MRI [180, 188] and in older infants with CF using CT [181].

Unlike CT, MR intensities from parenchyma and muscle is influenced by proton density as well as the T_1- and T_2*-weighting specific to each tissue. The T_1 values of normal neonatal lung parenchyma and muscle have not been reported. However, these values in neonates are likely similar to adult values ($\sim$1.1-1.2 s) [185, 186], and the relative neonatal lung and muscle T_1-weightings accrued with the small flip angles in this work are likely very similar, yielding very little change to the normalized UTE MRI intensity with a T_1 correction (to $\sim$0.001%, using adult values). Likewise, the T_2* of normal neonatal lung parenchyma has not been reported but is likely similar to (or longer than) the adult value ($\sim$2 ms at 1.5T) [119]. At the short echo times inherent to UTE acquisitions, T_2* weighting in both lung and muscle is small (with correction, UTE image intensity changes $<$10% and $<$1% for lung and muscle, respectively).

Further, diseased neonatal lung tissue is very heterogeneous, and relaxation times likely vary widely between regional pathologies (cysts, alveolar simplification, normal tissue, fibrosis, opacities, edema, etc.). Thus T_1 and T_2* corrections may be implemented most effectively on a regional basis and would require mapping of relaxation constants in different pathological conditions; such analysis could be the subject of future work. Even so, these results show strong associations between CT densities and normalized UTE image intensities, demonstrating that UTE MRI is effective at providing a primarily proton-density weighting without the need for specific localized corrections.

This study has limitations related to the nature of the clinical CT data. As clinical protocols changed slightly in response to individual patient management, subjects were imaged

under various levels of lung inflation, on two CT scanners from different manufacturers, with slightly different reconstructions, and with varying image resolutions. Notably, whole-lung parenchymal density analysis was performed during either free-breathing (n = 6) or at unknown inflation levels (n = 3) for the CT control cohort, compared to only end-expiration (n = 5) for the UTE MRI control cohort. The generally lower level of inflation at MRI may be responsible for the slightly increased whole-lung UTE intensity compared to whole-lung CT density, although we note that the variation in CT whole-lung density was itself larger than the difference between CT and MRI. Differences in the slopes between CT-measured density and UTE-measured intensity in ROIs of diseased subjects may also be related to the lack of well-controlled inflation levels at clinical CT. Additionally, the elevated CT densities for Subjects C-E likely stem from the use of contrast at clinical CT, which has been shown to increase parenchymal CT intensity in emphysematous adults [189]. This may also be responsible for the larger differences between MRI and CT in ROIs classified as normal, with ground glass opacities, and with other airspace opacities, since the relative amount of contrast is more variable in such tissue than in cystic or more lucent regions.

Likewise, the time-points at which diseased subjects' clinical CTs were obtained were not under control of the research team, and thus MRI scans were acquired on different days than CT scans (with the exception of Subject E, whose MRI and CT scans were performed on the same day); research CT scans are typically not performed in this patient population. In one case (Subject A), the CT exam was performed 11 weeks after the MRI exam. Evolution or resolution of lung pathology during this time could lessen the correlation between the measurements in a given ROI. Similarly, the CT control cohort was slightly older than the MRI control cohort (on average, 7 weeks older in chronological age and 10 weeks older in PMA). We further suspect that the mean whole-lung CT-measured density is slightly lower than UTE-measured image intensity in small part because of the decrease in lung density after birth as infants age [190]; CT-measured lung density is expected to decrease

by approximately 0.01 g/cm^3 between a chronological age of 4 weeks (mean age of the MRI cohort) to 11 weeks (mean age of the CT cohort) [190]. Additionally, because structural characteristics of lung disease evolve with time, there was a small degree of subjectivity in manual ROI selections on CTs and UTE MRIs acquired at different time-points. However, this was mitigated through matching of axial slices and in-plane anatomical positions of CT and UTE ROIs, in addition to a large number of ROIs per patient.

In conclusion, UTE MRI can be used to quantify both whole-lung and regional lung parenchymal density, providing tissue density quantification and visualization of pathologies similar to that achievable with CT. Unlike neonatal pulmonary CT, UTE MRI is non-ionizing, can be performed during free-breathing, and does not require sedation or anesthesia, which makes it a strong and safe choice for repeated assessment of neonatal lung disease in clinical settings. UTE MRI offers the potential to longitudinally image the regional progression of pulmonary pathologies like fibrosis, bronchiectasis, edema, and alveolar simplification. In the future, this quantification may aid in identifying individual phenotypes of and personalizing clinical therapies for neonatal lung disease.

11.3.2 MRI Scoring of BPD and Correlations to Clinical Outcomes

Background: As discussed previously (see Section 3.3.1), BPD is a serious (yet little-understood) neonatal pulmonary condition often associated with premature birth. As a non-ionizing modality, magnetic resonance imaging (MRI) is particularly appropriate for the repeated radiological assessment of pulmonary pathologies associated with BPD [191]. Indeed, quantitative MRI (qMRI) (performed by our group) has seen some initial successes using conventional Cartesian sequences to distinguish parenchymal intensities between neonates with and without BPD using intensity thresholding [124]. Since a typical gradient echo sequence implements an echo time (TE) on order with the parenchymal T_2* ($\sim$2 ms at 1.5T) [17], such acquisitions tend to perform adequately in visualizing in high-density tissues, which

have long T_2* values relative to TE, and suffer to some degree in visualizing normal or hypodense (alveolar simplification, emphysema, cysts, etc.) lung tissue, which have short T_2* values relative to TE.

This work can further be refined using a neonatal ultrashort echo time (UTE) radial acquisition sequence (developed and implemented by our group and collaborators) [128, 135, 140], which address many of the historical challenges to pulmonary MRI (e.g., low proton density of the lung parenchyma [115], short parenchymal T_2* ($\sim$2 ms at 1.5T) [119], and image artifacts from cardiac, respiratory, and bulk motion, all of which are significant considerations in a rapidly-breathing, non-compliant neonate).UTE MRI implements TE values much shorter than the parenchymal T_2* (typically less than a few hundred microseconds) to combat the rapid proton signal decay and has the added value of relative robustness to motion artifacts [140]. Because of this relatively short TE value (TE $<T_2*$), UTE MRI is ideal for visualizing normal or hypodense lung tissue. Further, UTE MRI has recently been shown to accurately quantify neonatal parenchymal density by direct comparison to CT [182], and as shown previously, sedation is not necessary to obtain high-quality neonatal pulmonary MR images using both gradient echo and UTE sequences [124, 135, 140, 182].

In this work, both gradient echo and UTE MRI were performed for comprehensive diagnostic quality images that could be used in future clinical studies, with the hypothesis that pulmonary neonatal MRI can predict short-term respiratory outcomes for infants diagnosed with BPD and can provide image-based phenotyping of disease severity. Since pulmonary MRI can be used safely for serial assessment, this technique has the potential to define the underlying structural abnormalities and time-course of neonatal pulmonary disease associated with extremely preterm birth.

Methods:

Study Subjects Subjects were recruited from the NICU with Institutional Review Board (IRB) approval and informed parental consent. Inclusion criteria for BPD patients included: history of prematurity ($<$37 weeks gestational age, GA); clinically diagnosed BPD; and $\leq$48 weeks PMA at MRI. Inclusion criteria for control patients included: full term birth ($\geq$37 weeks GA); no clinically suspected or apparent lung disease; and $\leq$48 weeks PMA at MRI. Exclusion criteria for BPD patients included: suspected muscular dystrophy or neurologic disorder that may affect lung development; significant genetic or chromosomal abnormalities that may affect lung development; evidence of any respiratory infection at the time of imaging; and standard MRI exclusion criteria. Exclusion criteria for control patients were the same as for BPD patients, with the addition of evidence of congenital diseases that may affect lung development (such as congenital heart disease, congenital diaphragmatic hernia, or other systemic pulmonary disease).

The study cohort was comprised of 42 neonates with varying levels of BPD severity, enrolled in a convenience sample distribution: 20 with severe BPD; 6 with moderate BPD; 7 with mild BPD; 4 preterm controls who were born at $<$37 weeks GA but were not diagnosed with BPD; and 5 term controls who were born at $\geq$37 weeks GA and were primarily diagnosed with seizures or gastrointestinal issues. Further demographic information for the cohort is given in Table 11.11.

Patients were fed, swaddled, and equipped with ear protection prior to imaging. Contrast agent was not administered as part of the imaging protocol, and subjects were free-breathing and non-sedated unless respiratory support or sedation were part of their ongoing NICU care. All subjects' heart rates and SpO$_2$ levels were monitored by NICU staff throughout each exam.

MR Imaging Neonatal research MRI exams were performed on a unique, small-footprint, neonatal 1.5T MRI system; see Section 5.3 for more detail. Two MR sequences

BPD severity	Cohort Size	Sex	Gestational age (weeks)	Post-menstrual age at MRI (weeks)	Birth weight (grams)
Term control	5	3M/2F	39 ± 1	42 ± 1	3270 ± 520
Preterm control	4	1M/3F	35 ± 1	39 ± 2	2510 ± 390
Mild BPD	7	6M/1F	27 ± 1	37 ± 2	1160 ± 230
Moderate BPD	6	5M/1F	27 ± 2	38 ± 2	990 ± 260
Severe BPD	20	10M/10F	25 ± 2	41 ± 3	690 ± 170

Table 11.11: Subject group demographics (± standard deviation, where applicable).

were used for pulmonary structural imaging and scoring: a conventional 3D fast gradient-recalled echo (GRE) sequence and a research 3D radial ultrashort echo time (UTE) sequence (see Section 5.3) [128, 135, 140, 182]. For some patients, only GRE (N = 5) or only UTE images (N = 1) were acquired, due to subject agitation or sustained bulk motion. Typical axial GRE acquisition parameters were: TE = 1.9 ms; repetition time (TR) = 7 ms; flip angle (FA) = 4°; bandwidth (BW) = ±90.9 kHz; field of view (FOV) = 18 cm; pixel resolution = 0.70-0.86 mm; slice thickness = 3 mm; number of averages = 5-10; and scan time = ~5 min. Typical UTE acquisition parameters were: TE = 0.2 ms; TR = 5 ms; FA = 5°; bandwidth (BW) = ±125 kHz; FOV = 18 cm; 3D isotropic resolution = 0.70-0.86 mm (in-plane isotropic pixel resolution identical to slice thickness); scan time = ~10-16 min; and number of radial projections = ~120,000–200,000. Parameters for UTE acquisitions were chosen to yield a highly proton-density-weighted intensity regime [182]. UTE images were reconstructed after discarding data acquired during bulk motion intervals [135].

MRI scoring of lung disease Imaging-based lung disease severity was independently assessed by two radiologists (with 22 and 6 years of experience) blinded to patients' diagnoses

Category	Score: 0	Score: 1	Score: 2	Quality of Visualization with UTE contrast weighting	Quality of Visualization with GRE contrast weighting
Hyperexpansion	None	Focal	Global	Strong	Strong
Mosaic lung attenuation	None	Unclear	Obvious	Moderate	Poor
Emphysema, number of cysts/regions	None	Single	Multiple	Strong (TE $<$ parenchymal T_2*)	Poor (TE $\approx$ parenchymal T_2*)
Emphysema, size	None	$<$5 mm	$>$5 mm	Strong (TE $<$ parenchymal T_2*)	Poor (TE $\approx$ parenchymal T_2*)
Fibrous/ interstitial, triangular subpleural opacities	None	1-3 lobes	4-6 lobes	Moderate	Strong
Distortion of bronchovascular bundles	Mild	Moderate	Severe	Moderate	Moderate
Subjective impression	Mild	Moderate	Severe	Strong	Strong

Table 11.12: Radiological scoring system for pulmonary MRI of neonatal BPD, with respective image contrast weighting contributions from UTE and GRE MRI sequences. With its very short echo time (TE $\sim$0.2 ms), UTE images visualize short T_2* specimens (i.e. non-fibrotic parenchymal tissue) better than GRE images (TE $\sim$2ms). For similar reasons, the GRE can yield improved contrast between fibrotic/interstitial/soft tissues and normal/hypodense parenchymal tissues.

using a modified Ochiai scoring system [124] that includes 7 categories (Table 11.12), with varying contrast weighting contributions from GRE and UTE images for each category as indicated. Each category was scored 0-2, with a total range of 0-14. All image sets were anonymized, with UTE and GRE image sets for a single subject evaluated together to yield one MRI score per radiologist for each subject. A final mean MRI score was generated for each subject by summing the average of the two radiologists' scores in each category.

Statistical Analysis   Inter-reader reliability of MRI scoring was evaluated in MAT-LAB (The MathWorks, Inc., Natick, Massachusetts) using a single-rater type intra-class correlation coefficient (ICC) test for absolute agreement.

Univariate ANOVA tests (SAS 9.3, SAS Institute Inc., Cary, North Carolina) were used to determine group differences in MRI scores, birth weight, and GA for three outcomes: 1) BPD severity levels (mild, moderate, severe, deceased from lung disease); 2) levels of respiratory support at NICU discharge (room air, oxygen, ventilator, or death); and 3) levels of respiratory support at 40 weeks PMA (room air, non-invasive oxygen [either nasal cannula or high-flow nasal cannula], or ventilator). Note that we had intended *a priori* to include a group of patients on non-invasive positive pressure, i.e. continuous positive airway pressure (CPAP), but no subjects utilized this interface by 40 weeks PMA.

Multi-variable linear regression models were used to analyze three continuous outcomes: 1) duration of ventilator support; 2) duration of any positive pressure ventilation (PPV) (ventilator or non-invasive pressure); and 3) duration of any support (ventilator, non-invasive pressure, or oxygen). Duration was censored to 150 days in all cases, a time frame that captured the support at hospital discharge but avoided excess leverage from patients on respiratory support for years. Models were built for three continuous predictor variables: MRI score, GA, and birth weight. A stepwise selection process was implemented, such that predictors that satisfied $P < 0.2$ were entered into the model but were removed if they did not then satisfy $P < 0.05$.

A general linear model (SAS 9.3) was used to assess the significance of additional continuous and categorical variables. Preliminary models included all recorded clinical data that may impact support duration, with both continuous variables (MRI score, GA, and birth weight) and categorical variables (multiparity of the pregnancy, administration of antenatal steroids, administration of postnatal steroids, administration of surfactant, highest level of respiratory support in NICU, need for systemic pulmonary arterial hypertension [PAH] med-

ications, and whether patients had a pneumonia while in the NICU). Since all patients were referred to our NICU from outside birthing hospitals, clinical data for postnatal steroids were incomplete and thus were excluded from analysis. A more limited multi-variable model was investigated more rigorously, including only variables which had higher clinical and statistical significance in the larger model (MRI score, GA, birth weight, multiparity, systemic PAH medications, and pneumonia). The level for statistical significance was set at $P < 0.05$ for all analyses.

Non-BPD patients were excluded from univariate, linear regression, and general linear models (see Discussion in this section).
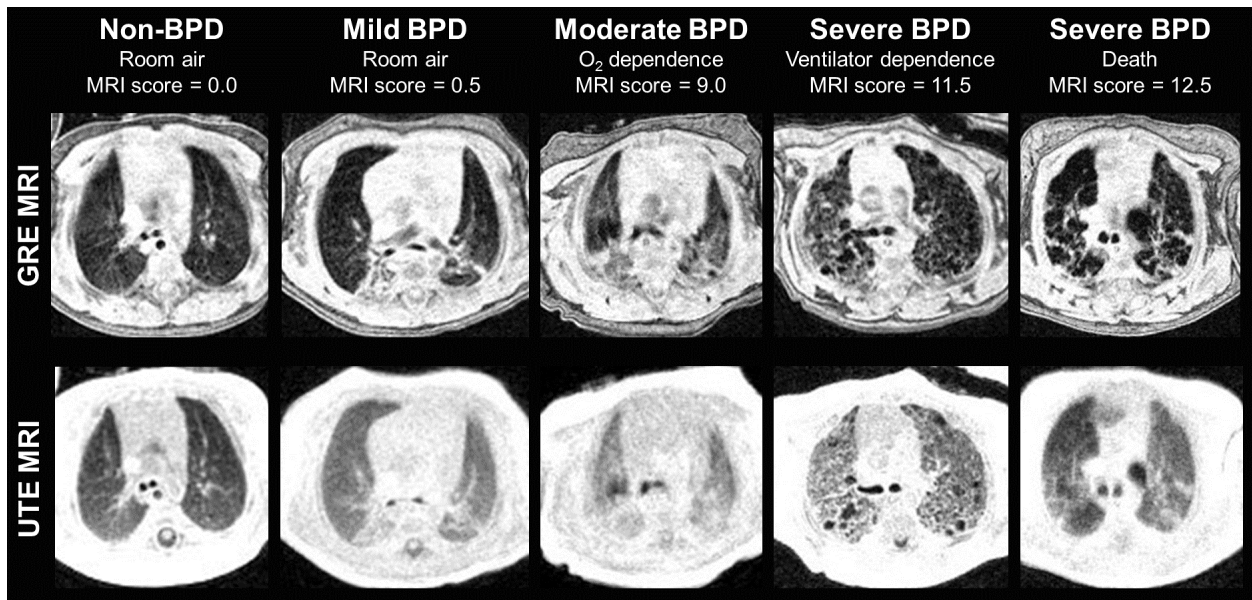
Figure 11.17: Representative axial gradient echo (GRE) and UTE MR images demonstrating the range of BPD severity. The level of respiratory support at NICU discharge and MRI scores are provided for each subject. Due to its relatively short TE value, the UTE sequence can visualize hypodense tissue with intensity above the noise floor, whereas in the same tissue the GRE is reconstructed with intensity near that of noise (for example, in the deceased severe BPD case at far right); UTE contrast weighting yields density-like relatively intensities between various pulmonary tissues. With its relatively long TE value, the GRE sequence can yield improved contrast between fibrotic/interstitial/soft tissues and normal/hypodense parenchymal tissues.

Results: Typical GRE and UTE images, level of respiratory support at discharge, and MRI scores across the spectrum of BPD severities are presented in Figure 11.17. Mean MRI scores for each patient group were: term control 0.5 ± 0.4, preterm controls 0.9 ± 0.8, mild BPD 1.9 ± 2.0, moderate BPD 4.4 ± 4.0, severe BPD 9.6 ± 3.0, and deceased from BPD 12.5 $\pm$ 0.0 (Figure 11.18). Inter-reader reliability for scores was good (r = 0.86, 95% confidence intervals [CI] 0.76-0.92).
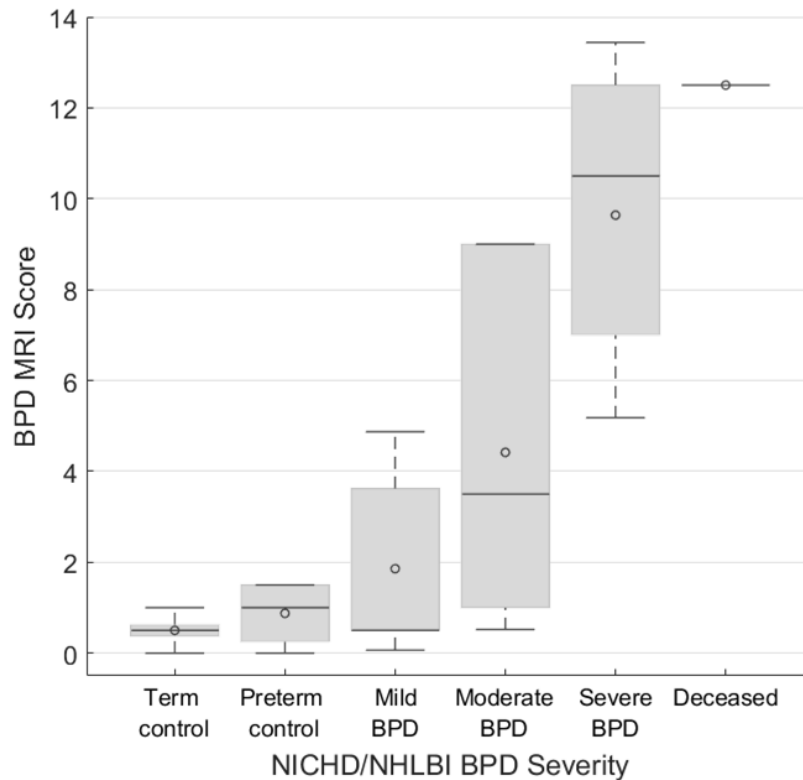
Figure 11.18: MRI score as a predictor of BPD disease severity (NICHD/NHLBI definition). Notably, MRI scores of preterm non-BPD subjects and term control subjects did not significantly differ.

NICHD BPD severity (Figure 11.19– top), respiratory support at NICU discharge (Figure 11.19– middle), and respiratory support at 40 weeks PMA (Figure 11.19– bottom) were predicted well by MRI score, fairly by birth weight, and poorly by GA. Note that the superiority of MRI scores was greater for concrete clinical outcomes (respiratory support at

40 weeks PMA and NICU discharge) than for NICHD BPD severity. NICHD severity level was not necessarily indicative of NICU discharge support (see Table 11.13); subjects with moderate BPD were equally split between discharge on oxygen and discharge on room air; and 3 subjects with severe BPD were discharged on room air, while 2 severe subjects died from pulmonary morbidities.

Frequency Distribution		BPD Severity Diagnosis		
		Mild	Moderate	Severe
Respiratory Support at NICU Discharge	None	7	3	3
	Oxygen	0	3	5
	Ventilator	0	0	8
	Deceased	0	0	2

Table 11.13: Frequency distribution of the various levels of NICHD severity and levels of respiratory support at NICU discharge, indicating that diagnosed severity is not necessarily indicative of respiratory outcomes at discharge.

In the stepwise selection regression models, duration of ventilator support was significantly predicted by MRI score ($R^2 = 0.78$), while birth weight and GA were not significant ($P > 0.2$); days on ventilator support increased by 12.9 ± 1.3 ($\pm$ standard error) days per 1 point increase in MRI score. Duration of any PPV was significantly predicted by MRI score and birth weight (partial $R^2 = 0.77$ and 0.07, respectively, with total $R^2 = 0.85$), while GA was not significant ($P > 0.2$); days on any PPV increased by 7.5 ± 1.1 days per 1 point increase in MRI score. Similarly, duration of any support was significantly predicted by MRI score and birth weight (partial $R^2 = 0.59$ and 0.11, respectively, with total $R^2 = 0.71$), while GA was not significant ($P > 0.2$); days on any support increased by 4.3 ± 1.3 days per 1 point increase in MRI score.

In the general linear modeling, administration of surfactant, administration of antenatal or postnatal steroids, and the highest level of respiratory support in the NICU had no impact on duration of any respiratory supports. Accounting for GA, birth weight, multiparous pregnancy, need for systemic PAH therapies, and occurrences of pneumonia in the NICU,
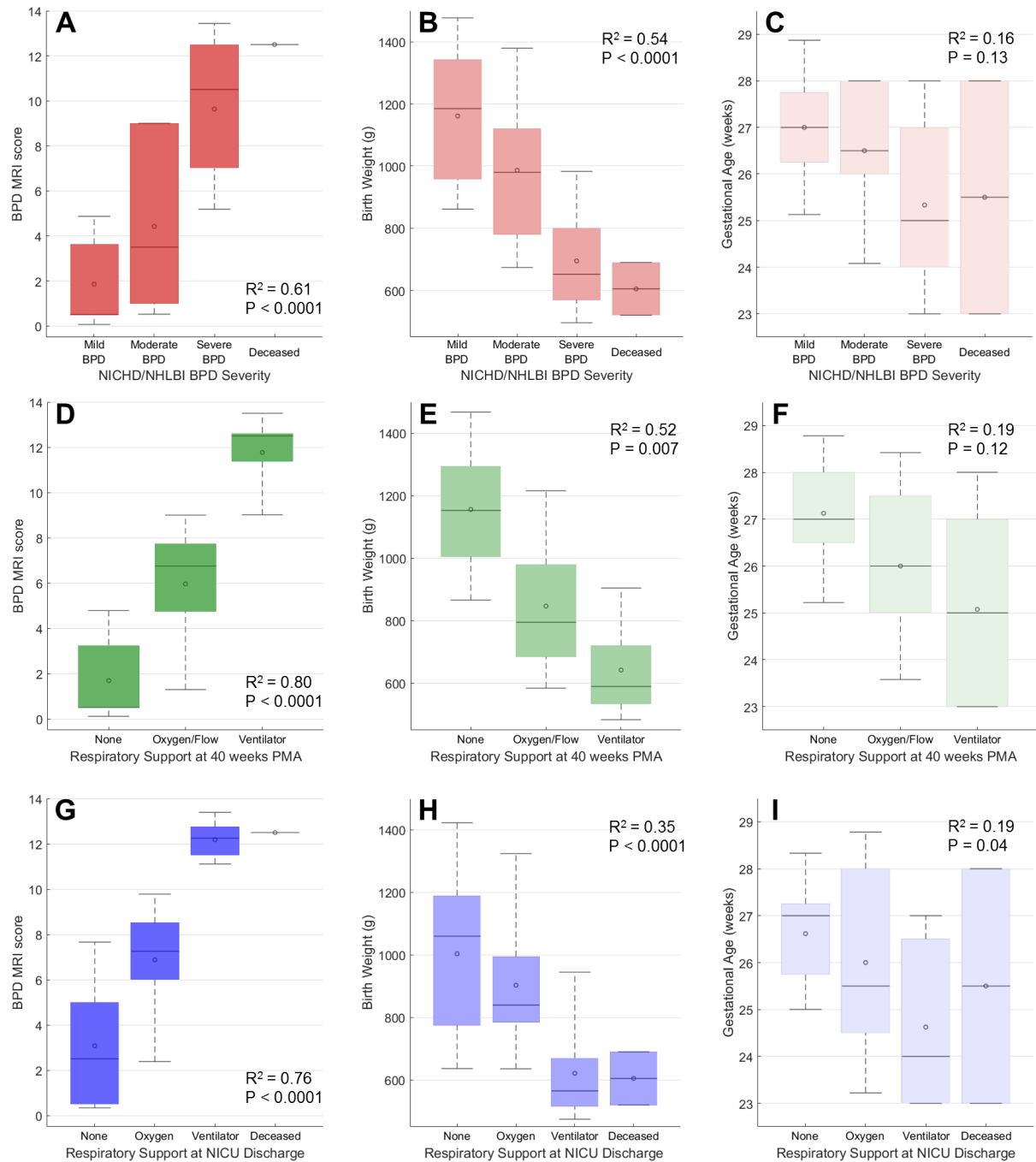
Figure 11.19: Using univariate analysis (ANOVA) including MRI score (left column), birth weight (middle column), and gestational age (right column), the following metrics are predicted: NICHD BPD severity (mild, moderate, severe, and deceased due to lung disease) (top row); respiratory support at NICU discharge (room air, oxygen, ventilator, and deceased due to lung disease) (middle row), and respiratory support at 40 weeks PMA (room air, oxygen/flow, and ventilator) (bottom row).

MRI score significantly predicted days on ventilator support (8.1 [95% CI 3.6-12.6] more days per 1 point increase in MRI score; total $R^2 = 0.86$), days on any PPV (6.7 [95% CI 4.3-9.6] more days per 1 point increase in MRI score; total $R^2 = 0.91$), and days on any support (6.3 [95% CI 2.8-9.7] more days per 1 point increase in MRI score; total $R^2 = 0.77$). In this multi-variable prediction model, MRI score was always the strongest predictor of duration of all respiratory support levels (Table 11.14).

Support level duration predicted (censored to 150 days of life)	Total R^2 of model	P-value of significant variables[a]	Increase in days of support duration per 1 point increase in MRI score [95% confidence intervals]
Any support	0.77	MRI score 0.001; Birth weight 0.002	6.3 [2.8-9.7]
Any positive pressure ventilation	0.91	MRI score <0.0001; Birth weight 0.002	6.7 [4.3-9.6]
Ventilation	0.86	MRI score 0.001; PAH therapy 0.025	8.1 [3.6-12.6]
[a]All other predictor variables were not significant in the model (P > 0.05).			

Table 11.14: A multi-variable linear regression model (more limited version) predicting duration of various levels of respiratory support, censored to 150 days of life. Predictor variables included MRI score, GA, birth weight, multiparity, systemic PAH medications, and pneumonia. MRI score was always the most significant predictor.

Discussion: Free-breathing pulmonary MRI can assess structural abnormalities of BPD without requiring sedation or ionizing radiation. To our knowledge, this work represents the first results demonstrating that pulmonary MRI in neonatal BPD patients can describe disease severity and predict short-term clinical outcomes better than any current standard clinical measure. Although both birth weight and MRI score can predict NICHD severity similarly well, NICHD severity level is not predictive of eventual discharge support. Since disease physiology should inform assessment of support [192], these results suggest that MRI can play an important, possibly even critical, role in revising the definition of BPD and may

aid in implementing precision medicine techniques for individualized disease trajectories.

CT scoring systems of infant BPD already exist [187, 193], but concerns over ionizing radiation exposure and sedation requirements for a pediatric CT scan [22, 23, 24, 25, 26] make the non-ionizing, non-sedated MRI techniques used in this study a safer choice, particularly for longitudinal imaging of neonatal subjects. The MRI scoring system used here could be refined to include only categories of greatest significance, to modify terminology to be more observational and less mechanistic, and to reduce scoring subjectivity. The addition of quantitative assessments of the structural patterns and distribution of parenchymal disease to ordinal scoring schemes is desirable and complement radiological phenotyping of disease. Previous work on CT of interstitial lung diseases has achieved quantitative textural analysis [194, 195], which reduces variation in inter- and intra-reader scoring and cuts down on evaluation time, but such work has yet to be extended to MR images or to the evaluation of neonatal BPD.

This study was performed using a unique, small footprint, neonatal-sized MRI scanner sited within our NICU. However, implementation of this technique does not require a dedicated NICU system; these scans are translatable to any adult-sized scanner with appropriately-sized coils for neonatal chest imaging. Further, gradient echo sequences are readily available on any conventional scanner, and all three major MRI manufacturers have sequences similar to the UTE sequence implemented here.

Historically, pulmonary MRI has been challenging due to the rapid proton signal decay ($T_2* \approx 2$ ms for non-fibrotic lung parenchyma at 1.5T). For TE values approximately equal to or longer than the parenchymal T_2*, MR signal from non-fibrotic tissue is not adequately acquired, and thus is visualized as a low-intensity region in the MR image. Thus, short TE values, for the UTE sequence, are essential for a complete evaluation of normal tissue and hypodense tissue (alveolar simplification, emphysema, cysts, etc.) (Table 11.12). Further, MR images can provide normalized signal intensities nearly identical to CT densities through

selection of MR parameters that yield a near-proton-density regime (i.e., small FA, short TR, $TE \leq$ T$_2$*) [182]. However, a sequence with a TE near the parenchymal T_2*, as implemented with the GRE sequence here, can complement the proton-density UTE images by yielding a higher contrast between lung parenchyma and soft tissues (fibrotic, interstitial, vasculature, etc.) (Table 11.12).

The largest limitation of our study is the uneven distribution of clinical severity, reflecting referral bias; as a primarily referral-based NICU with few in-born neonates, only preterm infants with severe sequelae of prematurity or infants with other complex co-morbidities are admitted. The uneven distribution of severity necessarily led to small sample sizes in sub-groups (such as those with only mild or moderate BPD). The referral patterns also led to incomplete representation of gestational ages; there were no subjects with gestational ages of 30-33 weeks.

In conclusion, early-life pulmonary MRI can quantitatively measure the structural abnor-malities of neonatal BPD, describe disease severity, and predict short-term outcomes better than any current standard clinical measure, without requiring sedation or ionizing radiation. These results demonstrate an ability to select preterm neonatal patients at increased risk for respiratory morbidities and therefore support the wider implementation of MRI at even ear-lier time points as a predictor of disease trajectories. Importantly, the regional and structural information inherent in imaging provides the potential to image-phenotype disease, which may be used to personalize treatment and monitor the efficacy of new therapies. Since pul-monary MRI can be used safely for serial assessment, this technique has the potential to define the time-course of neonatal pulmonary disease associated with extreme prematurity.

11.3.3 Parenchymal Density Distributions in BPD Subjects

With a proton-density regime from UTE MRI well established, there is potential for defining disease severity based on the proton density distributions of pathological parenchymal tis-

sue in neonatal patients with BPD. The following work illustrates preliminary quantitative characterization of BPD severity and outcomes via parenchymal intensity distributions.

With IRB approval, 5 quiet-breathing neonatal patients from the NICU (5 severe BPD, 2 moderate, 4 mild, 1 non-BPD control) underwent structural pulmonary MRI (ultrashort echo-time, UTE, $TE \approx 0.2$ms; gradient echo, $TE \approx$ 2ms) in a NICU-sited, neonatal-sized 1.5T scanner, with no procedurally-ordered sedation. Whole-lung segmentations from UTE images were generated in Amira, yielding normalized lung intensity distributions, a measurement akin to volumetric density (range 0-1 g/cm^3) [182]. These parenchymal lung intensity distributions were compared to NICHD severity and short-term outcomes.

Qualitatively, lung intensity distributions for controls demonstrated a homogeneous peak at ~ 0.5 g/cm^3 (expected in healthy newborns), with this peak broadening toward increased density with severity through moderate BPD. UTE MR images and density distributions from representative subjects are shown in Figure 11.20 with a control patient at the top and increasing in severity toward the bottom. Severe BPD subjects exhibited prominent and heterogeneous low- and high-density regions, particularly for deceased subjects. Areas of very low density in the deceased subject shown likely indicates highly simplified, non-alveolated airspaces. These trends in heterogeneous density distributions tended to follow level of respiratory support at discharge from the NICU, with the patients shown in Figure 11.20 increasing in support severity as distributions become more severely broadened.

Future work with more quantitative analysis potentially includes curve-fitting of the parenchymal intensity distributions to three Gaussians, representative of tissue with normal density (centered around ~ 0.5 g/cm^3), high-density tissue, and low-density tissue, or potentially binning into quantiles (likely quintiles), with similar representation of normal and abnormal tissue densities. This preliminary work qualitatively shows promise that tissue quantification from pulmonary neonatal MRI could yield the ability to phenotype BPD, with the potential to personalize clinical care via serial evaluation.
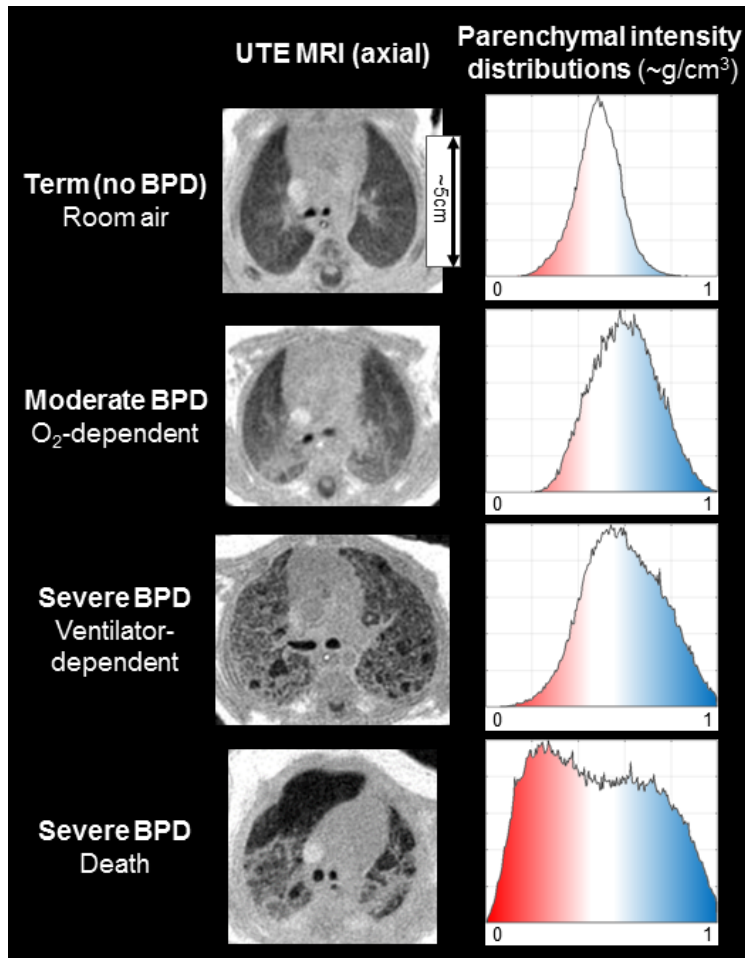
Figure 11.20: UTE MR images (left) and parenchymal tissue density distributions (right) from representative neonatal patients with BPD. A lung-control patient without BPD is shown at the top, with increasing severity downward. The x-axis of the distributions is pixel intensity, normalized to muscle, with an interval shown from 0-1 g/cm^3; this follows work by the author showing that UTE lung tissue intensities normalized to muscle are roughly equivalent to volumetric density in g/cm^3) [182]. The more severe cases clearly have heterogeneous lung tissue, with much high-density fibrosis, and a deceased case with very low density lucencies (potentially yielding highly simplified airway structures).

11.3.4   Parenchymal T_2* Measurements

Since MRI has historically provided strong contrast image weighting between various tissues, it is intuitive to extend the neonatal UTE capabilities demonstrated in this section for quantification of regional relaxation parameters in the infant lung. Previous work has examined

T_2* values in human lungs at 1.5T and 3T (noting that $T2*$ is inversely proportional to field strength) [115, 118, 119], but young infant lungs in normal or diseased conditions have yet to be explored at any field strength.

Regional estimates of the T_2* relaxation time (or R_2* relaxation rate; $T_2* = \frac{1}{R_{2*}}$) could serve as a potential pulmonary MRI biomarker in neonatal patients with little-understood pulmonary morbidities. The relationship between local T_2* and local parenchymal proton density, and identifying the sources of this relationship, may have clinically physiological information that could be useful for identifying various pathologies (such as microstructural morbidities including alveolar simplification). Further, determination of T_2* may yield bio-physical parameters important for the optimization of sequence design. With the feasibility of performing UTE MRI in free-breathing, non-sedated NICU patients already demonstrated ([135, 140, 182]), multi-TE UTE MRI is used here to quantify the parenchymal tissue density and T_2* in NICU infants. This work implements the retrospective respiratory gating tech-nique inherent in radial MRI to reconstruct images at end-expiration and end-inspiration from free-breathing subjects.

UTE MRI was acquired in one damp sea sponge (acting as a lung phantom), followed by one neonatal lung-control patient (no suspected lung morbidities) with IRB approval and written parental consent. The sequence described in Section 9.3 was modified to acquire each radial k-space trajectory at four TE values: 0.20 ms (the minimum achievable value), 0.95 ms, 1.70 ms, and 2.45 ms. Each trajectory was sampled at each TE value, followed by the subsequent trajectory (i.e. TE values were the inner loop of acquisition, while trajectory was the outer loop of acquisition). Typical acquisition parameters were: $TR = {\sim}7.4$ ms; FA = 5°; FOV = 18 cm; 3D isotropic resolution = 1.4 mm (in-plane isotropic pixel resolution identical to slice thickness); scan time = ${\sim}24$ min; and number of radial projections per TE = ${\sim}50{,}000\text{-}75{,}000$. UTE images were reconstructed for each kth echo (k = 1, 2, 3, or 4) without respiratory gating. Estimates of T_2* were calculated from mono-exponential signal

magnitude decay:

$$S(r) = S_0(r) \cdot e^{-TE/T_2*}, \tag{11.2}$$

where $S(r)$ is the measured signal, TE is the echo time, and r is the image coordinate that varies over all voxels. As described earlier, parenchymal tissue density was converted to near-volumetric density by normalization of lung intensity to muscle intensity (see Section 11.3.1).
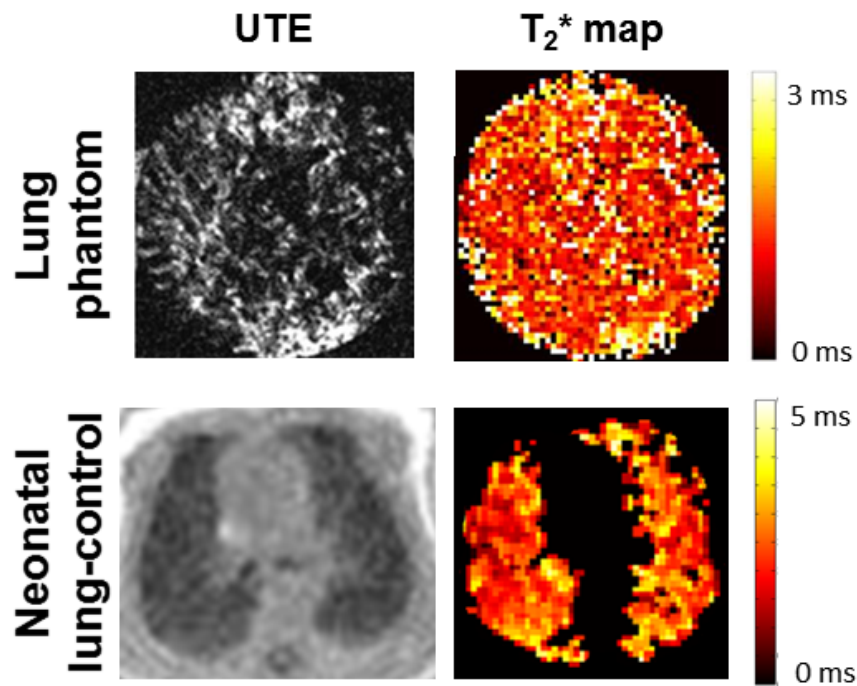
Figure 11.21: Representative proton density UTE MR images (minimum TE; left column) and corresponding T_2* maps (ungated). For the phantom and patient, whole-lung T_2* was approximately 1.4 ms and 2.2 ms.

Representative minimum-TE UTE images and resulting T_2* maps are shown in Figure 11.21. For the phantom and patient, whole-lung T_2* was approximately 1.4 ms and 2.2 ms. Future analysis of both whole-lung and regional T_2* information may help differentiate side-by-side pathologies, and could provide a future tool for quantification of disease. Thus

this technique may provide a greater understanding of neonatal lung disease physiology.

12 UTE MRI Journal and Conference Papers

The following journal and conference papers have resulted from the material presented in Part III: ^{1}H Ultrashort Echo Time MRI.

- Published/submitted papers:

  1. <u>Nara Higano</u>, David Spielberg, Robert Fleck, Andrew Schapiro, Laura Walkup, Andrew Hahn, Jean Tkach, Paul Kingma, Stephanie Merhar, Sean Fain, Jason Woods. Neonatal pulmonary MRI of bronchopulmonary dysplasia predicts short-term clinical outcomes. *Am J Resp Crit Care Med* [submitted November 2017].

  2. <u>Nara Higano</u>, Laura Walkup, Andrew Hahn, Robert Thomen, Stephanie Merhar, Paul Kingma, Jean Tkach, Sean Fain, Jason Woods. Quantification of neonatal lung parenchymal density via UTE MRI with comparison to CT. *J Magn Reson Imaging* 2017, doi 10.1002/jmri.25643.

  3. <u>Nara Higano</u>, Andrew Hahn, Jean Tkach, Xuefeng Cao, Laura Walkup, Robert Thomen, Stephanie Merhar, Paul Kingma, Sean Fain, Jason Woods. Retrospective respiratory self-gating and removal of bulk motion in pulmonary UTE MRI of neonates and adults. *Magn Reson Med* 2017, 77(3):1284-1295.

     - *(Featured as an Editor's Pick for March 2017)*

  4. <u>Nara Higano</u>, Alister Bates, Jean Tkach, Robert Fleck, Foong Lim, Jason Woods, Paul Kingma. Pre- and post-surgical repair visualization of neonatal esophageal atresia/tracheoesophageal fistula via MRI. *J Pediatr Surg Case Reports.* https://doi.org/10.1016/j.epsc.2017.10.001.

  5. Andrew Hahn, <u>Nara Higano</u>, Laura Walkup, Robert Thomen, Xuefeng Cao, Stephanie Merhar, Jean Tkach, Jason Woods, Sean Fain. Pulmonary MRI of

neonates in the intensive care unit using 3D UTE and a small foot-print MRI system. *J Magn Reson Imaging* 2017, 45(2):463-471.

6. Laura Walkup, Jean Tkach, <u>Nara Higano</u>, Robert Thomen, Sean Fain, Stephanie Merhar, Robert Fleck, Raouf Amin, Jason Woods. Quantitative MRI of bronchopulmonary dysplasia in the NICU Environment. *Am J Resp Crit Care Med* 2015, 192(10):1215-1222.

7. Melissa Schopper, Laura Walkup, Jean Tkach, <u>Nara Higano</u>, Foong Yen Lim, Beth Haberman, Jason Woods, Paul Kingma. Evaluation of neonatal lung growth in congenital diaphragmatic hernia by pulmonary MRI. *J Pediatr* 2017, pii: S0022-3476(17)30780-1.

- Papers in preparation:

  1. <u>Nara Higano</u>, Alister Bates, Erik Hysinger, Robert Fleck, Andrew Hahn, Sean Fain, Paul Kingma, Raouf Amin, Jason Woods. Quantitative geometric assessment of regional airway collapse in neonates via retrospectively respiratory-gated UTE MRI. *J Magn Reson Imaging* [in preparation].

  2. Erik Hysinger, Alister Bates, <u>Nara Higano</u>, Robert Fleck, Andrew Hahn, Sean Fain, Paul Kingma, Raouf Amin, Jason Woods. Validation of MRI assessment of dynamic airway collapse by comparison to bronchoscopy. [in preparation].

  3. Andrew Hahn, <u>Nara Higano</u>, Jean Tkach, Laura Walkup, Robert Thomen, Stephanie Merhar, Jason Woods, Sean Fain. Proton density and R_2^* estimation of neonatal lung parenchyma during free breathing with UTE MRI. [in preparation].

  4. Xuefeng Cao, <u>Nara Higano</u>, Jinbang Guo, Robert Thomen, Laura Walkup, Jean Tkach, Mark Conradi, Jason Woods. Origin of the self-gating waveform at k = 0 in pulmonary 3D radial UTE MRI. [in preparation].

5. Lauren Yoder, Nara Higano, Andrew Schapiro, Robert Fleck, Erik Hysinger, Alister Bates, Sean Fain, Jason Woods. Elevated lung volumes in neonates with BPD measured via free-breathing pulmonary MRI. [in preparation].

6. Corinne Hite, Nara Higano, Jean Tkach, Beth Haberman, Foong Lim, Jason Woods, Paul Kingma. Effect of post-natal surgical repair methods on diaphragmatic movement in infants with CDH. [in preparation].

7. Stephanie Herrin, Nara Higano, Jean Tkach, Jason Woods, Paul Kingma. MRI measurements of lung volume in CDH. [in preparation].

- Conference papers presented by Nara Higano:

  1. **Submitted**: Quantitative geometric assessment of regional airway collapse in neonates via retrospectively respiratory-gated UTE MRI. *International Society for Magnetic Resonance in Medicine*, Paris, France 2018.

  2. **Submitted**: Neonatal pulmonary MRI of BPD predicts short-term clinical outcomes. *American Thoracic Society*, San Diego, CA 2018.

  3. **Oral**: Quantitative characterization of BPD severity using neonatal pulmonary MRI and correlation to short-term outcomes. *Radiological Society of North America*, Chicago, IL 2017.

  4. **Poster discussion**: MRI-based scoring of BPD correlates with disease severity and short-term outcomes. *American Thoracic Society*, Washington, DC 2017.

     - *(One of four abstracts selected by the Neonatal and Developing Lung Interest Group of the ATS as best in the area of neonatal and lung development, out of more than 500 abstracts reviewed.)*

  5. **Poster**: Pre- and post-surgical repair visualization of neonatal EA/TEF via MRI. *American Thoracic Society*, Washington, DC 2017.

6. **Oral**: UTE MRI yields CT-like visualization of neonatal lung parenchymal pathologies and the potential for objective, quantitative characterization of neonatal lung disease severity. *University of Pennsylvania Workshop on Pulmonary Imaging*, Philadelphia, PA 2017.

7. **Oral**: Quantification of neonatal lung parenchymal density via UTE time MRI. *American Thoracic Society*, San Francisco, CA 2016.

8. **Poster discussion**: Imaging-based pulmonary functional measurements from self-gated neonatal UTE MRI. *American Thoracic Society*, San Francisco, CA 2016.

9. **Poster**: Retrospective bulk motion removal and respiratory self-gating in pulmonary 3D radial UTE MRI of non-sedated, free-breathing neonates and adults. *Experimental NMR Conference*, Pittsburgh, PA 2016.

10. **Poster discussion**: Self-gating of respiratory motion for pulmonary UTE MRI of infants in the NICU. *International Society for Magnetic Resonance in Medicine*, Toronto, Canada 2015.

11. **Poster discussion**: Neonatal lung imaging during quiet-breathing via UTE proton MRI and retrospective respiratory gating. *American Thoracic Society*, Denver, CO 2015.

Part IV

Dissertation Summary and Conclusions

The methods presented in this dissertation have strong promise for translation impact. UTE MRI yields density and resolutions similar to that of CT, without the ionizing radiation or

sedation, and further can yield novel dynamic anatomical and functional information via inherent retrospective respiratory-gating. Diffusion of hyperpolarized gases in the lungs can provide a sensitive biomarker of alveolar airspace sizes, and in some cases, of the alveolar geometry. As discussed in various sections of this dissertation, the development and progression of lung structure and function over time is of particular interest in pediatrics, and so the non-invasive and non-ionizing nature of MRI lends itself well to serial studies in children. Thus, the potential is high for both of these technologies to provide critical information in assessment of the neonatal lung in health and disease.

There are limitations to wider implementation associated with the presented methods. Radial sequences are not commercially available on any platform, although that is likely to change in the near future, and implementation of retrospective motion-tracking methods is very limited, in part due to the absence of stream-lined post-processing algorithms. Further, MRI scanners sited within the NICU are far and few; while the unique neonatal-sized scanner used in this work is not necessary for any of the presented methods, nearby access to a scanner from the NICU can avoid many logistical concerns posed when transporting vulnerable neonatal patients far from the NICU to a radiology department for imaging.

When considering specifically hyperpolarized gas studies, multi-nuclear scanner hardware can be expensive, and hyperpolarizing technology is not cheap, whether home-built or commercially purchased. Often it is desirable to have hyperpolarization expertise on the imaging team staff, which can be hard to come by since the field is relatively small. Additionally, the noble gases are not cheap; ^{3}He in particular has an extremely low natural abundance, with the current supply generated from the decay of tritium from nuclear weapon manufacturing. This has been the main impetus for the shifted focus in more recent years to both hyperpolarization and imaging techniques specific to ^{129}Xe. Finally, despite the fact that hyperpolarized gas pulmonary imaging uses inert noble gases, they are currently classified by the FDA as "investigational new drug" and so requires special protocol approvals when

administered to subjects.

The future looks promising and exciting for further development of the imaging physics methods presented in this thesis. There is strong value in the implementation of in-vivo neonatal ^{129}Xe diffusion imaging, particularly to regionally assess extent of alveolarization and size of alveolar airspaces in preterm infant and in infants with potentially compressed parenchyma, such as in CDH. Further, development of an anisotropically restricted gas diffusion model for ^{129}Xe in the heterogeneously alveolated infant lung airspaces could yield precise in-vivo morphometric measurements of microstructural geometry and dimension parameters. There is also potential in the future to utilize the solubility of ^{129}Xe and the slight chemical shift in red blood cells and plasma versus in air, to measure gas-blood diffusion, which may be of particular interest in premature infants in whom the interstitial wall thickness varies with stage of development. From the ^{1}H UTE MRI perspective, further investigation is needed into the sources of the motion modulation phenomenon at the k-space center. Rigorous validation of respiratory gating techniques in the quantitative geometric evaluation of laryngeal, tracheal, and bronchial airway dynamics by comparison to clinical bronchoscopy, and the dynamic airway methodology is prime for combination with CFD simulations to extract non-invasive, non-ionizing metrics on respiratory effort and energy in diseased neonates. The proton-density regime provided by UTE MRI provides an essential tomographic, yet non-ionizing, imaging tool for clinicians in assessment of lung disease in premature infants; its preliminary utility in prediction of respiratory outcomes was demonstrated in this thesis, but further investigation with larger cohorts is merited, as well as with more automated and objective evaluation of pathological pulmonary structures using textural analysis and/or machine learning algorithms for disease scoring.

This dissertation has utilized both ^{1}H radial UTE MRI and hyperpolarized noble gas MRI techniques to investigate the structure and function of neonatal and infant lungs. In neonatal pulmonary UTE MRI, it has been shown that utilization of k-space properties

and imaging physics can generate highly useful images of both infant lung macrostructure and dynamic function. With hyperpolarized gas diffusion MRI, this work has demonstrated that fundamental physical changes to gas diffusion modeling are key to producing promising in-vivo measurements of alveolar airspace sizes. The potential for clinical translation of the neonatal pulmonary MRI methods presented in this dissertation is very high, with the foundations of these techniques firmly rooted in physics.

Bibliography

[1] Slichter CP. *Principles of Magnetic Resonance.* Springer, 1990.

[2] Levitt MH. *Spin Dynamics: Basics of Nuclear Magnetic Resonance.* Chichester, West Sussex: John Wiley & Sons, 2008.

[3] Fukushima E, Roeder S. *Experimental Pulse NMR: A Nuts and Bolts Approach.* Westview Press, 1993.

[4] Mason R, Broaddus V, Martin T, King T, Schraufnagel D, Murray J, and Nadel J. *Murray and Nadel's Textbook of Respiratory Medicine: 2-Volume Set.* Expert consult title, Elsevier Health Sciences, 2010.

[5] Sacco JJ, Botten J, Macbeth F, Bagust A, and Clark P. The average body surface area of adult cancer patients in the UK: a multicentre retrospective study. *PLoS One* 2010 Jan 28;5(1):e8933.

[6] Schürch S. Surface tension at low lung volumes: dependence on time and alveolar size. *Respir Physiol* 1982 Jun;48(3):339-55.

[7] Jobe AH, Whitsett JA, and Abman SH. *Fetal and Neonatal Lung Development: Clinical Correlates and Technologies for the Future.* Cambridge University Press, 2016.

[8] Kajekar R. Environmental factors and developmental outcomes in the lung. *Pharmacol Ther* 2007 May;114(2):129-45.

[9] Stoll BJ, Hansen NI, Bell EF, Shankaran S, et al.; Eunice Kennedy Shriver National Institute of Child Health and Human Development Neonatal Research Network. Neonatal outcomes of extremely preterm infants from the NICHD Neonatal Research Network. *Pediatrics* 2010;126(3):443–456.

[10] Bhandari A, McGrath-Morrow S. Long-term pulmonary outcomes of patients with bronchopulmonary dysplasia. *Semin Perinatol* 2013;37(2):132–137.

[11] Gibson AM, Doyle LW. Respiratory outcomes for the tiniest or most immature infants. *Semin Fetal Neonatal Med* 2014;19(2):105–111.

[12] Simpson SJ, Hall GL, Wilson AC. Lung function following very preterm birth in the era of 'new' bronchopulmonary dysplasia. *Respirology* 2015;20(4):535-40.

[13] Jobe AH. Mechanisms of lung injury and bronchopulmonary dysplasia. *Am J Perinatol* 2016;33:1076–1078.

[14] Bose CL, Laughon MM, Allred EN, O'Shea TM, Van Marter LJ, Ehrenkranz RA, Fichorova RN, Leviton A; ELGAN Study Investigators. Systemic inflammation associated with mechanical ventilation among extremely preterm infants. *Cytokine* 2013;61:315–322.

[15] Cazzato S, Ridolfi L, Bernardi F, Faldella G, Bertelli L. Lung function outcome at school age in very low birth weight children. *Pediatr Pulmonol* 2013;48:830–837.

[16] Northway WH Jr, Rosan RC, Porter DY. Pulmonary disease following respiratory therapy of hyaline-membrane disease: bronchopulmonary dysplasia. *N Engl J Med* 1967;276:357–368.

[17] Jobe AH, Bancalari E. Bronchopulmonary dysplasia. *Am J Respir Crit Care Med* 2001;163(7):1723-9.

[18] Johnson TJ, Patel AL, Jegier BJ, Engstrom JL, Meier PP. Cost of morbidities in very low birth weight infants. *J Pediatr* 2013;162:243–249.e1.

[19] Carraro S, Filippone M, Da Dalt L, Ferraro V, Maretti M, Bressan S, El Mazloum D, Baraldi E. Bronchopulmonary dysplasia: the earliest and perhaps the longest lasting obstructive lung disease in humans. *Early Hum Dev* 2013;89:S3–S5.

[20] Poindexter BB, Feng R, Schmidt B, Aschner JL, Ballard RA, Hamvas A, Reynolds AM, Shaw PA, Jobe AH; Prematurity and Respiratory Outcomes Program. Comparisons and limitations of current definitions of bronchopulmonary dysplasia for the Prematurity and Respiratory Outcomes Program. *Ann Am Thorac Soc* 2015;12:1822–1830.

[21] Morrow LA, Wagner BD, Ingram DA, Poindexter BB, Schibler K, Cotten CM, Dagle J, Sontag MK, Mourani PM, Abman SH. Antenatal determinants of bronchopulmonary dysplasia and late respiratory disease in preterm infants. *Am J Respir Crit Care Med* 2017;196:364–374.

[22] Miglioretti DL, Johnson E, Williams A, et al. The use of computed tomography in pediatrics and the associated radiation exposure and estimated cancer risk. *JAMA Pediatr* 2013;167(8):700–707.

[23] Brenner D, Elliston C, Hall E, Berdon W. Estimated risks of radiation-induced fatal cancer from pediatric CT. *AJR Am J Roentgenol* 2001;176(2):289-296.

[24] Pearce MS, Salotti JA, Little MP, et al. Radiation exposure from CT scans in childhood and subsequent risk of leukaemia and brain tumours: a retrospective cohort study. *Lancet* 2012;380(9840):499-505.

[25] Cravero JP, Beach ML, Blike GT, Gallagher SM, Hertzog JH. Pediatric Sedation Research Consortium. The incidence and nature of adverse events during pediatric sedation/anesthesia with propofol for procedures outside the operating room: a report from the Pediatric Sedation Research Consortium. *Anesth Analg* 2009;108(3):795–804.

[26] Mahmoud M, Towe C, Fleck RJ. CT chest under general anesthesia: pulmonary, anesthetic and radiologic dilemmas. *Pediatr Radiol* 2015;45(7):977–981.

[27] Langham MR Jr, Kays DW, Ledbetter DJ, Frentzen B, Sanford LL, Richards DS. Congenital diaphragmatic hernia. Epidemiology and outcome. *Clin Perinatol* 1996;23:671-88.

[28] Coleman A, Phithakwatchara N, Shaaban A, Keswani S, Kline-Fath B, Kingma P, et al. Fetal lung growth represented by longitudinal changes in MRI-derived fetal lung volume parameters predicts survival in isolated left-sided congenital diaphragmatic hernia. *Prenat Diagn* 2015;35:160-6.

[29] Sfeir R, Michaud L, Salleron J, Gottrand F. Epidemiology of esophageal atresia. *Dis Esophagus* 2013;26(4):354-355.

[30] Spitz L. Oesophageal atresia. *Orphanet J Rare Dis* 2007 May 11;2:24.

[31] Gross RE. The surgery of infancy and childhood. *WB Saunders*; 1953.

[32] Gupta A and Gupta N. Ineffective Ventilation in A Neonate with A Large Pre-Carinal Tracheoesophageal Fistula and Bilateral Pneumonitis-Microcuff Endotracheal Tube to Our Rescue! *J Neonatal Surg* 2017 1;6(1):14.

[33] Mahalik SK, Sodhi KS, Narasimhan KL, Rao KL. Role of preoperative 3D CT reconstruction for evaluation of patients with esophageal atresia and tracheoesophageal fistula. *Pediatr Surg Int* 2012;28(10):961-966.

[34] Ngerncham M, Lee EY, Zurakowski D, Tracy DA, Jennings R. Tracheobronchomalacia in pediatric patients with esophageal atresia: comparison of diagnostic laryngoscopy/bronchoscopy and dynamic airway multidetector computed tomography. *J Pediatr Surg* 2015;50(3):402-407.

[35] Downing GJ, Kilbride HW. Evaluation of airway complications in high-risk preterm infants: application of flexible fiberoptic airway endoscopy. *Pediatr* 1995;95(4):567-72.

[36] Miller RW, Woo P, Kellman RK, Slagle TS. Tracheobronchial abnormalities in infants with bronchopulmonary dysplasia. *J Pediatr* 1987;111(5):779-82.

[37] Cohn RC, Kercsmar C, Dearborn D. Safety and efficacy of flexible endoscopy in children with bronchopulmonary dysplasia. *Am J Dis Child* 1988;142(11):1225-8.

[38] McCubbin M, Frey EE, Wagener JS, Tribby R, Smith WL. Large airway collapse in bronchopulmonary dysplasia. *J Pediatr* 1989;114(2):304-7.

[39] Hysinger E FN, Padula M, Shinohara R, Zhang H, Panitch H, and Kawut S. Tracheo-bronchomalacia Is Associated with Increased Morbidity in Bronchopulmonary Dysplasia. *Ann Am Thorac Soc* 2017 Jun 16. doi: 10.1513/AnnalsATS.201702-178OC. [Epub ahead of print]

[40] Hysinger EB, Panitch HB. Paediatric Tracheomalacia. *Paediatr Respir Rev* 2016;17:9-15.

[41] Baxter JD, Dunbar JS. Tracheomalacia. *Ann Otol Rhinol Laryngol* 1963;72:1013-23.

[42] Mair EA, Parsons DS. Pediatric tracheobronchomalacia and major airway collapse. *Ann Otol Rhinol Laryngol* 1992;101(4):300-9.

[43] Bhutani VK, Rubenstein SD, Shaffer TH. Pressure--volume relationships of tracheae in fetal newborn and adult rabbits. *Respir Physiol* 1981;43(3):221-31.

[44] Bhutani VK, Rubenstein D, Shaffer TH. Pressure-induced deformation in immature airways. *Pediatr Res* 1981;15(5):829-32.

[45] Sun M, Ernst A, Boiselle PM. MDCT of the central airways: comparison with bronchoscopy in the evaluation of complications of endotracheal and tracheostomy tubes. *J Thorac Imaging* 2007;22(2):136-42.

[46] Bouchiat MA, Carver TR, Varnum CM. Nuclear polarization of 3He gas induced byoptical pumping and dipolar exchange. *Phys Rev Lett* 1960;5: 373–375.

[47] Schearer LD, Walters GK. Nuclear spin-lattice relaxation in the presence of magnetic-field gradients. *Phys Rev* 1965;139:A1398–1402.

[48] Colegrove FD, Schearer LD, Walters GK. Polarization of 3He gas byoptical pumping. *Phys Rev A* 1963;132:2561–2572.

[49] Gamblin RL, Carver TR. Polarization and relaxation processes in 3He gas. *Phys Rev* 1965;138:A946–960.

[50] Altes TA, Powers PL, Knight-Scott J, et al. Hyperpolarized He-3 MR lung ventilation imaging in asthmatics: Preliminary findings. *J Magn Reson Imaging* 2001; 13(3):378-84.

[51] Kirby M, Svenningsen S, Kanhere N, et al. Pulmonary ventilation visualized using hyperpolarized helium-3 and xenon-129 magnetic resonance imaging: differences in COPD and relationship to emphysema. *J Appl Physiol* 2013; 114(6):707-15.

[52] Qing K, Mugler JP, 3rd, Altes TA, et al. Assessment of lung function in asthma and COPD using hyperpolarized 129Xe chemical shift saturation recovery spectroscopy and dissolved-phase MRI. *NMR Biomed* 2014; 27(12):1490-501.

[53] Capaldi DP, Sheikh K, Guo F, et al. Free-breathing pulmonary 1H and Hyperpolarized 3He MRI: comparison in COPD and bronchiectasis. *Acad Radiol* 2015 Mar;22(3):320-9.

[54] Thomen RP, Walkup LL, Roach DJ, Cleveland ZI, Clancy JP, Woods JC. Hyperpolarized 129Xe for investigation of mild cystic fibrosis lung disease in pediatric patients. *J Cyst Fibros* 2017; 16(2):275-82.

[55] Kanhere N, Couch MJ, Kowalik K, et al. Correlation of Lung Clearance Index with Hyperpolarized 129Xe Magnetic Resonance Imaging in Pediatric Subjects with Cystic Fibrosis. *Am J Respir Crit Care Med* 2017; 196(8):1073-5.

[56] Leawoods JC, Yablonskiy DA, Saam B, Gierada DS, and Conradi MS. Hyperpolarized ^{3}He gas production and MR imaging of the lung. *Concepts Magn Reson Part A* 2001;13:277–293.

[57] Happer W, Miron E, Schaefer S, Schreiber D, van Wijngaarden WA, and Zeng X. Polarization of the nuclear spins of noble-gas atoms by spin exchange with optically pumped alkali-metal atoms. *Phys Rev A* 1984;29:3092-3110.

[58] Walker TG, Bonin K, Happer W. Electron noble-gas spin-flip scattering at low energy. *Phys Rev A* 1987;35:3749-3752.

[59] Mackintosh FC, Wu Z, Happer W. A measurement of the spin-rotation coupling in naxe molecules. *Phys Lett* 1985;112A:435-439.

[60] Bhaskar ND, Happer W, McClelland T. Eciency of spin exchange between rubidium spins and 129Xe nuclei in a gas. *Phys Rev Lett* 1982;49:25-28.

[61] Woods JC, Walkup LL, Thomen RP, Higano NS, Cleveland ZI. Initial experience in pediatric imaging with a homebuilt xenon-129 hyperpolarizer. EUROMAR 2015, P129.

[62] Berry-Pusey BN, Anger BC, Laicher G, Saam B. Nuclear spin relaxation of 129Xe due to persistent xenon dimers. *Phys Rev A* 2006;74:063408

[63] Nikolaou P, Coffey AM, Walkup LL, et al. XeNA: an automated 'open-source' (129)Xe hyperpolarizer for clinical use. Magn Reson Imaging 2014;32:541–550.

[64] Barker JR. New Coil Systems for the Production of Uniform Magnetic Fields. *J Sci Instrum* 1949;26:273-275.

[65] Saam BT and Conradi MS. Low frequency NMR polarimeter for hyperpolarized gases. *J Magn Reson* 1998 Sep;134(1):67-71.

[66] Tkach JA, Hillman NH, Jobe AH, et al. An MRI system for imaging neonates in the NICU: initial feasibility study. *Pediatr Radiol* 2012;42(11):1347-56.

[67] Merhar SL, Tkach JA, Woods JC, South AP, Wiland EL, Rattan MS, Dumoulin CL, Kline-Fath BM. Neonatal imaging using an on-site small footprint MR scanner. *Pediatr Radiol* 2017 Jul;47(8):1001-1011.

[68] Pratt R, Giaquinto R, Ireland C, Daniels B, Loew W, Higano N, Cao X, Thomen R, Woods J, Dumoulin C. A Novel Switched Frequency ^{3}He/^{1}H High-Pass Birdcage Coil for Imaging at 1.5 Tesla. *Concepts Magn Reson B* 2015;45B(4):174–182.

[69] Tkach JA, Li Y, Pratt RG, et al. Characterization of acoustic noise in a neonatal intensive care unit MRI system. *Pediatr Radiol* 2014; 44(8):1011-9.

[70] Chen XJ, Möller HE, Chawla MS, Cofer GP, Driehuys B, Hedlund LW, Johnson GA. Spatially resolved measurements of hyperpolarized gas properties in the lung in vivo. Part I: diffusion coefficient. *Magn Reson Med* 1999 Oct;42(4):721-8.

[71] Yablonskiy DA, Sukstanskii AL, Woods JC, Gierada DS, Quirk JD, Hogg JC, Cooper JD, Conradi MS. Quantification of lung microstructure with hyperpolarized ^{3}He diffusion MRI. *J Appl Physiol* 2009 Oct;107(4):1258-65.

[72] Narayanan M, Owers-Bradley J, Beardsmore C, et al. Alveolarization continues during childhood and adolescence: new evidence from helium-3 magnetic resonance. *Am J Respir Crit Care Med* 2012;185(2):186-91

[73] Hajari A, Yablonskiy D, Quirk J, et al. Imaging alveolar-duct geometry during expiration via ^{3}He lung morphometry. *J Appl Physiol* 2011;110(5):1448-54.

[74] Wang W, Nguyen N, Yablonskiy D, et al. Imaging lung microstructure in mice with hyperpolarized ^{3}He diffusion MRI. *Magn Reson Med* 2011;65(3):620-6.

[75] Osmanagic E, Sukstanskii AL, Quirk JD, Woods JC, Pierce RA, Conradi MS, Weibel ER, and Yablonskiy DA. Quantitative assessment of lung microstructure in healthy mice using an MR-based ^{3}He lung morphometry technique. *J Appl Physiol* 2010;109(6):1592-9.

[76] Flors L, Mugler JP, Paget-Brown A, Froh DK, de Lange EE, Patrie JT, Altes TA. Hyperpolarized Helium-3 Diffusion-weighted Magnetic Resonance Imaging Detects Abnormalities of Lung Structure in Children With Bronchopulmonary Dysplasia. *J Thorac Imaging* 2017 Sep;32(5):323-332.

[77] Cadman RV, Lemanske RF Jr, Evans MD, Jackson DJ, Gern JE, Sorkness RL, Fain SB. Pulmonary ^{3}He magnetic resonance imaging of childhood asthma. *J Allergy Clin Immunol* 2013 Feb;131(2):369-76.e1-5.

[78] Altes TA, Meyer CH, Mata JF, Froh DK, Paget-Brown A, Gerald Teague W, Fain SB, de Lange EE, Ruppert K, Botfield MC, Johnson MA, and Mugler JP 3rd. Hyperpolarized helium-3 magnetic resonance lung imaging of non-sedated infants and young children: a proof-of-concept study. *Clin Imaging* 2017 Sep - Oct;45:105-110.

[79] Stejskal EO. Use of Spin Echoes in a Pulsed Magnetic-Field Gradient to Study Anisotropic, Restricted Diffusion and Flow. *J Chem Phys* 1965;43,3597-3603.

[80] Saam BT, Yablonskiy DA, Kodibagkar VD, Leawoods JC, Gierada DS, Cooper JD, Lefrak SS, Conradi MS. MR imaging of diffusion of (3)He gas in healthy and diseased lungs. *Magn Reson Med* 2000 Aug;44(2):174-9.

[81] Basser PJ, Mattiello J, LeBihan D. MR diffusion tensor spectroscopy and imaging. *Biophys J* 1994 Jan;66(1):259-67.

[82] Yablonskiy DA, Sukstanskii AL, Leawoods JC, Gierada DS, Bretthorst GL, Lefrak SS, Cooper JD, Conradi MS. Quantitative in vivo assessment of lung microstructure at the alveolar level with hyperpolarized 3He diffusion MRI. *Proc Natl Acad Sci U S A* 2002 Mar 5;99(5):3111-6.

[83] Fain SB, Altes TA, Panth SR, Evans MD, Waters B, Mugler JP 3rd, Korosec FR, Grist TM, Silverman M, Salerno M, Owers-Bradley J. Detection of age-dependent changes in healthy adult lungs with diffusion-weighted [3]He MRI. *Acad Radiol* 2005 Nov;12(11):1385-93.

[84] Thomen RP, Quirk JD, Roach D, Egan-Rojas T, Ruppert K, Yusen RD, Altes TA, Yablonskiy DA, Woods JC. Direct comparison of [129]Xe diffusion measurements with quantitative histology in human lungs. *Magn Reson Med* 2017 Jan;77(1):265-272.

[85] Weibel E. The Lung: Scientific Foundations. Eds. Crystal RG, West JB, Barnes PJ, Cherniack NS. Raven, New York, 1991; pp. 711-720.

[86] Sukstanskii AL, Yablonskiy DA. In vivo lung morphometry with hyperpolarized 3He diffusion MRI: theoretical background. *J Magn Reson* 2008 Feb;190(2):200-10.

[87] Lord A, Shapiro AJ, Saint-Martin C, Claveau M, Melançon S, Wintermark P. Filamin A mutation may be associated with diffuse lung disease mimicking bronchopulmonary dysplasia in premature newborns. *Respir Care* 2014 Nov;59(11):e171-7.

[88] Walkup LL, Thomen RP, Akinyi TG, Watters E, Ruppert K, Clancy JP, Woods JC, and Cleveland ZI. Feasibility, tolerability and safety of pediatric hyperpolarized ^{129}Xe magnetic resonance imaging in healthy volunteers and children with cystic fibrosis. *Pediatr Radiol* 2016;46(12):1651-1662.

[89] Lutey B, Lefrack S, Woods J, et al. Hyperpolarized ^{3}He MR imaging: physiologic monitoring observations and safety considerations in 100 consecutive subjects. *Radiol* 2008;248(2):655-661.

[90] Driehuys B, Martinez-Jimenez S, Cleveland Z, et al. Chronic obstructive pulmonary disease: safety and tolerability of hyperpolarized ^{129}Xe MR imaging in healthy volunteers and patients. *Radiol* 2012;262(1):279-89.

[91] Cleveland ZI, Cofer GP, Metz G, Beaver D, Nouls J, Kaushik SS, Kraft M, Wolber J, Kelly KT, McAdams HP, Driehuys B. Hyperpolarized Xe MR imaging of alveolar gas uptake in humans. *PLoS One* 2010 Aug 16;5(8):e12192.

[92] Cleveland ZI, Möller HE, Hedlund LW, Nouls JC, Freeman MS, Qi Y, Driehuys B. In vivo MR imaging of pulmonary perfusion and gas exchange in rats via continuous extracorporeal infusion of hyperpolarized 129Xe. *PLoS One* 2012;7(2):e31306.

[93] Kaushik SS, Freeman MS, Cleveland ZI, Davies J, Stiles J, Virgincar RS, Robertson SH, He M, Kelly KT, Foster WM, McAdams HP, Driehuys B. Probing the regional distribution of pulmonary gas exchange through single-breath gas- and dissolved-phase 129Xe MR imaging. *J Appl Physiol* 2013 Sep;115(6):850-60.

[94] Kaushik SS, Freeman MS, Yoon SW, Liljeroth MG, Stiles JV, Roos JE, Foster W, Rackley CR, McAdams HP, Driehuys B. Measuring diffusion limitation with a perfusion-limited gas--hyperpolarized 129Xe gas-transfer spectroscopy in patients with idiopathic pulmonary fibrosis. *J Appl Physiol* 2014 Sep 15;117(6):577-85.

[95] Altes TA and de Lange EE. Applications of hyperpolarized helium-3 gas magnetic resonance imaging in pediatric lung disease. *Top Magn Reson Imaging* 2003;14:231–236.

[96] Altes TA, Mata J, de Lange EE, et al. Assessment of lung development using hyperpolarized helium-3 diffusion MR imaging. *J Magn Reson Imaging* 2006;24:1277–1283.

[97] Altes TA, Mata J, Froh DK, et al. Abnormalities of lung structure in children with brochopulmonary dysplasia as assessed by diffusion hyperpolarized helium-3 MRI. *Proc Intl Soc Magn Reson Med* 2006;14:86.

[98] Kirby M, Coxson HO, and Parraga G. Pulmonary functional magnetic resonance imaging for paediatric lung disease. *Paediatr Respir Rev* 2013;14:180–9.

[99] de Lange EE, Altes TA, Patrie JT, et al. The variability of regional airflow obstruction within the lungs of patients with asthma: assessment with hyperpolarized helium-3 magnetic resonance imaging. *J Allergy Clin Immunol* 2007;119:1072–1078.

[100] McMahon CJ, Dodd JD, Hill C, et al. Hyperpolarized 3-helium magnetic resonance ventilation imaging of the lung in cystic fibrosis: comparison with high resolution CT and spirometry. *Eur Radiol* 2006;16:2483–2490.

[101] van Beek EJ, Hill C,Woodhouse N, et al. Assessment of lung disease in children with cystic fibrosis using hyperpolarized 3- helium MRI: comparison with Shwachman score, Chrispin- Norman score and spirometry. *Eur Radiol* 2007;17:1018–1024.

[102] Woodhouse N, Wild JM, van Beek EJ, et al. Assessment of hyperpolarized ^{3}He lung MRI for regional evaluation of interventional therapy: a pilot study in pediatric cystic fibrosis. *J Magn Reson Imaging* 2009;30:981–988.

[103] Koumellis P, van Beek EJ, Woodhouse N, et al. Quantitative analysis of regional airways obstruction using dynamic hyperpolarized ^{3}He MRI-preliminary results in children with cystic fibrosis. *J Magn Reson Imaging* 2005;22:420–426.

[104] Sun Y, O'Sullivan BP, Roche JP, et al. Using hyperpolarized ^{3}He MRI to evaluate treatment efficacy in cystic fibrosis patients. *J Magn Reson Imaging* 2011;34:1206–1211.

[105] Narayanan M, Beardsmore CS, Owers-Bradley J, et al. Catch-up alveolarization in ex-preterm children: evidence from (3)He magnetic resonance. *Am J Respir Crit Care Med* 2013;187: 1104–1109.

[106] Caught by Surprise: Causes and Consequences of the Helium-3 Supply Crisis. Hearing 73 before the Committee on Science and Technology, April 22, 2010, 74.

[107] Hersman FW, Ruset IC, Ketel S et al. Large production system for hyperpolarized ^{129}Xe for human lung imaging studies. Acad Radiol 2008;15:683–692.

[108] Korchak SE, Kilian W, and Mitschang L. Configuration and performance of a mobile (129)Xe polarizer. Appl Magn Reson 2013;44:65–80.

[109] Nikolaou P, Coffey AM, Walkup LL, et al. A 3D-printed high power nuclear spin polarizer. J Am Chem Soc 2014;136:1636–1642.

[110] Stewart NJ, Norquay G, Griffiths PD, et al.Feasibility of human lung ventilation imaging using highly polarized naturally abundant xenon and optimized three-dimensional steady-state free precession. Magn Reson Med 2015;74:346–352.

[111] Chen RY, Fan FC, Kim S, et al. Tissue-blood partition coefficient for xenon: temperature and hematocrit dependence. *J Appl Physiol Respir Environ Exerc Physiol* 1980;49:178–183.

[112] Sanders RD, Franks NP, and Maze M. Xenon: no stranger to anaesthesia. *Br J Anaesth* 2003;91:709–717.

[113] Nakata Y, Goto T, Ishiguro Y, et al. Minimum alveolar concentration (MAC) of xenon with sevoflurane in humans. *Anesthesiol* 2001;94:611–614.

[114] Shukla Y, Wheatley A, Kirby M, et al. Hyperpolarized [129]Xe magnetic resonance imaging: tolerability in healthy volunteers and subjects with pulmonary disease. *Acad Radiol* 2012;19:941–951.

[115] Hatabu H, Alsop DC, Listerud J, Bonnet M, Gefter WB. T_2* and proton density measurement of normal human lung parenchyma using submillisecond echo time gradient echo magnetic resonance imaging. *Eur J Radiol* 1999;29(3):245-252.

[116] Ohno Y, Koyama H, Yoshikawa T, Matsumoto K, Takahashi M, Van Cauteren M, Sugimura K. T_2* measurements of 3-T MRI with ultrashort TEs: capabilities of pulmonary function assessment and clinical stage classification in smokers. *AJR Am J Roentgenol* 2011;197(2):W279-285.

[117] Stock KW, Chen Q, Hatabu H, Edelman RR. Magnetic resonance T_2* measurements of the normal human lung in vivo with ultra-short echo times. *Magn Reson Imaging* 1999;17(7):997-1000.

[118] Theilmann RJ, Arai TJ, Samiee A, Dubowitz DJ, Hopkins SR, Buxton RB, Prisk GK. Quantitative MRI measurement of lung density must account for the change in T(2) (*) with lung inflation. *J Magn Reson Imaging* 2009;30(3):527-534.

[119] Yu J, Xue Y, Song HK. Comparison of lung T_2* during free-breathing at 1.5 T and 3.0 T with ultrashort echo time imaging. *Magn Reson Med* 2011;66(1):248-254.

[120] Vandenborne K, Walter G, Ploutz-Snyder L, Dudley G, Elliott MA, De Meirleir K. Relationship between muscle T_2* relaxation properties and metabolic state: a combined localized ^{31}P-spectroscopy and 1H-imaging study. *Eur J Appl Physiol* 2000;82(1-2):76-82.

[121] Kruger SJ, Fain SB, Johnson KM, Cadman RV, Nagle SK. Oxygen-enhanced 3D radial ultrashort echo time magnetic resonance imaging in the healthy human lung. *NMR Biomed* 2014;27(12):1535-1541.

[122] Stadler A, Jakob PM, Griswold M, Barth M, Bankier AA. T_1 mapping of the entire lung parenchyma: Influence of the respiratory phase in healthy individuals. *J Magn Reson Imaging* 2005;21(6):759-764.

[123] Schopper MA, Walkup LL, Tkach JA, Higano NS, Lim FY, Haberman B, Woods JC, Kingma PS. Evaluation of Neonatal Lung Volume Growth by Pulmonary Magnetic Resonance Imaging in Patients with Congenital Diaphragmatic Hernia. *J Pediatr* 2017 Sep;188:96-102.e1.

[124] Walkup LL, Tkach JA, Higano NS, et al. Quantitative magnetic resonance imaging of bronchopulmonary dysplasia in the neonatal intensive care unit environment. *Am J Resp Crit Care Med* 2015;192(10):1215–1222.

[125] Stahl M, Wielpütz MO, Graeber SY, Joachim C, Sommerburg O, Kauczor HU, Puderbach M, Eichinger M, Mall MA. Comparison of Lung Clearance Index and Magnetic Resonance Imaging for Assessment of Lung Disease in Children with Cystic Fibrosis. *Am J Respir Crit Care Med* 2017 Feb 1;195(3):349-359.

[126] Dournes G, Grodzki D, Macey J, Girodet PO, Fayon M, Chateil JF, Montaudon M, Berger P, Laurent F. Quiet Submillimeter MR Imaging of the Lung Is Feasible with a PETRA Sequence at 1.5 T. *Radiology* 2015;276(1):258-265.

[127] Gibiino F, Sacolick L, Menini A, Landini L, Wiesinger F. Free-breathing, zero-TE MR lung imaging. *MAGMA* 2015;28(3):207-215.

[128] Johnson KM, Fain SB, Schiebler ML, Nagle S. Optimized 3D ultrashort echo time pulmonary MRI. *Magn Reson Med* 2013;70(5):1241-1250.

[129] Lederlin M, Cremillieux Y. Three-dimensional assessment of lung tissue density using a clinical ultrashort echo time at 3 tesla: a feasibility study in healthy subjects. *J Magn Reson Imaging* 2014;40(4):839-847.

[130] Volker M, Ehses P, Weick S, Breuer FA, Blaimer M, Hintze C, Biederer J, Jakob PM. Free breathing 1H MRI of the human lung with an improved radial turbo spin-echo. *MAGMA* 2015;28(3):227-238.

[131] Glover GH, Pauly JM. Projection reconstruction techniques for reduction of motion effects in MRI. *Magn Reson Med* 1992;28(2):275-289.

[132] Weiger M, Brunner DO, Dietrich BE, Müller CF, Pruessmann KP. ZTE imaging in humans. *Magn Reson Med* 2013 Aug;70(2):328-32.

[133] Bauman G, Johnson KM, Bell LC, Velikina JV, Samsonov AA, Nagle SK, Fain SB. Three-dimensional pulmonary perfusion MRI with radial ultrashort echo time and spatial-temporal constrained reconstruction. *Magn Reson Med* 2015;73(2):555-564.

[134] Bianchi A, Dufort S, Fortin PY, Lux F, Raffard G, Tassali N, Tillement O, Coll JL, Cremillieux Y. In vivo MRI for effective non-invasive detection and follow-up of an orthotopic mouse model of lung cancer. *NMR Biomed* 2014;27(8):971-979.

[135] Higano NS, Hahn AD, Tkach JA, Cao X, Walkup LL, Thomen RP, Merhar SL, Kingma PS, Fain SB, and Woods JC. Retrospective respiratory self-gating and removal of bulk motion in pulmonary UTE MRI of neonates and adults. *Magn Reson Med* 2017 Mar;77(3):1284-1295.

[136] Dournes G, Menut F, Macey J, et al. Lung morphology assessment of cystic fibrosis using MRI with ultra-short echo time at submillimeter spatial resolution. *Eur Radiol* 2016;26(11):3811-3820.

[137] Sileo C, Corvol H, Boelle PY, Blondiaux E, Clement A, Ducou Le Pointe H. HRCT and MRI of the lung in children with cystic fibrosis: comparison of different scoring systems. *J Cyst Fibros* 2014;13:198-204

[138] Roach DJ, Crémillieux Y, Fleck RJ, Brody AS, Serai SD, Szczesniak RD, Kerlakian S, Clancy JP, Woods JC. Ultrashort echo-time magnetic resonance imaging is a sensitive method for the evaluation of early cystic fibrosis lung disease. *Ann Am Thorac Soc* 2016;13(11):1923-1931.

[139] Higano NS, Fleck RJ, Spielberg DR, Walkup LL, Hahn AD, Tkach JA, Merhar SL, Kingma PS, Fain SB, Woods JC. Quantitative characterization of bronchopulmonary dysplasia severity using neonatal pulmonary MRI and correlation to short-term outcomes. Proceedings of the Radiological Society of North America, Chicago 2017.

[140] Hahn AD, Higano NS, Walkup LL, et al. Pulmonary MRI of neonates in the intensive care unit using 3D ultrashort echo time and a small foot-print MRI system. *J Magn Reson Imag* 2017;45(2):463-471.

[141] Duyn JH, Yang Y, Frank JA, van der Veen JW. Simple correction method fork-space trajectory deviations in MRI. *J Magn Reson Imaging* 1998;132:150–153.

[142] Larson AC, White RD, Laub G, McVeigh ER, Li D, Simonetti OP. Self-gated cardiac cine MRI. *Magn Reson Med* 2004 Jan;51(1):93-102.

[143] Hu P, Hong S, Moghari MH, Goddu B, Goepfert L, Kissinger KV, Hauser TH, Manning WJ, Nezafat R. Motion correction using coil arrays (MOCCA) for free-breathing cardiac cine MRI. *Magn Reson Med* 2011 Aug;66(2):467-75.

[144] Lee GR, Chen Y, Gulani V. A correlation based approach to respiratory self navigation for multi channel non-Cartesian MRI. *Proc Intl Soc Magn Reson Med* 2015;0585.

[145] Tibiletti M, Paul J, Bianchi A, Wundrak S, Rottbauer W, Stiller D, Rasche V. Multistage three-dimensional UTE lung imaging by image-based self-gating. *Magn Reson Med* 2016 Mar;75(3):1324-32.

[146] Tibiletti M, Kjørstad Å, Bianchi A, Schad LR, Stiller D, Rasche V. Multistage self-gated lung imaging in small rodents. *Magn Reson Med* 2016 Jun;75(6):2448-54.

[147] Tibiletti M, Bianchi A, Kjørstad Å, Wundrak S, Stiller D, Rasche V. Respiratory self-gated 3D UTE for lung imaging in small animal MRI. *Magn Reson Med* 2017 Aug;78(2):739-745.

[148] Fogel MA, Pawlowski TW, Harris MA, Whitehead KK, Keller MS, Wilson J, Tipton D, Harris C. Comparison and usefulness of cardiac magnetic resonance versus computed tomography in infants six months of age or younger with aortic arch anomalies without deep sedation or anesthesia. *Am J Cardiol* 2011;108(1):120–125.

[149] Laing AI, Teele RL, Stark AR. Diaphragmatic movement in newborn infants. *J Pediatr* 1988;112(4):638–643.

[150] Vasanawala SS, Iwadate Y, Church DG, Herfkens RJ, Brau AC. Navigated abdominal

T1 MRI permits free-breathing image acquisition with less motion artifacts. *Pediatr Radiol* 2010;40(3):340–344.

[151] Ingle RR, Santos JM, Overall WR, McConnell MV, Hu BS, Nishimura DG. Self-gated fat-suppressed cardiac cine MRI. *Magn Reson Med* 2015;73(5):1764–1774.

[152] Liu J, Spincemaille P, Codella NC, Nguyen TD, Prince MR, Wang Y. Respiratory and cardiac self-gated free-breathing cardiac CINE imaging with multiecho 3D hybrid radial SSFP acquisition. *Magn Reson Med* 2010;63(5):1230–1237.

[153] Oechsner M, Pracht ED, Staeb D, Arn€old JF, Kostler H, Hahn D, Beer M, Jakob PM. Lung imaging under free-breathing conditions. *Magn Reson Med* 2009;61(3):723–727.

[154] Paul J, Divkovic E, Wundrak S, Bernhardt P, Rottbauer W, Neumann H, Rasche V. High-resolution respiratory self-gated golden angle cardiac MRI: comparison of self-gating methods in combination with k-t SPARSE SENSE. *Magn Reson Med* 2015;73(1):292–298.

[155] Axel L, Summers RM, Kressel HY, Charles C. Respiratory effects in two-dimensional Fourier transform MR imaging. *Radiology* 1986; 160(3):795–801.

[156] Weick S, Breuer FA, Ehses P, V€olker M, Hintze C, Biederer J, Jakob PM. DC-gated high resolution three-dimensional lung imaging during free-breathing. *J Magn Reson Imaging* 2013;37(3):727–732.

[157] Uribe S, Muthurangu V, Boubertakh R, Schaeffter T, Razavi R, Hill DL, Hansen MS. Whole-heart cine MRI using real-time respiratory self-gating. *Magn Reson Med* 2007;57(3):606–613.

[158] Uribe S, Tejos C, Razavi R, Schaeffter T. New respiratory gating technique for whole

heart cine imaging: integration of a navigator slice in steady state free precession sequences. *J Magn Reson Imaging* 2011; 34(1):211–219.

[159] Castillo R, Castillo E, Martinez J, Guerrero T. Ventilation from fourdimensional computed tomography: density versus Jacobian methods. *Phys Med Biol* 2010;55(16):4661–4685.

[160] Savitzky A, Golay MJE. Smoothing and differentiation of data by simplified least squares procedures. *Anal Chem* 1964;36:1627.

[161] Keszler M, Abubakar K. Volume guarantee: stability of tidal volume and incidence of hypocarbia. *Pediatr Pulmonol* 2004;38(3):240-245.

[162] Yushkevich PA, Piven J, Hazlett HC, Smith RG, Ho S, Gee JC, and Gerig G. User-guided 3D active contour segmentation of anatomical structures: Significantly improved efficiency and reliability. *Neuroimage* 2006 1;31(3):1116-28.

[163] Piccinelli M, Veneziani A, Steinman DA, Remuzzi A, Antiga L. A framework for geometric analysis of vascular structures: application to cerebral aneurysms. *IEEE Trans Med Imaging* 2009;28(8):1141-55.

[164] Bates AJ, Comerford A, Cetto R, Schroter RC, Tolley NS, and Doorly DJ. Power loss mechanisms in pathological tracheas. *J Biomech* 2016;49(11):2187-2192.

[165] Bates AJ, Cetto R, Doorly DJ, Schroter RC, Tolley NS, and Comerford A. The effects of curvature and constriction on airflow and energy loss in pathological tracheas. *Respir Physiol Neurobiol* 2016;234:69-78.

[166] Bates AJ, Comerford A, Cetto R, Doorly DJ, Schroter RC, and Tolley NS. Computational fluid dynamics benchmark dataset of airflow in tracheas. *Data Brief* 2017;10:101-7.

[167] Hamilton NJ, Kanani M, Roebuck DJ, et al. Tissue-Engineered Tracheal Replacement in a Child: A 4-Year Follow-Up Study. *Am J Transplant* 2015;15(10):2750-7.

[168] Bates AJ, Schuh A, Amine-Edine G, McConnell K, Loew W, Fleck RJ, Woods JC, Dumoulin CL, Amin RS. Assessing the Relationship Between Movement and Airflow in the Upper Airway using Computational Fluid Dynamics with Motion Determined from Magnetic Resonance Imaging. *Clin Biomech* 2017. pii: S0268-0033(17)30223-1. doi: 10.1016/j.clinbiomech.2017.10.011. [Epub ahead of print]

[169] Rueckert D, Sonoda LI, Hayes C, Hill DL, Leach MO, Hawkes DJ. Nonrigid registration using free-form deformations: application to breast MR images. *IEEE Trans Med Imaging* 1999;18(8):712-21.

[170] Bates AJ, Doorly DJ, Cetto R, Calmet H, Gambaruto AM, Tolley NS, Houzeaux G, and Schroter RC. Dynamics of airflow in a short inhalation. *J R Soc Interface* 2015;12(102):20140880.

[171] Calmet H, Gambaruto AM, Bates AJ, Vazquez M, Houzeaux G, and Doorly DJ. Large-scale CFD simulations of the transitional and turbulent regime for the large human airways during rapid inhalation. *Comput Biol Med* 2016;69:166-80.

[172] Higano NS, Bates AJ, Tkach JA, Fleck RJ, Lim F, Woods JC, and Kingma PS. Pre- and post-surgical repair visualization of neonatal esophageal atresia/tracheoesophageal fistula via magnetic resonance imaging: a case series. *J Pediatr Surger Case Reports* 2018; https://doi.org/10.1016/j.epsc.2017.10.001 [accepted Oct 2017].

[173] Hedenstierna G, Lundquist H, Lundh B, Tokics L, Strandberg A, Brismar B, Frostell C. Pulmonary densities during anaesthesia: an experimental study on lung morphology and gas exchange. *Euro Respir J* 1989;2(6):528–535.

[174] Deng Z, Pang J, Yang W, Yue Y, Sharif B, Tuli R, Li D, Fraass B, Fan Z. Four-dimensional MRI using three-dimensional radial sampling with respiratory self-gating to characterize temporal phase-resolved respiratory motion in the abdomen. *Magn Reson Med* 2016 Apr;75(4):1574-85.

[175] Aliverti A, Pennati F, Salito C, Woods JC. Regional lung function and heterogeneity of specific gas volume in healthy and emphysematous subjects. *Eur Respir J* 2013;41(5):1179–1188.

[176] Pennati F, Salito C, Baroni G, Woods J, Aliverti A. Comparison between multi-volume CT-based surrogates of regional ventilation in healthy subjects. *Acad Radiol* 2014;21(10):1268–1275.

[177] Simon BA. Non-invasive imaging of regional lung function using x-ray computed tomography. *J Clin Monit* 2000;16:433–442.

[178] Hayhurst MD, MacNee W, Flenley DC, Wright D, McLean A, Lamb D, Wightman AJ, Best J. Diagnosis of pulmonary emphysema by computerised tomography. *Lancet* 1984;2(8398):320-2.

[179] Nakata M, Saeki H, Takata I, Segawa Y, Mogami H, Mandai K, Eguchi K. Focal ground-glass opacity detected by low-dose helical CT. *Chest* 2002;121(5):1464-7.

[180] Pennati F, Quirk JD, Yablonskiy DA, Castro M, Aliverti A, Woods JC. Assessment of regional lung function with multivolume (1)H MR imaging in health and obstructive lung disease: comparison with (3)He MR imaging. *Radiology* 2014;273(2):580–590.

[181] Pennati F, Salito C, Roach D, Clancy JP, Woods JC, Aliverti A. Regional ventilation in infants quantified by multi-volume high resolution computed tomography (HRCT) and

multi-volume proton magnetic resonance imaging (MRI). *Eur Respir J* 2015;46(suppl 59):OA2949.

[182] Higano NS, Walkup LL, Hahn AD, Thomen RP, Merhar SL, Kingma PS, Tkach JA, Fain SB, and Woods JC. Quantification of Neonatal Lung Parenchymal Density via Ultrashort Echo Time MRI with Comparison to CT. *J Magn Reson Imaging* 2017 Oct;46(4):992-1000.

[183] Mendez J, Keys A. Density and Composition of Mammalian Muscle. Metabolism 1960;9:184-188.

[184] Roach DJ, Crémillieux Y, Serai SD, Thomen RP, Wang H, Zou Y, Szczesniak RD, Benzaquen S, Woods JC. Morphological and quantitative evaluation of emphysema in chronic obstructive pulmonary disease patients: A comparative study of MRI with CT. *J Magn Reson Imag* 2016;44(6):1656-1663.

[185] Jakob PM, Hillenbrand CM, Wang T, Schultz G, Hahn D, Haase A. Rapid quantitative lung (1)H T(1) mapping. *J Magn Reson Imaging* 2001;14(6):795-9.

[186] Gold GE, Han E, Stainsby J, Wright G, Brittain J, Beaulieu C. Musculoskeletal MRI at 3.0 T: relaxation times and image contrast. *AJR AM J Roentgenol* 2004;183(2):343-51.

[187] Ochiai M, Hikino S, Yabuuchi H, et al. A new scoring system for computed tomography of the chest for assessing the clinical status of bronchopulmonary dysplasia. *J Pediatr* 2008;152(1):90–5, 95.e91–3.

[188] Galbán CJ, Han MK, Boes JL, et al. Computed tomography-based biomarker provides unique signature for diagnosis of COPD phenotypes and disease progression. *Nat Med* 2012;18(11):1711-5.

[189] Heussel CP, Kappes J, Hantusch R, et al. Contrast enhanced CT-scans are not compa-
        rable to non-enhanced scans in emphysema quantification. *Eur J Radiol* 2010;74(3):473-
        8.

[190] Stein J, Walkup LL, Brody AS, Fleck RA, Woods JC. Quantitative CT character-
        ization of pediatric lung development using routine clinical imaging. *Pediatr Radiol*
        2016;46(13):1804-1812.

[191] Walkup LL, Woods JC. Newer Imaging Techniques for Bronchopulmonary Dysplasia.
        Clin Perinatol 2015 Dec;42(4):871-87.

[192] Moore PE, Poston JT, Boyer D, et al. ATS Core Curriculum 2017: Part II. Pediatric
        Pulmonary Medicine. *Ann Am Thorac Soc* 2017 Aug;14(Supplement_2):S165-S181.

[193] van Mastrigt E, Logie K, Ciet P, Reiss IK, Duijts L, Pijnenburg MW, Tiddens HA.
        Lung CT imaging in patients with bronchopulmonary dysplasia: A systematic review.
        Pediatr Pulmonol 2016;51(9):975-86.

[194] Hoffman EA, Reinhardt JM, Sonka M, et al. Characterization of the interstitial lung
        diseases via density-based and texture-based analysis of computed tomography images
        of lung structure and function. *Acad Radiol* 2003;10(10):1104-18.

[195] Jacob J, Bartholmai BJ, Brun AL, Egashira R, Rajagopalan S, Karwoski R, Kouranos
        V, Kokosi M, Hansell DM, Wells AU. Evaluation of visual and computer-based CT
        analysis for the identification of functional patterns of obstruction and restriction in
        hypersensitivity pneumonitis. *Respirology* 2017 Nov;22(8):1585-1591.

Copyright Clearance Permissions

Copyright permissions have been obtained for all prose and figures used in this dissertation which have been published in textbooks or peer-reviewed journals. See below for copyright permission statements from [4, 8, 68, 135, 172, 182].

This Agreement between Nara Higano ("You") and Elsevier ("Elsevier") consists of your license details and the terms and conditions provided by Elsevier and Copyright Clearance Center.

License Number	4243080604463
License date	Dec 06, 2017
Licensed Content Publisher	Elsevier
Licensed Content Publication	Elsevier Books
Licensed Content Title	Murray and Nadel's Textbook of Respiratory Medicine
Licensed Content Author	John M. Shannon,Kathryn A. Wikenheiser-Brokamp,James M. Greenberg
Licensed Content Date	Jan 1, 2016
Licensed Content Volume	n/a
Licensed Content Issue	n/a
Licensed Content Pages	14
Start Page	22
End Page	31.e4
Type of Use	reuse in a thesis/dissertation
Intended publisher of new work	other
Portion	figures/tables/illustrations
Number of figures/tables/illustrations	1
Format	both print and electronic
Are you the author of this Elsevier chapter?	No
Will you be translating?	No
Original figure numbers	Figure 2-1
Title of your thesis/dissertation	Investigation of Neonatal Pulmonary Structure and Function via Proton and Hyperpolarized Gas Magnetic Resonance Imaging
Expected completion date	Dec 2017
Estimated size (number of pages)	180
Requestor Location	Nara Higano 3333 Burnet Ave ML 5033 CINCINNATI, OH 45229 United States Attn: Nara Higano
Publisher Tax ID	98-0397604
Billing Type	Invoice
Billing Address	Nara Higano 3333 Burnet Ave ML 5033 CINCINNATI, OH 45229 United States Attn: Nara Higano
Total	0.00 USD

This Agreement between Nara Higano ("You") and Elsevier ("Elsevier") consists of your license details and the terms and conditions provided by Elsevier and Copyright Clearance Center.

License Number	4243080019969
License date	Dec 06, 2017
Licensed Content Publisher	Elsevier
Licensed Content Publication	Elsevier Books
Licensed Content Title	Murray and Nadel's Textbook of Respiratory Medicine
Licensed Content Author	Frank L. Powell,Peter D. Wagner,John B. West
Licensed Content Date	Jan 1, 2016
Licensed Content Volume	n/a
Licensed Content Issue	n/a
Licensed Content Pages	35
Start Page	44
End Page	75.e3
Type of Use	reuse in a thesis/dissertation
Portion	figures/tables/illustrations
Number of figures/tables/illustrations	2
Format	both print and electronic
Are you the author of this Elsevier chapter?	No
Will you be translating?	No
Original figure numbers	Figure 4-1, Figure 4-2
Title of your thesis/dissertation	Investigation of Neonatal Pulmonary Structure and Function via Proton and Hyperpolarized Gas Magnetic Resonance Imaging
Expected completion date	Dec 2017
Estimated size (number of pages)	180
Requestor Location	Nara Higano 3333 Burnet Ave ML 5033 CINCINNATI, OH 45229 United States Attn: Nara Higano
Publisher Tax ID	98-0397604
Billing Type	Invoice
Billing Address	Nara Higano 3333 Burnet Ave ML 5033 CINCINNATI, OH 45229 United States Attn: Nara Higano
Total	0.00 USD

This Agreement between Nara Higano ("You") and Elsevier ("Elsevier") consists of your license details and the terms and conditions provided by Elsevier and Copyright Clearance Center.

License Number	4220800334105
License date	Nov 02, 2017
Licensed Content Publisher	Elsevier
Licensed Content Publication	Pharmacology & Therapeutics
Licensed Content Title	Environmental factors and developmental outcomes in the lung
Licensed Content Author	Radhika Kajekar
Licensed Content Date	May 1, 2007
Licensed Content Volume	114
Licensed Content Issue	2
Licensed Content Pages	17
Start Page	129
End Page	145
Type of Use	reuse in a thesis/dissertation
Portion	figures/tables/illustrations
Number of figures/tables/illustrations	1
Format	both print and electronic
Are you the author of this Elsevier article?	No
Will you be translating?	No
Original figure numbers	Fig. 1
Title of your thesis/dissertation	Investigation of Neonatal Pulmonary Structure and Function via Proton and Hyperpolarized Gas Magnetic Resonance Imaging
Expected completion date	Dec 2017
Estimated size (number of pages)	180
Requestor Location	Nara Higano 3333 Burnet Ave ML 5033 CINCINNATI, OH 45229 United States Attn: Nara Higano
Publisher Tax ID	98-0397604
Total	0.00 USD

This Agreement between Nara Higano ("You") and John Wiley and Sons ("John Wiley and Sons") consists of your license details and the terms and conditions provided by John Wiley and Sons and Copyright Clearance Center.

License Number	4220360873113
License date	Nov 01, 2017
Licensed Content Publisher	John Wiley and Sons
Licensed Content Publication	Concepts in Magnetic Resonance: Part A, Bridging Education and Research
Licensed Content Title	A novel switched frequency 3He/1H high-pass birdcage coil for imaging at 1.5 tesla
Licensed Content Author	Ronald Pratt,Randy Giaquinto,Christopher Ireland,Barret Daniels,Wolfgang Loew,Nara Higano,Xuefeng Cao,Robert Thomen,Jason Woods,Charles L. Dumoulin
Licensed Content Date	Oct 6, 2015
Licensed Content Pages	9
Type of use	Dissertation/Thesis
Requestor type	Author of this Wiley article
Format	Print and electronic
Portion	Full article
Will you be translating?	No
Title of your thesis / dissertation	Investigation of Neonatal Pulmonary Structure and Function via Proton and Hyperpolarized Gas Magnetic Resonance Imaging
Expected completion date	Dec 2017
Expected size (number of pages)	180
Requestor Location	Nara Higano 3333 Burnet Ave ML 5033 CINCINNATI, OH 45229 United States Attn: Nara Higano
Publisher Tax ID	EU826007151
Billing Type	Invoice
Billing Address	Nara Higano 3333 Burnet Ave ML 5033 CINCINNATI, OH 45229 United States Attn: Nara Higano
Total	0.00 USD

This Agreement between Nara Higano ("You") and John Wiley and Sons ("John Wiley and Sons") consists of your license details and the terms and conditions provided by John Wiley and Sons and Copyright Clearance Center.

License Number	4220360512192
License date	Nov 01, 2017
Licensed Content Publisher	John Wiley and Sons
Licensed Content Publication	Magnetic Resonance in Medicine
Licensed Content Title	Retrospective respiratory self-gating and removal of bulk motion in pulmonary UTE MRI of neonates and adults
Licensed Content Author	Nara S. Higano,Andrew D. Hahn,Jean A. Tkach,Xuefeng Cao,Laura L. Walkup,Robert P. Thomen,Stephanie L. Merhar,Paul S. Kingma,Sean B. Fain,Jason C. Woods
Licensed Content Date	Mar 12, 2016
Licensed Content Pages	12
Type of use	Dissertation/Thesis
Requestor type	Author of this Wiley article
Format	Print and electronic
Portion	Full article
Will you be translating?	No
Title of your thesis / dissertation	Investigation of Neonatal Pulmonary Structure and Function via Proton and Hyperpolarized Gas Magnetic Resonance Imaging
Expected completion date	Dec 2017
Expected size (number of pages)	180
Requestor Location	Nara Higano 3333 Burnet Ave ML 5033 CINCINNATI, OH 45229 United States Attn: Nara Higano
Publisher Tax ID	EU826007151
Billing Type	Invoice
Billing Address	Nara Higano 3333 Burnet Ave ML 5033 CINCINNATI, OH 45229 United States Attn: Nara Higano
Total	0.00 USD

ELSEVIER

Title: Pre- and post-operative visualization of neonatal esophageal atresia/tracheoesophageal fistula via magnetic resonance imaging

Author: Nara S. Higano,Alister J. Bates,Jean A. Tkach,Robert J. Fleck,Foong Y. Lim,Jason C. Woods,Paul S. Kingma

Publication: Journal of Pediatric Surgery Case Reports

Publisher: Elsevier

Date: February 2018

© 2017 The Authors. Published by Elsevier Inc.

This Agreement between Nara Higano ("You") and John Wiley and Sons ("John Wiley and Sons") consists of your license details and the terms and conditions provided by John Wiley and Sons and Copyright Clearance Center.

License Number	4220360755296
License date	Nov 01, 2017
Licensed Content Publisher	John Wiley and Sons
Licensed Content Publication	Journal of Magnetic Resonance Imaging
Licensed Content Title	Quantification of neonatal lung parenchymal density via ultrashort echo time MRI with comparison to CT
Licensed Content Author	Nara S. Higano,Robert J. Fleck,David R. Spielberg,Laura L. Walkup,Andrew D. Hahn,Robert P. Thomen,Stephanie L. Merhar,Paul S. Kingma,Jean A. Tkach,Sean B. Fain,Jason C. Woods
Licensed Content Date	Feb 3, 2017
Licensed Content Pages	9
Type of use	Dissertation/Thesis
Requestor type	Author of this Wiley article
Format	Print and electronic
Portion	Full article
Will you be translating?	No
Title of your thesis / dissertation	Investigation of Neonatal Pulmonary Structure and Function via Proton and Hyperpolarized Gas Magnetic Resonance Imaging
Expected completion date	Dec 2017
Expected size (number of pages)	180
Requestor Location	Nara Higano 3333 Burnet Ave ML 5033 CINCINNATI, OH 45229 United States Attn: Nara Higano
Publisher Tax ID	EU826007151
Billing Type	Invoice
Billing Address	Nara Higano 3333 Burnet Ave ML 5033 CINCINNATI, OH 45229 United States Attn: Nara Higano
Total	0.00 USD